

Dissertation zur Erlangung des Doktorgrades
der Fakultät für Chemie und Pharmazie der
Ludwig-Maximilians-Universität München

Nanotools for Cancer Research and Therapy

Bernhard Fabian Illes

aus

Weilheim i. OB, Deutschland

2020

Erklärung

Diese Dissertation wurde im Sinne von § 7 der Promotionsordnung vom 28. November 2011 von Frau Ass. Prof. Dr. Hanna Engelke betreut.

Eidesstattliche Versicherung

Diese Dissertation wurde eigenständig und ohne unerlaubte Hilfe erarbeitet.

München, 15.12.2020

Bernhard Illes

Dissertation eingereicht am: 28.10.2020

1. Gutachterin: Ass. Prof. Hanna Engelke

2. Gutachter: Prof. Stefan Zahler

Mündliche Prüfung am 01.12.2020

Danksagung

Zuallererst möchte ich Hanna dafür danken dass sie mich eingestellt hat, obwohl Flo meine einzige Referenz war. Auch für deine wunderbare Betreuung und deine Begabung auch den schlechtesten Ergebnissen noch etwas Positives abgewinnen zu können gebührt dir mein Dank. Ich denke man kann sich keine bessere Doktormutter wünschen: Ohne dich wäre das ganze hier sicher nicht passiert.

Stefan Zahler möchte ich herzlichst für die Übernahme des Zweitgutachtens und die gute Zusammenarbeit beim gemeinsamen YAP Projekt danken.

Bei Thomas möchte ich mich dafür bedanken dass er mich die ganzen Jahre über in seinen Büros und Labors hat arbeiten lassen und das er, obwohl es doch recht biochemisch wurde, stets großes Interesse an meinen Ausführungen in den Subgroupmeetings gezeigt.

Stefan Wuttke möchte ich dafür danken dass er bei den MOF Projekten ein starker Antrieb war, denn ohne ihn wären diese zwei Publikationen so wohl nicht entstanden. Dafür verzeihe ich ihm auch dass er ein Paper ohne SI eingereicht hat während ich im Urlaub war.

Regina und Corinna danke ich für die gute Organisation und das Übernahme von so einigem Papierkram und Tina für das Besorgen und Auffüllen von Chemikalien, aber auch für die Sorptions- und TGA Messungen.

Florian Gegenfurtner möchte ich für die qPCR und DNA Damage Experimente und generell dafür danken ein guter Kooperationspartner zu sein. Evelyn und Adrian möchte ich für die unermüdliche Suche nach schönen Antikörperstainingbildern danken und auch dafür, dass sie sich nicht haben entmutigen lassen.

Von meinen Mitdoktoranden gebührt der größte Dank natürlich Mo. Danke, dass du es die ganzen Jahre mit mir in einem Büro (mit kleiner Pause) ausgehalten hast. Das war sicher nicht immer einfach. Hat einen Riesenspaß mit dir gemacht und manchmal gab es a sogar ernste Gespräche darüber, was jetzt schon wieder nicht funktioniert hat. Flo Z und Daniel möchte ich dafür danken dass sie mich in ihrem Büro beherbergt haben auch nachdem plötzlich noch ein ägyptischer Gast aufgetaucht ist. Vielleicht kann man ja nochmal zusammen ein Radler trinken. Wastl gebührt zunächst dank für seine unermüdliche Aufgabe als Getränkeverantwortlicher,

aber auch darüber hinaus als Mittäter für die alljährlichen Weihnachtsverbrechen.

Von meinen Mesobiokollegen gilt der größte Dank Stefan und Noggi in deren Projekten ich mitwirken durfte und Patrick für die Kooperation bei den MOFs. Natürlich möchte ich auch der ganzen MesoBiosubgroup danken für die manchmal sogar hilfreichen Anmerkungen während der Subgroupmeetings und der Unterstützung.

Ich danke auch nochmal pauschal dem ganzen AK Bein für die schöne Zeit und vielleicht sieht man sich ja nochmal auf der ein oder anderen Feier, sobald es wieder geht.

Zuletzt möchte ich meine Eltern danken, dafür dass sie sich immer wieder meine Beschwerden angehört haben und mich unterstützt haben wo es nur ging, auch wenn das mit dem Doktor dann doch etwas länger gedauert hat als geplant.

Vielen Dank!

Abstract

Cancer remains one of the most dominant diseases and is responsible for almost 10 million deaths worldwide each year. To combat it, both a deeper understanding of its mechanisms and novel treatment options are necessary. In this work we present a new tool for cancer research and a variety of novel drug delivery systems.

Firstly, it is known that tumor progression and invasion are strongly influenced by the mechanical properties of the extracellular matrix. A key regulator of translating mechanical cues from the extracellular surroundings is the mechanotransduction protein Yes-associated protein (YAP). Although there is evidence that YAP plays a role in both tumor progression and metastasis, it is unclear as of yet, if YAP activation on its own is enough to trigger the onset of invasion. To investigate YAP's role in cancer invasion, we designed a research tool that is based on optogenetics. This tool – a photo-activatable YAP (optoYAP) - allows for spatio-temporal control of YAP's activation. As YAP is only active in the nucleus, the tool facilitates its activation via nuclear translocation upon an optical trigger. After activation, optoYAP induces downstream signaling for several hours. Additionally, its activation induces growth, leading to increased proliferation in two-dimensional and increased spheroid size in three-dimensional cultures. When applied to cancer spheroids, activation of optoYAP lead to invasion of the surrounding collagen matrix. Strikingly, site-selective activation of optoYAP in cancer spheroids exclusively leads to invasion from the activated site. This strongly hints at YAP activation being enough to trigger the onset of invasion.

Secondly, conventional chemotherapy involves systemic administration of toxic drugs at high dosage, which leads to severe adverse effects on the patient's health. One possible solution to prevent these negative effects is the reduction of the drug dosage through the direct delivery of anti-cancer drugs to the tumor. For this purpose, we designed a delivery system that is a synergistic combination of metal-organic framework (MOF) nanoparticles and exosomes for drug delivery, which takes advantage of the beneficial properties of each compound. This approach enables highly efficient drug loading of exosomes, by successfully coating drug-loaded MOF nanoparticles with exosomes via lipid fusion. The resulting exosome-

coated nanoparticles show an efficient release of their cargo after cell uptake with no premature leakage. Loading with a chemotherapeutic agent as biologically active cargo results in a steep decrease of cell viability. The proposed release mechanism is mainly based on the decomposition of the MOF nanocarrier. This, in combination with possible endogenous exosomal release mechanisms, allows for drug escape from the endosome. The combination of the chemical tunability of the MOF core and the cell-derived exosome shell provides a promising drug delivery platform for biomedical applications.

Thirdly, effective treatment of cancer is frequently hindered by resistances, which often require combination therapy for successful treatment. The main challenge drug carriers, e.g. liposomes, face in combination therapy, is the effective loading and retention of desired drug ratios. The potential of nanoparticle-based biomedicine for theranostic applications has increasingly come into the spotlight, as these systems offer potential solutions for the challenges, which limit success of conventional therapies. We present an effective, biocompatible and controlled drug delivery system with on-demand release abilities, and its usage as a versatile and powerful class of nanocarriers. To directly address the challenge of cancer resistance that results in the need for combination therapy, we made use of the previously developed liposome coated MOF nanoparticles. These hybrid nanoparticles combine the advantages of liposomes with the easy and efficient loading process of MOFs. Liposome coated MOF nanoparticles were successfully synthesized via the fusion method. Once loaded, the nanoparticles exhibit no premature leakage and an efficient release. We demonstrate their successful loading with both single and multiple drugs at the same time, which makes them a potential candidate for use in combination therapy.

Fourthly, we report the synthesis of a novel biocompatible and multifunctional drug delivery system. It is entirely build out of covalently crosslinked organic molecules. We crosslinked β -cyclodextrin structures with rigid organic linker molecules to obtain β -CD nanoparticles. These small, thermally stable and highly water-dispersable nanoparticles possess an accessible pore system. Covalently labeling them with dye molecules allowed for effective tracking of them in *in vitro* cell experiments. The β -CD nanoparticles show an incredibly fast cell-uptake within only 30 minutes in HeLa cells, which is based on rapid sugar-mediated cell-uptake kinetics. Furthermore, the particles were successfully loaded with various cargo molecules and possess

pH-responsive release behavior. Both nuclei staining with Hoechst 33342 dye as cargo and effective cell killing with doxorubicin as cargo was demonstrated in live-cell experiments. This nanocarrier system is a promising platform for the development of novel adaptable and highly biocompatible theranostic systems.

Lastly, another potential approach to overcome the inherent toxicity of conventional chemotherapeutics is the use of calcium phosphate and citrate. While both have been discussed as very promising, non-toxic anti-cancer agents, their development as therapeutics and specifically their successful administration has been hindered by the strict regulatory mechanisms of the cell. Here, we present the successful development of a novel administration system for the combinatorial administration of calcium, phosphate, and citrate. They are administered as colloidal nanoparticles (CPC) that can selectively kill cancer cells without the need for any inherently toxic drugs. The presented particles show no toxicity before the endosomal release nor after their degradation. This highly selective toxicity of CPCs was used to successfully treat two different aggressive pleural tumors in mice. After only two local applications tumor size was decreased by about 40% and 70%, respectively. The only sign of adverse effects was a slight pleural thickening effect after up to 8 applications during long term studies. These results are a breakthrough for the successful application of calcium and citrate in chemotherapeutics and a promising start for further refinement.

In summary, we have developed a novel tool to photocontrol YAP activity and induce growth in cells and potentially trigger the onset of invasion. Additionally we developed and characterized a variety of novel drug delivery systems: liposome coated MIL-88A nanoparticles proved suitable for drug delivery and showed high cell uptake and an efficient release in vitro, both for single and combination drug therapy approaches. We also developed a β -cyclodextrin based nanoparticle with fast cell uptake and successful delivery in vitro. Lastly, we created liposome coated calcium phosphate-citrate nanoparticles that proved to be highly selective towards cancer cells and showed strong anti-cancer effects both in vitro and in vivo.

Table of Contents

Chapter 1	2
Introduction	2
1.1 Cancer.....	3
1.1.1 Cancer Invasion and Metastasis	4
1.1.2 Mechanics of cancer: spread and invasion	6
1.2 Yes associated protein (YAP)	9
1.2.1 YAP's role in the cell	9
1.2.3 YAP's role in cancer.....	12
1.3 Photochemical control of cellular processes	14
1.3.1 Photocontrol based on natural photoreceptors.....	15
1.3.2 Photocontrol based on synthetic photoreceptors	16
1.4 Metal Organic Frameworks for Drug Delivery	18
1.4.1 Metal Organic Frameworks	18
1.4.2 MOFs as Drug Carriers.....	19
1.5 References	22
Chapter 2	32
Characterization Methods	32
2.1 X-Ray Diffraction.....	33
2.2 Nuclear Magnetic Resonance Spectroscopy.....	34
2.3 Dynamic Light Scattering.....	35
2.4 Zeta Potential.....	36
2.5 Thermogravimetric Analysis (TGA)	37
2.6 UV-Vis Spectroscopy.....	38
2.7 Fluorescence Spectroscopy.....	39
2.8 Fluorescence Microscopy and Confocal Microscopy	40
2.9 Sorption Analysis.....	42
2.10 Scanning Electron Microscopy and Transmission Electron Microscopy	45
2.11 Polymerase Chain Reaction	48
2.12 References	49
Chapter 3	50
Spatio-selective activation of nuclear translocation of YAP with light directs invasion of cancer cell spheroids	50
3.1 Introduction	51
3.2 Results and Discussion	51
3.3 Appendix.....	58
3.3.1 Plasmid construction of optoYAP	58

3.3.2 Synthesis and characterization of the caged Lysine.....	59
3.3.3 Cell Culture and optoYAP Functionality Assays	62
3.3.4 Fluorescence imaging and staining	69
3.3.5 Spheroid control experiments	72
3.4 References.....	74
Chapter 4	76
Exosome-coated Metal-Organic Framework Nanoparticles: An Efficient Drug Delivery Platform	76
4.1 Introduction.....	77
4.2 Results and Discussion.....	79
4.3 Conclusion	84
4.4 Appendix	85
4.4.1 Methods and Characterization	85
4.4.2 Synthesis of the uncoated and coated MIL-88A nanoparticles.....	88
4.4.3 Characterization of MIL-88A NPs.....	90
4.4.4 Stability Measurements.....	102
4.4.5 Cell Release Experiments	107
4.4.6 MTT-assays	115
4.4.7 Cell targeting.....	117
4.5 References.....	118
Chapter 5	120
Liposome coated iron fumarate metal-organic framework nanoparticles for combination therapy	120
5.1 Introduction.....	121
5.2 Results and Discussion.....	122
5.2.1 MOF nanoparticle synthesis and their lipid coating	122
5.2.2 Loading capacity	122
5.2.3 Fluorescence Release Experiments	123
5.2.4 Cell Release Experiments	125
5.2.5 Single Drug MTT Assays.....	126
5.2.6 Multi Drug MTT-Assays.....	127
5.3. Conclusion	129
5.4. Materials and Methods.....	130
5.4.1. UV/Vis Measurements	130
5.4.2. Fluorescence Microscopy	130
5.4.3. Fluorescence Spectroscopy	130
5.4.4. Cell culture.....	131

5.4.5. MTT Assays.....	131
5.4.6. Synthesis of the uncoated and coated MIL-88A nanoparticles	131
5.5 Appendix.....	133
5.5.1 Additional Methods	133
5.5.2 Characterization.....	135
5.5.3 MTT-Assays	147
5.6 References	150
Chapter 6	152
Biocompatible crosslinked β-cyclodextrin nanoparticles as multifunctional carriers for cellular delivery	152
6.1 Introduction	153
6.2 Results and Discussion	155
6.3 Conclusion	163
6.4 Experimental Part	164
6.5 Appendix.....	168
6.6 References.....	173
Chapter 7	176
Synergistic Combination of Calcium and Citrate in Mesoporous Nanoparticles Targets Pleural Tumors	176
7.1 Introduction	177
7.2 Results	178
7.3 Conclusion.....	188
7.4 Materials and Methods	188
7.5 Appendix.....	196
7.6 References:	220
Chapter 8	222
Conclusion	222
Chapter 9	226
Publications, Posters and Presentations	226
9.1 Publications	227
9.2 Posters and Presentations	229

Chapter 1

Introduction

1.1 Cancer

Cancer is one of the most dominant causes of death, leading to over 9.6 million deaths worldwide in 2018 alone making it the second leading cause of death, according to the WHO.¹ What is colloquially called cancer, invoking the image of a singular disease is actually a large group of diverse diseases – currently over 100 types of cancer have been identified. They all share similar symptoms: the abnormal growth of cells with the potential for invasion and spread to other parts of the body.² While the emergence of cancer can have a great many causes – smoking, infection, chemicals, radiation, etc. - and they differ in body region and behavior, all types of cancer have several things in common which were first formalized as the hallmarks of cancer by Hanahan and Weinberg in 2000 and were revisited by the same authors in 2011 (Figure 1.1).^{3, 4} All of these hallmarks are potential targets for cancer treatments, however the most effective way to target cancer is through its prevention and early recognizance, which requires a deeper understanding of the processes that turn healthy cells into cancer cells. The hallmarks relevant to this work are the activation of invasion and metastasis and sustained proliferative signaling prevalent in cancer, as well as cancer's resistance to cell death.

The common cause of all types of cancer is the malfunction of the body's tissue growth apparatus and its associated genes. These malfunctioning genes can broadly be separated into two categories: oncogenes, which regulate cell growth and reproduction, and tumor suppression genes, which are responsible for inhibiting cell division and regulating cell survival. As such cancer is caused by either an overexpression of oncogenes or an overinhibition of tumor suppressing genes.⁵ While normally several genes are involved in the transformation of cells into cancer cells,⁶ it has been shown that even mutation of single genes can be enough to trigger carcinogenesis.⁷ Although progress is made in improving established cancer therapies – surgery, chemotherapy and radiation – and immunotherapy has emerged as a promising new approach to combatting it, one of the main difficulties remains the diversity of cancer and a limited understanding of its emergence and the mechanism of its spreading and invasion of the surrounding tissue.

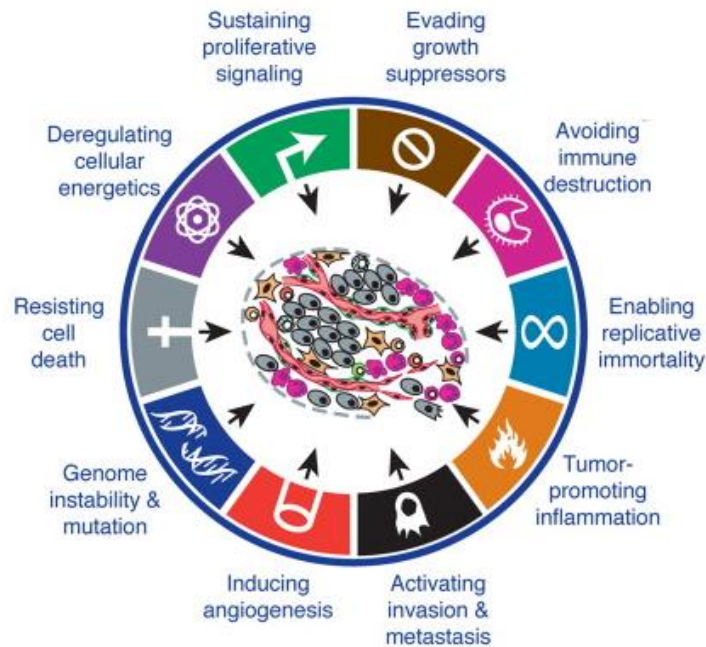


Figure 1.1: Hallmarks of cancer. Adapted from Hanahan, D. & Weinberg, Robert A. Hallmarks of Cancer: The Next Generation. Cell 144, 646-674 (2011).³

1.1.1 Cancer Invasion and Metastasis

Cancer invasion is the direct extension and spread of a tumor into the surrounding tissue (Figure 1.2). This uncontrolled spread is the true malignancy and danger of cancer, as even if the primary tumor could be located and removed, there will always remain the danger of a reemergence at a later date due to untreated offshoots. The two observed main patterns of invasion are collective cell migration and individual cell migration.⁸⁻¹¹ The pattern of individual cell migration is just as the name implies a foray of single cancer cells (mesenchymal or amoeboid) venturing forth from the tumor into the surrounding tissue independently, which leads to a less concerted and slower spread of the tumor compared to the collective cell migration.^{10, 12}

Collective cell migration has been observed in a wide variety of cancer types: breast cancer, lung cancer, prostate cancer, melanoma and endometrial cancer to name a few.^{8, 11, 13-15} Parts of the tumor mass or multicellular groups penetrate the surrounding tissue and form various structures like short cords, clusters, stripes and fields.^{8, 10, 11, 16, 17} These groups of cells contain “leading edges” composed of “leader cells”. The cells at the leading edge degrade the ECM

proteolytically to make space for further invasion of the surrounding tissue.^{10, 11} Leader cells have been shown to “recruit” surrounding mesenchymal cells to modify and rebuild the surrounding matrix. Subsequently the surrounding epithelial cells follow them. This is especially true of fibroblasts, which create a “highway” for other cells to follow by creating regions of low matrix concentration surrounded by pathways of thick collagen bundles.^{18, 19} Clusters of collectively invading cells are connected by adhesive proteins and signaling junctures extend from the main body of the tumor into the surrounding tissue.^{9, 10} The leading edges form pseudopodia, which develop contacts with the actin cytoskeletons of surrounding cells.^{10, 11} They are interconnected by cadherin and intercellular gap junctions and leader cells exhibit a different gene expression than the “follower” cells with a preferential expression of integrins and proteases.^{13, 20} The cells involved in collective cell migration show differences in polarities due to the expressed surface receptors in the leader cells, most likely due to chemokines, like the fibroblast growth factor or the transforming growth factor β .^{13, 21, 22}

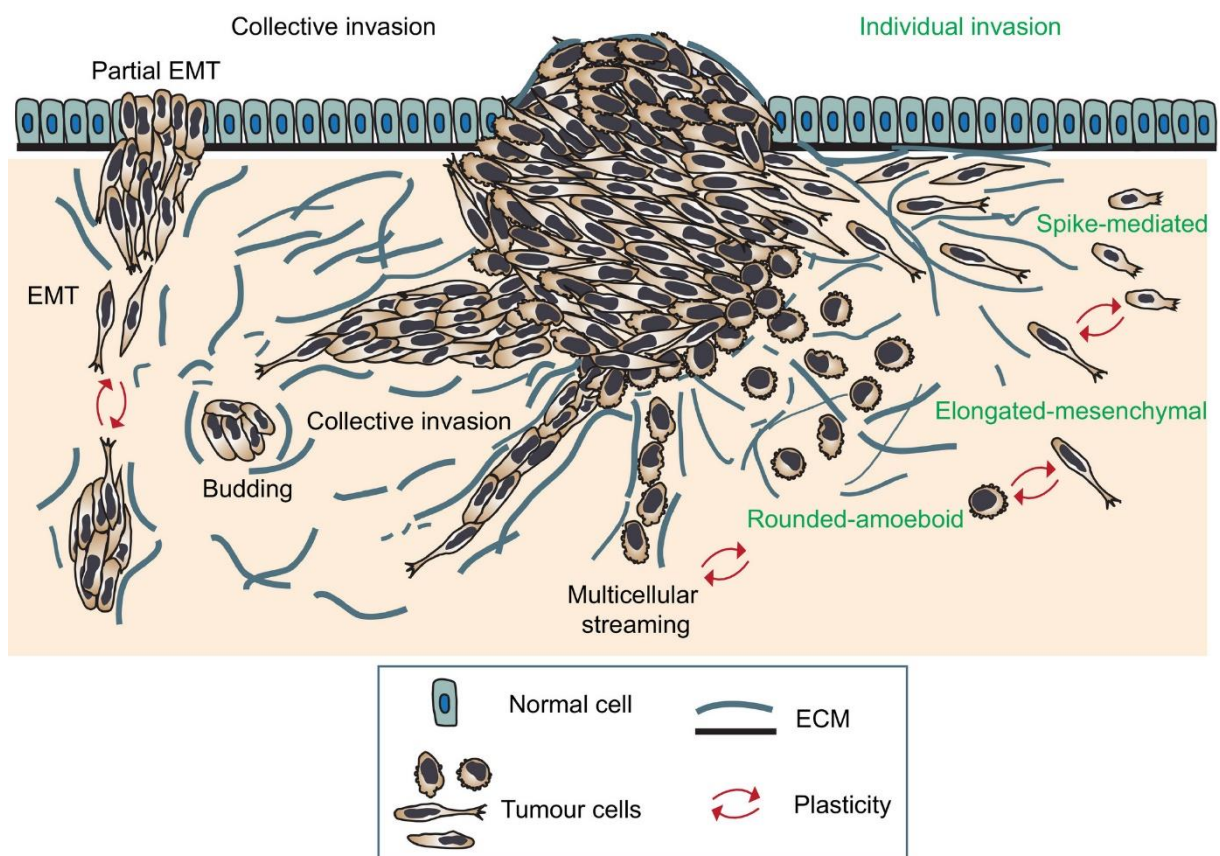


Figure 1.2: Patterns of cancer invasion: collective cell and individual cell migration²³

Cancer is, however, not limited to the invasion of the area surrounding the tumor. It can spread far beyond the neighboring tissue through the entire body in a process called metastasis.²⁴ If

a malignant tumor spreads close to the circulatory system it can invade into the vessels. Circulating tumor cells can penetrate the vessel and then form secondary tumors at a different site after re-penetrating into the surrounding tissue.²⁵ This process is greatly helped by the tumor's ability to induce angiogenesis and create new blood vessels, which act as a connection to the circulatory system and are a convenient launching point for metastasis.²⁶ The penetration requires gaps in the endothelium whose formation is largely regulated by mechanical forces.²⁷

To further the understanding of how and why cancer spread is set into motion and propagates itself, it is important to look at the external stimuli that start cancer development and sustain it. One external stimulus that is always present are the mechanical cues from the cell's surrounding tissue. The interplay between the mechanics of the tumor microenvironment, especially the surrounding ECM, and the tumor itself play a major role in continued tumor growth and expansion.

1.1.2 Mechanics of cancer: spread and invasion

The tumor microenvironment is constantly changing and exposes its components to constantly changing stresses. These changing stresses are mostly the result of changes in the extracellular matrix (ECM) and tumor expansion.²⁸ In general, cells encounter three types of mechanical stress in the tumor environment: tensile stress, e.g. from actomyosin contraction in response to ECM stiffness, compressive stress from tumor expansion in a confined space and shear stress from blood and interstitial fluid flow.^{28, 29} These three types of stress all activate downstream signaling pathways through mechanotransduction. Many of the activated signaling pathways are the same pathways that are also activated by oncogenes. As such tumors actively shape their microenvironment through prolonged stress signaling.²⁹

Normal responses of cells to external stress are translated into action via mechanotransduction. The physical communication between cells and between cells and the ECM is mediated by focal adhesion and adherens junction protein complexes, which influence intracellular tension, which in turn influences tissue stiffness and morphology. Mechanical

stresses on the cell membrane can also lead to the opening of stress sensitive ion channels like Piezo1 and Piezo2.³⁰ These ion channels are regulated by GTPases and play a role in mediating proliferation³¹ and cell polarity.³² They are often dysregulated in tumors, making them a potential driver of tumor progression.^{30, 33} Sustained responses to mechanical stimuli require the alteration of gene expressions. These alterations can be caused by changes in the ECM/substrate, e.g. a stiff substrate lead to an increased expression of integrins³⁴ and ECM proteins³⁵. The altered gene expressions influence the mechanical properties of the affected cells by changing the expression of cytoskeletal proteins and thus the composition of the cytoskeleton.^{36, 37} Among these are the downregulation of E-cadherin and the switch from keratin to vimentin intermediate filament expression, which drastically alters the tension exerted on the surrounding cells and the ECM.^{28, 29, 38, 39} This is commonly associated with epithelial-to-mesenchymal-transformation (EMT), which is often linked to highly metastatic and invasive tumor cells.

Changes in the ECM structure and in turn its mechanical properties are closely associated with cancer progression and disturb normal tissue morphology.⁴⁰ Tumors remodel the surrounding ECM through the sustained expression of matrix proteins, their assembly, their crosslinking and their turnover by matrix metalloproteases. This overexpression contributes to ECM stiffening, mainly through increased collagen deposition, crosslinking and parallel reorientation, which is correlated to faster tumor progression and worse clinical outcome.^{28, 29, 36, 41} High ECM stiffness is linked to an increased risk of cancer development, e.g. breast cancer,⁴² which can be explained by a positive feedback loop that promotes tumor growth. Collagen crosslinking enhances integrin activation through integrin clustering caused by a more bulky glycocalyx at the cell surface, which increase tension on matrix-bound integrins.⁴³ The stabilization of the focal adhesion through vinculin mediated by a stiff ECM stimulates PI3K/AKT signaling which in turn promotes tumor cell invasion/metastasis.^{44, 45} Enhanced ECM rigidity also leads to increased actomyosin contractility, which is associated with increased invasion and matrix degradation.^{46, 47} All of these changes to the ECM promote an increased likelihood of tumor spread through invasion or metastasis through enhanced interstitial fluid pressure gradients and compression induced stress, which promote tumor cell escape from the primary tumor.⁴¹

One of the most important questions is how to prevent further spread of cancer from the initial tumor into the surrounding tissue or other regions of the body, via invasion or metastasis. As mechanical stimulus plays such an important role in this process by changing signaling and protein regulation, mechanotransduction proteins that translate external cues into action have come into the focus of cancer research. These proteins could be lynchpins for cancer development as the misregulation of a single protein can result in the over or under expression of its downstream proteins and in the worst case cancer. One of these proteins playing a role in many types of cancer is Yes-Associated-Protein.

1.2 Yes associated protein (YAP)

YAP has first been independently isolated as an interactor of Yes kinase in 1994⁴⁸, hence the name, followed by further isolations as a cofactor of the TEAD factors in 2001⁴⁹ and as an interactor of 14-3-3 proteins in 2003⁵⁰. Further interest in YAP came up once its homologue Yki (yorkie) in the *Drosophila melanogaster* was identified as the mediator of downstream signaling of the Hippo pathway, which is responsible for organ size control.⁵¹ After this, similar findings for YAP followed with studies exposing YAP's involvement in hyperproliferation, organ overgrowth, anchorage independent growth and cancer.⁵²⁻⁵⁶ Due to this wide array of interactions YAP and its paralogue TAZ have since become proteins of wide interest to many interlocking fields of research.

1.2.1 YAP's role in the cell

YAP/TAZ are mechanotransduction proteins, translating the stimulus of the cells environment, specifically the ECM stiffness, into action for the cells.⁵⁷ They are involved in many biological processes but their main function is cell proliferation.⁵⁸ Forced YAP expression strongly promotes cell proliferation in vitro and can lead to organ overgrowth in vivo and ultimately cancer.⁵⁹ In addition YAP/TAZ expression also shows the ability to devolve mature, differentiated cells into their less-differentiated progenitors akin to embryonic precursors.⁶⁰⁻⁶² This function of YAP is not required in most adult tissues,⁶³⁻⁶⁵ but indispensable in the early stages of life during embryonic development and during regenerative processes like wound healing.^{58, 59, 66} Their regenerative and reprogrammative abilities are of great interest in medical research concerning regeneration of organs and tissue that normally lack this function.⁶⁰

To achieve this, YAP acts as a transcriptional regulator for genes involved in cell proliferation and apoptosis. This function hinges on its interactions with TEAD related transcription factors as well as others like LATS1/2 or RUNX.^{67, 68} YAP mutants unable to interact with TEAD show very little biological activity. YAP-TEAD complexes mostly regulate gene activity by recruiting chromatin modifiers and through interaction with other regulating complexes, like Myc or the

serum response factor.^{67, 69, 70} In addition to transcriptional regulation YAP can also regulate non-transcriptional processes, like microRNA biogenesis in the nucleus⁷¹ or the degradation of β -Cat in the cytosol.⁷² YAP's target genes include matricellular proteins CTGF and CYR61,⁷³ as well as genes responsible for the G1/S phase transition of the cell cycle, DNA replication, DNA repair, nucleotide metabolism and mitosis.^{53, 74-76} It also regulates the expression of the upstream regulators of the Hippo pathway and proteins responsible for the cytoskeleton, which allows it to indirectly influence its own activity.^{77, 78} Furthermore, YAP/TAZ are downstream of or in crosstalk with many well-known oncogenes, like the Ras family of proteins^{79, 80} and are both necessary for the survival of tumor cells.⁵⁸ This and YAP's involvement with many growth related processes makes YAP a very interesting target in oncology.

Other important functions of YAP include the induction of the epithelial-to-mesenchymal transition (EMT),⁸¹ regulation of angiogenesis and heart development,⁸² promotion of peripheral axons myelination⁸³ and the regulation of endocrine pancreas differentiation.⁸⁴ Due to its involvement in many of the cells key functions YAP is strongly regulated.

1.2.2 YAP Regulation by the Cell Environment

The main regulator of YAP/TAZ is the Hippo signaling pathway, which is responsible for organ size and tumor suppression. They are only active when residing in the nucleus and are both regulated via phosphorylation of a serine residue initiating their transport to the cytoplasm by 14-3-3 proteins where they are inactive.^{85, 86} This phosphorylation is regulated by MST1/2 and LATS1/2 - known tumor suppressors. If the Hippo pathway is inactive YAP/TAZ enter the nucleus and regulate gene activity through TEAD1-4.^{67, 69, 74, 87} While the Hippo pathway appears to be one of the main regulators of YAP/TAZ, contrastingly to many other signaling pathways, which are regulated by one specific binding ligand,⁸⁸ YAP/TAZ has a slew of other regulators: cell-cell adhesion, cell polarity, the surrounding ECM and forces exhibited by it, metabolic pathways and extracellular growth factors all play a part in YAP/TAZ regulation (Figure 1.3).⁸⁹

Of these, the most important is likely the cell-cell interactions and the influence of the

surrounding microenvironment. The cell-cell contacts of a normal epithelial environment inhibit YAP activity. The apical and basolateral polarity complexes present in such an environment act as tumor suppressants and keep YAP inactive.^{90, 91} In addition, many of its negative regulators are localized to cell-cell junctions further enhancing this effect. This, however, means that even partial EMT, which removes cell polarity and reduces cell-cell adhesion, will lead to YAP activation.⁹² The observations that epithelial polarity inhibits YAP/TAZ is not universally true, however. This is most notable during the strong formative role YAP/TAZ play in the early stages of life during the formation and further development of the blastocyst, where YAP is continually active in the trophoblast and inactivated in the inner cell mass.⁹³ Adding to this complex behavior of YAP in regards to cell polarity, polarity proteins, e.g. Mark1-4 and PARD 3 and PARD 6, can both activate and inhibit YAP depending on the circumstances.^{94, 95} These examples show that there appear to be as of yet unexplored factors at play in the regulation of YAP.

Another factor that plays a large role in YAP regulation are the mechanical properties of the cell microenvironment.⁹⁶ In general YAP/TAZ activity seems to be dependent on the stiffness of its surroundings, with increased stiffness leading to higher YAP activity. The inhibition of factors necessary for cytoskeletal contractility, like RHO GTPases or F-actin leads to a loss of YAP activity.^{56, 63} The reverse is also true as inactivation of F-actin inhibiting factors leads to an increased YAP activity.⁸⁵ Cells confined to small spaces with no chance to escape either through movement or deformation show similarly low levels of YAP/TAZ activity as F-actin suppressed cells, because they do not have sufficient space to stretch to develop cytoskeletal contractility.^{57, 64, 97} Similar results can also be achieved by exposition to other tissue forces like stretching and shear stress.^{98, 99} These results would explain why YAP appears to be activated by default in standard 2D cell culture, leading to rapid proliferation due to the hard surface of many standard cell culture well plates.⁹⁶ However, if soft substrates, e.g. in the form of hydrogels, are introduced, YAP is restricted to the cytosol of cells and remains inactive.^{57, 96} As this softness is far closer to the usual environment cells experience in the epithelial architecture, YAP/TAZ is often far more restricted in vivo than in vitro.⁷ Another reason for the high YAP activity in vitro is the presence of serum, which normally contains lysophosphatidic acid and sphingosine 1-phosphate, which inhibit the Hippo pathway kinases LATS1/2 and thus leads to YAP activation.¹⁰⁰

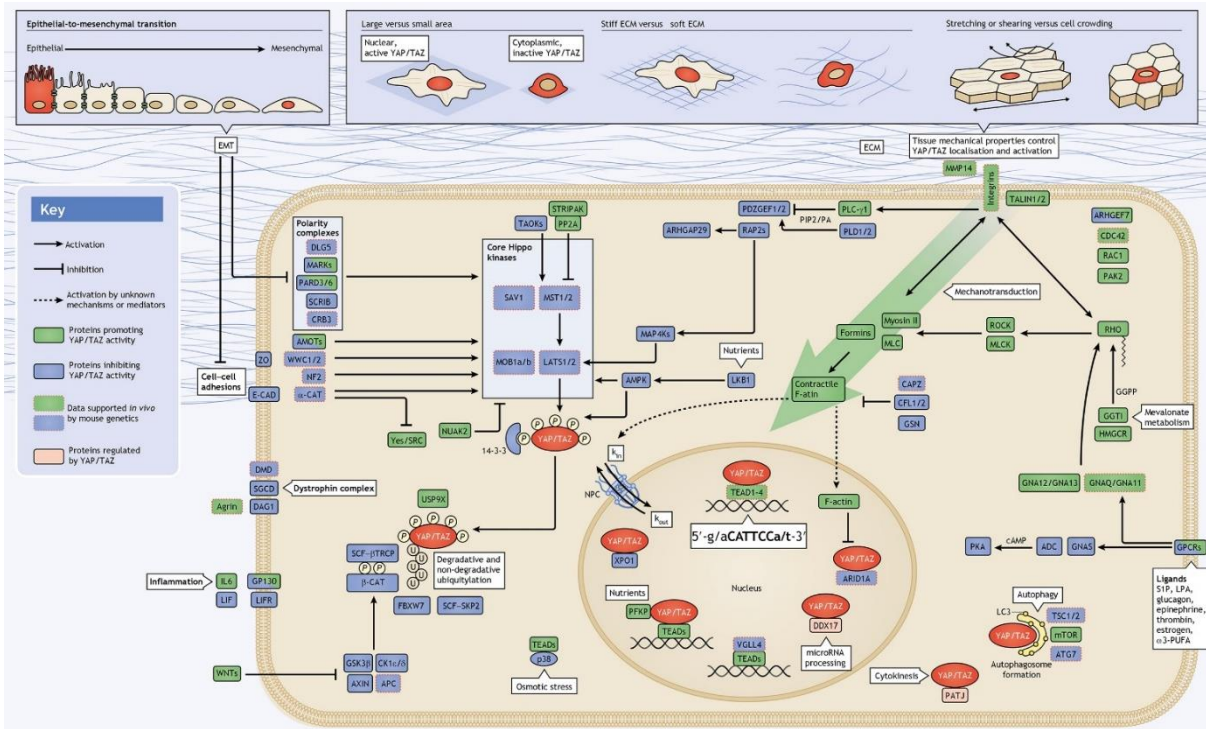


Figure 1.3: Overview of YAP/TAZ functions and regulation with upstream and downstream influences.¹⁰¹

1.2.3 YAP's role in cancer

Looking at the many roles YAP/TAZ play in the cell it becomes obvious that their activity enhances many key attributes of cancer:³ They play a role in enhanced proliferation and enhanced survivability and take part in the creation of stem cells – all hallmarks of cancer, which will be explored in more detail in the following. Firstly, sustained YAP activation promotes aberrant cell proliferation,^{52, 102} due to a broad transcriptional apparatus involved in cell cycle progression downstream of YAP/TAZ, which also involves other proto-oncogenic transcription factors like c-Myc.^{74, 103} Secondly, another typical property of cancer cells is their increased resistance to cell death, which can also be influenced by increased YAP/TAZ concentrations, by preventing anoikis⁸⁵ or inhibiting the mitochondrial-induced apoptosis pathway by upregulating Bcl2¹⁰⁴ and the additional apoptosis cascade initiated by tumor necrosis factor α and FAS ligands.⁵³ Thirdly, YAP/TAZ are active in cancer stem cells (CSC) and are required for their expansion and can reprogram non-stem tumor cells into full CSCs,^{92, 105} which are associated with tumor formation, chemoresistance and metastasis. Lastly, tumors are heterogeneous, complex tissues that need constant crosstalk between cancer cells and the normal cells in the tumor stroma.¹⁰⁶ YAP/TAZ facilitate this crosstalk by secreting growth

factors like AREG and matricellular proteins like Cyr61 and CTGF.⁶⁸ In epithelial cells they increase the expression of attractants for T-cell suppressing myeloid cells¹⁰⁷, while they increase the production of inflammatory interleukins and the deposition of a rigid ECM in cancer fibroblasts.¹⁰⁸ The enhanced ECM rigidity in turn increases YAP activity, which leads to greater expression of growth factors and attractants. This creates a feedback loop in both epithelial cells and fibroblasts allowing YAP/TAZ to self-sustain their activity, further enhancing tumor growth.¹⁰⁹

The above are all valid reasons to suspect YAP/TAZ play a vital role in cancer and a closer look at various common types of cancer confirms this. YAP/TAZ show heightened expression in lung cancers and their expression can be correlated to poor patient outcome. Furthermore, high YAP/TAZ expression correlates with poor prognosis.^{110, 111} Similar observation of irregular YAP/TAZ expression can be found for breast cancer,¹¹² colorectal cancer,¹¹³ liver cancer,¹¹⁴ gastric cancer,¹¹⁵ pancreatic cancer¹¹⁶ and gliomas.¹¹⁷

One possible explanation for this increased activity could be the enhanced ECM density observed in many tumor environments and the correlation between the ECM stiffness and invasive potential of tumors.¹¹⁸⁻¹²⁰ As YAP is activated in stiff environments, there have been many studies associating YAP with the onset of cancer invasion and metastasis^{121, 122} As a mechanotransduction protein YAP might just be the missing link between poor cancer prognosis, related to spread via invasion or metastasis, and external, mechanical stimulus. While YAP is strongly associated with cancer invasion and possibly metastasis, it is still not clear if it can also act as an invasion trigger. One avenue to further the understanding of YAP is the development of new tools allowing to control its spatial and temporal activity. A possible approach for obtaining such fine control over protein activity is the introduction of photochemical triggers that restrict normal protein function until activated.

1.3 Photochemical control of cellular processes

Effective biological, biophysical and biochemical studies of cellular processes require temporal and spatial control over protein function. Drug related methods of controlling protein activity are already well established.¹²³ However, they are a bulk approach that offers little temporal and, due to diffusion of the drugs, almost no spatial control. A possible pathway to controlling protein function that allows for both temporal and spatial control of its activation and deactivation is to use light as a trigger.¹²⁴ In addition to less direct approaches like modifying a protein's synthesis or degradation rate through optical interactions, there are generally two main concepts for optical control of protein functions: Inhibiting a protein's active site and mislocalization of the protein prior to optical activation.¹²⁵ The first method makes use of caging groups to mask the active site or lock the protein in a particular conformation. It can then be reactivated by removing the caging group or reversing the conformational changes via a light trigger.¹²⁶⁻¹²⁹ The second method of mislocalization relies on blocking the protein from the cell compartment it normally resides in when active and enabling the localization and subsequent activation with a light trigger.¹³⁰⁻¹³² Masking active sites is very specialized as the active sites and the components necessary to block them differ from protein to protein and as such require trial and error for each new application. Often they are also promiscuous and very difficult to block. Using mislocalization to control protein activity instead often allows for a more generalist approach for control. Proteins that are active in the same region of the cell, e.g. the nucleus, the membrane, or the endoplasmic reticulum, can be blocked and translocated with the same tools. Due to these advantages the method of mislocalization was used in this work.

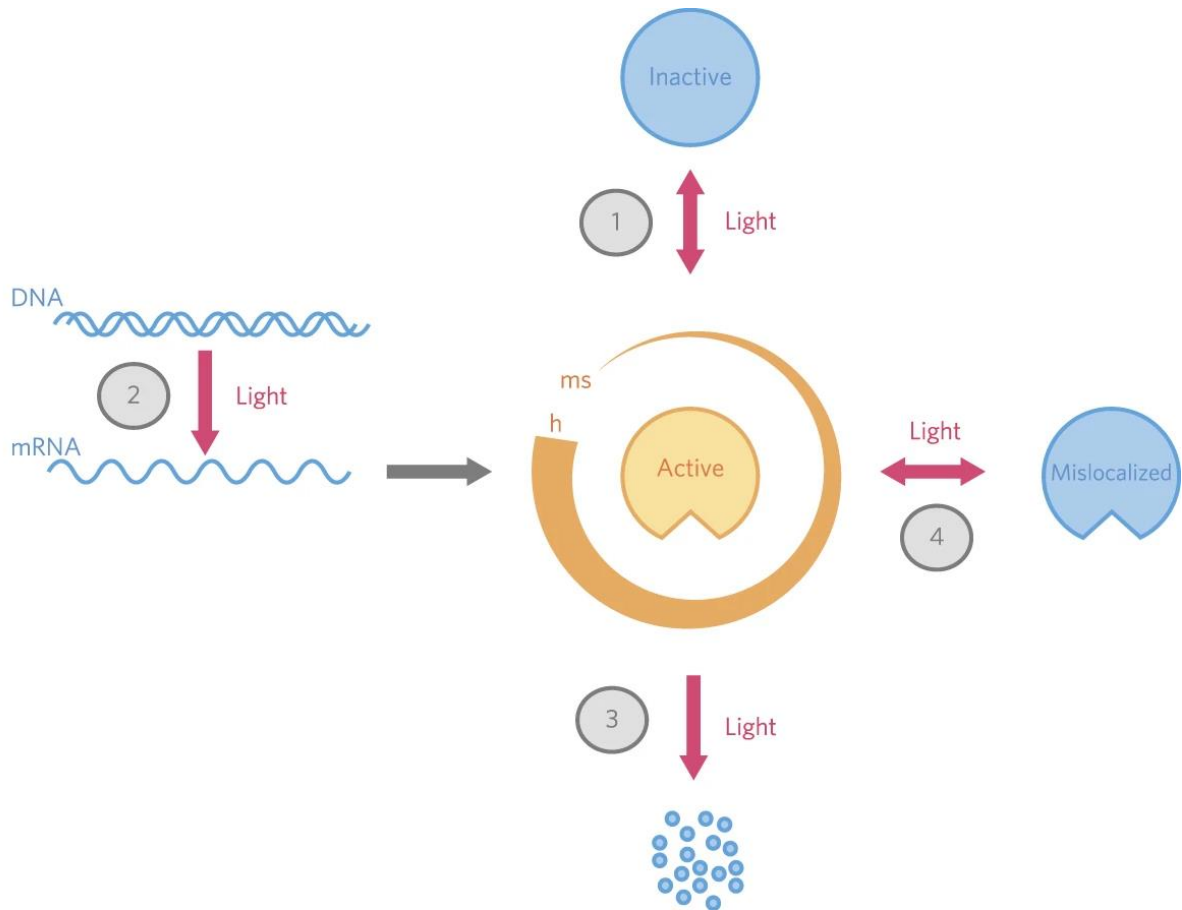


Figure 1.4: Options for photocontrolling proteins: 1) Direct change of the proteins active state, 2) modifying protein concentration via synthesis rate 3) modifying degradation rate and 4) affecting compartmentalization. Adapted from A. Gautier.¹²⁵

1.3.1 Photocontrol based on natural photoreceptors

Photochemical control of a protein requires either an intrinsic light sensitivity of the protein or the addition of a light sensitive molecule to the protein structure. Some of the first attempts at photocontrol of proteins made use of the natural photoreceptors of the rhodopsin family, later followed by flavoproteins and phytochromes.¹³³ The chromophores commonly isomerize under illumination leading to a conformational change in the protein and thus a change in its activity. Rhodopsins commonly function as ion channels or pumps^{134, 135} and play a role in cell polarization and depolarization. Tools based on members of the rhodopsin family have been used to control signal transduction via G-proteins, second messengers^{136, 137} and even the embryonic stem cell differentiation.¹³⁸ Flavoproteins possess a riboflavin based chromophore, and are present in almost all cells. Three types of flavoproteins are commonly used

photochemical tools: light-, oxygen- or voltage-sensing (LOV) proteins; blue light-utilizing flavin (BLUF) proteins and the plant light-sensitive cryptochrome (CRY2).^{139, 140} They function similarly to the third mentioned group of naturally light sensitive proteins phytochromes (PHY).¹²⁹ All of the flavoproteins and phytochromes used as tools lead to a photoisomerization of the chromophores which leads to a conformational change in the targeted protein, which in turn directly masks or unmasks a protein function or leads to a change in protein-protein interactions changing its activity. These tools have been used to photocontrol DNA transcription¹⁴¹ and recombination¹⁴², protein translocation,¹²⁹ enzymatic activity,¹⁴³ cell morphology¹⁴⁴, signaling pathways¹⁴⁵ and protein degradation¹⁴⁶. Each of the mentioned classes of proteins is sensitive to a different part of the visible spectrum with rhodopsin reacting to blue, green and yellow, phytochromes to red and infrared and flavoproteins to blue and low energy UV. However, these natural proteins are not without their disadvantages. They are fairly bulky and as such it can prove difficult to attach them to the target protein in such a manner that proper function is assured in one conformation and blocked in the other. Additionally they do not stay in their changed conformational state constantly, but rather relax back to their energetically preferred conformation.^{147, 148} As such prolonged illumination is required to keep the target in its active state. Both of these disadvantages can be rectified by using synthetic photoreceptors instead.

1.3.2 Photocontrol based on synthetic photoreceptors

Concurrently with the development of photocontrol tools based on natural photoreceptors, tools using synthetic light sensitive molecules in addition to genetic modifications of the target proteins were created. This approach to photocontrol has the advantage of a far larger pool of photochemistries to choose from.^{149, 150} A common approach when using synthetic photoreceptors is the use of photolabile protective groups, known as caging groups.¹⁵¹ These photoactive molecules can be used to block or cage the active sites of proteins. They can then be cleaved via illumination to restore normal function, creating proteins that can be activated at will. Synthetic tools that allow the induction of a conformational change in the protein and as such allow to switch it off or on are also available, if reversibility is desired. One major problem of regular caging approaches with molecules like azobenzenes is that they are introduced with chemical synthesis and as such form chemical bonds, which might lead to

conformational changes of the protein on their own and thus changes in protein activity and functionality.¹⁵² This is especially problematic for proteins like YAP, which are fairly sensitive to even small changes to their active domains. Furthermore, their delivery into the cell is challenging, restricting their use mainly to membrane proteins. The solution to this challenge is the site-specific insertion of caged amino acids into the protein. The most common amino acids used for this purpose are lysine,^{132, 153} tyrosine¹⁵⁴ and cysteine.¹⁵⁵ While far more difficult and involved than more common caging approaches, it avoids the risk of chemical derivatization and circumvents the need for cell delivery. The insertion of artificial caged amino acids into proteins requires engineered tRNA/aminoacyl-tRNA synthetase pairs and commonly makes use of amber stop codons introduced at the site of interest.¹⁵⁶ This will ensure that the modified amino acid is inserted at the right position, when the protein is assembled. The required caged amino acid can either be manufactured by the cell itself, which requires further modifications, or can simply be added to the medium. This approach has been used to control signal transduction^{154, 157} gene expression¹⁵⁴ and protein localization.^{132, 158}

Specifically, the control of protein localization with artificial amino acids carrying photo-caging groups can be achieved by making use of nuclear localization signals (NLS) of proteins. Blocking a protein's inherent localization mechanisms and applying a modified foreign NLS allows for the translocation to the target region upon optical activation. Usually NLS are very small and as such their insertion generally does not lead to large conformational changes.^{159, 160} One NLS of note is the NLS of SATB1, a transcription factor.¹⁶¹ It is composed of only 20 amino acids¹⁶² and is sensitive to the change of a single amino acid and can thus be deactivated by introducing a single caged amino acid. For this purpose Lys29 was mutated to the TAG amber stop codon, in preparation for the later insertion of the caged lysine via tRNA/tRNA synthetase pair.¹³² This optoNLS could then be used as a tool to control the nuclear import, and thus activity, of nuclear active proteins, like FOXO3 and the TEV.¹³² In this work we attached the optoNLS to YAP, to contain it in the cytosol and keep it inactive. Upon illumination with 365 nm UV light the caging group attached to the lysine is cleaved off and YAP will be transported into the nucleus and will be activated. This control over YAP's activity allows to investigate YAP's influence on cell proliferation in 2D and invasive behavior in 3D.

1.4 Metal Organic Frameworks for Drug Delivery

1.4.1 Metal Organic Frameworks

Another major part of this work focuses on nanoparticles as drug carriers for drug delivery with a focus on metal organic frameworks (MOF) and cancer treatment. MOFs are a relatively new, but quickly growing group of materials with the first MOF being discovered in 1995 by Yaghi et al, with others following soon after.^{163, 164} They are porous one-, two-, or three-dimensional coordination networks composed of metal or metal cluster ions connected by organic linker molecules with currently around 70000 different known structures according to the Cambridge database of crystallography.¹⁶⁵ The structure and properties of a MOF are largely determined by the geometry and connectivity of the organic linkers, but also by their and the metal ions chemistry.¹⁶⁶ Shared among all MOFs due to their periodic porous structure are a very large BET surface area, possibly exceeding $7000 \text{ m}^2/\text{g}$ ¹⁶⁷, low mechanical stability (shear moduli of 1-10 GPa and bulk moduli of 40 GPa)¹⁶⁸ and low thermal conductivity of around 0.1 W/m K due to their porous structure and low density.^{169, 170} The use of MOFs for applications often requires further optimizations, which can come in the form of bulk-processing, the optimization of their morphology and post-synthetic modifications, like linker exchanges. The resulting structures can, in some cases, be influenced by the presence of a template during synthesis. While the overall structure of the MOF is determined by the geometry of the linker molecule, the properties of the surface and especially the pores are heavily dependent on the functional groups of the linker molecules. By selecting the right linkers it becomes possible to tune the properties of a MOF before and after synthesis by functionalizing through reacting with the exposed electron bonds of the functional groups of the linker molecules.¹⁷¹⁻¹⁷³ Due to their large surface area, tunable functionalities and many different possible structures and morphologies MOFs can be used for a wide variety of applications, including both carrier materials for catalytically active species^{174, 175} or being used as catalysts themselves.¹⁷⁶⁻¹⁷⁸ Gas storage, notably hydrogen or methane storage, also profits from the MOFs high surface area, low sorption enthalpies and high cyclability.^{179, 180} Other possible applications include heat pumps,¹⁸¹ air dehumidification,¹⁸² water purification¹⁸³ and gas separation.¹⁸⁴ This versatility is further increased, when one considers MOFs in the nano-regime, adding short diffusion paths, fast sorption/desorption kinetics as well as size

dependent optical, electrical and magnetic properties.¹⁸⁵ These properties open up applications in catalysis, adsorption and electrical applications like as composite materials in supercapacitors.¹⁸⁶⁻¹⁸⁸ In addition the move to the nanoscale opens up possibilities for MOFs to be used in biomedical applications, such as drug delivery.¹⁸⁹

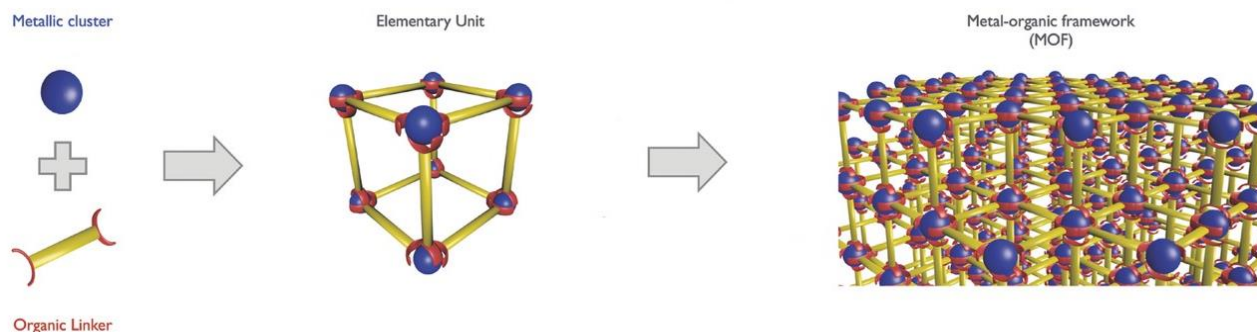


Figure 1.5: Schematic of MOF synthesis from metal ions/clusters (blue) and linker molecules (yellow/red). Adapted from Lismont, M., Dreesen, L., Wuttke, S., *Adv. Funct. Mater.* 2017, 27, 1606314.¹⁹⁰

1.4.2 MOFs as Drug Carriers

There have been many different types of nanocarriers developed for the purpose of drug delivery, among them are mesoporous inorganic silica, quantum dots, metal nanoparticles and organic micelles, liposomes and dendrimers.¹⁹¹⁻¹⁹⁶ All of these carriers come with their own limitations, however. Inorganic porous materials, have high surface areas, but often suffer from unacceptable degradability in biological environments or are outright toxic, while micelles, liposomes and dendrimers show high cell uptake and evasion of bodily regulators, but generally suffer from far lower loading capacities.¹⁹⁷⁻¹⁹⁹ MOFs, as a class of materials, combine several of the advantages of the previous examples with few of their drawbacks. They possess a highly versatile, diverse and modifiable structure, which still allows for high uniformity and the control of size and shape.²⁰⁰⁻²⁰² Their very high surface area and high porosity, can lead to high loading capacities and their coordination bonds make them biodegradable, but still stable enough to survive biological conditions for a while. Together these properties make MOFs a promising material for drug delivery.

MOFs were first proposed as drug delivery vehicles in 2006 by Férey et al.²⁰³ They reported the considerable loading capacity of two Cr-based tricarboxylic acid MOFs MIL100 and MIL-101 of 0.35 g g⁻¹ and 1.4 g g⁻¹ IBU/dehydrated MOF respectively. These MOFs also showed a complete,

gradual release of their cargo over a matter of days. These results were comparable to established silica based drug carriers like MCM-41. Since then a variety of different MOFs have been used to load a wide variety of therapeutic cargo molecules, like doxorubicin or cidofovir.^{201, 204} Even the loading of larger cargo, like proteins or other large biomolecules is possible through biomineralization, where a MOF is grown around the cargo molecules during synthesis.²⁰⁵

An important factor for drug delivery is an effective release of the cargo. To facilitate a controlled release MOFs that are responsive to various external stimuli have been investigated. The most established type of sensitive MOF are pH responsive MOFs. The intention is to make use of the more acidic microenvironment of tumors and the sensitivity of coordination bonds to changes in pH. The loaded MOFs show high drug retention at neutral or slightly basic pH, but degrade and release their cargo upon exposure to acidic pH.²⁰⁶⁻²⁰⁸ Additional types of stimuli used to induce an effective release include: magnetism in mostly iron-based MOFs,^{209, 210} that react to changes in the magnetic field; electrostatic interactions, which make use of ion exchange to release ionic cargo;^{211, 212} temperature^{213, 214} and even pressure.²¹⁵

The first Cr-based MOFs used by Férey et al. and follow-up studies were fairly toxic.^{189, 203} One of the first improvements was to replace the toxic chrome with less toxic metals like iron, calcium²¹⁶ or zinc.^{217, 218} Biocompatibility is an obvious requirement for any drug delivery molecule to be used in the human body. The toxicity of a MOF is mainly influenced by the metal and organic linker components individually. This mostly limits the available metal ions to the few cations that are already naturally present in the human body, like Fe, Ca and the linkers are similarly restricted.¹⁸⁹ The single components of the MOF being naturally present in the body has the additional advantage that they can be processed via the regular pathways, preventing a buildup of the MOF and ensuring a clean degradation.²¹⁹ Additional factors that determine the toxicity of nanoparticles, which are fairly independent of their composition, are their morphology and surface charge.^{219, 220} Highly charged particles or needle like morphologies can have toxic effects. Closely related to the overall biocompatibility of a drug carrier is its retention in the biological system.

A large concern is that the particles have to avoid being cleared by the immune or reticular system. To prevent this, the surface of the particles can be coated, e.g. with polymers or lipids.^{213, 221-223} These coatings can also fulfill multiple purposes. Aside from helping to prevent premature detection in the body, and mediating a potentially higher cell uptake,²²⁴ they also help by preventing premature leakage of the cargo, acting as capping agents.^{223, 225} The coatings can also be functionalized for targeting purposes or to become stimuli responsive.²²⁶ Particularly, liposome targeting is a well-established field going back decades.^{227, 228} They can be modified to target specific receptors that are overexpressed on many cancer cells, like folate or transferrin receptors.^{229, 230} These advances into efficient cancer targeting can be transferred to MOF nanoparticles through a lipid coating. Combining the advantages of MOFs and liposomes into one drug carrier creates a potent new class of drug carriers.

MIL-88A, the MOF used in this work, combines many of the advantageous properties of MOFs discussed above. It is biocompatible due to being composed of Fe and fumaric acid, which are both endogenous. While the pore size and surface area of MIL-88A are fairly small for a MOF, this can be offset by choosing a small enough cargo or using biomineralization to load the cargo. Premature leakage could be prevented by coating the MOF particles with a lipid membrane. The lipid coated MOF showed high cell uptake, an effective release of the cargo, facilitated by quick degradation in the lysosome once it entered the cells.

1.5 References

1. Cancer. *WHO* (2020). (https://www.who.int/health-topics/cancer#tab=tab_1). Retrieval date 09.07.2020
2. What is Cancer? *National Cancer Institute* (2015). (<https://www.cancer.gov/about-cancer/understanding/what-is-cancer>). Retrieval date 09.07.2020
3. Hanahan, D. & Weinberg, Robert A. Hallmarks of Cancer: The Next Generation. *Cell* **144**, 646-674 (2011).
4. Hanahan, D. & Weinberg, R.A. The Hallmarks of Cancer. *Cell* **100**, 57-70 (2000).
5. Croce, C.M. Oncogenes and Cancer. *N. Engl. J. Med.* **358**, 502-511 (2008).
6. Knudson, A.G. Two genetic hits (more or less) to cancer. *Nature Reviews Cancer* **1**, 157-162 (2001).
7. Panciera, T. et al. Reprogramming normal cells into tumour precursors requires ECM stiffness and oncogene-mediated changes of cell mechanical properties. *Nature Materials* **19**, 797-806 (2020).
8. van Zijl, F., Krupitza, G. & Mikulits, W. Initial steps of metastasis: cell invasion and endothelial transmigration. *Mutat. Res.* **728**, 23-34 (2011).
9. Khalil, A.A. & Friedl, P. Determinants of leader cells in collective cell migration. *Integr. Biol. (Camb.)* **2**, 568-574 (2010).
10. Friedl, P., Locker, J., Sahai, E. & Segall, J.E. Classifying collective cancer cell invasion. *Nat. Cell Biol.* **14**, 777-783 (2012).
11. Yilmaz, M. & Christofori, G. Mechanisms of motility in metastasizing cells. *Mol. Cancer Res.* **8**, 629-642 (2010).
12. Panková, K., Rösel, D., Novotný, M. & Brábek, J. The molecular mechanisms of transition between mesenchymal and amoeboid invasiveness in tumor cells. *Cell. Mol. Life Sci.* **67**, 63-71 (2010).
13. Friedl, P. & Gilmour, D. Collective cell migration in morphogenesis, regeneration and cancer. *Nat. Rev. Mol. Cell Biol.* **10**, 445-457 (2009).
14. Kitamura, T. et al. SMAD4-deficient intestinal tumors recruit CCR1+ myeloid cells that promote invasion. *Nat. Genet.* **39**, 467-475 (2007).
15. Giampieri, S. et al. Localized and reversible TGFbeta signalling switches breast cancer cells from cohesive to single cell motility. *Nat. Cell Biol.* **11**, 1287-1296 (2009).
16. Spano, D., Heck, C., De Antonellis, P., Christofori, G. & Zollo, M. Molecular networks that regulate cancer metastasis. *Semin. Cancer Biol.* **22**, 234-249 (2012).
17. Sanz-Moreno, V. & Marshall, C.J. The plasticity of cytoskeletal dynamics underlying neoplastic cell migration. *Curr. Opin. Cell Biol.* **22**, 690-696 (2010).
18. Gaggioli, C. et al. Fibroblast-led collective invasion of carcinoma cells with differing roles for RhoGTPases in leading and following cells. *Nat. Cell Biol.* **9**, 1392-1400 (2007).
19. Friedl, P. & Wolf, K. Tube travel: the role of proteases in individual and collective cancer cell invasion. *Cancer Res.* **68**, 7247-7249 (2008).
20. Lecaudey, V., Cakan-Akdogan, G., Norton, W.H. & Gilmour, D. Dynamic Fgf signaling couples morphogenesis and migration in the zebrafish lateral line primordium. *Development* **135**, 2695-2705 (2008).
21. Aman, A. & Piotrowski, T. Wnt/beta-catenin and Fgf signaling control collective cell migration by restricting chemokine receptor expression. *Dev. Cell* **15**, 749-761 (2008).
22. Vitorino, P. & Meyer, T. Modular control of endothelial sheet migration. *Genes Dev.* **22**, 3268-3281 (2008).
23. Pandya, P., Orgaz, J.L. & Sanz-Moreno, V. Modes of invasion during tumour dissemination. *Mol. Oncol.* **11**, 5-27 (2017).
24. Klein, C.A. The Metastasis Cascade. *Science* **321**, 1785 (2008).
25. Maheswaran, S. & Haber, D.A. Circulating tumor cells: a window into cancer biology and metastasis. *Curr. Opin. Genet. Dev.* **20**, 96-99 (2010).
26. Carmeliet, P. & Jain, R.K. Angiogenesis in cancer and other diseases. *Nature* **407**, 249-257 (2000).
27. Escribano, J. et al. Balance of mechanical forces drives endothelial gap formation and may facilitate cancer and immune-cell extravasation. *PLoS Comput. Biol.* **15**, e1006395 (2019).
28. Kumar, S. & Weaver, V.M. Mechanics, malignancy, and metastasis: The force journey of a tumor cell. *Cancer Metastasis Rev.* **28**, 113-127 (2009).
29. Yu, H., Mouw, J.K. & Weaver, V.M. Forcing form and function: biomechanical regulation of tumor evolution. *Trends Cell Biol.* **21**, 47-56 (2011).
30. Maroto, R., Kurosky, A. & Hamill, O.P. Mechanosensitive Ca²⁺ permeant cation channels in human prostate tumor cells. *Channels* **6**, 290-307 (2012).

31. Basson, M.D., Zeng, B., Downey, C., Sirivelu, M.P. & Tepe, J.J. Increased extracellular pressure stimulates tumor proliferation by a mechanosensitive calcium channel and PKC- β . *Mol. Oncol.* **9**, 513-526 (2015).
32. Huang, Y.-W. et al. Mechanosensitive store-operated calcium entry regulates the formation of cell polarity. *J. Cell. Physiol.* **230**, 2086-2097 (2015).
33. Morachevskaya, E., Sudarikova, A. & Negulyaev, Y. Mechanosensitive channel activity and F-actin organization in cholesterol-depleted human leukaemia cells. *Cell Biol. Int.* **31**, 374-381 (2007).
34. Delcommenne, M. & Streuli, C.H. Control of Integrin Expression by Extracellular Matrix. *J. Biol. Chem.* **270**, 26794-26801 (1995).
35. Nukuda, A. et al. Stiff substrates increase YAP-signaling-mediated matrix metalloproteinase-7 expression. *Oncogenesis* **4**, e165-e165 (2015).
36. Butcher, D.T., Alliston, T. & Weaver, V.M. A tense situation: forcing tumour progression. *Nature Reviews Cancer* **9**, 108-122 (2009).
37. McGrail, D.J., Kieu, Q.M.N., Iandoli, J.A. & Dawson, M.R. Actomyosin tension as a determinant of metastatic cancer mechanical tropism. *Phys. Biol.* **12**, 026001 (2015).
38. Wirtz, D., Konstantopoulos, K. & Searson, P.C. The physics of cancer: the role of physical interactions and mechanical forces in metastasis. *Nature Reviews Cancer* **11**, 512-522 (2011).
39. Thiery, J.P. Epithelial–mesenchymal transitions in tumour progression. *Nature Reviews Cancer* **2**, 442-454 (2002).
40. Paszek, M.J. et al. Tensional homeostasis and the malignant phenotype. *Cancer Cell* **8**, 241-254 (2005).
41. Acerbi, I. et al. Human breast cancer invasion and aggression correlates with ECM stiffening and immune cell infiltration. *Integrative Biology* **7**, 1120-1134 (2015).
42. Razzaghi, H. et al. Mammographic density and breast cancer risk in White and African American Women. *Breast Cancer Res. Treat.* **135**, 571-580 (2012).
43. Paszek, M.J. et al. The cancer glycocalyx mechanically primes integrin-mediated growth and survival. *Nature* **511**, 319-325 (2014).
44. Rubashkin, M.G. et al. Force Engages Vinculin and Promotes Tumor Progression by Enhancing PI3K Activation of Phosphatidylinositol (3,4,5)-Triphosphate. *Cancer Res.* **74**, 4597 (2014).
45. Levental, K.R. et al. Matrix Crosslinking Forces Tumor Progression by Enhancing Integrin Signaling. *Cell* **139**, 891-906 (2009).
46. Jerrell, R.J. & Parekh, A. Cellular traction stresses mediate extracellular matrix degradation by invadopodia. *Acta Biomater.* **10**, 1886-1896 (2014).
47. Aung, A. et al. 3D Traction Stresses Activate Protease-Dependent Invasion of Cancer Cells. *Biophys. J.* **107**, 2528-2537 (2014).
48. Sudol, M. Yes-Associated Protein (YAP65) is a proline-rich phosphoprotein that binds to the SH3 domain of the Yes proto-oncogene product. *Oncogene* **9**, 2145-2152 (1994).
49. Vassilev, A., Kaneko, K.J., Shu, H., Zhao, Y. & DePamphilis, M.L. TEAD/TEF transcription factors utilize the activation domain of YAP65, a Src/Yes-associated protein localized in the cytoplasm. *Genes Dev.* **15**, 1229-1241 (2001).
50. Basu, S., Totty, N.F., Irwin, M.S., Sudol, M. & Downward, J. Akt phosphorylates the Yes-associated protein, YAP, to induce interaction with 14-3-3 and attenuation of p73-mediated apoptosis. *Mol. Cell* **11**, 11-23 (2003).
51. Huang, J., Wu, S., Barrera, J., Matthews, K. & Pan, D. The Hippo signaling pathway coordinately regulates cell proliferation and apoptosis by inactivating Yorkie, the Drosophila Homolog of YAP. *Cell* **122**, 421-434 (2005).
52. Camargo, F.D. et al. YAP1 increases organ size and expands undifferentiated progenitor cells. *Curr. Biol.* **17**, 2054-2060 (2007).
53. Dong, J. et al. Elucidation of a universal size-control mechanism in Drosophila and mammals. *Cell* **130**, 1120-1133 (2007).
54. Ota, M. & Sasaki, H. Mammalian Tead proteins regulate cell proliferation and contact inhibition as transcriptional mediators of Hippo signaling. *Development* **135**, 4059-4069 (2008).
55. Overholtzer, M. et al. Transforming properties of YAP, a candidate oncogene on the chromosome 11q22 amplicon. *Proc. Natl. Acad. Sci. U. S. A.* **103**, 12405-12410 (2006).
56. Zhao, B. et al. Inactivation of YAP oncoprotein by the Hippo pathway is involved in cell contact inhibition and tissue growth control. *Genes Dev.* **21**, 2747-2761 (2007).
57. Dupont, S. et al. Role of YAP/TAZ in mechanotransduction. *Nature* **474**, 179-183 (2011).
58. Ma, S., Meng, Z., Chen, R. & Guan, K.-L. The Hippo Pathway: Biology and Pathophysiology. *Annu. Rev. Biochem.* **88**, 577-604 (2019).

59. Zanconato, F., Cordenonsi, M. & Piccolo, S. YAP/TAZ at the Roots of Cancer. *Cancer Cell* **29**, 783-803 (2016).
60. Moya, I.M. & Halder, G. Hippo–YAP/TAZ signalling in organ regeneration and regenerative medicine. *Nature Reviews Molecular Cell Biology* **20**, 211-226 (2019).
61. Yimlamai, D. et al. Hippo pathway activity influences liver cell fate. *Cell* **157**, 1324-1338 (2014).
62. Yui, S. et al. YAP/TAZ-Dependent Reprogramming of Colonic Epithelium Links ECM Remodeling to Tissue Regeneration. *Cell Stem Cell* **22**, 35-49.e37 (2018).
63. Gregorieff, A., Liu, Y., Inanlou, M.R., Khomchuk, Y. & Wrana, J.L. Yap-dependent reprogramming of Lgr5(+) stem cells drives intestinal regeneration and cancer. *Nature* **526**, 715-718 (2015).
64. Aragona, M. et al. A mechanical checkpoint controls multicellular growth through YAP/TAZ regulation by actin-processing factors. *Cell* **154**, 1047-1059 (2013).
65. Cai, J. et al. The Hippo signaling pathway restricts the oncogenic potential of an intestinal regeneration program. *Genes Dev.* **24**, 2383-2388 (2010).
66. Moya, I.M. & Halder, G. Hippo-YAP/TAZ signalling in organ regeneration and regenerative medicine. *Nat. Rev. Mol. Cell Biol.* **20**, 211-226 (2019).
67. Stein, C. et al. YAP1 Exerts Its Transcriptional Control via TEAD-Mediated Activation of Enhancers. *PLoS Genet.* **11**, e1005465 (2015).
68. Piccolo, S., Dupont, S. & Cordenonsi, M. The biology of YAP/TAZ: hippo signaling and beyond. *Physiol. Rev.* **94**, 1287-1312 (2014).
69. Croci, O. et al. Transcriptional integration of mitogenic and mechanical signals by Myc and YAP. *Genes Dev.* **31**, 2017-2022 (2017).
70. Foster, C.T., Gualdrini, F. & Treisman, R. Mutual dependence of the MRTF–SRF and YAP–TEAD pathways in cancer-associated fibroblasts is indirect and mediated by cytoskeletal dynamics. *Genes Dev.* **31**, 2361-2375 (2017).
71. Mori, M. et al. Hippo signaling regulates microprocessor and links cell-density-dependent miRNA biogenesis to cancer. *Cell* **156**, 893-906 (2014).
72. Azzolin, L. et al. YAP/TAZ incorporation in the β -catenin destruction complex orchestrates the Wnt response. *Cell* **158**, 157-170 (2014).
73. Quan, T. et al. Elevated YAP and its downstream targets CCN1 and CCN2 in basal cell carcinoma: impact on keratinocyte proliferation and stromal cell activation. *The American journal of pathology* **184**, 937-943 (2014).
74. Zanconato, F. et al. Genome-wide association between YAP/TAZ/TEAD and AP-1 at enhancers drives oncogenic growth. *Nat. Cell Biol.* **17**, 1218-1227 (2015).
75. Santinon, G. et al. dNTP metabolism links mechanical cues and YAP/TAZ to cell growth and oncogene-induced senescence. *The EMBO Journal* **37**, e97780 (2018).
76. Zhao, B. et al. TEAD mediates YAP-dependent gene induction and growth control. *Genes Dev.* **22**, 1962-1971 (2008).
77. Moroishi, T. et al. A YAP/TAZ-induced feedback mechanism regulates Hippo pathway homeostasis. *Genes Dev.* **29**, 1271-1284 (2015).
78. Nardone, G. et al. YAP regulates cell mechanics by controlling focal adhesion assembly. *Nature communications* **8**, 15321 (2017).
79. Pylayeva-Gupta, Y., Grabocka, E. & Bar-Sagi, D. RAS oncogenes: weaving a tumorigenic web. *Nature reviews. Cancer* **11**, 761-774 (2011).
80. Corbo, V., Ponz-Sarvisse, M. & Tuveson, D.A. The RAS and YAP1 dance, who is leading? *The EMBO journal* **33**, 2437-2438 (2014).
81. Shao, Diane D. et al. KRAS and YAP1 Converge to Regulate EMT and Tumor Survival. *Cell* **158**, 171-184 (2014).
82. Kim, J. et al. YAP/TAZ regulates sprouting angiogenesis and vascular barrier maturation. *The Journal of Clinical Investigation* **127**, 3441-3461 (2017).
83. Deng, Y. et al. A reciprocal regulatory loop between TAZ/YAP and G-protein Gas regulates Schwann cell proliferation and myelination. *Nature communications* **8**, 15161 (2017).
84. George, N.M., Day, C.E., Boerner, B.P., Johnson, R.L. & Sarvetnick, N.E. Hippo Signaling Regulates Pancreas Development through Inactivation of Yap. *Mol. Cell. Biol.* **32**, 5116 (2012).
85. Zhao, B. et al. Cell detachment activates the Hippo pathway via cytoskeleton reorganization to induce anoikis. *Genes Dev.* **26**, 54-68 (2012).
86. Meng, Z. et al. RAP2 mediates mechanoresponses of the Hippo pathway. *Nature* **560**, 655-660 (2018).
87. Galli, G.G. et al. YAP Drives Growth by Controlling Transcriptional Pause Release from Dynamic

- Enhancers. *Mol. Cell* **60**, 328-337 (2015).
88. Heldin, C.-H., Lu, B., Evans, R. & Gutkind, J.S. Signals and Receptors. *Cold Spring Harb. Perspect. Biol.* **8**, a005900-a005900 (2016).
 89. Totaro, A., Panciera, T. & Piccolo, S. YAP/TAZ upstream signals and downstream responses. *Nat. Cell Biol.* **20**, 888-899 (2018).
 90. Szymaniak, Aleksander D., Mahoney, John E., Cardoso, Wellington V. & Varelas, X. Crumbs3-Mediated Polarity Directs Airway Epithelial Cell Fate through the Hippo Pathway Effector Yap. *Dev. Cell* **34**, 283-296 (2015).
 91. Silvis, M.R. et al. α -Catenin Is a Tumor Suppressor That Controls Cell Accumulation by Regulating the Localization and Activity of the Transcriptional Coactivator Yap1. *Science Signaling* **4**, ra33 (2011).
 92. Cordenonsi, M. et al. The Hippo transducer TAZ confers cancer stem cell-related traits on breast cancer cells. *Cell* **147**, 759-772 (2011).
 93. Sasaki, H. Roles and regulations of Hippo signaling during preimplantation mouse development. *Dev. Growth Differ.* **59**, 12-20 (2017).
 94. Liu, W.A. et al. PARD3 dysfunction in conjunction with dynamic HIPPO signaling drives cortical enlargement with massive heterotopia. *Genes Dev.* **32**, 763-780 (2018).
 95. Mohseni, M. et al. A genetic screen identifies an LKB1–MARK signalling axis controlling the Hippo–YAP pathway. *Nat. Cell Biol.* **16**, 108-117 (2014).
 96. Dupont, S. Role of YAP/TAZ in cell-matrix adhesion-mediated signalling and mechanotransduction. *Exp. Cell Res.* **343**, 42-53 (2016).
 97. Wada, K.-I., Itoga, K., Okano, T., Yonemura, S. & Sasaki, H. Hippo pathway regulation by cell morphology and stress fibers. *Development* **138**, 3907 (2011).
 98. Nakajima, H. et al. Flow-Dependent Endothelial YAP Regulation Contributes to Vessel Maintenance. *Dev. Cell* **40**, 523-536.e526 (2017).
 99. Wang, K.-C. et al. Flow-dependent YAP/TAZ activities regulate endothelial phenotypes and atherosclerosis. *Proc. Natl. Acad. Sci. U. S. A.* **113**, 11525 (2016).
 100. Yu, F.-X. et al. Regulation of the Hippo-YAP pathway by G-protein-coupled receptor signaling. *Cell* **150**, 780-791 (2012).
 101. Pocaterra, A., Romani, P. & Dupont, S. YAP/TAZ functions and their regulation at a glance. *J. Cell Sci.* **133**, jcs230425 (2020).
 102. Zhao, B. et al. Inactivation of YAP oncoprotein by the Hippo pathway is involved in cell contact inhibition and tissue growth control. *Genes Dev.* **21**, 2747-2761 (2007).
 103. Kapoor, A. et al. Yap1 Activation Enables Bypass of Oncogenic Kras Addiction in Pancreatic Cancer. *Cell* **158**, 185-197 (2014).
 104. Rosenbluh, J. et al. β -Catenin-driven cancers require a YAP1 transcriptional complex for survival and tumorigenesis. *Cell* **151**, 1457-1473 (2012).
 105. Bartucci, M. et al. TAZ is required for metastatic activity and chemoresistance of breast cancer stem cells. *Oncogene* **34**, 681-690 (2015).
 106. Bissell, M.J. & Hines, W.C. Why don't we get more cancer? A proposed role of the microenvironment in restraining cancer progression. *Nat. Med.* **17**, 320-329 (2011).
 107. Wang, G. et al. Targeting YAP-Dependent MDSC Infiltration Impairs Tumor Progression. *Cancer Discov.* **6**, 80-95 (2016).
 108. Halder, G., Dupont, S. & Piccolo, S. Transduction of mechanical and cytoskeletal cues by YAP and TAZ. *Nat. Rev. Mol. Cell Biol.* **13**, 591-600 (2012).
 109. Calvo, F. et al. Mechanotransduction and YAP-dependent matrix remodelling is required for the generation and maintenance of cancer-associated fibroblasts. *Nat. Cell Biol.* **15**, 637-646 (2013).
 110. Lau, A.N. et al. Tumor-propagating cells and Yap/Taz activity contribute to lung tumor progression and metastasis. *EMBO J.* **33**, 468-481 (2014).
 111. Su, L.L. et al. Expression of Yes-associated protein in non-small cell lung cancer and its relationship with clinical pathological factors. *Chin. Med. J. (Engl.)* **125**, 4003-4008 (2012).
 112. Kim, T. et al. A basal-like breast cancer-specific role for SRF-IL6 in YAP-induced cancer stemness. *Nature communications* **6**, 10186 (2015).
 113. Lee, K.W. et al. Significant association of oncogene YAP1 with poor prognosis and cetuximab resistance in colorectal cancer patients. *Clin. Cancer Res.* **21**, 357-364 (2015).
 114. Han, S.X. et al. Expression and clinical significance of YAP, TAZ, and AREG in hepatocellular carcinoma. *Journal of immunology research* **2014**, 261365 (2014).
 115. Da, C.L., Xin, Y., Zhao, J. & Luo, X.D. Significance and relationship between Yes-associated protein and

- survivin expression in gastric carcinoma and precancerous lesions. *World J. Gastroenterol.* **15**, 4055-4061 (2009).
116. Morvaridi, S., Dhall, D., Greene, M.I., Pandol, S.J. & Wang, Q. Role of YAP and TAZ in pancreatic ductal adenocarcinoma and in stellate cells associated with cancer and chronic pancreatitis. *Sci. Rep.* **5**, 16759 (2015).
117. Orr, B.A. et al. Yes-associated protein 1 is widely expressed in human brain tumors and promotes glioblastoma growth. *J. Neuropathol. Exp. Neurol.* **70**, 568-577 (2011).
118. Wullkopf, L. et al. Cancer cells' ability to mechanically adjust to extracellular matrix stiffness correlates with their invasive potential. *Mol. Biol. Cell* **29**, 2378-2385 (2018).
119. Reid, S.E. et al. Tumor matrix stiffness promotes metastatic cancer cell interaction with the endothelium. *The EMBO Journal* **36**, 2373-2389 (2017).
120. Liu, C., Pei, H. & Tan, F. Matrix Stiffness and Colorectal Cancer. *Onco Targets Ther.* **13**, 2747-2755 (2020).
121. Zhang, X. et al. The Hippo pathway oncoprotein YAP promotes melanoma cell invasion and spontaneous metastasis. *Oncogene* **39**, 5267-5281 (2020).
122. Yang, S. et al. Active YAP promotes pancreatic cancer cell motility, invasion and tumorigenesis in a mitotic phosphorylation-dependent manner through LPAR3. *Oncotarget* **6**, 36019-36031 (2015).
123. Banaszynski, L.A. & Wandless, T.J. Conditional Control of Protein Function. *Chem. Biol.* **13**, 11-21 (2006).
124. Riggsbee, C.W. & Deiters, A. Recent advances in the photochemical control of protein function. *Trends Biotechnol.* **28**, 468-475 (2010).
125. Gautier, A. et al. How to control proteins with light in living systems. *Nat. Chem. Biol.* **10**, 533-541 (2014).
126. Yazawa, M., Sadaghiani, A.M., Hsueh, B. & Dolmetsch, R.E. Induction of protein-protein interactions in live cells using light. *Nat. Biotechnol.* **27**, 941-945 (2009).
127. Polstein, L.R. & Gersbach, C.A. Light-Inducible Spatiotemporal Control of Gene Activation by Customizable Zinc Finger Transcription Factors. *J. Am. Chem. Soc.* **134**, 16480-16483 (2012).
128. Hemphill, J., Chou, C., Chin, J.W. & Deiters, A. Genetically Encoded Light-Activated Transcription for Spatiotemporal Control of Gene Expression and Gene Silencing in Mammalian Cells. *J. Am. Chem. Soc.* **135**, 13433-13439 (2013).
129. Levsikaya, A., Weiner, O.D., Lim, W.A. & Voigt, C.A. Spatiotemporal control of cell signalling using a light-switchable protein interaction. *Nature* **461**, 997-1001 (2009).
130. Idevall-Hagren, O., Dickson, E.J., Hille, B., Toomre, D.K. & De Camilli, P. Optogenetic control of phosphoinositide metabolism. *Proc. Natl. Acad. Sci. U. S. A.* **109**, E2316-2323 (2012).
131. Lemke, E.A., Summerer, D., Geierstanger, B.H., Brittain, S.M. & Schultz, P.G. Control of protein phosphorylation with a genetically encoded photocaged amino acid. *Nat. Chem. Biol.* **3**, 769-772 (2007).
132. Engelke, H., Chou, C., Uprety, R., Jess, P. & Deiters, A. Control of protein function through optochemical translocation. *ACS Synth Biol* **3**, 731-736 (2014).
133. Fenno, L., Yizhar, O. & Deisseroth, K. The development and application of optogenetics. *Annu. Rev. Neurosci.* **34**, 389-412 (2011).
134. Sasaki, J. et al. Conversion of bacteriorhodopsin into a chloride ion pump. *Science* **269**, 73-75 (1995).
135. Nagel, G. et al. Channelrhodopsin-2, a directly light-gated cation-selective membrane channel. *Proc. Natl. Acad. Sci. U. S. A.* **100**, 13940 (2003).
136. Airan, R.D., Thompson, K.R., Fenno, L.E., Bernstein, H. & Deisseroth, K. Temporally precise in vivo control of intracellular signalling. *Nature* **458**, 1025-1029 (2009).
137. Oh, E., Maejima, T., Liu, C., Deneris, E. & Herlitze, S. Substitution of 5-HT1A receptor signaling by a light-activated G protein-coupled receptor. *J. Biol. Chem.* **285**, 30825-30836 (2010).
138. Stroh, A. et al. Tracking stem cell differentiation in the setting of automated optogenetic stimulation. *Stem Cells* **29**, 78-88 (2011).
139. Christie, J.M., Gawthorne, J., Young, G., Fraser, N.J. & Roe, A.J. LOV to BLUF: Flavoprotein Contributions to the Optogenetic Toolkit. *Molecular Plant* **5**, 533-544 (2012).
140. Chaves, I. et al. The Cryptochromes: Blue Light Photoreceptors in Plants and Animals. *Annu. Rev. Plant Biol.* **62**, 335-364 (2011).
141. Imayoshi, I. et al. Oscillatory Control of Factors Determining Multipotency and Fate in Mouse Neural Progenitors. *Science* **342**, 1203 (2013).
142. Kennedy, M.J. et al. Rapid blue-light-mediated induction of protein interactions in living cells. *Nat. Methods* **7**, 973-975 (2010).
143. Stierl, M. et al. Light Modulation of Cellular cAMP by a Small Bacterial Photoactivated Adenylyl Cyclase, bPAC, of the Soil Bacterium *Beggiatoa*. *J. Biol. Chem.* **286**, 1181-1188 (2011).
144. Leung, D.W., Otomo, C., Chory, J. & Rosen, M.K. Genetically encoded photoswitching of actin assembly

- through the Cdc42-WASP-Arp2/3 complex pathway. *Proc. Natl. Acad. Sci. U. S. A.* **105**, 12797-12802 (2008).
145. Raffelberg, S. et al. A LOV-domain-mediated blue-light-activated adenylate (adenylyl) cyclase from the cyanobacterium *Microcoleus chthonoplastes* PCC 7420. *Biochem. J* **455**, 359-365 (2013).
146. Bongor, K.M., Rakhit, R., Payumo, A.Y., Chen, J.K. & Wandless, T.J. General method for regulating protein stability with light. *ACS Chem. Biol.* **9**, 111-115 (2014).
147. Dowbaj, A.M., Jenkins, R.P., Hahn, K., Montagner, M. & Sahai, E. An optogenetic method for interrogating YAP1 and TAZ nuclear-cytoplasmic shuttling. *bioRxiv*, 2020.2006.2008.140228 (2020).
148. Christie, J.M., Gawthorne, J., Young, G., Fraser, N.J. & Roe, A.J. LOV to BLUF: flavoprotein contributions to the optogenetic toolkit. *Mol Plant* **5**, 533-544 (2012).
149. Brieke, C., Rohrbach, F., Gottschalk, A., Mayer, G. & Heckel, A. Light-Controlled Tools. *Angew. Chem. Int. Ed.* **51**, 8446-8476 (2012).
150. Ellis-Davies, G.C. Caged compounds: photorelease technology for control of cellular chemistry and physiology. *Nat. Methods* **4**, 619-628 (2007).
151. Bardhan, A. & Deiters, A. Development of photolabile protecting groups and their application to the optochemical control of cell signaling. *Curr. Opin. Struct. Biol.* **57**, 164-175 (2019).
152. Beharry, A.A. & Woolley, G.A. Azobenzene photoswitches for biomolecules. *Chem. Soc. Rev.* **40**, 4422-4437 (2011).
153. Gautier, A. et al. Genetically Encoded Photocontrol of Protein Localization in Mammalian Cells. *J. Am. Chem. Soc.* **132**, 4086-4088 (2010).
154. Arbely, E., Torres-Kolbus, J., Deiters, A. & Chin, J.W. Photocontrol of Tyrosine Phosphorylation in Mammalian Cells via Genetic Encoding of Photocaged Tyrosine. *J. Am. Chem. Soc.* **134**, 11912-11915 (2012).
155. Nguyen, D.P. et al. Genetic Encoding of Photocaged Cysteine Allows Photoactivation of TEV Protease in Live Mammalian Cells. *J. Am. Chem. Soc.* **136**, 2240-2243 (2014).
156. Chin, J.W. Expanding and reprogramming the genetic code. *Nature* **550**, 53-60 (2017).
157. Gautier, A., Deiters, A. & Chin, J.W. Light-activated kinases enable temporal dissection of signaling networks in living cells. *J. Am. Chem. Soc.* **133**, 2124-2127 (2011).
158. Gautier, A. et al. Genetically encoded photocontrol of protein localization in mammalian cells. *J. Am. Chem. Soc.* **132**, 4086-4088 (2010).
159. Marfori, M. et al. Molecular basis for specificity of nuclear import and prediction of nuclear localization. *Biochim. Biophys. Acta* **1813**, 1562-1577 (2011).
160. Cokol, M., Nair, R. & Rost, B. Finding nuclear localization signals. *EMBO reports* **1**, 411-415 (2000).
161. Cai, S., Han, H.J. & Kohwi-Shigematsu, T. Tissue-specific nuclear architecture and gene expression regulated by SATB1. *Nat. Genet.* **34**, 42-51 (2003).
162. Nakayama, Y., Mian, I.S., Kohwi-Shigematsu, T. & Ogawa, T. A nuclear targeting determinant for SATB1, a genome organizer in the T cell lineage. *Cell cycle (Georgetown, Tex.)* **4**, 1099-1106 (2005).
163. Yaghi, O.M. & Li, G. Mutually Interpenetrating Sheets and Channels in the Extended Structure of [Cu(4,4'-bpy)Cl]. *Angewandte Chemie International Edition in English* **34**, 207-209 (1995).
164. Yaghi, O.M., Li, G. & Li, H. Selective binding and removal of guests in a microporous metal-organic framework. *Nature* **378**, 703-706 (1995).
165. Moghadam, P.Z. et al. Development of a Cambridge Structural Database Subset: A Collection of Metal-Organic Frameworks for Past, Present, and Future. *Chem. Mater.* **29**, 2618-2625 (2017).
166. Yaghi, O.M. et al. Reticular synthesis and the design of new materials. *Nature* **423**, 705-714 (2003).
167. Farha, O.K. et al. Metal-Organic Framework Materials with Ultrahigh Surface Areas: Is the Sky the Limit? *J. Am. Chem. Soc.* **134**, 15016-15021 (2012).
168. Wu, H., Yildirim, T. & Zhou, W. Exceptional Mechanical Stability of Highly Porous Zirconium Metal-Organic Framework UiO-66 and Its Important Implications. *The Journal of Physical Chemistry Letters* **4**, 925-930 (2013).
169. Liu, D. et al. MOF-5 composites exhibiting improved thermal conductivity. *Int. J. Hydrogen Energy* **37**, 6109-6117 (2012).
170. Babaei, H., McGaughey, A.J.H. & Wilmer, C.E. Effect of pore size and shape on the thermal conductivity of metal-organic frameworks. *Chemical Science* **8**, 583-589 (2017).
171. Farha, O.K. & Hupp, J.T. Rational Design, Synthesis, Purification, and Activation of Metal-Organic Framework Materials. *Acc. Chem. Res.* **43**, 1166-1175 (2010).
172. Tanabe, K.K. & Cohen, S.M. Postsynthetic modification of metal-organic frameworks—a progress report. *Chem. Soc. Rev.* **40**, 498-519 (2011).

173. Lu, W. et al. Tuning the structure and function of metal–organic frameworks via linker design. *Chem. Soc. Rev.* **43**, 5561-5593 (2014).
174. Pascanu, V. et al. Sustainable Catalysis: Rational Pd Loading on MIL-101Cr-NH₂ for More Efficient and Recyclable Suzuki–Miyaura Reactions. *Chemistry – A European Journal* **19**, 17483-17493 (2013).
175. Dybtsev, D.N. et al. Reversible sorption of hydrogen on the novel hybrid material based on mesoporous chromium(iii) terephthalate with included rhenium clusters. *Russ. Chem. Bull.* **58**, 1623-1626 (2009).
176. Isaeva, V.I. & Kustov, L.M. The application of metal-organic frameworks in catalysis (Review). *Petroleum Chemistry* **50**, 167-180 (2010).
177. Luan, Y. et al. A general post-synthetic modification approach of amino-tagged metal–organic frameworks to access efficient catalysts for the Knoevenagel condensation reaction. *Journal of Materials Chemistry A* **3**, 17320-17331 (2015).
178. Wang, C., Zheng, M. & Lin, W. Asymmetric Catalysis with Chiral Porous Metal–Organic Frameworks: Critical Issues. *The Journal of Physical Chemistry Letters* **2**, 1701-1709 (2011).
179. Balderas-Xicohténcatl, R., Schlichtenmayer, M. & Hirscher, M. Volumetric Hydrogen Storage Capacity in Metal–Organic Frameworks. *Energy Technology* **6**, 578-582 (2018).
180. Li, B., Wen, H.-M., Zhou, W., Xu, J. & Chen, B. Porous Metal-Organic Frameworks: Promising Materials for Methane Storage. *Chem* **1**, 557-580 (2016).
181. de Lange, M.F., Verouden, K.J.F.M., Vlugt, T.J.H., Gascon, J. & Kapteijn, F. Adsorption-Driven Heat Pumps: The Potential of Metal–Organic Frameworks. *Chem. Rev.* **115**, 12205-12250 (2015).
182. AbdulHalim, R.G. et al. A Fine-Tuned Metal–Organic Framework for Autonomous Indoor Moisture Control. *J. Am. Chem. Soc.* **139**, 10715-10722 (2017).
183. Peng, Y., Yao, R. & Yang, W. A poly(amidoamine) nanoparticle cross-linked two-dimensional metal–organic framework nanosheet membrane for water purification. *Chem. Commun.* **55**, 3935-3938 (2019).
184. Kang, Z., Fan, L. & Sun, D. Recent advances and challenges of metal–organic framework membranes for gas separation. *Journal of Materials Chemistry A* **5**, 10073-10091 (2017).
185. Carné, A., Carbonell, C., Imaz, I. & Maspoch, D. Nanoscale metal-organic materials. *Chem. Soc. Rev.* **40**, 291-305 (2011).
186. Archana, K., Pillai, N.G., Rhee, K.Y. & Asif, A. Super paramagnetic ZIF-67 metal organic framework nanocomposite. *Composites Part B: Engineering* **158**, 384-389 (2019).
187. Tanaka, D. et al. Rapid preparation of flexible porous coordination polymer nanocrystals with accelerated guest adsorption kinetics. *Nat. Chem.* **2**, 410-416 (2010).
188. Li, P. et al. Synthesis of nanocrystals of Zr-based metal–organic frameworks with csq-net: significant enhancement in the degradation of a nerve agent simulant. *Chem. Commun.* **51**, 10925-10928 (2015).
189. Horcajada, P. et al. Metal–Organic Frameworks in Biomedicine. *Chem. Rev.* **112**, 1232-1268 (2012).
190. Lismont, M., Dreesen, L. & Wuttke, S. Metal-Organic Framework Nanoparticles in Photodynamic Therapy: Current Status and Perspectives. *Adv. Funct. Mater.* **27**, 1606314 (2017).
191. He, Q., Shi, J., Chen, F., Zhu, M. & Zhang, L. An anticancer drug delivery system based on surfactant-templated mesoporous silica nanoparticles. *Biomaterials* **31**, 3335-3346 (2010).
192. Al-Jamal, W.T. & Kostarelos, K. Liposomes: from a clinically established drug delivery system to a nanoparticle platform for theranostic nanomedicine. *Acc. Chem. Res.* **44**, 1094-1104 (2011).
193. Deng, C., Jiang, Y., Cheng, R., Meng, F. & Zhong, Z. Biodegradable polymeric micelles for targeted and controlled anticancer drug delivery: Promises, progress and prospects. *Nano Today* **7**, 467-480 (2012).
194. Karthik, S. et al. Photoresponsive coumarin-tethered multifunctional magnetic nanoparticles for release of anticancer drug. *ACS applied materials & interfaces* **5**, 5232-5238 (2013).
195. Fu, F. et al. Multifunctional lactobionic acid-modified dendrimers for targeted drug delivery to liver cancer cells: investigating the role played by PEG spacer. *ACS applied materials & interfaces* **6**, 16416-16425 (2014).
196. Mendes, R.G., Bachmatiuk, A., Büchner, B., Cuniberti, G. & Rummeli, M.H. Carbon nanostructures as multi-functional drug delivery platforms. *Journal of Materials Chemistry B* **1**, 401-428 (2013).
197. Greenwald, R.B., Choe, Y.H., McGuire, J. & Conover, C.D. Effective drug delivery by PEGylated drug conjugates. *Adv Drug Deliv Rev* **55**, 217-250 (2003).
198. Tang, S., Huang, X., Chen, X. & Zheng, N. Hollow Mesoporous Zirconia Nanocapsules for Drug Delivery. *Adv. Funct. Mater.* **20**, 2442-2447 (2010).
199. Yang, P., Gai, S. & Lin, J. Functionalized mesoporous silica materials for controlled drug delivery. *Chem. Soc. Rev.* **41**, 3679-3698 (2012).
200. Park, J., Jiang, Q., Feng, D., Mao, L. & Zhou, H.-C. Size-Controlled Synthesis of Porphyrinic Metal–Organic Framework and Functionalization for Targeted Photodynamic Therapy. *J. Am. Chem. Soc.* **138**, 3518-3525

- (2016).
201. Horcajada, P. et al. Porous metal-organic-framework nanoscale carriers as a potential platform for drug delivery and imaging. *Nat Mater* **9**, 172-178 (2010).
 202. Mura, S., Nicolas, J. & Couvreur, P. Stimuli-responsive nanocarriers for drug delivery. *Nat Mater* **12**, 991-1003 (2013).
 203. Horcajada, P. et al. Metal–Organic Frameworks as Efficient Materials for Drug Delivery. *Angew. Chem. Int. Ed.* **45**, 5974-5978 (2006).
 204. Huxford, R.C., Della Rocca, J. & Lin, W. Metal-organic frameworks as potential drug carriers. *Curr. Opin. Chem. Biol.* **14**, 262-268 (2010).
 205. Liang, K. et al. Biomimetic mineralization of metal-organic frameworks as protective coatings for biomacromolecules. *Nature communications* **6**, 7240 (2015).
 206. Kundu, T. et al. Mechanical downsizing of a gadolinium(III)-based metal-organic framework for anticancer drug delivery. *Chemistry (Easton)* **20**, 10514-10518 (2014).
 207. Yang, Y. et al. A Large Capacity Cationic Metal-Organic Framework Nanocarrier for Physiological pH Responsive Drug Delivery. *Mol. Pharm.* **13**, 2782-2786 (2016).
 208. Ren, H. et al. Polyacrylic acid@zeolitic imidazolate framework-8 nanoparticles with ultrahigh drug loading capability for pH-sensitive drug release. *Chem. Commun. (Camb.)* **50**, 1000-1002 (2014).
 209. Lee, N. & Hyeon, T. Designed synthesis of uniformly sized iron oxide nanoparticles for efficient magnetic resonance imaging contrast agents. *Chem. Soc. Rev.* **41**, 2575-2589 (2012).
 210. Wu, Y.-n. et al. Magnetic Metal–Organic Frameworks: γ -Fe₂O₃@MOFs via Confined In Situ Pyrolysis Method for Drug Delivery. *Small* **10**, 2927-2936 (2014).
 211. An, J., Geib, S.J. & Rosi, N.L. Cation-Triggered Drug Release from a Porous Zinc–Adeninate Metal–Organic Framework. *J. Am. Chem. Soc.* **131**, 8376-8377 (2009).
 212. Hu, Q. et al. A Low Cytotoxic Cationic Metal–Organic Framework Carrier for Controllable Drug Release. *J. Med. Chem.* **57**, 5679-5685 (2014).
 213. Nagata, S., Kokado, K. & Sada, K. Metal-organic framework tethering PNIPAM for ON-OFF controlled release in solution. *Chem. Commun. (Camb.)* **51**, 8614-8617 (2015).
 214. Lin, W. et al. Low Cytotoxic Metal-Organic Frameworks as Temperature-Responsive Drug Carriers. *ChemPlusChem* **81**, 804-810 (2016).
 215. Jiang, K. et al. Pressure controlled drug release in a Zr-cluster-based MOF. *Journal of materials chemistry. B* **4**, 6398-6401 (2016).
 216. Sumida, K., Hu, M., Furukawa, S. & Kitagawa, S. Structuralization of Ca(2+)-Based Metal-Organic Frameworks Prepared via Coordination Replication of Calcium Carbonate. *Inorg. Chem.* **55**, 3700-3705 (2016).
 217. Baati, T. et al. In depth analysis of the in vivo toxicity of nanoparticles of porous iron(iii) metal–organic frameworks. *Chemical Science* **4**, 1597-1607 (2013).
 218. Sun, C.-Y. et al. Chiral Nanoporous Metal-Organic Frameworks with High Porosity as Materials for Drug Delivery. *Adv. Mater.* **23**, 5629-5632 (2011).
 219. Jiang, J., Oberdörster, G. & Biswas, P. Characterization of size, surface charge, and agglomeration state of nanoparticle dispersions for toxicological studies. *J. Nanopart. Res.* **11**, 77-89 (2009).
 220. Freund, R., Lächelt, U., Gruber, T., Rühle, B. & Wuttke, S. Multifunctional Efficiency: Extending the Concept of Atom Economy to Functional Nanomaterials. *ACS Nano* **12**, 2094-2105 (2018).
 221. Wang, S. et al. Surface-Specific Functionalization of Nanoscale Metal–Organic Frameworks. *Angew. Chem. Int. Ed.* **54**, 14738-14742 (2015).
 222. Abánades Lázaro, I. et al. Selective Surface PEGylation of UiO-66 Nanoparticles for Enhanced Stability, Cell Uptake, and pH-Responsive Drug Delivery. *Chem* **2**, 561-578 (2017).
 223. Ramishetti, S. & Huang, L. Intelligent design of multifunctional lipid-coated nanoparticle platforms for cancer therapy. *Ther. Deliv.* **3**, 1429-1445 (2012).
 224. Wuttke, S. et al. MOF nanoparticles coated by lipid bilayers and their uptake by cancer cells. *Chem. Commun.* **51**, 15752-15755 (2015).
 225. Agostoni, V. et al. A “green” strategy to construct non-covalent, stable and bioactive coatings on porous MOF nanoparticles. *Sci. Rep.* **5**, 7925 (2015).
 226. Wang, X.G. et al. A multifunctional metal-organic framework based tumor targeting drug delivery system for cancer therapy. *Nanoscale* **7**, 16061-16070 (2015).
 227. Deshpande, P.P., Biswas, S. & Torchilin, V.P. Current trends in the use of liposomes for tumor targeting. *Nanomedicine (London, England)* **8**, 1509-1528 (2013).
 228. Gabizon, A.A. Stealth Liposomes and Tumor Targeting: One Step Further in the Quest for the Magic

- Bullet. *Clin. Cancer Res.* **7**, 223 (2001).
229. Torchilin, V.P. Targeted pharmaceutical nanocarriers for cancer therapy and imaging. *The AAPS journal* **9**, E128-147 (2007).
230. Egusquiaguirre, S.P., Igartua, M., Hernández, R.M. & Pedraz, J.L. Nanoparticle delivery systems for cancer therapy: advances in clinical and preclinical research. *Clin. Transl. Oncol.* **14**, 83-93 (2012).

Chapter 2

Characterization Methods

2.1 X-Ray Diffraction

X-ray diffraction (XRD) measurements give information about the crystallinity and structure of a sample. X-rays used in XRD are generally emitted from metal sources with characteristic wavelengths such as Cu-K α = 1.54182 Å with wavelengths in the region of Ångstroms (0.1 nm)¹, which is in the same order of magnitude as the size of atoms and the length of chemical bonds. The distance between the atoms corresponds to the diffracted wavelength and as such the crystal structure can be determined. Diffraction is the bending of a wave when it encounters an obstacle or slit. The wave will bend around the edges of the obstacle into the geometrical shadow of the object. The X-rays are diffracted by interacting with the electron densities of the lattice planes of the sample (Figure 2.1). As crystal structures are periodic networks both constructive and destructive interference are possible. Constructive interference of x-rays is described by Bragg's relation²:

$$n\lambda = 2d\sin\theta$$

N: Integer number; λ : Wavelength ;d: distance between lattice planes, θ : angle of incident

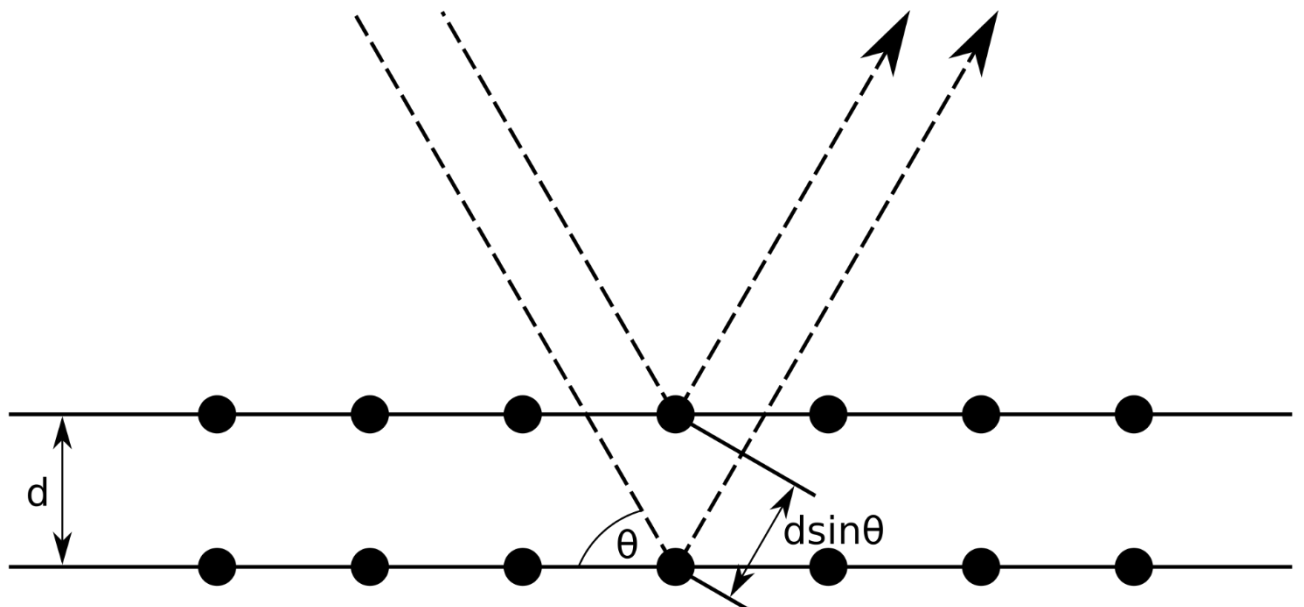


Figure 2.1: Scheme of Bragg diffraction³

Each crystal structure possesses a unique diffraction pattern with signals centered around the reflection angles that correspond to a path difference that is a multiple integer of the wavelength of the X-ray waves. As can be deduced from Bragg's relation the smaller the

distance between the lattice planes the larger the observed reflection angles will be and vice versa. This means that a closer investigation of the small scattering angles of $10^\circ > 2\theta$ (small angle X-ray scattering (SAXS)) allows to determine the mesoporous nature of porous samples while the wide angle X-ray scattering (WAXS) with 2θ of 10° to 60° can be used to determine the crystallinity of the particles. XRD measurements of porous samples for this work were taken with a STOE Transmission-Diffraktometer System STADI P with a Ge(111) primary monochromator using Cu- $K_{\alpha 1}$ radiation in transmission geometry.

2.2 Nuclear Magnetic Resonance Spectroscopy

Nuclear magnetic resonance spectroscopy (NMR) is a very sensitive investigation method for the chemical structure of organic molecules. The main requirement of NMR spectroscopy is that the target molecule must contain nuclei with a magnetic dipole moment of $\mu \neq 0$. The magnetic dipole moment of nuclei is defined by the nuclear spin and an inherent factor the magnetogyric ratio γ . The latter is constant for each element and isotope and is as such an indicator of how suitable they are for NMR spectroscopy. Applying an external static magnetic field to a suitable nucleus leads to a split in the degenerated energy levels of the examined nuclei due to the Zeeman effect.⁴ The energy to create the split is provided in the form of electromagnetic waves in the 300 MHz to 1000 MHz range. The resonance frequency of a nucleus is called the Larmor frequency:

$$\Delta E = \hbar\gamma B_0 = \hbar\omega_0$$

ΔE : Energy required for spin resonance; γ : magnetogyric ratio; B_0 : External magnetic field strength; ω_0 : Larmor frequency.

In isolation all nuclei of the same element would possess the same Larmor frequency, but in reality the local magnetic fields can differ from the overall magnetic field due to interactions with the magnetic fields of surrounding nuclei or electron densities. This makes NMR a powerful tool for structural analysis of organic molecules. When measuring liquid samples deuterated solvents are used to prevent the NMR active nuclei in the solvent from interfering with the measurement of the diluted sample. ^1H and ^{13}C NMR spectra for this work were

recorded on a *Bruker Avance III-400* MHz and a *Bruker Avance III-270* MHz spectrometer.

2.3 Dynamic Light Scattering

Dynamic light scattering (DLS), also known as photon correlation spectroscopy or quasi-elastic light scattering, is used to determine the hydrodynamic diameter of nanoparticles in suspension.⁵ DLS is based on the interaction between electromagnetic radiation and particles in comparable size range to its wavelength. As the laser has a wavelength of 633 nm there's large potential for interference in the typical size range of nanoparticles. To detect stray light the refractive index of the sample has to differ from that of the used solvent. If the sample is properly diluted in the measured suspension the Brownian motion of the particles leads to a fluctuation of the scattered light intensity. This movement of the scattering centers causes an observable frequency shift due to the Doppler Effect, which is then measured by an autocorrelation function. These shifts are corresponding to the size of the particles, due to larger particles possessing a slower average Brownian motion. This velocity depends on the translational diffusion coefficient, which can be used to calculate the hydrodynamic diameter of the particles with the Stokes-Einstein equation, if the viscosity of the solvent is also known.

$$d(H) = \frac{kT}{3\pi\eta D}$$

Stokes-Einstein equation. $d(H)$: hydrodynamic particle diameter, D : translational diffusion coefficient, k : Boltzmann's constant, T : temperature, η : the viscosity of the suspending medium.

The calculated diameter is the diameter of a sphere with the measured translational diffusion coefficient. The coefficient can be influenced by the ionic strength of the solvent as well as the particle surface, which can lead to errors when determining the diffusion speed. In addition the light scattering is size dependent with large particles showing significantly more scattering. Due to this DLS is susceptible to particle agglomerates as well as impurities in the sample and only delivers reliable results for monodisperse and uncontaminated samples. If this is taken into consideration DLS is a fast and reliable method to determine the hydrodynamic size of particles in a wide range between 1 nm and 1000 nm. DLS measurements were carried out using a Malvern Zetasizer-Nano instrument with a 4 mW He-Ne laser ($\lambda = 633$ nm) and an avalanche photo detector.

2.4 Zeta Potential

Zeta potential measurements are used to determine the outer surface charge of nanoparticles, which allows to assess the colloidal stability of suspended nanoparticles. Particles are usually slightly charged in aqueous solution, due to adsorption of solvent molecules (hydration hull) or dissociation of surface groups, which leads to the creation of an electrostatic potential due to the formation of a layer of oppositely charged molecules around the particle (Figure 2.2). These counter ions are separated into the tightly bound Stern layer and the slipping plane which consists of loosely bound counter charges. The Stern layer follows the Brownian motion of the particles while the slipping plane remains in place. The potential between the Stern layer and the slipping plane is the Zeta potential (ζ).⁶ The Zeta potential is often dependent on pH.

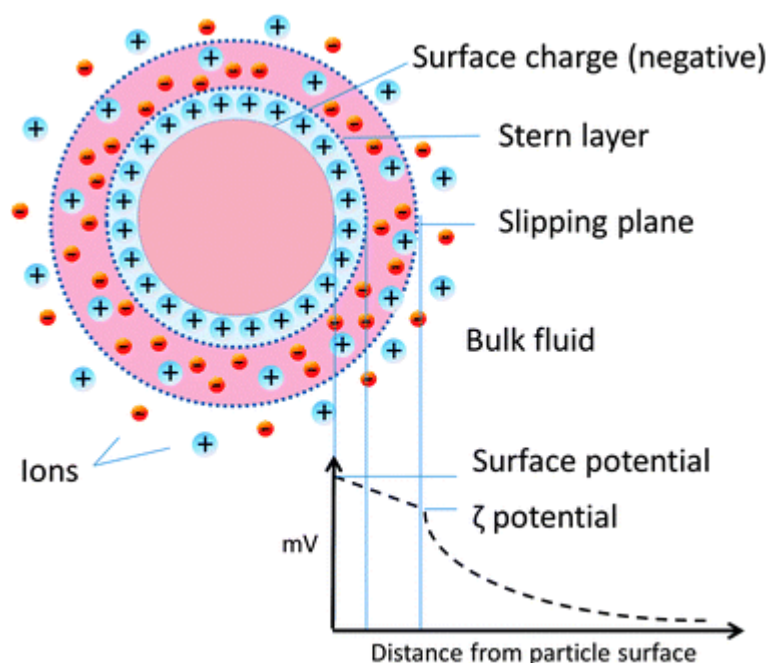


Figure 2.2: Schematic of the potential landscape of a suspended particle⁷

This electrical potential can be modified by an external electric field and can hinder the induction of motion into the sample. Depending on the direction four different electrokinetic effects are observed: electrophoresis, electroosmosis, streaming potential and sedimentation potential. While the Zeta potential cannot be measured directly, it is related to the electrophoretic mobility (U_E) via the Henry equation. U_E can be measured by applying a voltage and observing the velocity of the particle to the oppositely charged electrode relative to the medium. Additional factors needed to calculate the zeta potential are the dielectric constant ϵ and viscosity η of the solvent as well as the field strength which are all accounted for in the

Henry equation:

$$U_E = \frac{2\varepsilon\zeta f(\kappa a)}{3\eta}$$

Henry equation: U_E : electrophoretic mobility; ε : dielectric constant of the medium; η : viscosity of the medium; ζ : zeta potential; $f(\kappa a)$ Henry function with κ Debye length and a particle radius

For particles larger than 200 nm in a polar medium the Henry function can be approximated to 1.5 using the Smoluchowski model or to 1.0 for small particles suspended in a non-polar medium. Using these approximations the Zeta potential of particles can be calculated. Zeta potential measurements were carried out with a Malvern Zetasizer Nanio equipped with a 4 mW He-Ne laser ($\lambda = 633$ nm) and an avalanche photodetector.

2.5 Thermogravimetric Analysis (TGA)

Thermogravimetric Analysis (TGA) determines the mass change of a sample as a function of temperature or time. In a thermobalance the sample and a reference are measured simultaneously.⁸ The temperature is raised over time and information on the mass change (TGA), the temperature change (differential thermal analysis (DTA)) and the heat change (differential scanning calorimetry (DSC)) can be obtained. These changes are caused by decomposition or combustion of the sample. Additionally, chemical reactions can also play a role. These measurements allow to deduce the thermal stability of a sample as well as the relative amount of incorporated organic substances.

2.6 UV-Vis Spectroscopy

UV-Vis spectroscopy makes use of the absorption of specific wavelengths in the visible and low energy UV spectrum by molecules. It is commonly used in qualitative and quantitative drug analysis. A sample – usually in suspension in a cuvette – is exposed to UV or visible light with variable wavelength produced by a monochromator. A commonly used wavelength range is from about 800 nm to 350 nm with step sizes of 2 nm. The incoming electromagnetic waves are absorbed by electrons, usually outer shell valence electrons, which are excited to higher energy levels. The transmitted energy is compared to that of the incident beam to obtain the energy absorbed by the sample. This process is repeated for each distinctive wavelength and the absorption bands show a distinct position, intensity and fine structure that are associated with defined transitions in the sample. As these transitions are often accompanied by rotational and vibrational transitions the fine structures are overlain resulting in broad absorption bands. The absorption is defined by the Beer-Lambert-Bouguer Law:⁹

$$A = \log \frac{I_0}{I} = \varepsilon \cdot c \cdot d$$

A: absorbance; I_0 : Intensity of incident beam; I : Intensity of transmitted beam; d : Path length of sample cell; c : concentration of diluted sample; ε : extinction coefficient

The only factor that cannot be controlled through the experimental setup and that is sample specific, is the extinction coefficient. As such any observed changes in the absorption behavior of a sample must either come from structural changes or the presence of additional molecules inside the sample. This allows to determine the concentration of samples with known extinction coefficients and in turn the loading capacity of drug carriers for specific target molecules, as well as changes in a molecules absorption pattern after functionalization.

2.7 Fluorescence Spectroscopy

Fluorescence spectroscopy is a type of electromagnetic spectroscopy and is a non-destructive analytical method in which the optical emission spectrum of fluorescent samples is measured. The fluorophores can be among others: aromatic hydrocarbons, proteins, fluorescent elements like lanthanides.¹⁰ Light absorption causes a transition from the electronic ground states S_0 to an electronic excited state S_1 in the sample. The excitation is followed by a rapid vibrational relaxation to the lowest of the S_1 energy levels. From this state a fast spin-allowed rapid relaxation back to the ground state accompanied by the emission of light or in other words fluorescence can occur. Another possibility is the slow spin-forbidden emission of light, phosphorescence, following an intersystem crossing from an excited triplet state, with average lifetimes of milliseconds to seconds. This difference between phosphorescence and fluorescence is illustrated in a Jablonski diagram¹¹ (Figure 2.3). The wavelength of the emitted light is red-shifted (Stokes shift) due to energy loss from vibrational relaxation, the used solvent, complexation or energy transfer effects.¹⁰

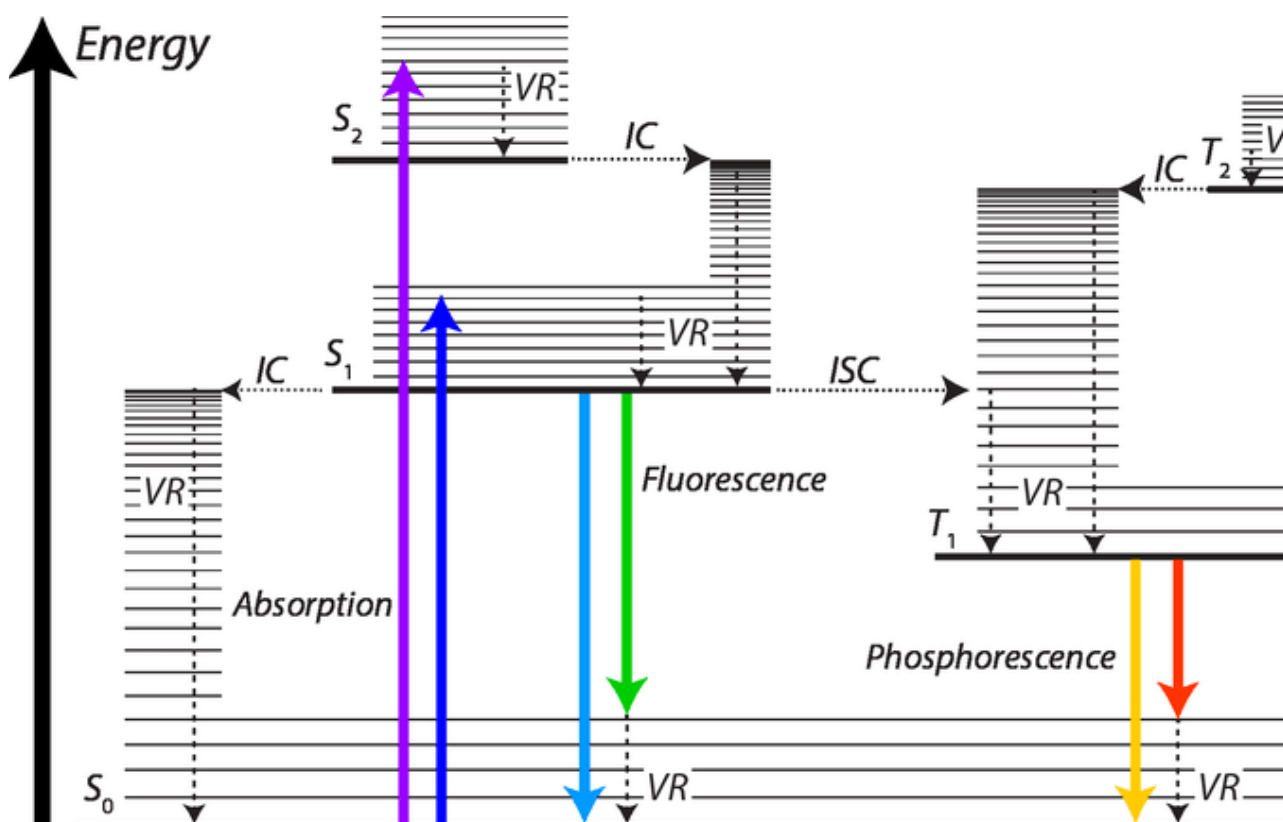


Figure 2.3: Jablonski diagram. VR: vibrational relaxation. IC: internal conversion, ISC: intersystem crossing. Vertical lines represent singlet (S_n) and triplet (T_n) states.¹²

The typical setup of a fluorescence spectrometer consists of a radiation source, like a Xenon arc lamp, that is spectrally selected by a monochromator and focused onto the sample. The emitted light is absorbed by photomultiplier detectors that are commonly situated orthogonally to the light path. The signal is then converted into a spectrum. Aside from excitation and emission spectra, time dependent fluorescence measurements can also be performed. In this work fluorescence experiments were performed on a PTI spectrometer equipped with a UXL-75XE USHIO xenon short arc lamp and a 810/814 photomultiplier system.

2.8 Fluorescence Microscopy and Confocal Microscopy

Fluorescence microscopy is used to visualize fluorescent samples. In most cases either the sample itself can have fluorescent properties (autofluorescence) or fluorescent markers binding to the sample are used¹³. A common trait of most fluorophores is an aromatic ring system and a fairly small molecules size of 200-1000 Dalton although far larger natural fluorophores such as green fluorescent protein also exist.¹⁴ To avoid the excitation of spectrally neighboring fluorophores and generating background noise fluorescence microscopy requires near-monochromatic, strong light sources and as such mostly LEDs, lasers or Xenon arc lamps are used. The mechanism of fluorescence has already been discussed in chapter 2.7. The three common ways to stain biological samples are the use of biological fluorescent stains, which can be used for live cell imaging and directly bind to components of the cell, immunofluorescence making use of labeled antibodies that then bind to the corresponding antigen – this requires fixation of the cells due to the need for permeabilization - and finally the use of altered, fusion proteins, which can be directly expressed by the target cells through transfection with plasmids.

Confocal fluorescence microscopy (Figure 2.4) is intended to increase the optical resolution in all three spatial dimensions compared to a standard light microscope. It was invented by Minsky making use of a combination of a lamp, a lens, and a pinhole.¹⁵ Light from the light source is passing through the excitation aperture before being focused on the sample by the objective. The light reflected or emitted as fluorescence by the sample passes through the objective and a dichroic mirror before reaching a pinhole. The pinhole eliminates light coming from image planes other than the focus plane. As such only the current focal point is recorded

by a point detector and the entire image range has to be scanned over to acquire the image. To speed up image acquisition, modern confocal microscopes often use a spinning disc featuring multiple concentrically arranged pinholes, which allow for scanning multiple spots of the sample simultaneously drastically speeding up image generation.¹⁶

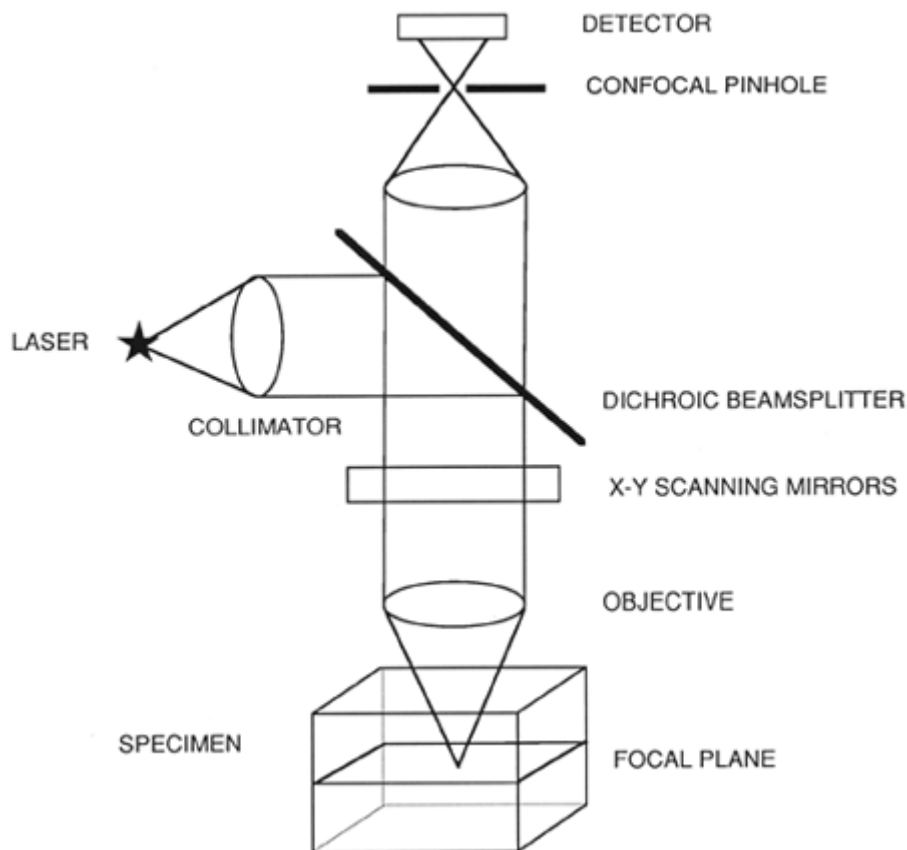


Figure 2.4: Schematic of the light path of a confocal microscope¹⁷

The fluorescence microscopy images in this work we performed with a confocal fluorescence microscope based on the Zeiss Cell Observer SD utilizing a Yokogawa spinning disk unit CSU-X1. Additional spheroid and single cell imaging was done with a Nikon Eclipse Ti2-E microscope. High throughput imaging was performed on an ImageXPress Micro XLS from Molecular Devices.

2.9 Sorption Analysis

Gas adsorption is commonly used to determine the characteristics of porous materials and allows to determine pore size, volume and shape, as well as the total surface area. It makes use of the adsorption and desorption of unreactive gases (adsorbate) on an, often porous, material (adsorbent).¹⁸ The volume of the adsorbed gas, commonly nitrogen or argon, is measured at different relative pressure at low temperatures (77 K). The interactions between adsorbate and adsorbent are restricted to van-der-Waals forces in this case and no chemical changes occur. Depending on the porous structure of the material six different major types of adsorption isotherms can be observed as a result, as categorized by the International Union of Pure and Applied Chemistry (Figure 2.5).¹⁸

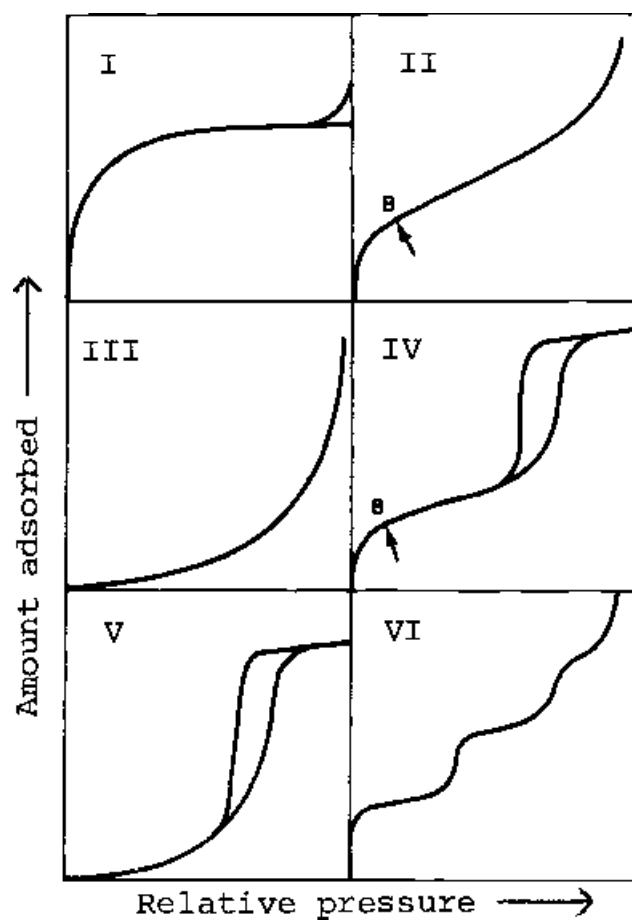


Figure 2.5: Six major types of adsorption isotherms according to IUPAC.¹⁸

These isotherms allow to deduce the pore type (micro-, meso-, macro-, or non-porous) and also can give insight into the pore shape. Type I isotherms show a fast rise of adsorbed gas volume for low relative pressures (pore filling), before reaching a plateau. They are common for microporous materials with relatively small external surfaces. Type II isotherms are

typically found for macroporous materials and start out similar to Type I isotherms but do not reach a plateau. Instead the amount of adsorbed gas is steadily increasing due to unrestricted monolayer-multilayer adsorption. Type III looks similar to exponential growth of the adsorbed gas volume and is typical for macroporous or non-porous materials if the interactions between adsorbate and adsorbent are significantly weaker than the interactions between adsorbates. Type IV isotherms are common for mesoporous materials. They show the pore filling and monolayer-multilayer adsorption, but also include a hysteresis loop, which is associated with capillary condensation of the adsorbate in the pores. During desorption the capillary pressure results in adsorbate requiring lower relative pressures to leave the pores than was required for filling them. Type V is similar to Type III isotherms with the difference of including a hysteresis loop, due to some capillary condensation occurring. Type VI is common for the stepwise multilayer adsorption of non-porous substrate, with each step representing one filled monolayer.

Several models exist to calculate the surface area of porous materials from sorption data. The first was the Langmuir model¹⁹, which makes four general assumptions and is as such of limited use for more complex sorption behaviors:

1. The adsorbing gas is immobile while adsorbed
2. All adsorption sites are equivalent
3. Each site allows for the adsorption of exactly one molecule
4. No interaction between adsorbed molecules occurs

This model closely resembles Type I isotherms, but only describes monolayer adsorption. More complex adsorption mechanics including multilayer adsorption is more adequately described by the Brunnauer, Emmet, Teller (BET) theory,²⁰ which makes different assumptions:

1. Multilayer adsorption has no limits
2. Only the first layer has a distinct adsorption enthalpy from the interactions with the adsorbate
3. Every further layer has the same enthalpy due to only interacting with the underlying monolayer

These assumptions are reflected in the following equation:

$$\frac{p}{n^a(p_0 - p)} = \frac{1}{n_m^a C} + \frac{(C - 1)}{n_m^a C} \cdot \frac{p}{p_0}$$

n^a : Amount of the adsorbate at relative pressure p/p_0 ; n_m^a : Capacity of a single monolayer; C : BET constant

n_m^a can be obtained from the linear relation of $\frac{p}{n^a(p_0 - p)}$ plotted against p/p_0 . The linear region is restricted to a limited part of the isotherm – mostly below $p/p_0 = 0.3$ – under the BET theory which allows to calculate n_m^a . This in turn allows to calculate the BET surface area:

$$A(BET) = n_m^a \cdot N_A \cdot a_m$$

n_m^a : Capacity of a single monolayer, N_A : Avogadro constant; a_m : Surface area occupied by a single adsorbate molecule

To calculate the pore size and pore volume from the BET data the density functional theory (DFT) is applied. DFT is used to describe the interaction between fluids and hard walls of solids. Non-local density functional theory (NLDFT) was successfully used for pore calculations in zeolites and other silica materials.²¹ NLDFT makes the assumption of homogenous pore structures, but still delivers mostly accurate results for micro- and mesoporous materials. An updated method is the quenched-solid density functional theory (QSDFT) which accounts for surface roughness and heterogeneity.²¹ The BET theory was used for surface area calculations and the QSDFT method was used to calculate pore volume and size. Nitrogen sorption analysis was performed on a Quantachrome Instrument Nova 4000e at 77 K. All samples were degassed prior to the measurements for 12 h at 120 °C.

2.10 Scanning Electron Microscopy and Transmission Electron Microscopy

Electron microscopy is a powerful tool for analyzing the morphology and composition of solid samples with nanoscale or below resolution. Resolutions on this scale would normally be impossible for light microscopes due to the Abbe limit,²² which postulates a resolution limit of around 200 nm. While this can be circumvented with modern super resolution techniques, electron microscopy remains a valued tool. The limiting factor of the resolution is the wavelength and using a smaller wavelength allows for a better resolution. The wavelength λ of moving particles in relation to their momentum p is described by the De Broglie equation:²³

$$\lambda = \frac{h}{p} = \frac{h}{mv}$$

λ : Wavelength; h : Planck's constant; p : momentum; m : mass; v velocity;

As such the wavelength of electrons solely depends on their velocity which can be influenced by applying an acceleration voltage. Acceleration voltages commonly used for electron microscopy are in the range of 0.1 keV to 300 keV (depending on intended application), which result in electron wavelengths in the low nano- to picometer range and allow for very high resolutions. Avoiding any background signals from gases between the electron source and the sample, requires operation in high or ultrahigh vacuum. Accelerated electrons can interact with the sample in various ways (Figure 2.6). They can pass right through the sample without any interaction or energy loss, or they can interact with the sample under energy loss, leading to elastic or inelastic scattering.

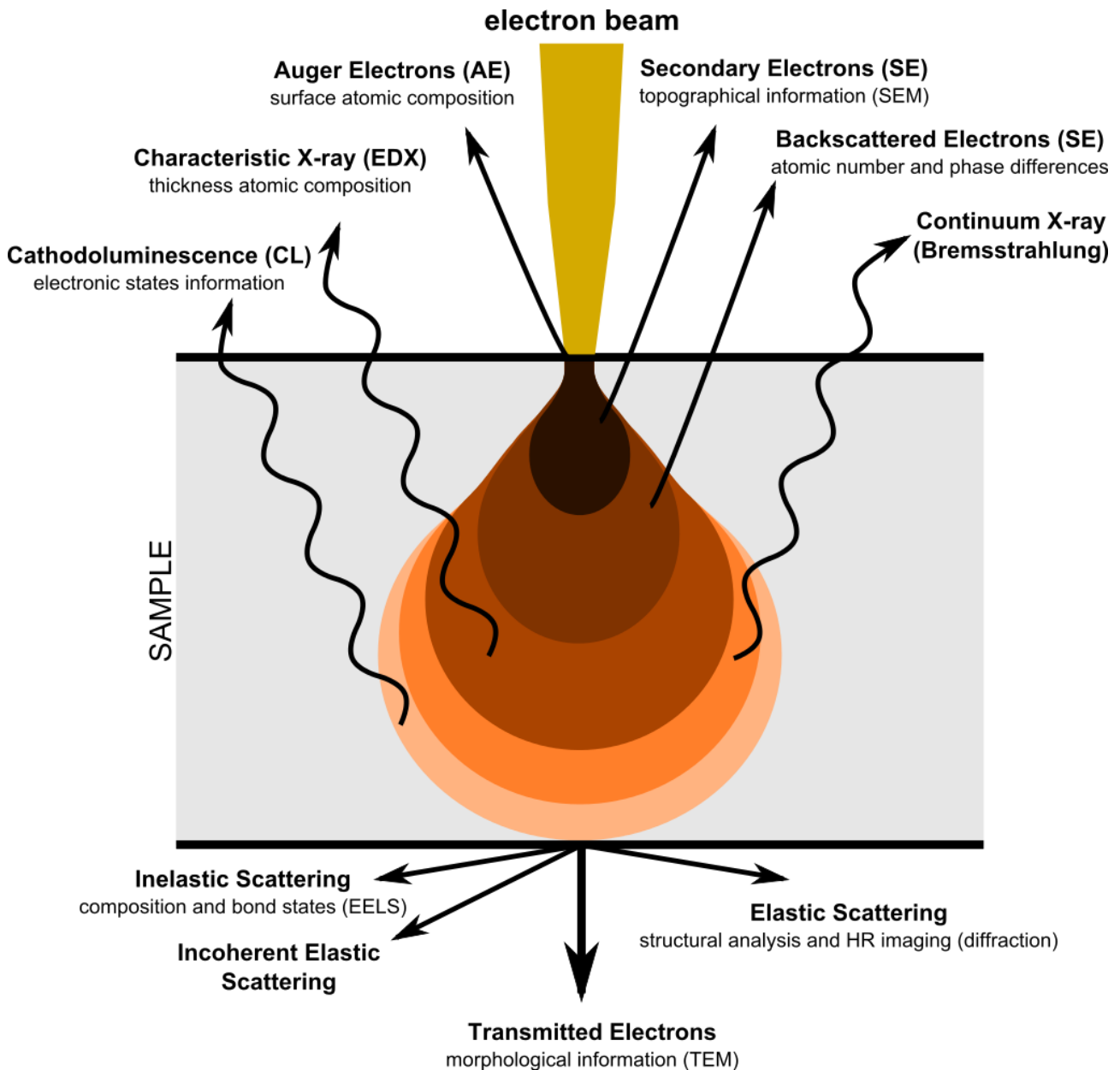


Figure 2.6: Diagram illustrating the phenomena resulting from the interaction of highly energetic electrons with matter²⁴

Elastic scattering is caused by Coulomb interactions of the electron beam and the samples electron clouds. The scattering angle depends on the elemental composition of the sample with light elements scattering at low angles while heavy elements scatter at greater angles. Backscattered electrons are scattered back towards the direction of the electron source. Inelastic scattering is the result of an energy transfer from the beam electrons to the sample. Secondary electrons are electrons that get knocked loose by the electron beam and leave the sample. The resulting vacancy will be filled by an electron of the same atom with a higher energy, which results in either an element specific x-ray to be ejected, which is used for the elemental analysis in EDX, or the emission of an Auger electron. Auger electrons are electrons

that were excited by the energy created by filling the hole a secondary electron left behind and are in turn also ejected from the sample.²⁵ Secondary electrons are commonly used for SEM imaging, but the other types are also used in more specialized imaging techniques. Deflected electrons and their deflection angles can be recorded with a CCD camera or a fluorescent screen and based on this information on the local sample morphology can be obtained.

As opposed to SEM which mainly makes use of secondary electrons, transmission electron microscopy (TEM) makes use of electrons that pass through the sample. For this purpose the sample has to be relatively thin with thickness of several hundred nanometers. In addition high acceleration voltages of 60 keV to 300 keV are used. If electrons don't interact with the sample they just pass through as an extension of the primary beam. Inelastically scattered electrons can be examined via electron energy loss spectroscopy (EELS), which uses the energy difference between incident and detected electrons. Elastic scattering results in a diffraction pattern similar to that of X-ray diffraction, but can also be used for imaging. The contrast in the obtained images and the detected scattering angle (brightfield vs darkfield) allows to make deductions about the atomic number and density of the elements in the sample.

In this thesis scanning electron microscopy measurements were performed on a *Helios G3 UC (FEI)*. All samples were prepared by drying particle dispersions on carbon pads that are situated on aluminum sample holders. If not stated otherwise the microscope was operated at 3 kV using a through-lens detector. TEM samples were prepared by drying nanoparticle dispersions on a carbon-coated copper grid. Measurements were performed on a *Titan Themis (FEI)* operated at 300 kV.

2.11 Polymerase Chain Reaction

Polymerase chain reaction (PCR) is a method to rapidly make copies of specific DNA samples that is used in biological research, but also other fields like forensics.^{26, 27} The idea of PCR was first described by Klempe et al. in 1971²⁸, but its invention is commonly credited to Mullis in 1983.²⁹ PCR is usually performed with a thermal cycler and relies on thermal cycling. Needed for a PCR reaction are the target DNA containing the sequence that is supposed to be amplified and/or altered, a temperature stable DNA polymerase, a pair of primers that are complementary to the DNA target, deoxynucleotide triphosphates (dNTPs) and a suitable buffer.³⁰ The reactants are exposed to cycles of heating and cooling leading to DNA melting and polymerase-driven DNA replication (Figure 2.7). In the first step the two strands of double stranded DNA are physically separated through high temperatures. Next the temperature is lowered and the primers bind to the corresponding DNA. These DNA strands then function as templates for the polymerase to amplify DNA using dNTPs. The newly generated DNA can then be used as a template for amplification in the next cycling steps leading to an exponential amplification of the DNA sample.

Polymerase chain reaction - PCR

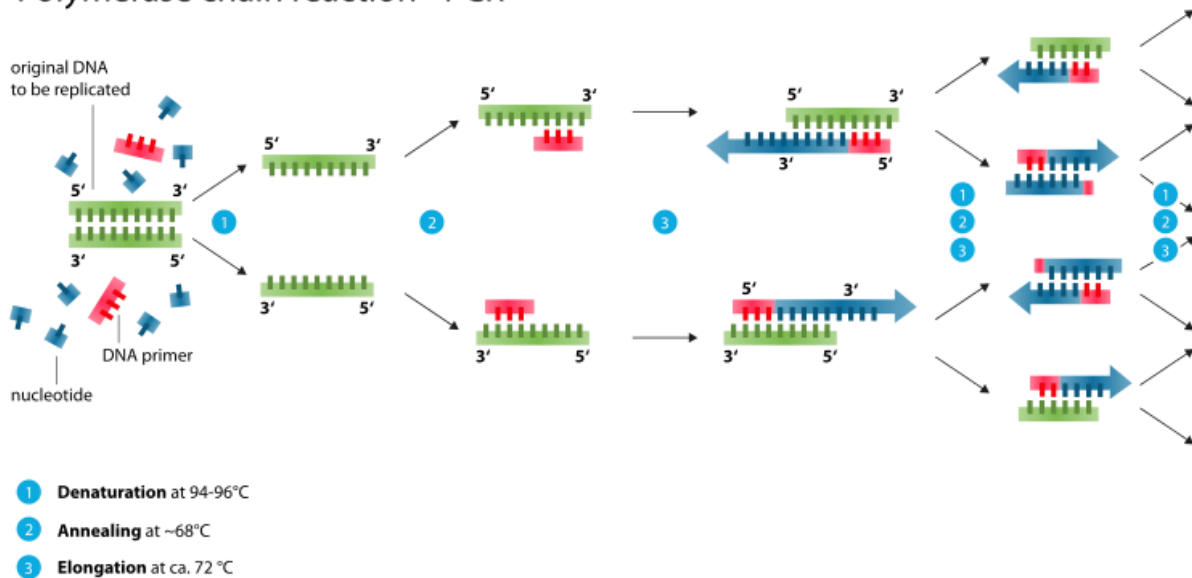


Figure 2.7: Schematic illustration of the PCR cycle³¹

2.12 References

1. Markowicz, A. in Handbook of X-Ray Spectroscopy 1-92 (CRC Press, 2001).
2. Bragg, W.H. & Bragg, W.L. The reflection of X-rays by crystals. *Proceedings of the Royal Society of London. Series A, Containing Papers of a Mathematical and Physical Character* **88**, 428-438 (1913).
3. Furiouslettuce Bragg Diffraction Planes (2009). (<https://en.wikipedia.org/wiki/File%3ABraggPlaneDiffraction.svg>). Retrieval Date 29.06.2020.
4. Zeeman, P. The Effect of Magnetisation on the Nature of Light Emitted by a Substance. *Nature* **55**, 347-347 (1897).
5. Pecora, R. Dynamic Light Scattering Measurement of Nanometer Particles in Liquids. *J. Nanopart. Res.* **2**, 123-131 (2000).
6. Lyklema, J. Fundamentals of Interface and Colloid Science, Vol. 2. (1995).
7. Herrada García, R., Pérez Corona, M., Shrestha, R., Pamukcu, S. & Bustos, E. 37/661 (2014).
8. Coats, A.W. & Redfern, J.P. Thermogravimetric analysis. A review. *Analyst* **88**, 906-924 (1963).
9. Beer Bestimmung der Absorption des rothen Lichts in farbigen Flüssigkeiten. *Annalen der Physik* **162**, 78-88 (1852).
10. Lakowicz, J.R. Principles of Fluorescence Spectroscopy, Vol. 3. edn., (Springer, 2006).
11. Jablonski, A. Efficiency of Anti-Stokes Fluorescence in Dyes. *Nature* **131**, 839-840 (1933).
12. Dzebo, D. Photon Upconversion through Triplet-Triplet Annihilation: Towards Higher Efficiency and Solid State Applications (2016).
13. Spring K. R., D.M.W. (Nikon MicroscopyU).
14. Junjia, L., Chen, L. & Wei, H. Fluorophores and Their Applications as Molecular Probes in Living Cells. *Curr. Org. Chem.* **17**, 564-579 (2013).
15. Minsky, M. Memoir on inventing the confocal scanning microscope. *Scanning* **10**, 128-138 (1988).
16. Cox, G. in Optical Imaging Techniques in Cell Biology, Edn. 1st 115-122 (CRC Press, 2006).
17. Masters, B.R. in Handbook of Coherent Domain Optical Methods: Biomedical Diagnostics, Environmental and Material Science. (ed. V.V. Tuchin) 895-947 (Springer US, New York, NY; 2004).
18. Sing, K.S.W. Reporting physisorption data for gas/solid systems with special reference to the determination of surface area and porosity (Recommendations 1984). *Pure Appl. Chem.* **57**, 603 - 619 (1985).
19. Langmuir, I. THE ADSORPTION OF GASES ON PLANE SURFACES OF GLASS, MICA AND PLATINUM. *J. Am. Chem. Soc.* **40**, 1361-1403 (1918).
20. Brunauer, S., Emmett, P.H. & Teller, E. Adsorption of Gases in Multimolecular Layers. *J. Am. Chem. Soc.* **60**, 309-319 (1938).
21. Landers, J., Gor, G.Y. & Neimark, A.V. Density functional theory methods for characterization of porous materials. *Colloids Surf. Physicochem. Eng. Aspects* **437**, 3-32 (2013).
22. Abbe, E. Beiträge zur Theorie des Mikroskops und der mikroskopischen Wahrnehmung. *Archiv für Mikroskopische Anatomie* **9**, 413-468 (1873).
23. de Broglie, L. The reinterpretation of wave mechanics. *Found. Phys.* **1**, 5-15 (1970).
24. Claudionico, Electron Interaction with Matter (2013). (https://commons.wikimedia.org/wiki/File:Electron_Interaction_with_Matter.svg). Retrieval Date 03.07.2020.
25. Meitner, L. Über dieβ-Strahl-Spektren und ihren Zusammenhang mit der γ-Strahlung. *Z. Phys.* **11**, 35-54 (1922).
26. Saiki, R. et al. Enzymatic amplification of beta-globin genomic sequences and restriction site analysis for diagnosis of sickle cell anemia. *Science* **230**, 1350-1354 (1985).
27. Saiki, R. et al. Primer-directed enzymatic amplification of DNA with a thermostable DNA polymerase. *Science* **239**, 487-491 (1988).
28. Kleppe, K., Ohtsuka, E., Kleppe, R., Molineux, I. & Khorana, H.G. Studies on polynucleotides: XCVI. Repair replication of short synthetic DNA's as catalyzed by DNA polymerases. *J. Mol. Biol.* **56**, 341-361 (1971).
29. Rabinov, P. Making PCR: A Story of Biotechnology. (University of Chicago Press, Chicago; 1996).
30. Joseph Sambrook, D.W.R. in Molecular Cloning: A Laboratory Manual, Edn. 3 (Cold Spring Harbor Laboratory Press, Cold Spring Harbor; 2001).
31. Enzoklop Schematic Drawing of the PCR cycle (2014). (https://commons.wikimedia.org/wiki/File:Polymerase_chain_reaction.svg). Retrieval Date 06.07.2020.

Chapter 3

Spatio-selective activation of nuclear translocation of YAP with light directs invasion of cancer cell spheroids

Bernhard Illes, Adrian Fuchs, Florian Gegenfurtner, Evelyn Ploetz, Stefan Zahler, Angelika M. Vollmar, Hanna Engelke

This chapter is submitted for publication.

3.1 Introduction

Yes-associated protein (YAP) is a key regulator of mechanosignaling. It translates mechanical cues from the extracellular matrix into intracellular signals.¹ This process is mediated via its localization within the cell: YAP is cytoplasmic on soft substrates and translocates into the nucleus upon sensing mechanical forces e.g. by a stiff substrate.^{1, 2} In the nucleus, it activates downstream signaling. High nuclear YAP has been shown to be associated with invasion and altered matrix properties in tumors.^{3, 4} However, due to lack of control over its translocation it is not clear, whether nuclear YAP is sufficient to induce invasion or whether it is rather just associated with invasion. YAP is able to induce symmetry breaks in cell collectives.⁵ We therefore hypothesized that it may be responsible for triggering the symmetry break, which is essential for the occurrence of invasive buds of a tumor and, subsequently, invasion. For a test of this hypothesis, we needed a local activation of YAP to ensure a sufficiently asymmetrical cue that induces the symmetry break. To obtain the necessary spatio-temporal control of YAP's translocation into the nucleus, we developed an optical control of YAP's nuclear translocation.⁶

3.2 Results and Discussion

In the cell, localization of YAP is regulated by several different processes and the exact regulation principles are not entirely known yet.⁷ To keep the interference with other signaling processes low and maximize the amount of control, we prepend a small (20 amino acids) photo-controlled nuclear localization signal (optoNLS),⁸ which we developed earlier, to YAP resulting in a photo-activatable YAP (optoYAP). The optoNLS is based on genetic insertion of a photocaged lysine⁹ into a nuclear localization signal, which blocks nuclear import entirely.⁸ Uncaging the lysine with light yields the functional signal and restores nuclear import. The small size of optoNLS and caging group minimizes their impact on protein function. To visualize protein localization and block nuclear import via diffusion by an increase in size, we use a YAP fused to two eGFPs. A major interaction of cytosolic YAP is its binding to Hippo-Signaling proteins after phosphorylation of Ser127.¹⁰ This interaction might block nuclear import of optoYAP. Therefore, we introduced a mutation Ser127Ala to the optoYAP construct (Figure 3.1a). The plasmid was then transfected into cells without YAP knock-out. This yields a system, which allows us to spatio-temporally control YAP activity by light and to super-impose that

onto cellular signaling while keeping Hippo- and WNT-signaling besides the photo-activation at normal levels.

Figure 3.1b shows images of optoYAP-transfected cells. YAP was kept cytosolic either by serum depletion or mechanically by keeping the cells on a soft matrigel substrate. Before illumination, the entire optoYAP signal is cytosolic. Less than an hour after photoactivation, most of the optoYAP signal is located in the nucleus. This successful photo-activated translocation occurred independently of whether serum depletion or matrigel was used to prime cytosolic YAP with natural signaling. After successful nuclear translocation, functionality tests were performed to show that optoYAP is fully functional and able to activate downstream signaling in the nucleus. qPCR of CCN1 (CYR61) and CCN2 (CTGF) - proteins, which are upregulated downstream of YAP activation,¹¹ - reveal an enhanced signal compared to controls after photoactivation of YAP on RNA level (Figure 3.1c). On protein level, a luciferase reporter¹ responsive to YAP signaling clearly showed enhanced expression (Figure 3.1d, Appendix Figure 3.6) upon photo-activation of optoYAP revealing functional YAP-responsive signaling. The absence of permanent DNA damage due to the illumination was also confirmed (Appendix Figure 3.7).

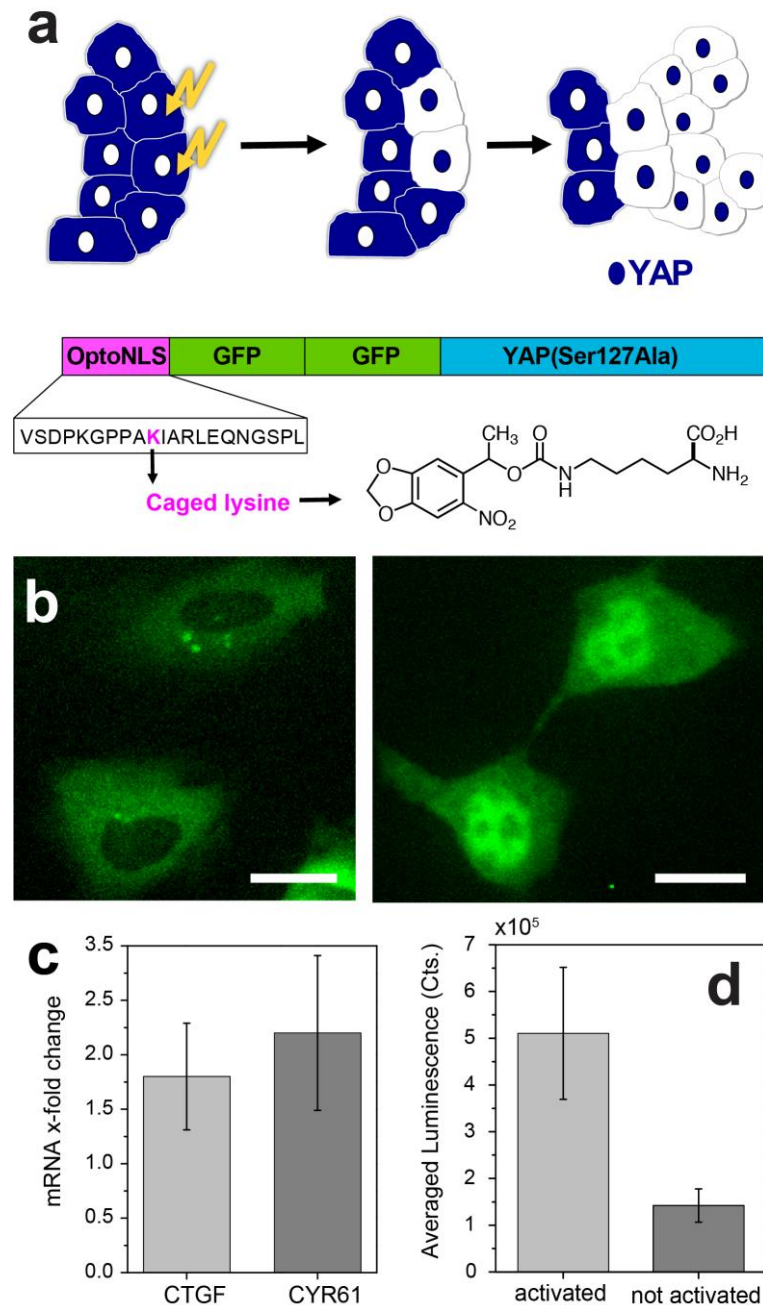


Figure 3.1: Photo-activation of YAP. **a**) Schematics of optoYAP. OptoYAP is composed of the optoNLS with a caged lysine and two GFP prepended to YAP Ser127Ala. The optoNLS is activated by uncaging the lysine with light leading to nuclear localization of optoYAP followed by enhanced proliferation in the photo-activated area. **b**) HeLa cells transfected with optoYAP show YAP localization in the cytosol before activation. Approximately 30 min after photo-activation, optoYAP is localized in the nucleus. **c**) qPCR shows an increase in RNA levels of YAP downstream proteins CTGF and CYR61 (with GAPDH as gatekeeper). **d**) Yap functionality assay based on a TEAD luciferase reporter shows four times higher activity in activated samples compared to controls, which were not activated, confirming increased YAP activity.

Having thus established a functional, photoactivatable YAP, we next studied the influence of YAP activation on HeLa cells cultured on two-dimensional substrates (Figure 3.2a, Appendix Figure 3.8). Inactivation of YAP via serum depletion on plastic substrates did not change cell

morphology. Accordingly, photo-activation of optoYAP did not lead to changes in cell morphology either (Figure 3.2b). However, proliferation was significantly increased: while the number of control cells without YAP activation increased after 24 h by 12.5 % only, the number of cells after photoactivation of optoYAP was enhanced much stronger by 94 % (Figure 3.2c). Note that cells with photo-activated YAP reach proliferation levels known for standard culture conditions on a plastic substrate in medium supplemented with FBS, which induce active YAP. Cells with inactivated YAP proliferate much slower. Mechanical inactivation of YAP via growth on a soft matrigel substrate leads to a round cell morphology. Upon photoactivation of YAP, interestingly, cells did not change morphology to the stretched shape found on stiff substrates (Appendix Figure 3.9). However, similarly to serum-depleted, activated cells, they showed increased proliferation compared to controls resulting in enhanced growth of cell spheroids on the matrigel (Appendix Figure 3.10). Thus, the different cell morphologies on stiff and soft substrates, respectively, do not stem from the difference in YAP activation. The results rather suggest them to be a direct consequence of mechanical forces or other signaling pathways.

To further understand the effect of the photo-activated YAP on cells, we investigated the time course of proliferation. Figure 3.2c already suggests the strongest effect of YAP to happen during the first day, which is then amplified by the exponential growth. A logarithmic plot and analysis (Figure 3.11) confirm that the growth rate of activated cells is enhanced during the first day and returns to non-activated levels on day 2 and thereafter. On a molecular level, we find an increased amount of nuclear YAP after activation. While nuclear YAP can be clearly seen 4h after activation, the amount of nuclear YAP is decreased after 6 h (Figure 3.2d). 8 h after activation it is almost back to cytosolic localization as in the non-activated state. A time course of the luciferase reporter assay also shows an increase in downstream signaling reaching a maximum around 4-6 h post illumination and decreasing afterward (Figure 3.6a). The time evolution of YAP's localization and downstream luciferase expression combined with the fact that proliferation is enhanced for one day suggests that activation of YAP as performed with our photo-activation induces a boost in downstream events, which lasts for several hours and vanishes over the course of a day.

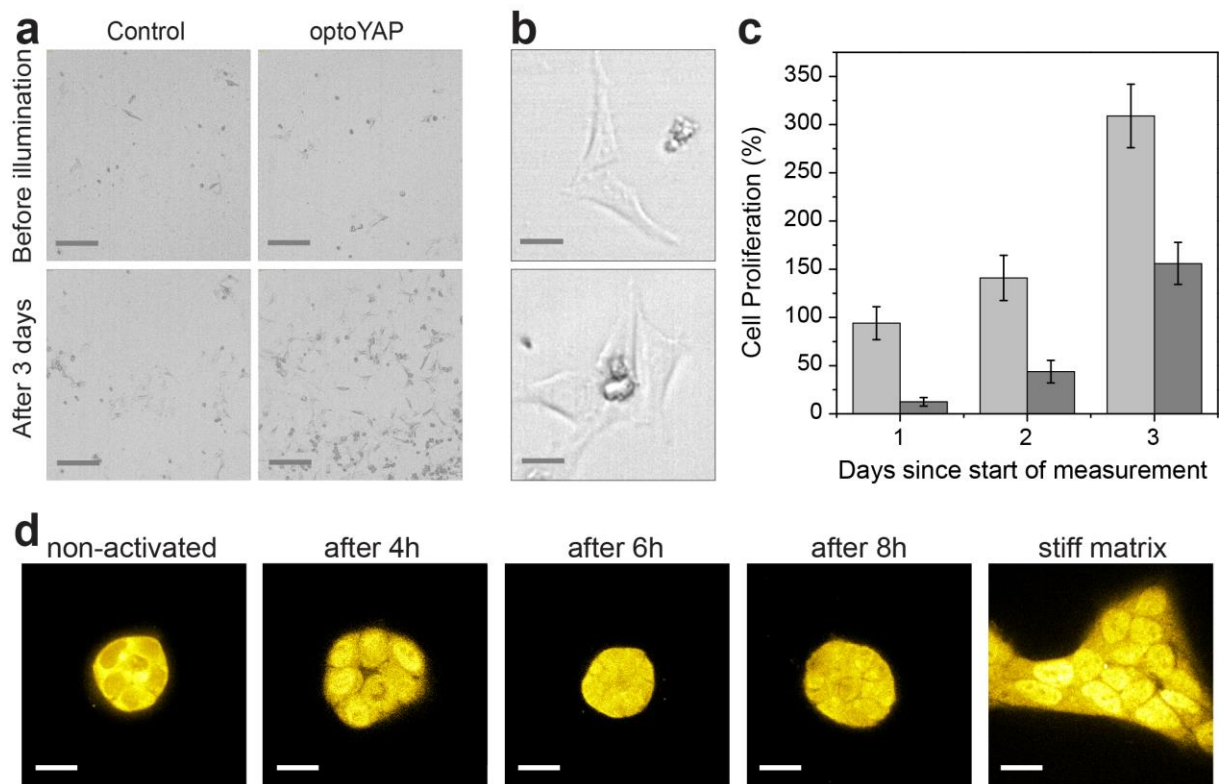


Figure 3.2: Proliferation and localization after optoYAP activation **a**) Proliferation of cells with optoYAP in FBS-depleted medium is strongly enhanced by photo-activation of optoYAP compared to controls without optoYAP. Scale bar: 200 μm **b**) Higher magnification images of cells in FBS-depleted medium show no changes in morphology after photo-activation. Scale bar: 20 μm **c**) Quantitative analysis of proliferation reveals a strong increase in the growth rate of photo-activated cells (light gray) compared to controls without optoYAP (dark gray) during the first day. This difference is amplified in the following days albeit at similar growth rates compared to the control. Note that growth rates on day 1 with activated optoYAP reach levels as known for proliferation under commonly used cell culture conditions (stiff substrate, medium supplemented with FBS), which generally exhibit activated YAP. **d**) Antibody staining of optoYAP transfected HeLa cells on matrigel before and after photo-activation. YAP is mainly cytosolic before activation, 4h after activation it is located mainly in the nucleus, and at later time points, it returns to mainly cytosolic localization. For comparison, the nuclear localization of YAP in cells on a stiff matrix is shown. Scale bar: 20 μm .

Next, we investigated the effect of YAP activation on cell spheroids. To this end, spheroids were grown and embedded in collagen gels. In this three-dimensional model system, we also observed an increase in proliferation upon photo-activation of optoYAP in entire spheroids as shown in Figure 3.3a. Quantitative analysis (Figure 3.3b) reveals an increase in spheroid size by a factor of almost 4 (measured as the area of the z-projection including all connected invasive buds) over the course of three days after photo-activation of optoYAP, whereas controls hardly grew at all. Next to the enhanced size, YAP-activated spheroids also underwent morphological changes. YAP-activation leads to an increased number of invading buds and network-like structures of invading cells as depicted in Figure 3.3a. These results already strongly suggest that activation of YAP can induce invasion.

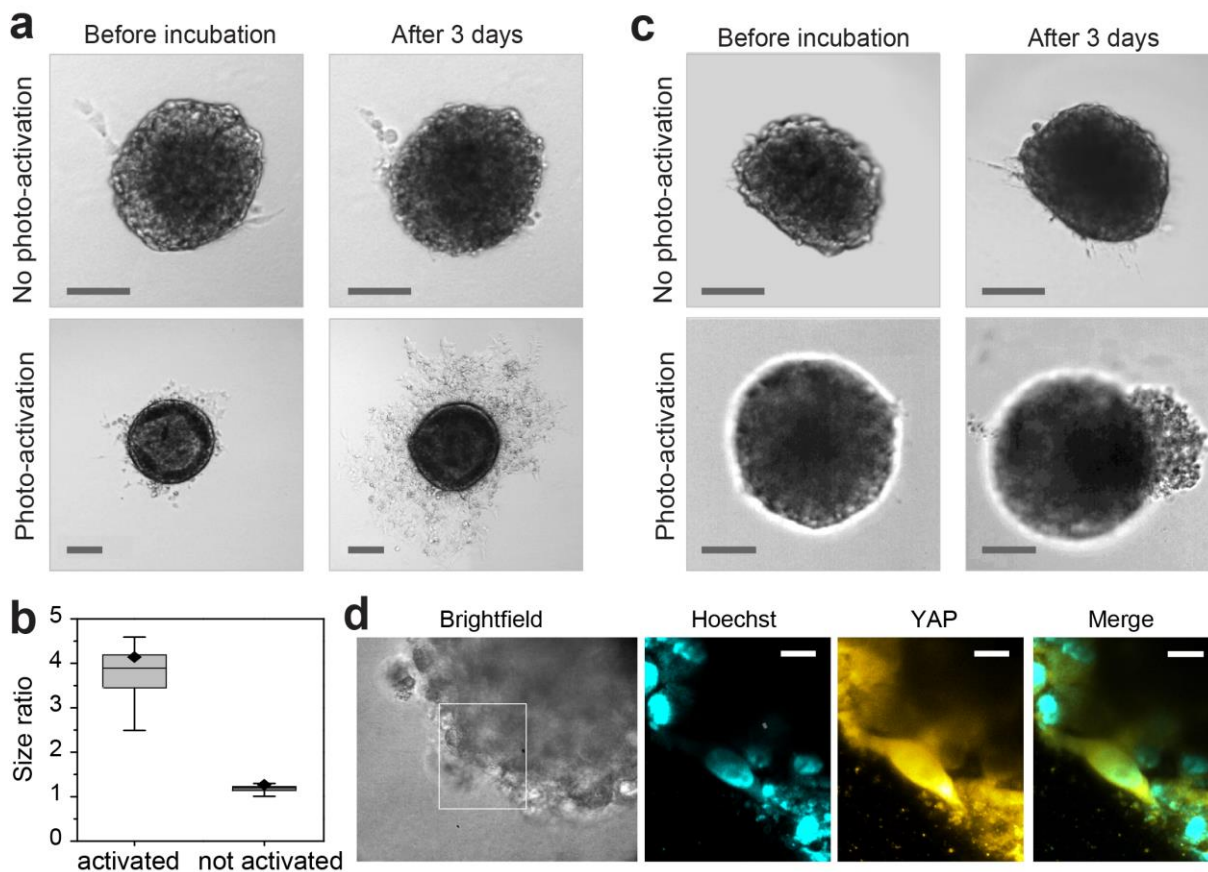


Figure 3.3: YAP triggers directed growth in spheroids **a)** HeLa spheroids in collagen gels transfected with optoYAP three days after photo-activation show increased invasion leading to a larger size of the spheroid compared to non-activated controls, which barely invade at all. Scale bars: 100 μm . **b)** Quantification of the average spheroid size change over three days. Activated samples (light gray) show a fourfold increase in their size (measured as area of the central plane) over three days while non-activated samples (dark gray) grew only by a factor of 1.2. **c)** Spatio-selective photo-activation of spheroids with optoYAP in collagen gels on the right side of the spheroid induces directed invasion on that side, while controls, which were not photo-activated, do not show directed growth. Scale bars: 100 μm . **d)** High resolution and fluorescence imaging of activated YAP in a cell in a spheroid. Scale bars: 5 μm .

Finally, we made use of the spatio-temporal control provided by the photo-activation. We used the spheroids in collagen gels and restricted optoYAP activation locally to a selected area of the spheroid. While non-activated controls grew symmetrically into all directions, strikingly, spatially selective activation of optoYAP was followed by invasion on the activated sites. Figure 3.3c shows the spherical non-illuminated spheroids and the invasive mass in the illuminated areas of photo-activated spheroids. Thus, local activation of YAP can induce a symmetry break and trigger invasion. Further microscopy studies of protein localization within the spheroids after photoactivation show the activated YAP 4 h after illumination (Figure 3.3d).

In conclusion, photo-activation of optoYAP in spheroids confirmed the hypothesis that YAP

translocation into the nucleus is able to trigger invasion from the spheroids into the surrounding matrix. The results thus suggest YAP to be an important regulator of the onset of invasion. The developed optoYAP may also prove to be a useful tool for future investigations of the role of YAP in organ development, contact inhibition, and other processes in development and disease.¹²

3.3 Appendix

3.3.1 Plasmid construction of optoYAP

PCR

Plasmids for optoYAP and optoYAP(Ser127Ala) were obtained using the SLIC cloning method.^{13, 14}

The PAG plasmid for the insertion of the photocaged lysine was used as described in Deiters et al, ACS Synth Biol, 2014. 8

OptoYAP Sequencing

Plasmid sequencing was performed by Eurofins Genomics.

Primers were ordered from Metabion.

Mutation Sequencing Primer:

GCTCTTCAACGCCGTCATGAAC

3.3.2 Synthesis and characterization of the caged Lysine

Synthesis

1-(6-Nitrobenzo[d][1,3]dioxol-5-yl)ethanol (500 mg, 2.36 mmol) and Na₂CO₃ (247 mg, 2.36 mmol) were added to THF (5 mL) and cooled to 0 °C under stirring. Next, triphosgene (701 mg, 2.36 mmol) was added to the suspension and the reaction was kept stirring overnight at RT. The reaction was centrifuged to remove Na₂CO₃ and the liquids were subsequently evaporated without heating. The residue was dried under vacuum, to yield a greyish solid (644 mg, 2.36 mmol). NMR confirms the successful synthesis of 1-(6-nitrobenzo[d][1,3]dioxol-5-yl)ethyl carbonochloridate (Figure 3.4).

Nε-Boc-lysine (500 mg, 2.02 mmol) was dissolved in THF/1 M NaOH (aq.) (1:4 mixture, 8 mL total) under stirring and the solution was cooled to 0 °C. Next 1-(6-nitrobenzo[d][1,3]dioxol-5-yl)ethyl carbonochloridate (496 mg, 1.82 mmol) was added and the reaction was stirred overnight, at RT. The aqueous layer was washed with Et₂O (5 mL) and subsequently acidified with ice-cold 1 M HCl (20 mL) to pH 1 and then extracted with EtOAc (30 mL). The organic layer was dried over Na₂SO₄, filtered, and the volatiles were evaporated, leaving a yellow foam. The yellow foam was dissolved in DCM:TFA (1:1 mixture, 14 mL total) and the reaction was allowed to stir for 40 min. The volatiles were subsequently evaporated and the residue was redissolved in MeOH (5 mL) and precipitated into Et₂O (250 mL), yielding a white solid (679 mg, 1.42 mmol). NMR confirmed the successful synthesis of (2*S*)-2-(*tert*-Butoxycarbonylamino)-6-[1-(6-nitrobenzo[d][1,3]dioxol-5-yl)ethoxy]carbonylaminohexanoic acid which will be called caged lysine from now on (Figure 3.5). For use on cells 100 mg of the caged lysine were dissolved in 1 mL H₂O and filtered with a 0.2 μm syringe filter to avoid contamination.

Characterization by $^1\text{H-NMR}$

1-(6-nitrobenzo[d][1,3]dioxol-5-yl)ethyl carbonochloridate

$^1\text{H NMR}$ (400 MHz, CDCl_3): δ (ppm) = 7.52 (d, $J = 0.2$ Hz, 1 H, H-7), 7.05 (dd, $J = 0.2$ Hz, 1 H, H-4), 6.47 (qd, $J = 6.4, 0.4$ Hz 1 H, H-1'), 6.15 (s, 2 H, H-2), 1.72 (d, $J = 6.4$ Hz, 3 H, H-2').



Figure 3.4: $^1\text{H NMR}$ spectrum of 1-(6-nitrobenzo[d][1,3]dioxol-5-yl)ethyl-carbonochloridate that is obtained as an intermediate product of the synthesis of the caged lysine

(2S)-2-(*tert*-Butoxycarbonylamino)-6-[1-(6-nitrobenzo[d][1,3]dioxol-5-yl)ethoxy]carbonyl-aminohexanoic acid aka Caged Lysine

¹H NMR (400 MHz, CDCl₃): δ (ppm) = 7.58 (s, 1 H, H-7''), 7.16 (s, 1 H, H-4''), 6.18 (d, *J* = 3.5 Hz, 2 H, H-2''), 6.12 (d, *J* = 6.4 Hz 1 H, H-1'), 3.79 (t, *J* = 6.1 Hz, 2 H), 3.19 – 3.00 (m, 5 H), 1.92 (m, 3 H), 1.62 – 1.38 (m, 3 H).

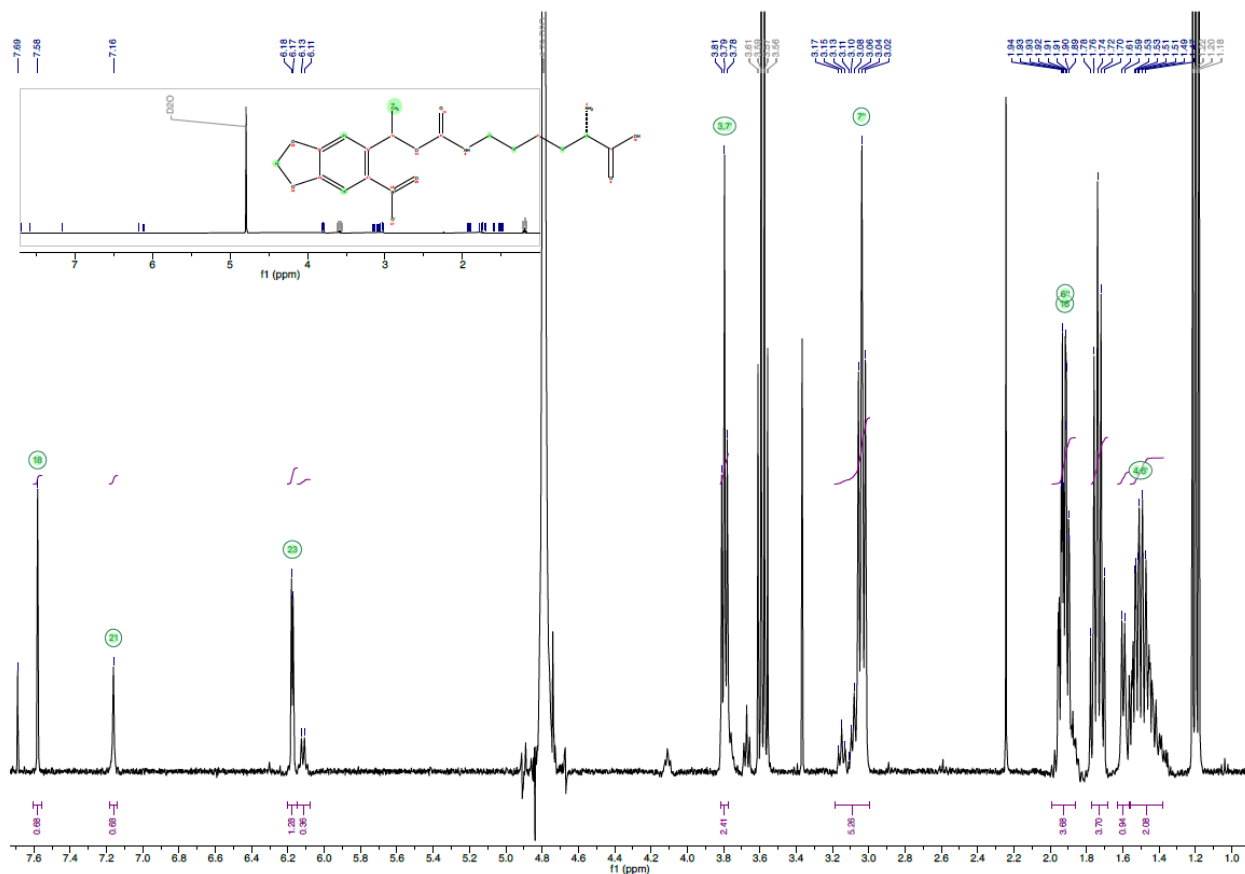


Figure 3.5: NMR spectrum of the caged lysine.

3.3.3 Cell Culture and optoYAP Functionality Assays

All cell experiments were prepared in a *Hera-Safe* cell culture unit from *Heraeus*. The cells were incubated in *Hera Cell incubators* also from *Heraeus*. The cells were cultured in DMEM with 10% FBS and 1% Penicillin/Streptomycin at 37°C/5% CO₂.

Experiments in which cells were not embedded in collagen gels or seeded on matrigel were performed in FBS-free DMEM to keep YAP in the cytosol prior to the photo-activation.

Experiments with cells in collagen gel or on matrigel were performed in the presence of FBS as the gels were sufficiently soft to prevent a nuclear localization of YAP even in the presence of FBS.

Cells were either seeded into *ibidi* 8-well, 6-well plates, or *Corning* 96-well plates.

Standard cell numbers for experiments were 5000 cells per well unless noted otherwise.

Transfection experiments

Transfections of cells in 8-wells plates were carried out by preparing an Optimem solution containing optoYAP plasmid (1 ug/100 µL), PAG plasmid (1 ug/100 µL) and the Xtreme Gene 9 Transfection reagent (3 µl/100 µL). After mixing carefully by tapping against the tube, the solution was then incubated at RT for 20 min. For each 8-well 10 µL of the transfection mixture were used and 3 µL of the caged Lysine were added before incubation. For the luciferase assay (1 ug/100 µL) of the 8xGTIIIC-luciferase plasmid was added as well.

Transfections in 96 well plates used 5 µL of the transfection mixture and 1 µL of the caged lysine per well. The transfection procedure for single cells and spheroids was carried out in the same manner.

Photo-activation

For non-directed photo-activation of optoYAP a *Spectroline E-Series* UV lamp (365 nm, 0.6mW/mm²) was used to illuminate the sample for 20 s. For directed photo-activation a laser (405 nm, integrated in a *Zeiss Observer SD* spinning disk confocal microscope) or LED (365 nm, integrated in a *Nikon Eclipse Ti-E*) regulated to the same output as the UV lamp was used to illuminate the sample for 20 s.

Spheroid formation

To form spheroids, 500 cells were seeded in each well (100 μ L DMEM) of a 96-well plate with ultra-low adhesion and incubated at 37°C/5%CO₂ until the spheroids reached the desired size. Spheroids used for experiments had a diameter of 200-300 μ m for HeLa spheroids and 100-150 μ m for A431 spheroids. For transferring the spheroids into gels disposable plastic pipettes were used.

Cell Spheroid/Collagen Gel preparation

150 μ L of collagen (8.36 mg/mL) were prepared in a 1.5 mL Eppendorf-tube on ice and 47.5 μ L PBS and 2.5 μ L 1M NaOH, both pre-cooled to 0°C on ice, were added for each well of an ibidi 8-Well plate. The reagents were mixed by pipetting up and down before applying them to the well. Aggregates were carefully aspirated with a pipette and transferred to the gels (2 per well) for a total volume of 400 μ L. The spheroids were incubated for 24 h at 37°C/5%CO₂ before transfection.

Spheroid Growth Rate

To compare the growth rate of activated and inactivated optoYAP transfected spheroids, collagen embedded spheroids were imaged before activation of optoYAP and then again after three days of incubation after activation. As a control, non-activated spheroids were measured as well. The growth analysis was performed using *Fiji* by comparing 2D projections of the total area covered by spheroids and cell outgrowths before and after incubation.

RNA extraction for qPCR

RNA Extraction, purification and cDNA synthesis was carried out according to the instructions provided in the RNeasy Mini Kit from *QIAGEN*.

Luciferase Functionality Assays

HeLa cells were seeded in a 96-well plate with 5000 cells per well and then transfected with optoYAP and 8xGTIIC-luciferase plasmid. After an incubation of 24 hours, optoYAP was activated and after an additional 24 the *Bright-Glo Luciferase Assay* from *Promega* was carried out according to the instructions provided in the manual. The assays were performed on a *Berthold Tristar² LB 942*. 8xGTIIC-luciferase was a gift from Stefano Piccolo (Addgene plasmid

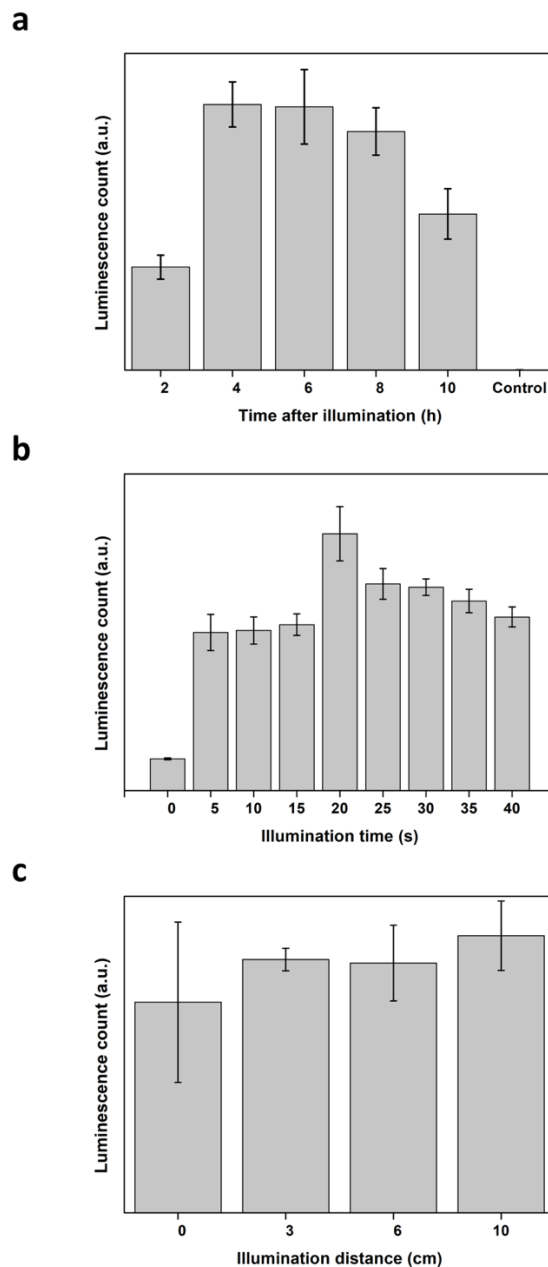
34615; <http://n2t.net/addgene:34615> ; RRID:Addgene_34615)

Figure 3.6: a) Time-dependence of optoYAP activity. The observed luciferase count, and thus optoYAP activity, is time-dependent. Measurements taken at different time points after illumination show a clear maximum in activity at 4 to 6 h after photo-activation with a steady decline afterward. b) Dependence of optoYAP activity on illumination time. To gauge the effect of variations in illumination time on optoYAP activity, transfected HeLa cells were illuminated for different time periods to photo-activate optoYAP. Subsequently, the corresponding luciferase activity was recorded. The results show a clear peak in luciferase count and thus YAP activity at an illumination time of 20 seconds. c) Distance dependence of the photo-activation: The distance between light source and sample during photo-activation and thus the power needed to activate optoYAP was investigated. Photo-activation was performed at the indicated distances between light source and sample and the subsequent luciferase activity was recorded. While there was a slight deviation in recorded luminescence in case of full contact of the UV light to the sample (0 cm distance), no significant differences could be observed for larger distances. The luciferase activity shows thus little sensitivity to deviations in light intensity of the UV light source. Mean values and standard deviations represent the average of triplicates.

Assessment of UV damage caused by photo-activation

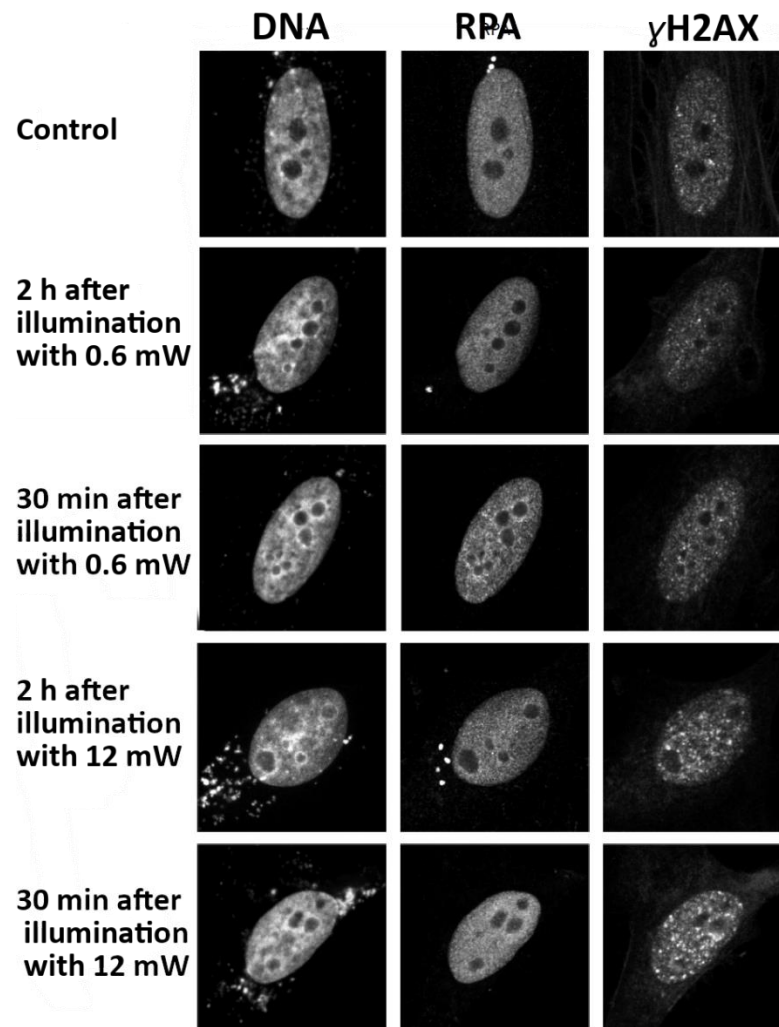


Figure 3.7: Assessment of the damage caused during photo-activation with 20 s UV light (365 nm) illumination. HeLa cells were seeded on an 8-well microscopy slide and transfected with optoYAP. After photo-activation at different intensities the damage to the cells was investigated with markers for DNA and as a marker of DNA damage with the DNA damage repair proteins RPA and γ H2AX. Comparing the activated samples to a transfected non-activated control shows that the higher intensity leads to some DNA damage (visible by an increase in RPA and γ H2AX signal) that is almost repaired after 2 h. The lower intensity of 0.6 mW leads to negligible DNA damage, which cannot be detected anymore after 2h. Thus, this intensity was chosen for all experiments.

Proliferation Assay

500 HeLa cells were seeded into each well of a 96-well plate in media without FBS and then transfected with optoYAP after 24 hours. After an additional 24 hours, half of the wells were illuminated with UV light at 365 nm to photo-activate optoYAP. The remaining wells served as the control and were not treated with UV. Afterward, cell images were recorded every 24 hours to observe cell proliferation with and without activation of optoYAP.

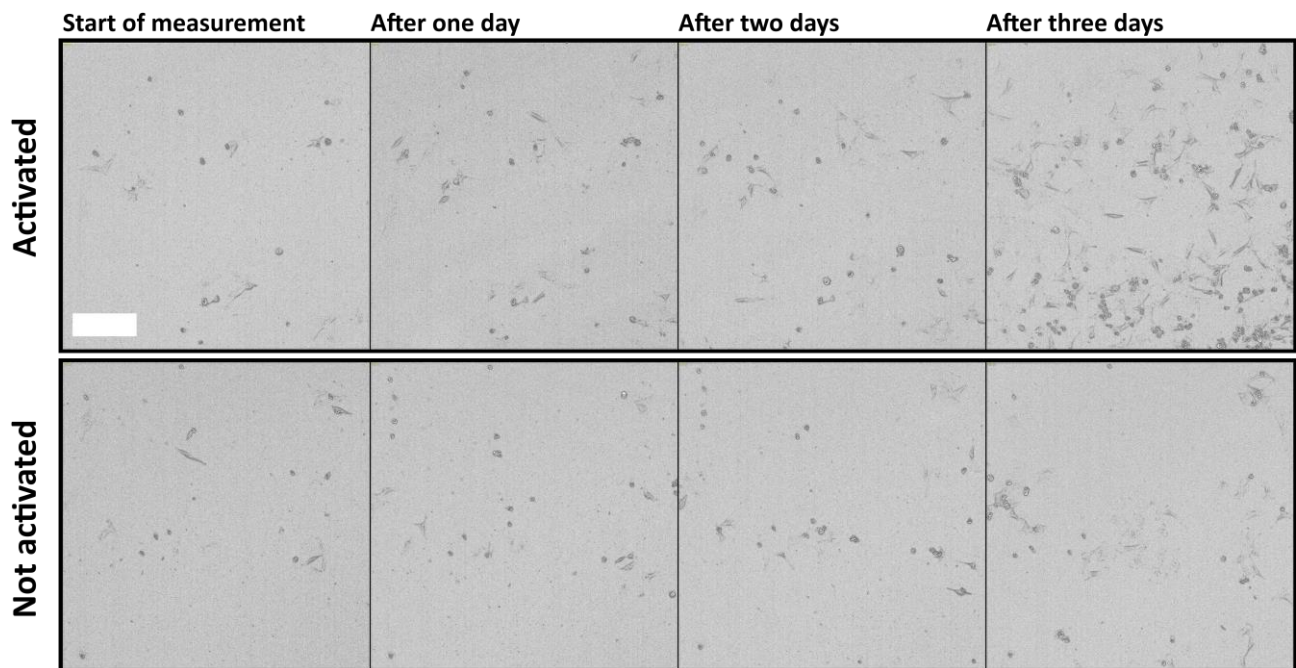


Figure 3.8: Proliferation assay on optoYAP-transfected HeLa cells (time measured after optoYAP activation). The upper row shows activated cells, the lower row non-activated controls. The images show a clear increase in overall growth upon optoYAP activation. Scale bar: 200 μm .

Morphology of optoYAP transfected HeLa cells on matrigel

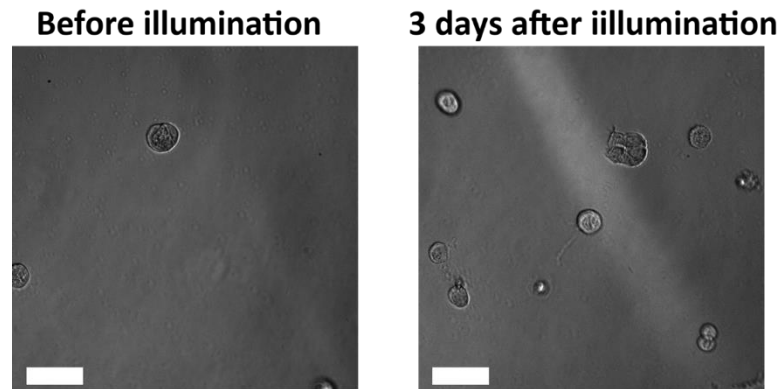


Figure 3.9: OptoYAP transfected HeLa cells on a layer of matrigel before and three days after photo-activation. Cell morphology of transfected cells on matrigel did not change after photo-activation even after several days of incubation. Scale bar: 200 μm .

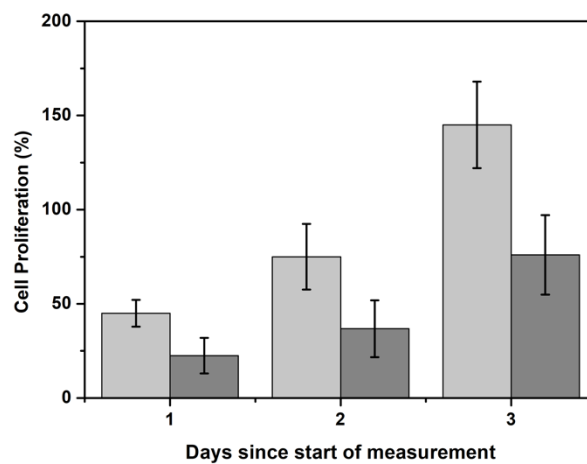


Figure 3.10: Cell proliferation of activated (light grey) and non-activated (dark grey) optoYAP transfected HeLa cells on matrigel in presence of FBS. The overall growth rate on matrigel is about a factor of two smaller in comparison to cell proliferation on a plastic substrate without FBS. Yet, likewise, the activated samples show a strongly increased proliferation compared to the non-activated samples. Mean values and standard deviations represent the average of triplicates.

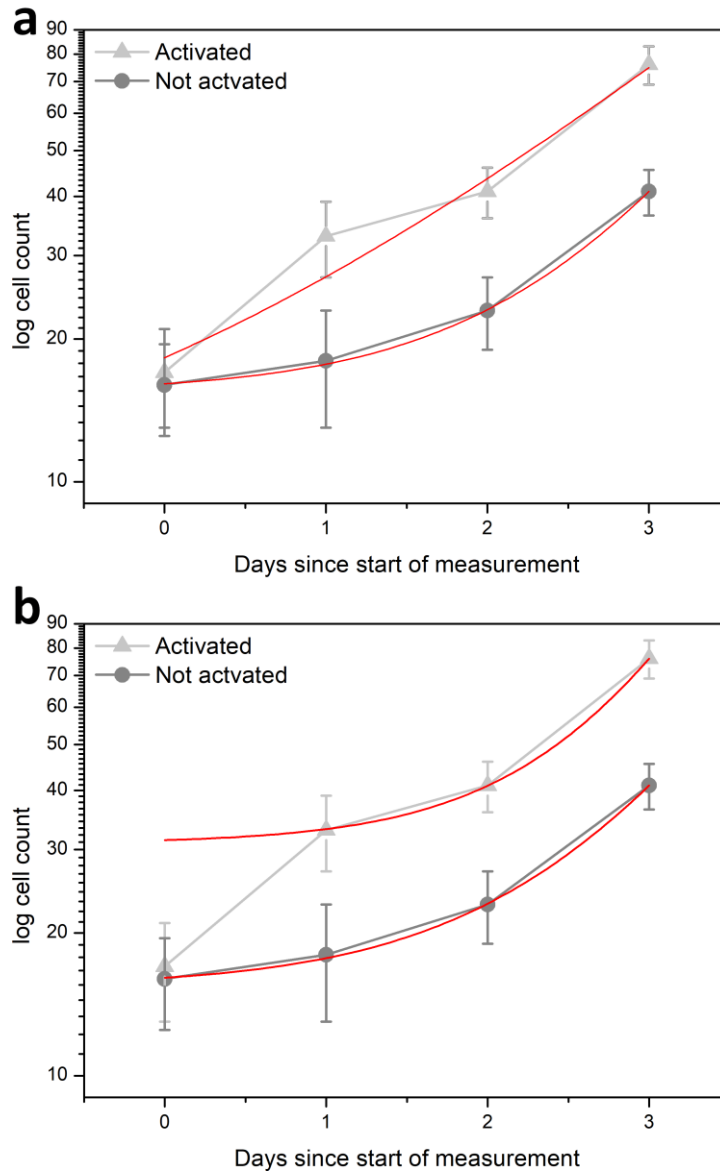


Figure 3.11: Logarithmic plot of the cell count with exponential fits. a) Fitting exponential growth curves to the data yields an average growth rate of 0.49/d for activated and 0.31/d for non-activated cells indicating the increase in growth upon optoYAP activation. However, due to the apparent reduction in growth rate of the activated sample after day 1 the fit is only a rough approximation. b) Fitting only the last three data points of the activated sample yields a fit of much better quality and a growth rate of 0.27/d, which is very similar to that of non-activated cells. The strong deviation of the first data point from this curve shows the strongly increased growth during the first 24 h of the experiment. This leads to the conclusion that the observed difference between activated and non-activated samples mainly stems from the cell proliferation of the first day of observation, while the proliferation returns to normal growth rates after the first day. Mean values and standard deviations represent the average of triplicates.

3.3.4 Fluorescence imaging and staining

Confocal laser scanning microscopy

High-magnification brightfield and fluorescence microscopy was carried out utilizing a *Zeiss Observer SD* spinning disk confocal microscope with a Yokogawa CSU-X1 spinning disc unit, an oil objective with 63x magnification. For excitation, a 488 nm (GFP) and 561 nm (YAP) were used. Emission was filtered with a BP 525/50 and LP 690/50 filter, respectively. The setup was heated to 37°C and a CO₂ source was provided to keep the atmosphere at 5% for living samples. The images were recorded and processed with the *Zen* software by *Zeiss*.

High-Throughput Brightfield imaging

The proliferation assay and general spheroid growth quantification measurements were performed with the *ImageXpress Micro XLS* from *Molecular Devices* using an objective with 10x magnification and the resulting images were evaluated with the *MetaXpress* software.

Further image data analysis was performed with *ImageJ/Fiji*.¹⁵ Specific analysis methods are described at the respective assays.

High-resolution Fluorescence Confocal Microscopy

Imaging was carried out on a confocal scanning microscope (TE 300; Nikon) with mounted bright-field illumination and camera. The two-photon excitation source for Hoechst staining was a fiber-based, frequency-doubled erbium laser (FemtoFiber dichro bioMP; Toptica Photonics) running at 774 nm. The excitation laser line for YAP staining was a DPSS CW laser running at 561 nm (Cobolt Jive 50, Cobolt AB). The laser powers were 3.3 mW at 774 nm and 2.9 μW at 561, measured in front of the microscope entrance. The laser light was coupled into the microscope via a dichroic mirror (Penta Line zt405/488/561/640/785rpc; AHF Analysetechnik) that separates laser excitation and fluorescence emission. Scanning of the sample in 3D was achieved by using an xyz piezo stage (BIO3.200; PiezoConcept). The laser excitation was focused onto the sample with a 60x (water) 1.20-NA plan apochromat objective (Plan APO VC 60x 1.2 NA, Nikon). The emission was collected by the same objective and spectrally separated by a 647-nm dichroic mirror (BS 647 SP; AHF Analysetechnik). The emission was recorded with two APD detectors (Count Blue; Count Red; Laser Components) and its photons stream registered using a TCSPC card (TH260 pico dual; PicoQuant GmbH). The

filter sets for the red APD were: 710/130 bandpass fluorescence filter (HQ 710/130 M; AHF Analysetechnik) and a 750 shortpass (FES0750; Thorlabs GmbH) to additionally block the 774 nm laser line. The filter sets for the blue APD were: 692/40 bandpass fluorescence filter (692/40 BrightLine HC; AHF Analysetechnik) and a 680 shortpass (HC 680/SP; AHF Analysetechnik) to additionally block the 774-nm laser line. The experiment was controlled using a home-written program written in C#. The confocal data was extracted and evaluated afterward by PAM¹⁶ and ImageJ¹⁵.

Antibody Staining

Primary and secondary antibodies for were purchased *as stated in the following list*.

List of used antibodies:

YAP

- YAP1 polyclonal rabbit antibody; PA1-46189 *Thermo Fisher Scientific*.
- Donkey anti-Rabbit IgG (H+L) Highly Cross-Adsorbed Secondary Antibody, Alexa Fluor 546; A-10040 *Thermo Fisher Scientific*.

RPA2

- RPA32/RPA2 mouse monoclonal antibody; ab2175, *Abcam*
- Goat anti-Mouse IgG (H+L) Highly Cross-Adsorbed Secondary Antibody, Alexa Fluor 488; A-11001 *Thermo Fisher Scientific*.

gH2A.

- gH2A.X rabbit antibody; 2577 *Cell Signaling Technology*
- Goat anti-Rabbit IgG (H+L) Highly Cross-Adsorbed Secondary Antibody, Alexa Fluor 647; A-21245 *Thermo Fisher Scientific*.

2D Antibody Staining

HeLa cells were seeded on matrigel to prevent the nuclear localization of YAP and transfected with optoYAP 24h after seeding. 24 hours after transfection, cells were illuminated with UV light (365 nm) for 20 s. After another 6-24 h cells were washed with PBS (pH 7.4) before being fixed with 4% PFA for 10 min. Afterwards, cells were washed three times with PBS for 5 min each. Cells were then permeabilized with triton 100-X (0.15% in PBS) for 10 min and washed with PBS for 5 min an additional three times. Cells were blocked with 1% BSA containing

glycine for 30 min before primary antibodies were applied diluted in PBS with 1% BSA (1 μ g antibody per well). After 1 h of incubation, at room temperature (or overnight at 4°C) the cells were washed 5 min with PBS three times. Next, the secondary antibodies were applied diluted in 1% BSA. After one hour of incubation the sample was washed again and Hoechst was applied before imaging.

3D Antibody Staining

HeLa spheroids embedded into collagen were fixed with 4% PFA for 40 minutes and washed with PBS twice for 20 minutes. The cells were permeabilized for 20 minutes with 0.5% Triton X-100 in PBS and subsequently washed with PBS for 30 minutes. The cells were blocked with 1% BSA in PBS overnight. Primary antibodies were diluted 1:100 with 1% BSA in PBS and cells were incubated for 72 hours. Prior to incubation with secondary antibodies (1:200 in 1% BSA), the cells were washed twice with PBS for 30 minutes. The cells were incubated with secondary antibodies for 48 hours. Afterwards, the cells were washed with PBS for 30 minutes and Hoechst 33342 (0.5 μ g/ml) for 40 minutes. Prior to imaging, the cells were washed again with PBS for 30 minutes. Finally, the PBS was renewed and kept in the reservoirs during confocal microscopy.

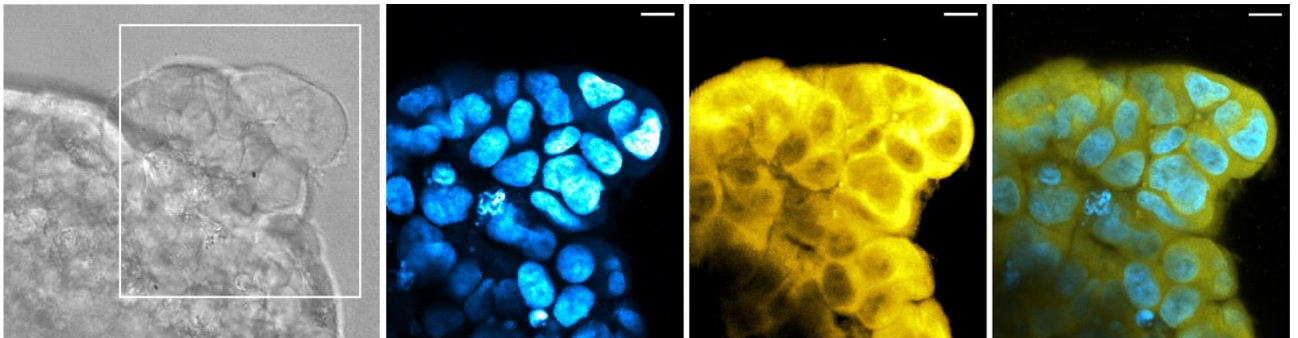


Figure 3.12 Two-photon excitation microscopy image of the inside of a fixed HeLa spheroid transfected with optoYAP that is embedded in a collagen gel and was completely illuminated for activation. The spheroid was fixed 3 days after activation. YAP appears concentrated in the cytosol. Scale bars: 5 μ m.

3.3.5 Spheroid control experiments

Growth of A431 Spheroids

To investigate if the effects of optoYAP can also be observed in other cell lines A431 spheroids were transfected according to the same protocol described for HeLa spheroids and selectively activated as well. The treated A431 spheroids showed similar results to those obtained from HeLa spheroids exhibiting no discernible invasion behavior for non-activated samples and growth and invasion starting from the illuminated area for activated samples.

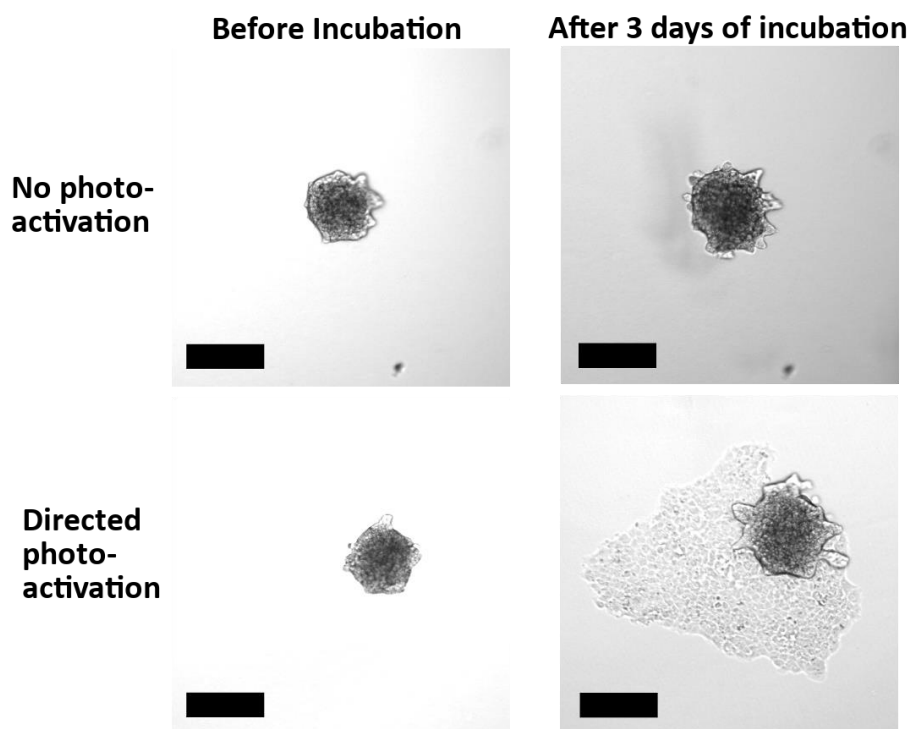


Figure 3.13: optoYAP transfected A431 spheroids embedded into collagen gel. To investigate if the effects of optoYAP activation can also be observed in other cell lines, A431 spheroids were transfected according to the same protocol described for HeLa spheroids and selectively activated. The treated A431 spheroids showed similar results to those obtained from HeLa spheroids: non-activated samples exhibit no discernible invasive behavior aside from general growth of the spheroid, while activated samples show significant invasion starting from the activated area. Scale bars: 150 μm .

HeLa Spheroid Control Experiments

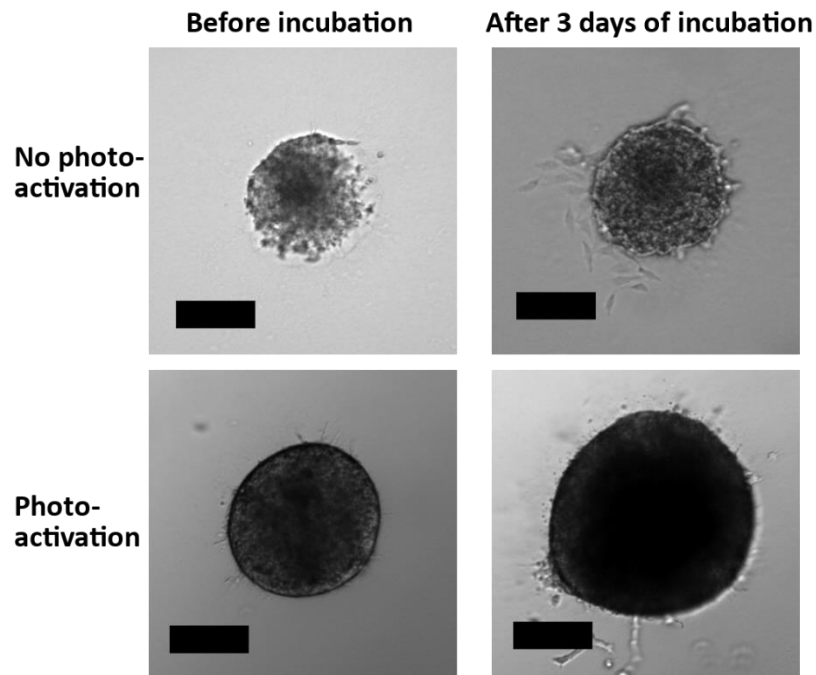


Figure 3.14: Non-transfected HeLa spheroids embedded in collagen gel. To investigate if the observed behaviors of the treated HeLa spheroids are indeed caused by optoYAP, non-transfected HeLa spheroids were used as controls and activated the same way as optoYAP. Neither the activated nor the non-activated samples show invasive behavior comparable to that of the optoYAP transfected spheroids. The only discernible difference between before and after incubation is an increase in overall spheroid size in both cases – with and without activation. Scale bars: 100 μm

3.4 References

1. Dupont, S. et al. Role of YAP/TAZ in mechanotransduction. *Nature* **474**, 179-183 (2011).
2. Elosegui-Artola, A. et al. Force Triggers YAP Nuclear Entry by Regulating Transport across Nuclear Pores. *Cell* **171**, 1397-1410.e1314 (2017).
3. Zanconato, F., Cordenonsi, M. & Piccolo, S. YAP/TAZ at the Roots of Cancer. *Cancer Cell* **29**, 783-803 (2016).
4. Lin, C.H. et al. Microenvironment rigidity modulates responses to the HER2 receptor tyrosine kinase inhibitor lapatinib via YAP and TAZ transcription factors. *Mol. Biol. Cell* **26**, 3946-3953 (2015).
5. Serra, D. et al. Self-organization and symmetry breaking in intestinal organoid development. *Nature* **569**, 66-72 (2019).
6. Valon, L., Marín-Llauradó, A., Wyatt, T., Charras, G. & Trepát, X. Optogenetic control of cellular forces and mechanotransduction. *Nature communications* **8**, 14396 (2017).
7. Pocaterra, A., Romani, P. & Dupont, S. YAP/TAZ functions and their regulation at a glance. *J. Cell Sci.* **133**, jcs230425 (2020).
8. Engelke, H., Chou, C., Uprety, R., Jess, P. & Deiters, A. Control of protein function through optochemical translocation. *ACS Synth Biol* **3**, 731-736 (2014).
9. Gautier, A. et al. Genetically encoded photocontrol of protein localization in mammalian cells. *J. Am. Chem. Soc.* **132**, 4086-4088 (2010).
10. Zhao, B. et al. Inactivation of YAP oncoprotein by the Hippo pathway is involved in cell contact inhibition and tissue growth control. *Genes Dev.* **21**, 2747-2761 (2007).
11. Totaro, A., Panciera, T. & Piccolo, S. YAP/TAZ upstream signals and downstream responses. *Nat. Cell Biol.* **20**, 888-899 (2018).
12. Low, B.C. et al. YAP/TAZ as mechanosensors and mechanotransducers in regulating organ size and tumor growth. *FEBS Lett.* **588**, 2663-2670 (2014).
13. Li, M.Z. & Elledge, S.J. Harnessing homologous recombination in vitro to generate recombinant DNA via SLIC. *Nat. Methods* **4**, 251-256 (2007).
14. Li, M.Z. & Elledge, S.J. SLIC: a method for sequence- and ligation-independent cloning. *Methods Mol. Biol.* **852**, 51-59 (2012).
15. Schindelin, J. et al. Fiji: an open-source platform for biological-image analysis. *Nat. Methods* **9**, 676-682 (2012).
16. Schrimpf, W., Barth, A., Hendrix, J. & Lamb, D.C. PAM: A Framework for Integrated Analysis of Imaging, Single-Molecule, and Ensemble Fluorescence Data. *Biophys. J.* **114**, 1518-1528 (2018).

Chapter 4

Exosome-coated Metal- Organic Framework Nanoparticles: An Efficient Drug Delivery Platform

Bernhard Illes, Patrick Hirschle, Sabine Barnert, Valentina Cauda, Stefan Wuttke, Hanna Engelke

Reprinted with permission from Chem. Mater. 2017, 29, 19, 8042–8046. Copyright 2017 American Chemical Society.

4.1 Introduction

Drug delivery systems aim at a reduction of side effects in chemotherapy. This is achieved by encapsulation of drugs in nanocarriers followed by controlled release of these drugs at the site of the diseased tissue. While inorganic or polymeric nanoparticles (NPs) are often used as nanocarriers¹, hybrid nanomaterials such as metal-organic framework (MOF) NPs have recently emerged as a valuable alternative.¹⁻³ They are synthesized from inorganic and organic building block units to create porous three-dimensional frameworks. Due to this building principle, the composition and structure of these materials are highly tunable.^{1, 4-6} Furthermore, both external and internal surfaces can be functionalized independently. With these properties, MOF NPs can be designed to fit the specific requirements of the desired application.¹ For drug delivery purposes these so called “design materials” have been synthesized with high porosity allowing for high drug loading capacities. They also have been designed to be biodegradable. Specifically, iron-based MOF NPs have attracted great attention. In addition to the above-mentioned properties, they can be detected via magnetic resonance imaging (MRI), rendering them an ideal platform for theranostics.^{7, 8} In our study we focus on one of these iron-based MOFs, namely MIL-88A NPs, which are composed of iron(III) and fumaric acid.^{8, 9} Both compounds can be found in the body and the NPs are reported to be non-toxic.¹⁰ Additionally, MIL-88A NPs have been shown to efficiently host chemotherapeutic drugs.¹¹ Thus, they represent a promising nanocarrier.

To complete the drug delivery system, nanocarriers need a capping system that prevents leakage of the drug, protects both drug and NP from degrading enzymes, and hides them from the immune system to avoid premature clearance from the circulatory and reticuloendothelial systems. Out of many potential capping systems, such as proteins or polymers, lipid bilayers are especially advantageous: they prevent enhanced NP aggregation in biological environments (e.g. human blood), they provide an efficient sealing, and they can be easily equipped with targeting ligands.¹²⁻¹⁵ Up to now, release from lipid coated NPs after endosomal uptake has been achieved using toxic photosensitizers that need to be protected from sunlight^{12, 16, 17}, membrane-permeable drugs¹², or cationic lipids^{13, 18}, all of which need to be optimized regarding their interaction with NPs to avoid premature leakage of the drug. Recently, a lipid coating has been applied to MOF NPs as a capping system, yielding a

nanocarrier that efficiently encapsulates dye molecules and is taken up by cells.¹⁹ However, no intracellular release was shown – possibly due to lack of an opening mechanism.

Exosomes might provide additional important advantages as compared to artificial lipid layers as a capping system. They are endogenous liposomes present in many body liquids. They supposedly are non-immunogenic and are used by cells for communication purposes.^{20, 21} Hence, they combine the advantages of a lipid bilayer with a potential shielding from the immune system and – unlike artificial lipid bilayers – they have a not yet understood endogenous mechanism that supports release from the endosomal entrapment.⁸ With these properties they overcome the main challenges of drug delivery: leakage-free delivery, release as well as endosomal escape of the drug, shielding from the immune system for long circulation times, and full biocompatibility.⁸ However, loading exosomes with biologically active molecules (e.g. drugs) is a major challenge. No technique has been reported yet that achieves efficient loading of exosomes. Here, we overcome this challenge and facilitate simple drug loading, leakage-free delivery and efficient release by a synergistic combination of the advantages of MOF NPs, specifically MIL-88A, as chemically tunable nanocarriers with those of exosomes as a capping system.

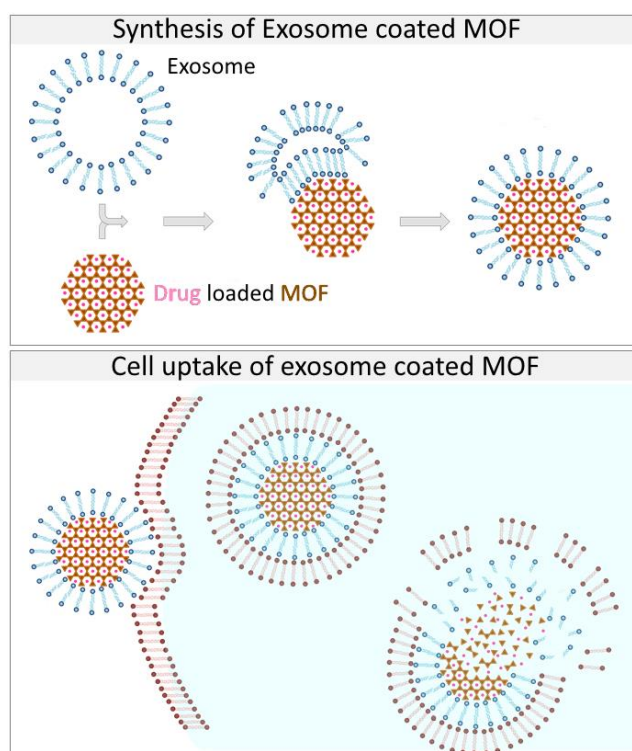


Figure 4.1: Schematic illustration of the synthesis of the exosome coated MOF and the subsequent cell uptake and proposed release mechanism of the cargo.

4.2 Results and Discussion

MIL-88A NPs were synthesized via microwave synthesis,⁸ loaded with cargo, and subsequently coated with exosomes derived from HeLa cell culture (synthesis and characterization in appendix, Figures 4.6-4.16). The coating was achieved using the fusion method, which we employ here for the first time for MOF NPs (Figure 4.1)²² Up to now MOF NPs have been coated with lipids using a solvent exchange method that would involve total disassembly of the exosomal bilayer.¹² The fusion method allows for leaving the bilayer of the exosomes mainly intact during the coating process and thus does not obstruct the advantageous properties of the exosome as much. To investigate the uptake and possible release behavior of the newly synthesized NPs, we used membrane-impermeable calcein as a model cargo and incubated the exosome coated MOF NPs on HeLa-cells. After two days of incubation the cells showed uptake of particles, but no release of calcein into the cell was visible yet (Figure 4.2a and appendix, Figure 4.22). Strikingly, after three days of incubation the exosome coated particles showed release in several cells resulting in a spread of calcein over the entire cell (Appendix, Figures 4.23-4.24). The number of cells exhibiting release increased slightly after 4 days of incubation (Figure 4.2b). This release of a membrane-impermeable dye without the use of toxic photosensitizers, renders the exosome-coated MIL-88A NPs a promising drug delivery system.

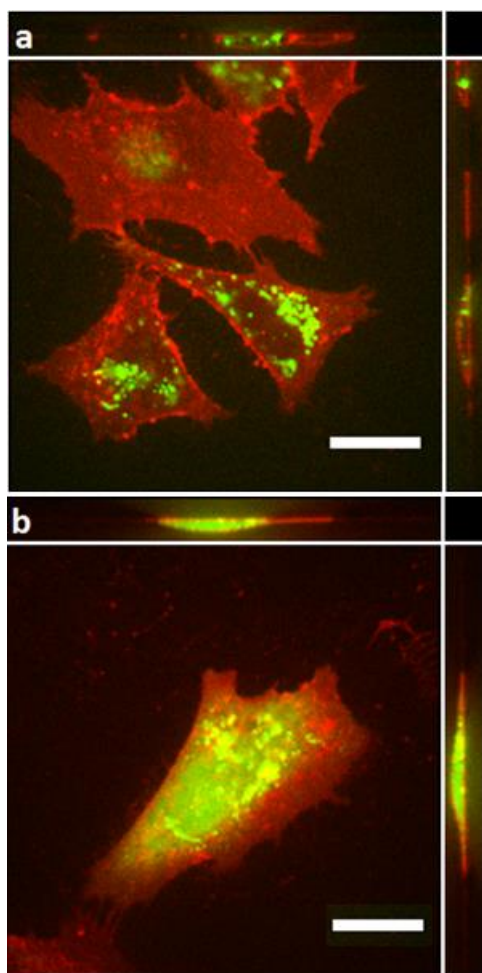


Figure 4.2: a) HeLa-Cells (red) with exosome coated calcein loaded particles (green) after 2 days of incubation. The particles have arrived inside the cell, but there is no sign of release. b) HeLa-Cells (red) with exosome coated calcein loaded particles (green) after 4 days of incubation. The particles have arrived inside the cell, and release of calcein from the particles is clearly visible. The side view on top and on the right side of the images shows that the particles reside inside of the cell and the release of the calcein is also confined to the cell. The white scale bar represents 20 μm .

To further understand and validate the promise of this system, fluorescence release experiments in a custom-built setup were conducted with the coated NPs (Figure 4.3).¹² To confirm the successful coating and to investigate the sealing properties of the exosomal bilayer, calcein-loaded MIL-88A NPs were coated with exosomes and fluorescence release was measured in water. Even over long times (Figure 4.3 and Appendix Figure 4.25), no release was detected indicating a very tight coating without premature leakage, while uncoated particles leaked steadily. Next, we disassembled the exosome coating by addition of the nonionic surfactant Triton X-100. As expected, this led to an instant release of calcein resulting in an increase of fluorescence intensity that reaches saturation over time. The release is even

stronger than from uncoated particles, possibly due to the sudden release upon addition of Triton and/or release-promoting interaction of Triton and particle or due to premature leakage of the uncoated particles during the preparation process. To simulate the environment that particles encounter inside cells during endocytosis, the experiment was repeated in artificial lysosomal fluid (ALF) instead of water. Even in the absence of Triton, this led to a strong intensity increase over the course of a few hours. The observed release is even stronger than that in water with Triton X-100. Stability measurements of the coated MOF NPs reveal their rapid decomposition in ALF (see Appendix, Figures 4.17-4.19) and might deliver a possible explanation for this efficient release: the particles completely decompose in ALF leading to an enhanced osmotic pressure in the exosome coating, which might lead to a burst of the exosome followed by a complete release of all loaded calcein molecules (Figure 4.1). Such a release following complete disintegration is more efficient than that triggered by Triton X-100. The latter only destroys the coating, which does not necessarily lead to the release of all cargo molecules due to interactions with the MOF-lattice.²³ Since ALF simulates the lysosomal environment in the cell at advanced stages of endocytosis, the release observed in cells might be mediated by the decomposition of the MOF similarly to the release experiments here, in addition to possible endogenous release mechanisms of exosomes. The molecules of the dissolved NPs (i.e. fumaric acid and iron(III) ions) in combination with the protons pumped into the lysosome by the cell might enhance the osmotic pressure in the exosome coating and the lysosome and thus create cracks in both membranes that enable the release. All in all, the release experiments confirm the successful coating of MIL-88A NPs as well as the efficient storage and release (quantification see SI) of dye molecules inside the MOF core without premature leakage. They also deliver a possible explanation for the observed efficient release inside cells with the decomposition of the MOF in the lysosome acting as an “onboard-trigger”.

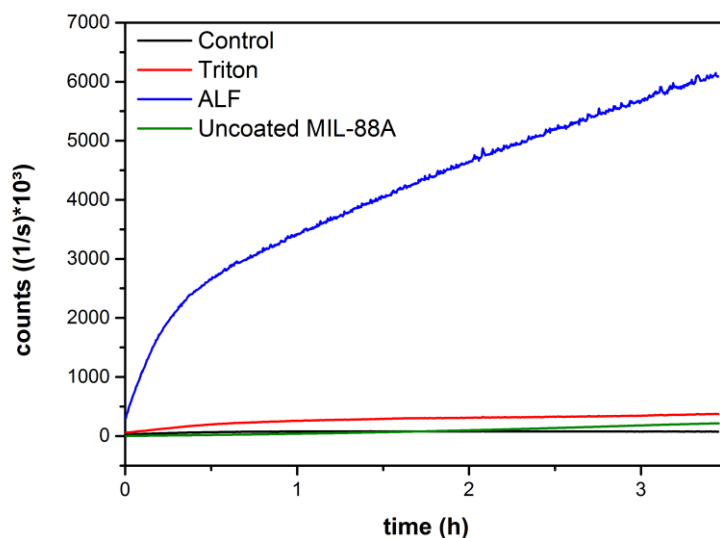


Figure 4.3. Fluorescence release experiments of encapsulated calcein in exosome coated MIL-88A(Fe) nanoparticles (the data points correspond to the intensities at the peak maxima at 512 nm of the spectrum for calcein). A solution of the coated particles in water was used as a negative control, while a Triton-X100 solution was used as a positive control. Uncoated MIL-88A NPs were used to test the effectiveness of the exosome coating in preventing leakage. The higher release in the ALF solution is caused by the decomposition of the MIL-88A NPs in this media and as a consequence a strong calcein release is observed. At the bottom a schematic of the measurement can be seen. 1) The cap is filled with loaded NPs. 2) The cap is sealed with a dialysis membrane. 3) The released calcein permeates through the membrane, while the particles stay in the cap.

Next, we assessed the efficiency of our novel drug delivery system further and quantified intracellular release in high-content experiments. HeLa cells were incubated with different concentrations (10-140 $\mu\text{g}/\text{ml}$) of exosome-coated MIL-88A NPs loaded with calcein (Figure 4.4). Release of calcein was evaluated in at least 1000 cells per concentration after three and four days of incubation using a high-content fluorescence microscope. The percentage of cells with clear calcein release was measured relative to the total number of cells. With increasing NP concentration we found an increasing percentage of cells that showed release, culminating in about 70 % at the highest concentration used. The percentage of cells with calcein release is not much higher after 4 days of incubation as compared to 3 days. The widely spread release measured here further establishes the promise of the exosome coated NPs as an efficient drug delivery system.

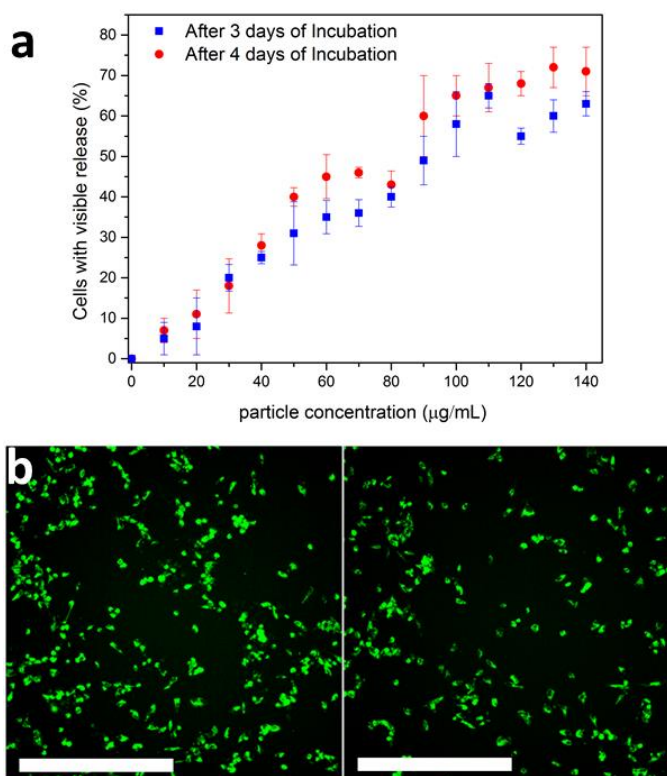


Figure 4.4 a) Release measured in cells after 3 (blue) and 4 (red) days of incubation with exosome coated, calcein loaded MIL-88A NPs. Each data point and its error bar have been compiled from 12 measurements and are based on a total number of at least 1000 investigated cells. The error bars mark the SD. b) Fluorescence microscopy images of cells incubated with calcein loaded exosome coated MIL-88A nanoparticles. (Left: three days, right: four days; 12 µg/ml). The scale bars represent 500 µm.

To test the therapeutic potential of our drug delivery system, we finally replaced the cargo calcein with a chemotherapeutic drug and studied its effect on cell viability. We chose SBHA, a histone inhibitor and anti-cancer drug,²⁴ as active cargo and measured the cell viability at different concentrations of NPs with MTT-tests. While the exosome coated particles without cargo showed no significant impact on cell viability, they efficiently caused cell death even at very low concentrations when loaded with SBHA as shown in Figure 4.5. The IC₅₀ value after 3 days of incubation was calculated to be 4.78 µg/mL. This is 3 times higher than the IC₅₀ of free SBHA (see SI). The supernatant of the NP solution did not affect cell viability – a proof of the encapsulation efficiency of the exosome coating. These results demonstrate that exosome coated MIL-88A NPs can store, deliver and release therapeutic molecules efficiently to cancer cells with minimal premature leakage. Hence, they show great potential to serve as smart drug delivery system.

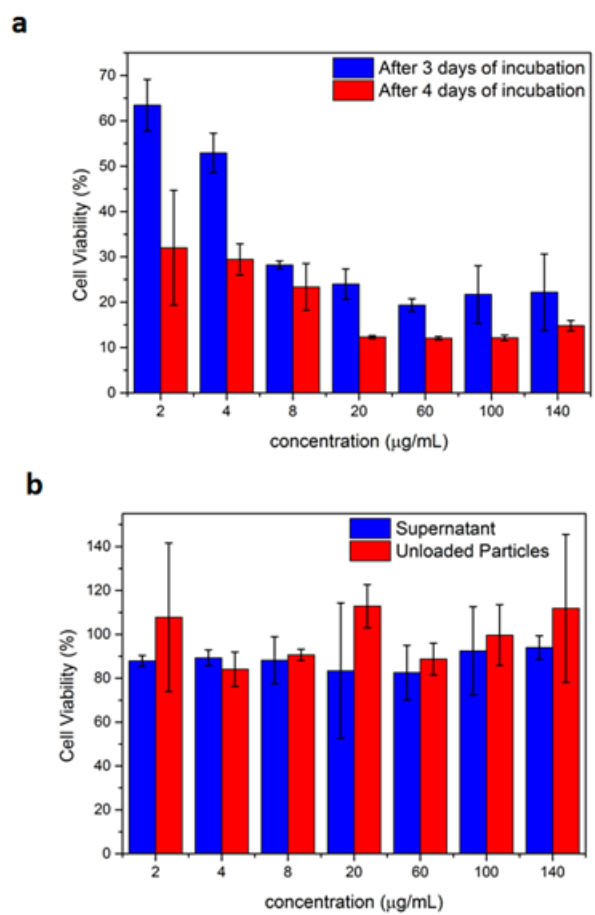


Figure 4.5: MTT-Assay results of HeLa-cells that were exposed to different concentrations of SBHA loaded MIL-88A NPs coated with exosomes. a) Cell viability after incubation for 3 and 4 days. b) Cell viability for the supernatant and unloaded coated particles. The error bars in both images signify the SD.

4.3 Conclusion

In conclusion, we report for the first time on exosome coated MOF NPs as a smart and efficient drug delivery system with “onboard-trigger”. It synergistically combines the features of MOF NPs and exosomes yielding a promising system that facilitates easy and efficient loading and sealing. Furthermore, it shows high therapeutic efficiency, yet no premature leakage. Intracellular cargo release is possibly mediated by a combination of the endogenous exosomal release mechanism and degradation of the nanocarrier, which decomposes into substances that are naturally present in the body. In the future, further advantages of the system will be exploited and analyzed: the MOF NP core will facilitate loading of several different drugs at the same time and monitoring of the NPs via MRI, targeting can be readily achieved by insertion of targeting ligands into the exosomal bilayer, and the use of autologous exosomes will ensure that they are not susceptible to responses from the immune system, allowing for longer circulation times.

4.4 Appendix

4.4.1 Methods and Characterization

Dynamic Light Scattering (DLS): DLS was performed on a *Zetasizer Nano Series* (Nano-ZS, *Malvern*) equipped with a laser with the wavelength $\lambda = 633$ nm. For sample preparation the freshly prepared nanoparticles (NPs) were dispersed in ethanol or phosphate-buffered saline (PBS) in the case of the capped NPs.

Scanning Electron Microscopy (SEM): All SEM micrographs were recorded with a *Helios NanoLab G3UC* (FEI) operating at 5 kV. During sample preparation an ethanolic NP dispersion was dried on a carbon film placed on an aluminum sample holder. The sample was stored overnight to evaporate the solvent followed by carbon sputtering prior to the measurement. For evaluation of the SEM micrographs the software *ImageJ v1.49* was used.

Transmission Electron Microscopy (TEM): The TEM micrographs of the sample particles were taken on a *Titan Themis* (Fei) that was operated at an acceleration voltage of 300 kV. For sample preparation, an ethanolic NP solution was dried overnight on a carbon-coated copper grid.

Cryogenic Transmission Electron Microscopy (CryoTEM): The CryoTEM images were measured on a *Leo 912 Omega* that was operated at 120 keV. The sample was applied to a carbon-coated copper grid and flash frozen with Kryogen (90 k) for the measurements.

Thermogravimetric Analysis (TGA): A dried sample of MIL-88A NPs (3.125 mg) was heated using a *TASC 414/4* (Netzsch). The sample was heated under synthetic air at 10 °C/min up to 900 °C. The resulting data was evaluated using the software *Proteus v4.3*.

Nitrogen sorption: Nitrogen sorption experiments were conducted with an *Autosorb-1 (Quantachrome)*. Prior to the measurement the sample (27.9 mg) was outgassed under high vacuum at 120 °C for 38 h. The resulting data was evaluated with the software *ASiQwin v3.0*. The linearized form of the BET equation was used to calculate BET surface areas. For the calculation of the pore size distribution a QSDFT equilibrium based model was used assuming slit and cylindrical pores.

X-Ray Diffraction: X-ray diffraction experiments were performed on the initial MIL-88A NPs. The samples were measured on a *STOE Transmissions-Diffraktometer System STADI P* operating in transmission mode. The setup is using $\text{CuK}\alpha_1$ -radiation with a wavelength $\lambda = 0.15418$ nm. The resulting diffraction pattern was evaluated using the software package *WinXPOW RawDat v3.0.2.5* and *WinXPOW PowDat_n v3.0.2.7*.

Fluorescence Microscopy: The fluorescence microscope images were recorded with a *Zeiss Observer SD* spinning disk confocal microscope using a Yokogawa CSU-X1 spinning disc unit and an oil objective with 63x magnification and BP 525/50 and LP 690/50 filters. The setup was heated to 37 °C and a CO_2 source was provided to keep the atmosphere at 5% CO_2 . For both excitation of the calcein and the cell marker a laser with a wavelength $\lambda = 488$ nm was used. The images were processed with the *Zen* software by *Zeiss* to optimize contrast and provide the orthogonal views.

Fluorescence Spectroscopy: The fluorescence spectroscopy experiments were recorded with a MD-5020 setup from *PTI Photon Technology International*. The software *Felix32* was used for recording and evaluating the measured data.

UV/Vis Measurements: The UV/Vis measurements were performed on a Lambda 1050 UV/Vis/NIR spectrometer from *Perkin Elmer*. The software used to record the measured spectra was *Perkin Elmer UVWinLab*.

High-Content Quantification: The release quantification measurements were performed with a *ImageXpress Micro XLS* from *Molecular Devices* using an objective with 10x magnification with a GFP filter and the resulting images were evaluated with the *MetaXpress* software.

Cell culture: All cell experiments were prepared in a *Hera-Safe* cell culture unit from *Heraus*. The cells were incubated in *Hera Cell incubators* also from *Heraus*.

MTT Assays: The MTT-Assays were performed with a *Spectra Fluor Plus* from *Tecan* and were then evaluated with *Excel 2010*

4.4.2 Synthesis of the uncoated and coated MIL-88A nanoparticles

Synthesis of MIL-88A NPs

MIL-88A NPs were synthesized in a microwave assisted approach based on the results of Chalati et al.²⁴ In this synthesis route an aqueous solution of $\text{FeCl}_3 \cdot 6 \text{H}_2\text{O}$ (1.084 g, 4.01 mmol) and fumaric acid (485 mg, 4.18 mmol) are given to water (20 ml, Milli-Q). The reaction mixture was stirred until the metal salt was completely dissolved. The reaction mixture was then given into a Teflon tube (80 ml) and placed into a microwave oven (*Synthos 3000, Anton-Paar*) along with 3 additional vessels. Two of these vessels are filled with water (20 ml), the third vessel is filled with an aqueous FeCl_3 (20 ml, 1.084 g, 4.01 mmol) and is used to monitor the reaction progress. The vessels were heated under stirring with the sequence shown in Table 4.1:

Table 4.1: MW Heating program for the MIL-88(A) NPs synthesis

Heating	Dwelling	Cooling
30 s	5 min	45 min
To 80 °C	80 °C	To RT

To remove residual reactants the sample was subsequently washed via centrifugation (7840 rpm, 20 min) and redispersion of the pellet in ethanol (20 ml). This washing cycle was repeated 3 additional times. To remove also bulk material formed during the reaction, the dispersion was then centrifuged 3 times (3 min, 3000 rpm) and the pellet fraction of the product discarded.

Preparation of the exosome coating solution

Approximately 100000 HeLa cells were transferred to a 75 cm culture flask and incubated in 10 mL fetal bovine serum (FBS)-free Dulbecco's modified Eagle Medium (DMEM) for three days. The exosomes were then extracted from the medium using the *Exospin* kit from *Cell Guidance Systems* following the protocol from the kit.

Preparation of the loaded and coated particles

1 mg of MIL-88A NPs were solved in 1 mL of a 1 mM solution of calcein or suberohydroxamic acid (SBHA) and incubated overnight for loading. Next they were centrifuged for 5 min at 14000 rpm, to discard the supernatant and the pellet was dissolved in 0.2 mL of the exosome coating solution and 0.2 mL water and incubated for 2 h. The particles were then centrifuged (5 min at 14000 rpm) and redispersed in 1 mL PBS after washing several times.

4.4.3 Characterization of MIL-88A NPs

Scanning Electron microscopy

An overview picture of the MIL-88A NPs used in this work is presented in Figure 4.6

Verweisquelle konnte nicht gefunden werden..

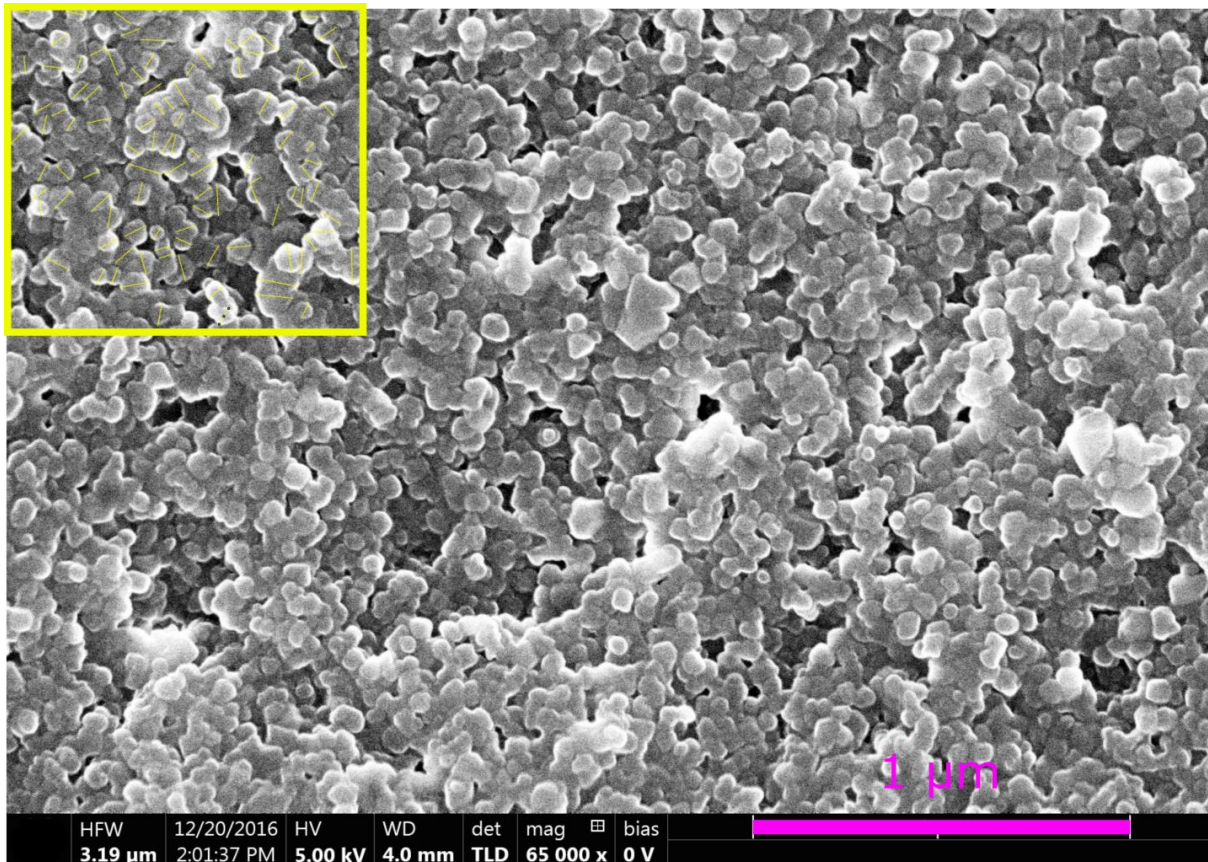


Figure 4.6: Scanning Electron micrograph of MIL-88A nanoparticles.

The particles look uniform and feature a roundish morphology. For further characterization, the particles marked in the yellow box were used to determine a particle size distribution of the sample.²⁴

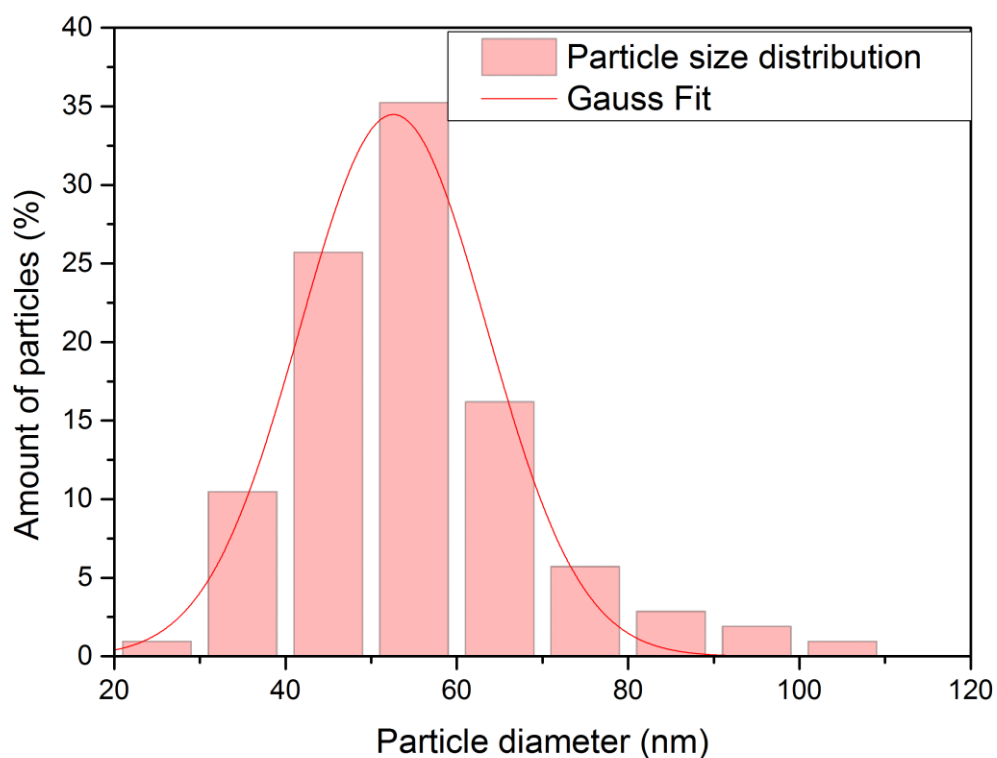


Figure 4.7: Particle size distribution determined from the SEM micrograph shown in Figure 4.6 (yellow box).

The particle size distribution was determined by manually measuring the diameter of ~ 150 particles (Figure 4.6 yellow box) and fitting the data with a Gaussian function using the software Origin v9.0.0.²⁴ This results in an average particle diameter of 52 nm with a standard deviation of 11 nm.

Transmission Electron microscopy

Figure 4.8 and 4.9 depict TEM micrographs of the MIL-88A NP sample. The particles feature a round morphology and are connected via thin necks. The MIL-88A sample is fairly homogenous, which is also shown in a particle size distribution given in Figure 4..

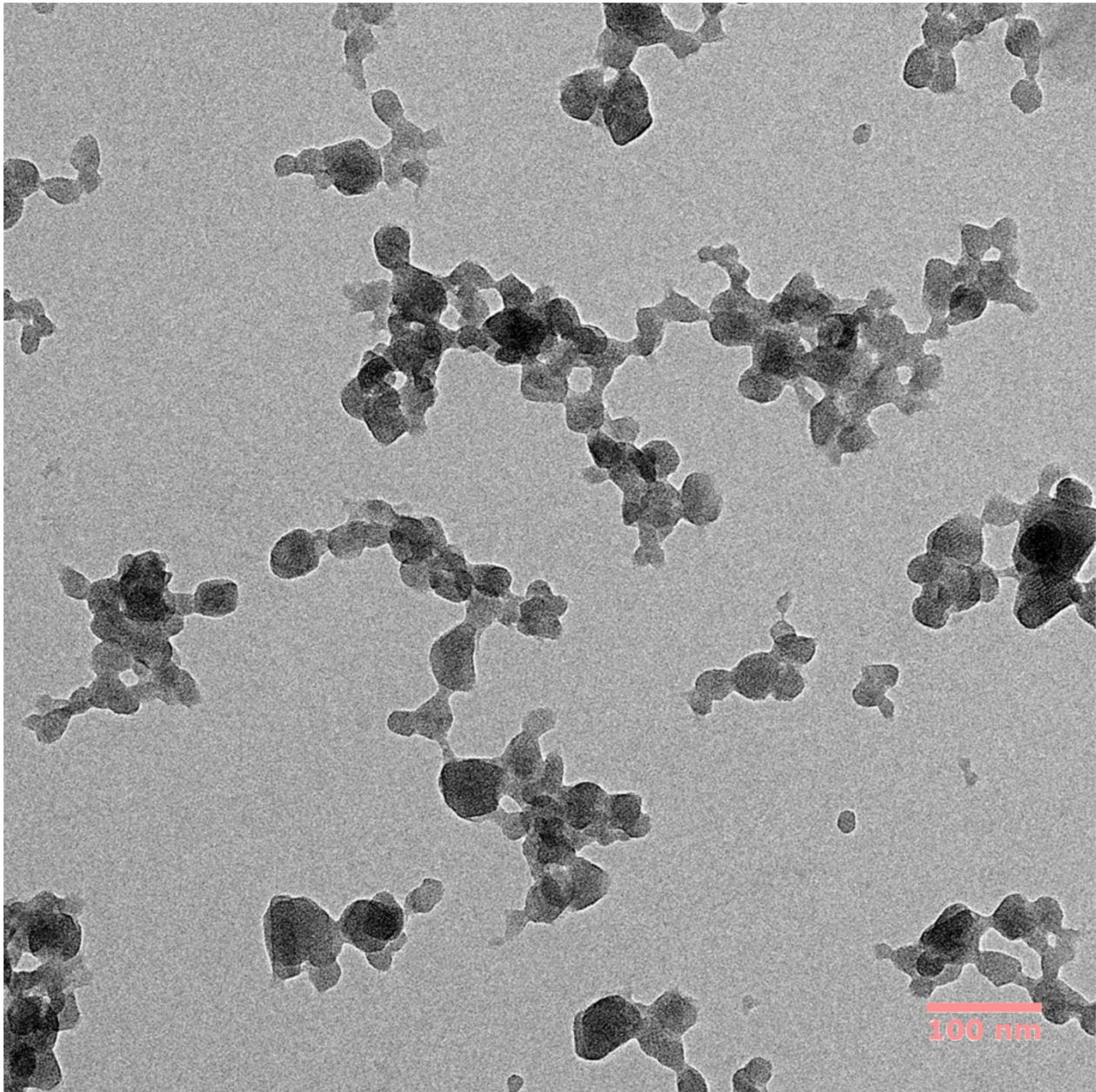


Figure 4.8: Transmission electron micrograph of MIL-88A NPs – detailed image.

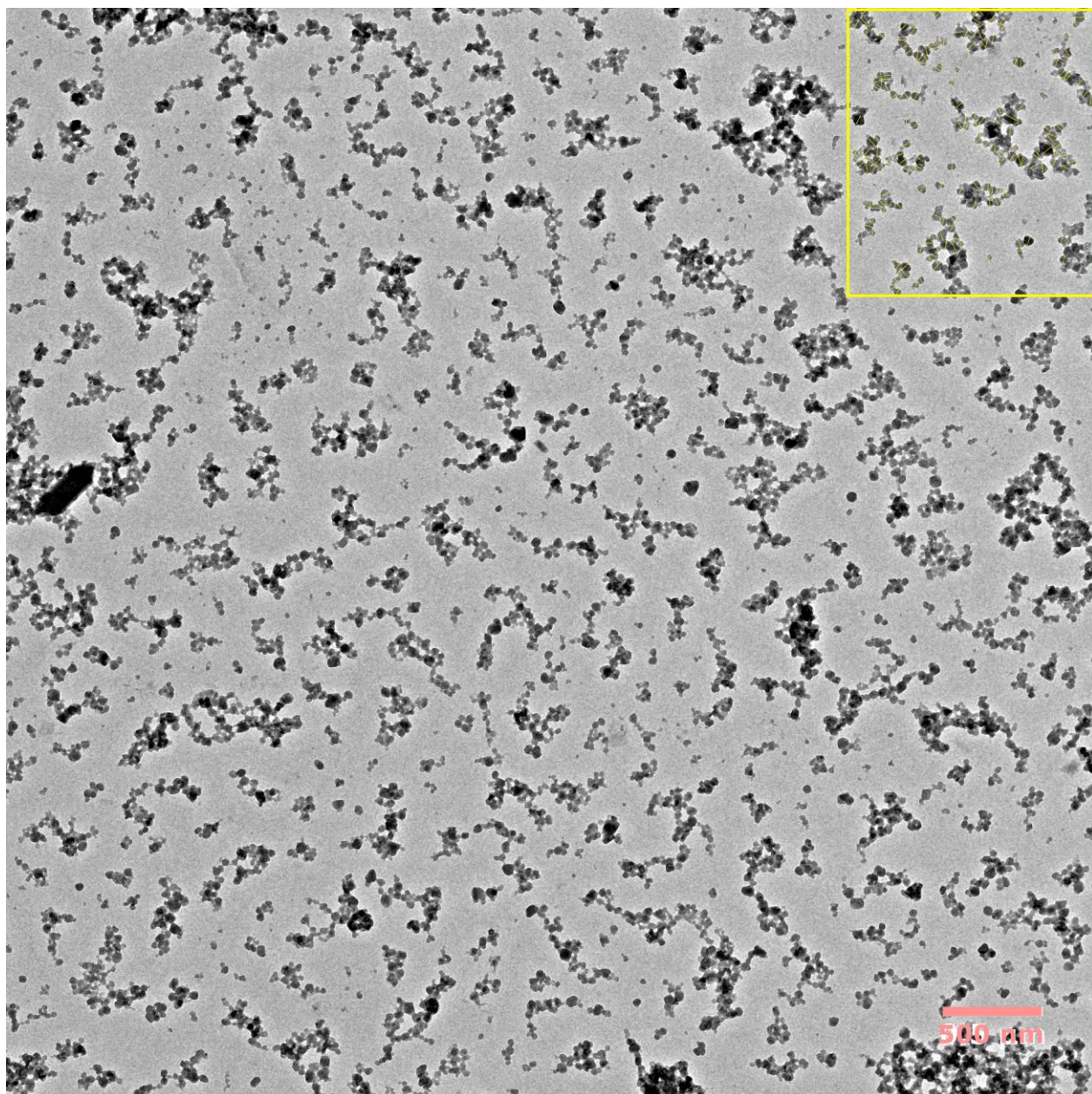


Figure 4.9: Transmission electron micrograph of MIL-88A NPs.

The particle size distribution was determined by manually measuring the diameter of ~ 200 particles and fitting the data with a Gaussian function using the software Origin v9.0.0.²³ The average diameter was determined at 36 nm with a standard deviation of 9 nm.

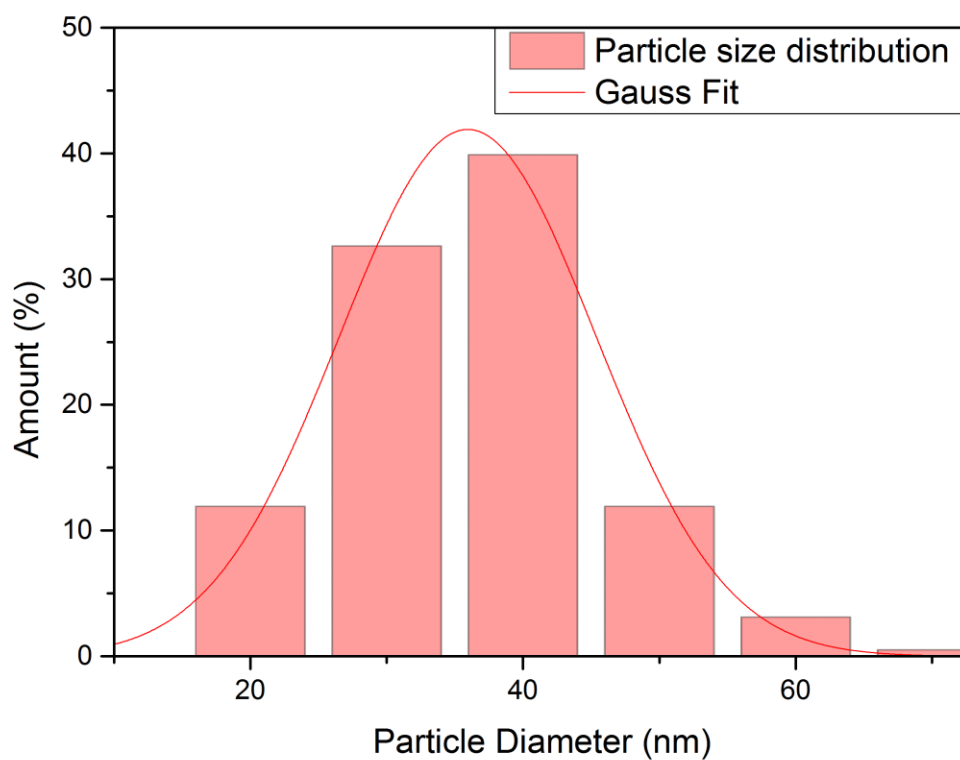


Figure 4.10: Particle Size distribution determined from the TEM micrograph shown in Figure S4 (yellow box).

This diameter differs from the results shown in the SEM measurements. This behavior however is not unusual in size determination of MOFs with SEM and TEM. Beam damage of a sample is a known problem in TEM mostly with high-energy electron beams ($E > 100$ keV).²⁵

Dynamic Light Scattering

The results of the DLS measurements of the unfunctionalized MIL-88A NPs are shown in Figure 4.11. In water, the particles have an intensity based hydrodynamic average diameter of 99 nm with a polydispersity index (PDI) of 0.131, which translates to a good monodisperse particle size distribution.

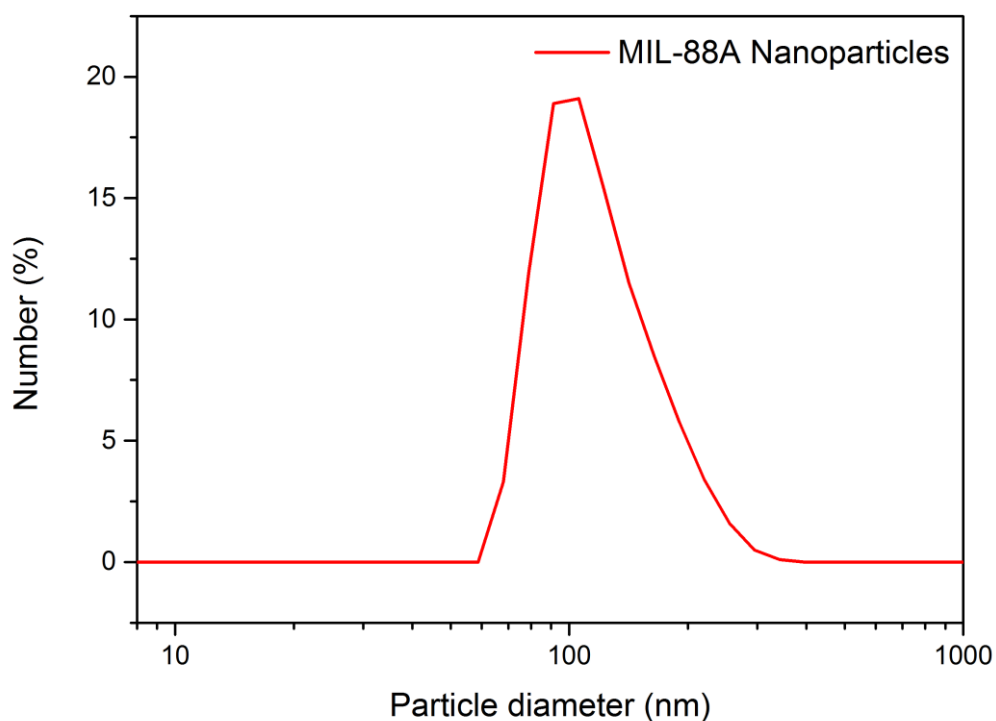


Figure 4.11: DLS size distribution of MIL-88A NPs showing the percentage of particles for each size.

DLS measurements of the exosome coated MIL-88A NPs can be seen in Figure 4.12. In PBS the exosome coated particles possess an average diameter of 101 nm. The measured PDI is 0.143 meaning that sample possesses a good monodispersity.

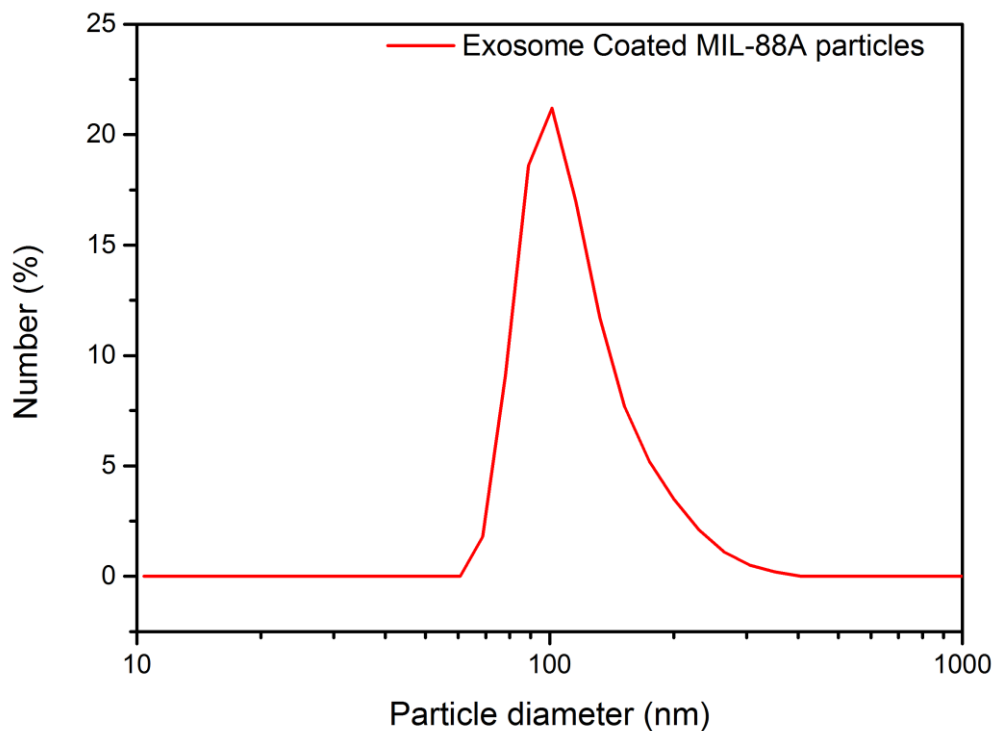


Figure 4.12: DLS size distribution of exosome coated MIL-88A NPs showing the percentage of particles for each size.

DLS measurements of the exosomes can be seen in Figure 4.13. In PBS the exosomes possess an average diameter of 100 nm. The measured PDI is 0.157 meaning that sample possesses a good monodispersity.

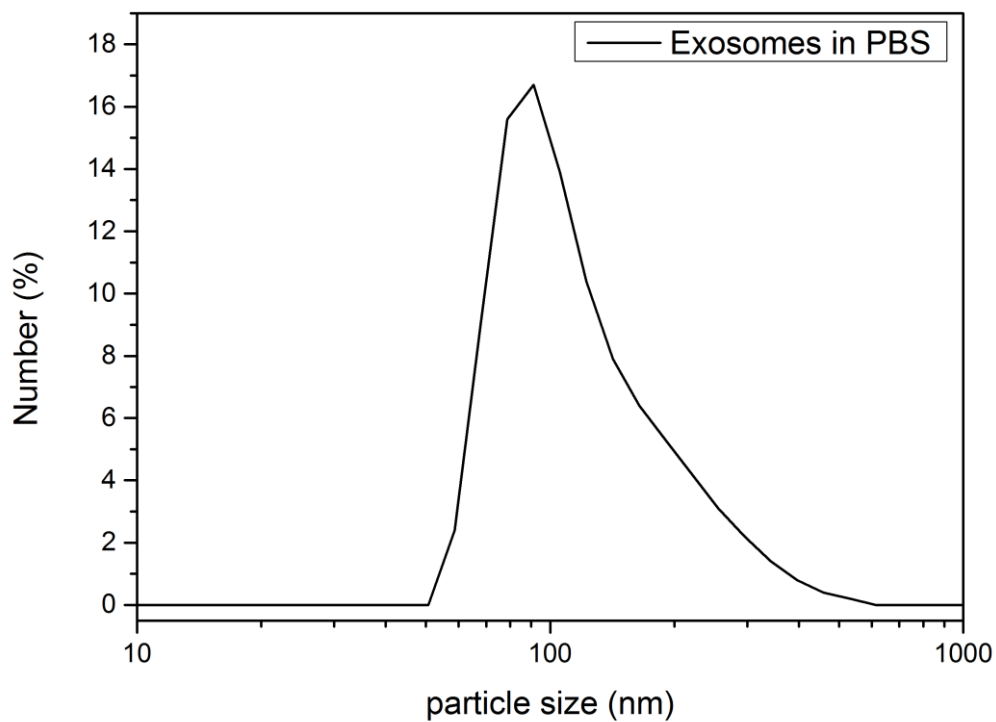


Figure 4.13: DLS size distribution of exosomes recovered with the Exospin kit showing the percentage of exosomes and extracellular vesicles for each size.

X-Ray Diffraction

Figure 4.14 shows the X-ray diffraction pattern of the initial MIL-88A NPs. The peak at $2\theta = 10^\circ$ is fairly weak suggesting an overall rather amorphous nature of the particles and less pronounced crystallinity than in other MOF structures. The diffractogram however is in good agreement with the data reported in literature for MIL-88A NPs.²⁵

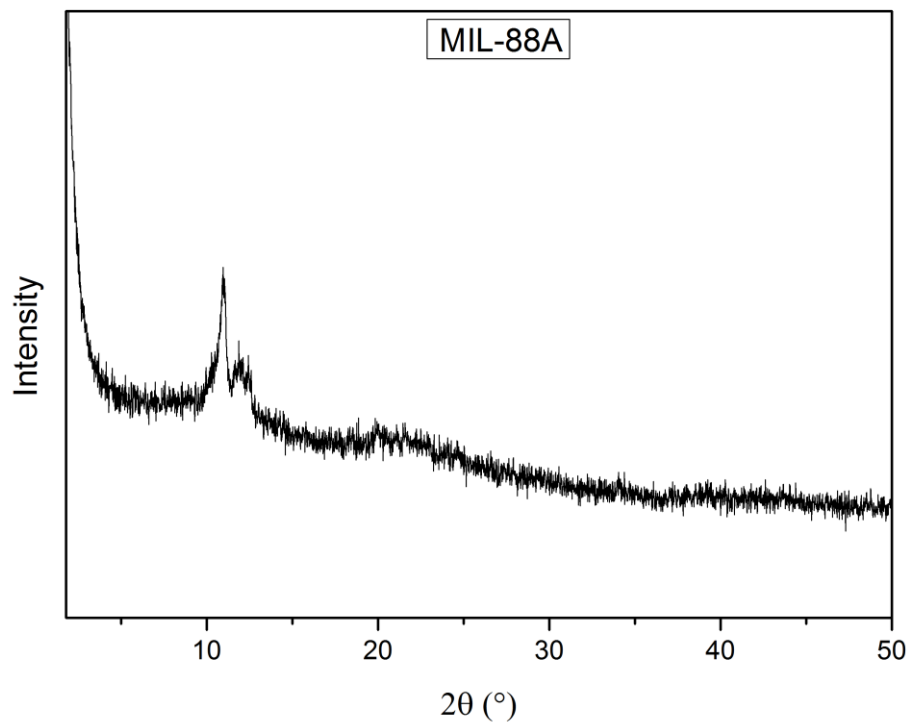


Figure 4.14: X-ray diffraction pattern of dried MIL-88A NPs.

Thermogravimetric Analysis

The results of the thermogravimetric analysis of the initial MIL-88A NPs are shown in Figure 4.15. Up to 204 °C the residual solvent in the sample is desorbed resulting in a mass loss of 6 %. Subsequently, in a range between 204 – 433 °C the framework decomposes. The residual mass left of the sample remains at 42%. This data is in agreement with literature data for MIL-88A NPs and shows the successful synthesis of the MOF.²⁵

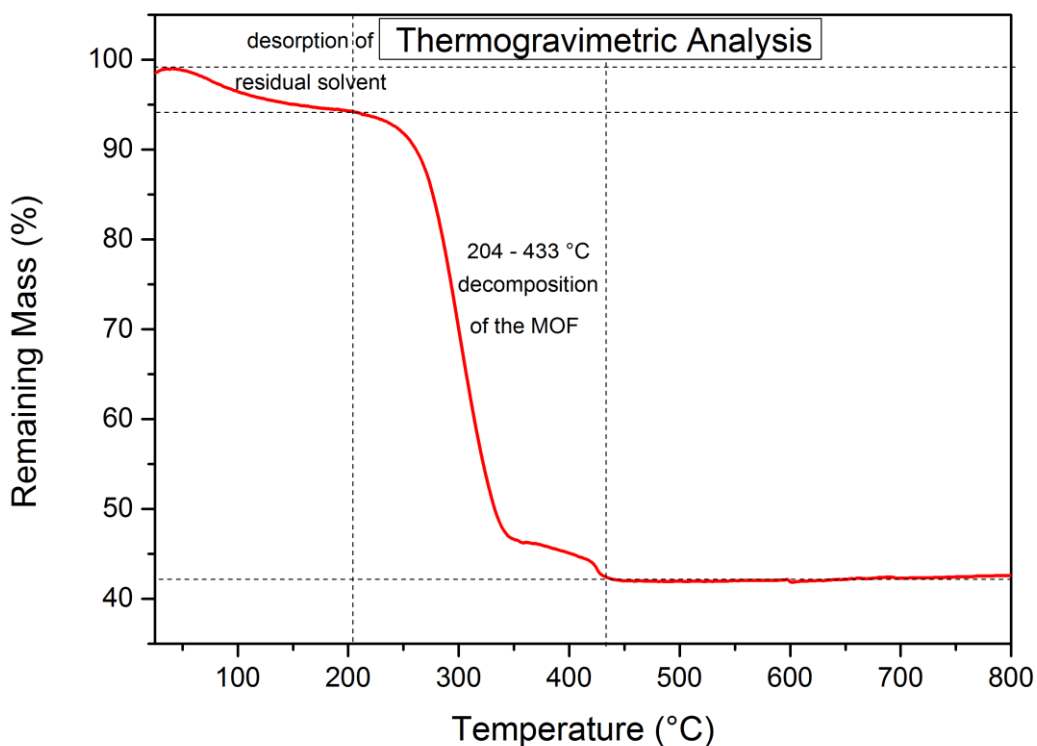


Figure 4.15: Thermogravimetric analysis of MIL-88A NPs.

Nitrogen Sorption

The results of the nitrogen sorption experiments are shown in Figure 4.16 which depicts the sorption isotherm and the corresponding pore size distribution. The results are summarized in Table 4.22 as well. The nitrogen uptake is in good agreement with reported data of MIL-88A NPs.²⁶

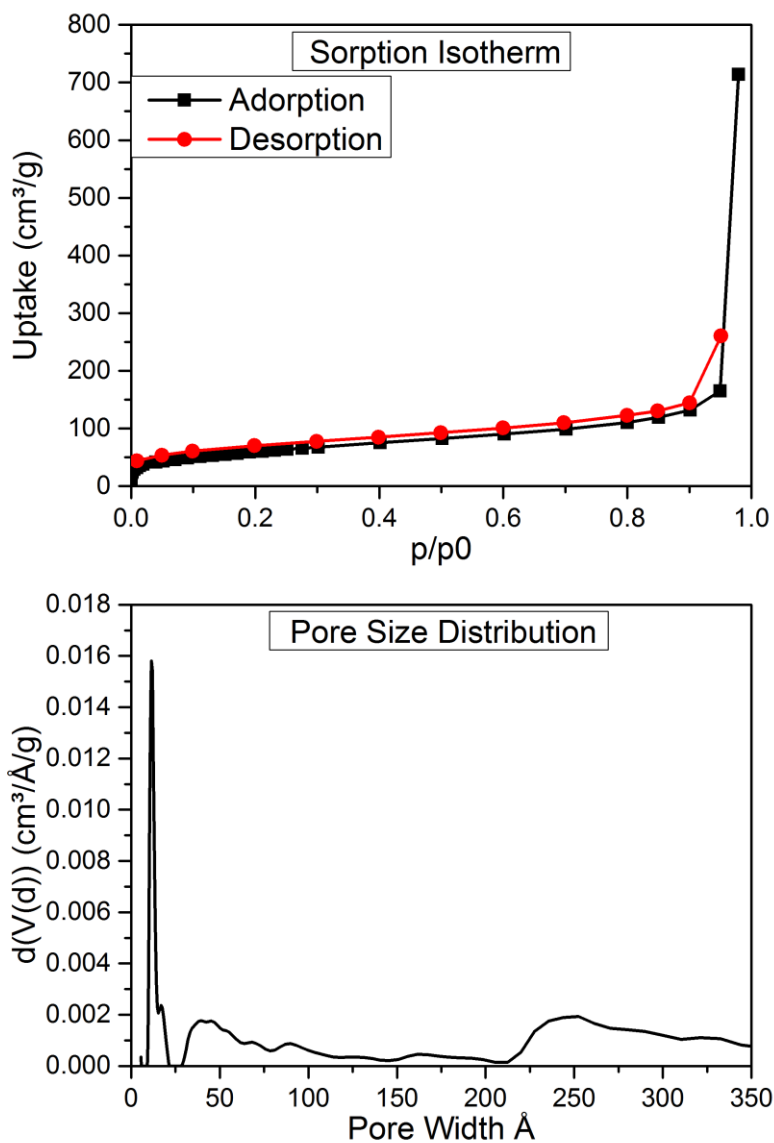


Figure 4.16: Nitrogen sorption isotherm and pore size distribution.

Table 4.2: Results of the BET analysis

Sample	MIL-88A
BET-surface area [m ² /g]	218 m ² /g
Relative pressure range used for calculation	0.11-0.23
Correlation coefficient	0.999
C-constant	Positive
Pore Size	11.44 Å

4.4.4 Stability Measurements

To investigate the stability of the particles in body relevant media, 500 μg of the coated and uncoated nanoparticles were dispersed in 1 mL ALF²⁷. After a day of incubation the solutions were measured again. The solutions were clear and no particles could be recovered via centrifugation (Figure 4.17). The original particles seem to have been completely disassembled in the ALF media as it can be observed in the XRD and the SEM image (Figure 4.18, Figure 4.).

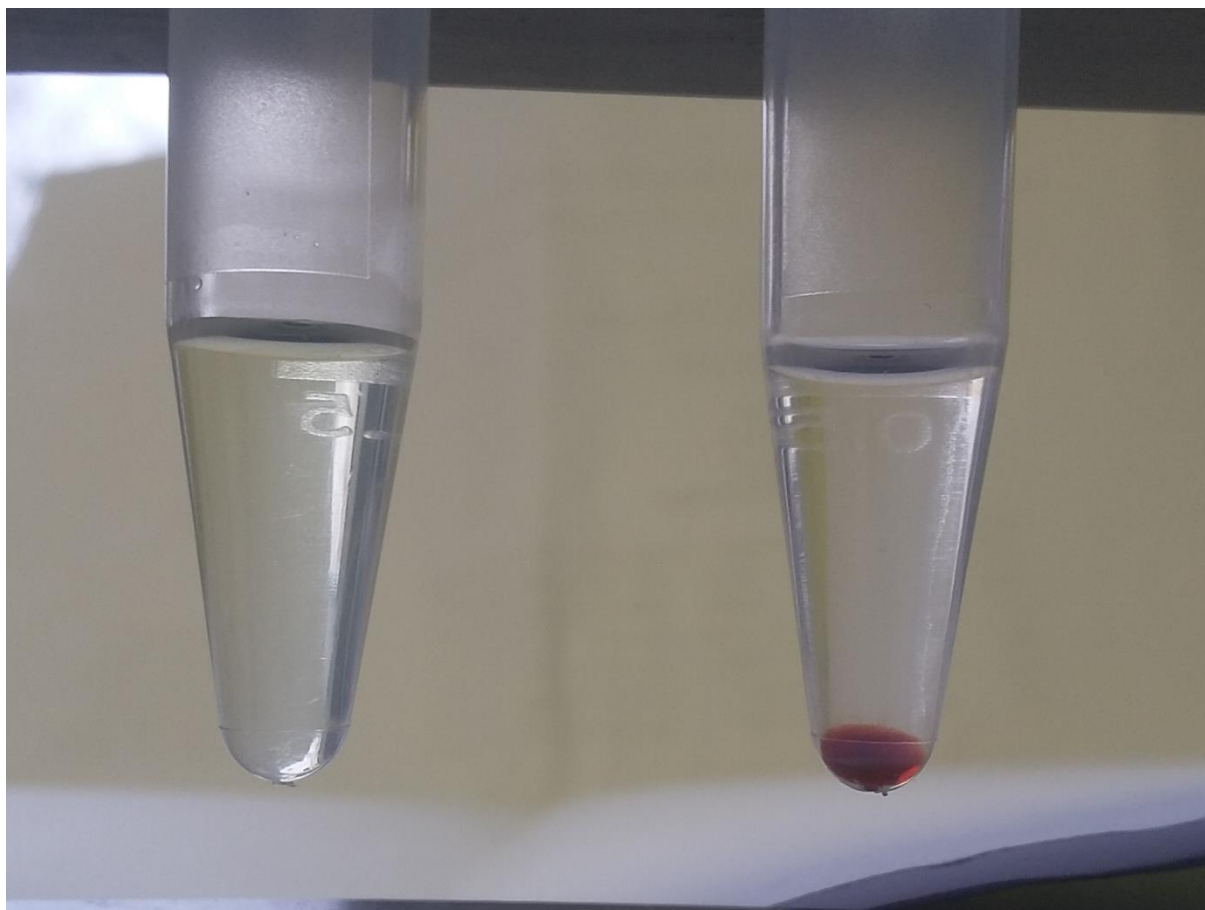


Figure 4.17: MIL-88A NPs before (right) and after (left) treatment with ALF. The particles in the untreated sample were recovered via centrifugation (14000 rpm, 5 min), while no particles could be recovered in the treated sample.

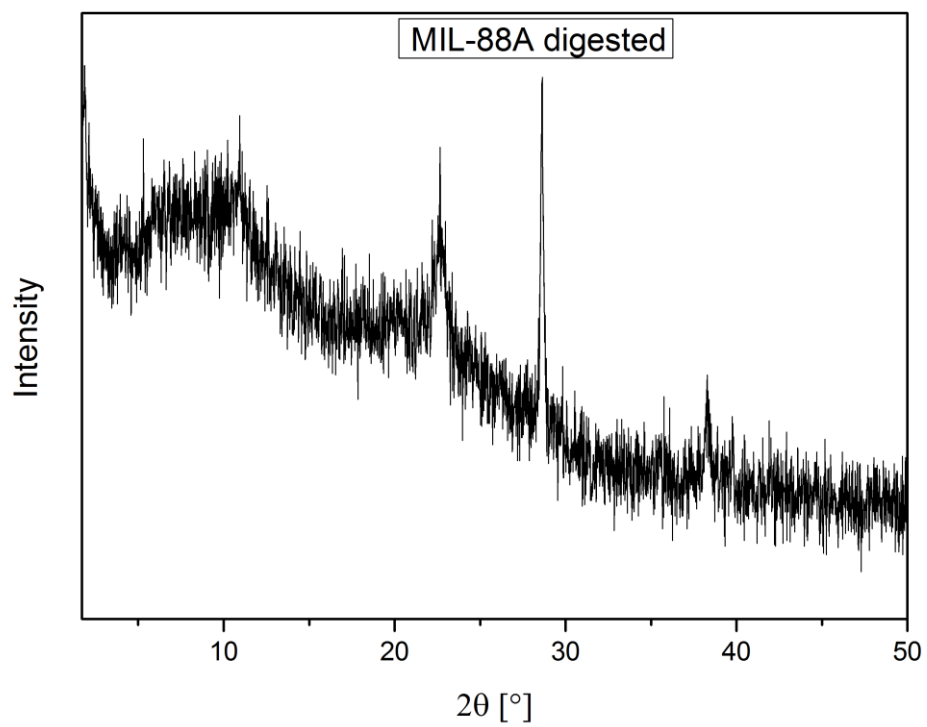


Figure 4.18: XRD of the residue after treatment of the MIL-88A nanoparticles with ALF, showing that the characteristic reflexes of MIL-88A at about 10° are no longer visible.

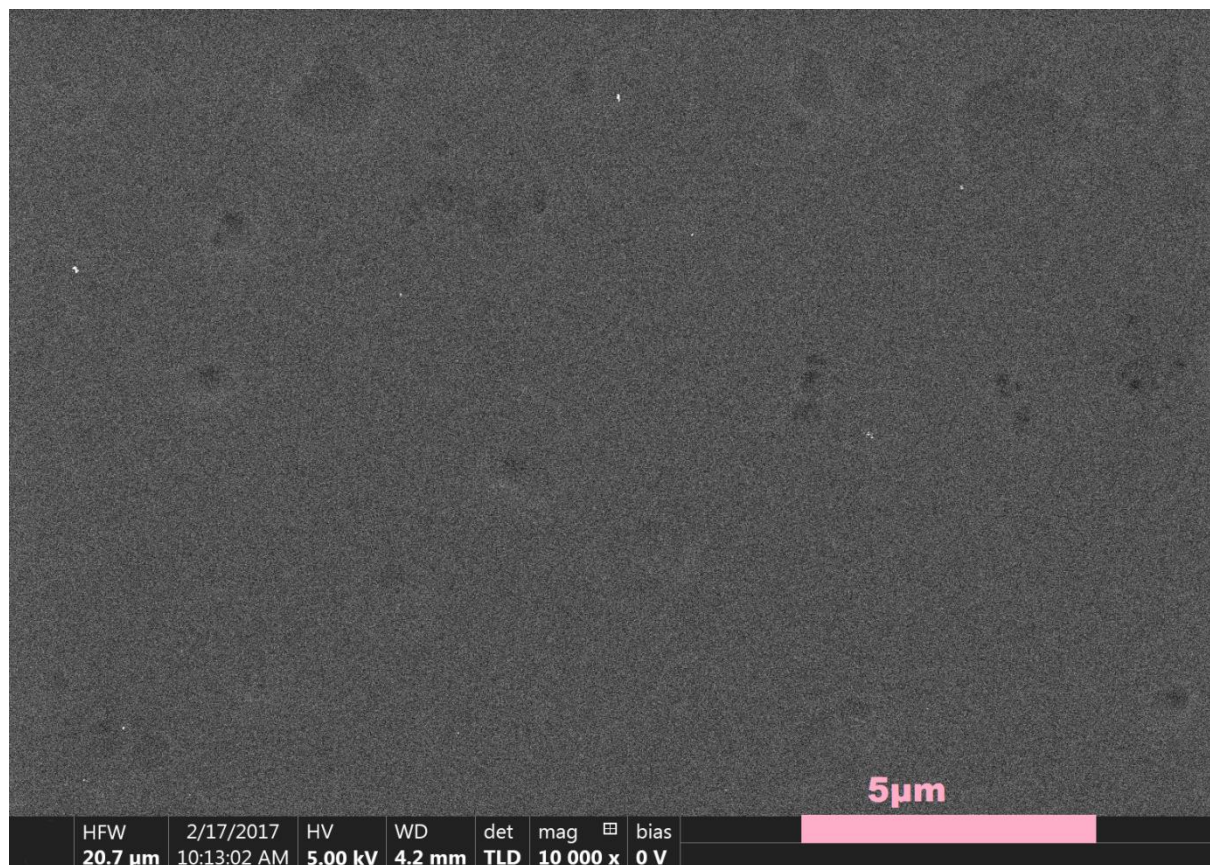


Figure 4.19: SEM images of the residue left after treating uncoated MIL-88A NPs with ALF, showing no discernible crystallites.

In addition to the ALF measurements the same procedures were carried out with an aqueous 10% FBS solution, showing no particle degradation after incubation overnight (Figure 4.20).

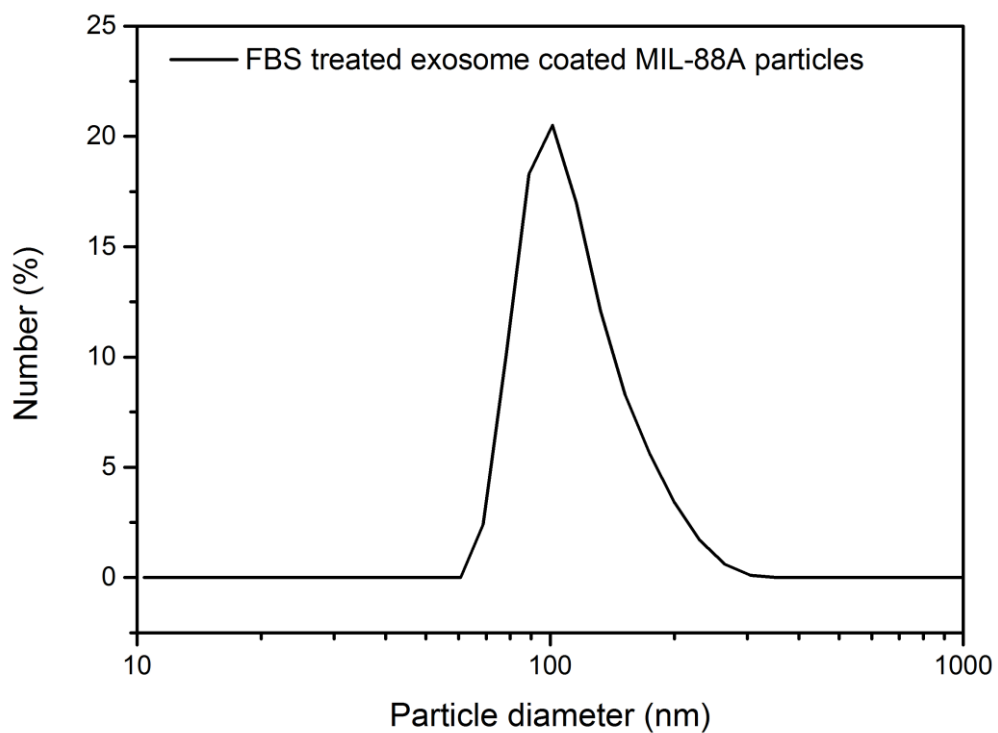


Figure 4.20: DLS size distribution of exosome coated MIL-88A NPs showing the percentage of particles for each size after overnight treatment with FBS.

Visualizing the Exosome coating

As proof of a successful exosome coating of the MOF nanoparticles we performed fluorescence colocalization experiments. We labeled the MOF nanoparticles with Fluo-3, which stains the iron contained in the particles, and the exosomes with CellMaskOrange. Successful coating should result in a colocalization of both dyes, while they should be independently distributed in the case of failed coating. The merged image both channels shows that we indeed obtain colocalization of both dyes suggesting a successful coating. The slight offset of both channels can be explained by the time it took to switch between the different excitation wavelengths needed for the two different dyes: the particles slightly moved due to the Brownian motion preventing a complete overlap of both images in the merged channel. Careful control experiments excluded spectral overlap of the dyes and confirm that the colocalization of the signals is indeed due to successful coating.

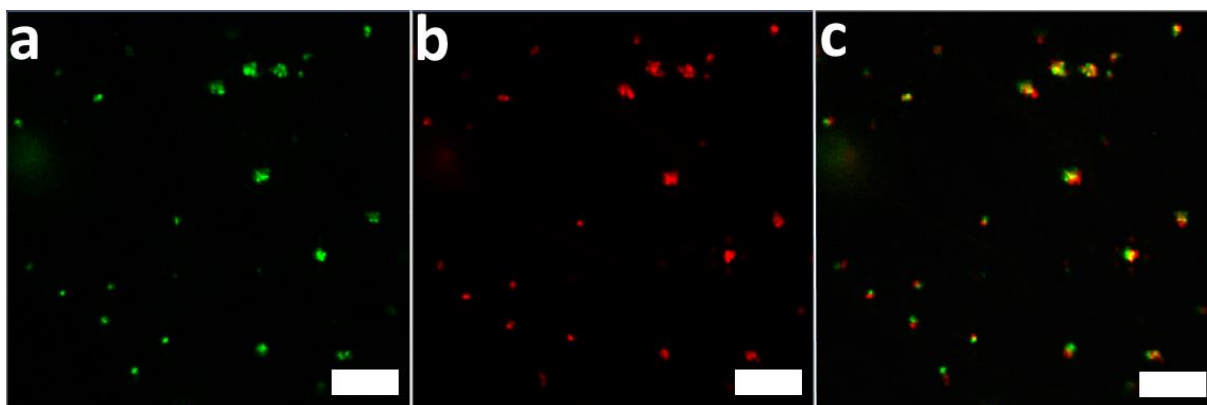


Figure 4.21: Fluorescence Cross Correlation Images of the exosome coated MIL-88A nanoparticles. The particles were marked with Fluo-3 (green, a) and iron marker, while the exosomes were marked with CellMask Orange (red, b). c shows the merged image of both channels.

4.4.5 Cell Release Experiments

For the cell release experiments 5000 HeLa cells were seeded in each well of ibidi 8-well plates and after one day 5, 10, 15 or 20 μg of the MIL-88A particles were added to each well. Incubation times of two, three and four days were investigated and can be seen in Figure 4.22, Figure 4.23 and Figure 4.24, respectively. The cells were marked with CellMask Orange, by adding 1 μL masking agent, incubating for 5 minutes at 37 $^{\circ}\text{C}/5\% \text{CO}_2$ and washing three times with DMEM to remove the remaining masking agent. The microscope images were taken with a Zeiss spinning disk microscope with an oil objective with 63x magnification. In addition to normal images Z-Stacks were also recorded, allowing for an orthogonal view of the cells, proving that the particles have entered the cell after 2 days of incubation.

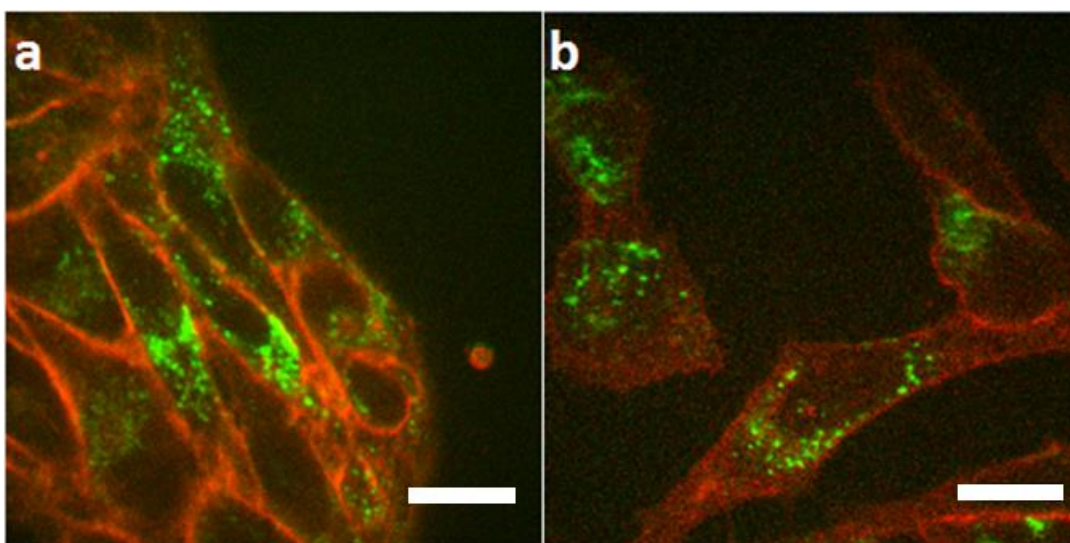


Figure 4.22: a, b) HeLa cells with exosome coated MIL-88A particles after two days of incubation. The scalebars (white) represent 20 μm .

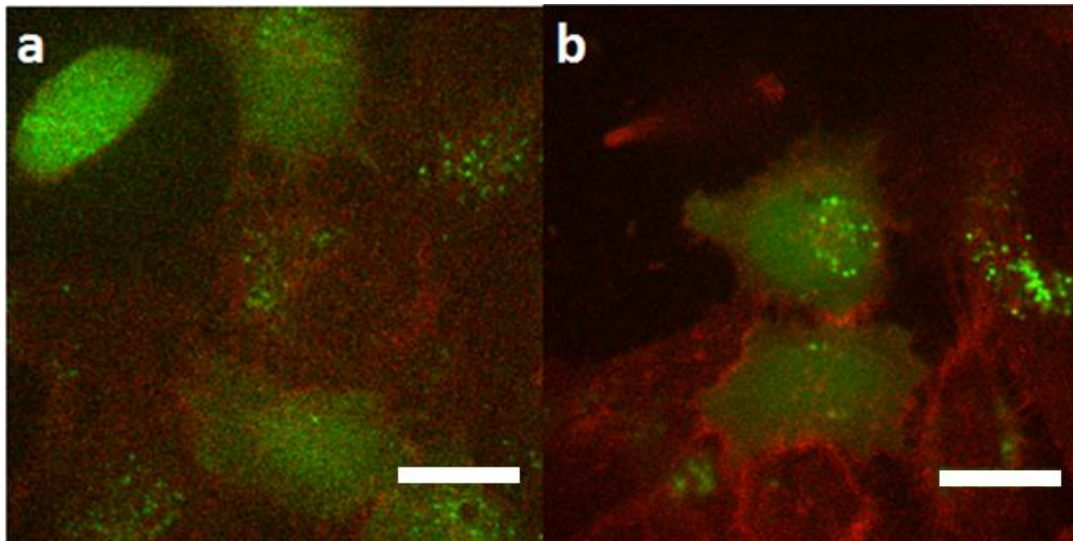


Figure 4.23: a, b) HeLa cells with exosome coated MIL-88A particles after three days of incubation. The scalebars (white) represent 20 μm.

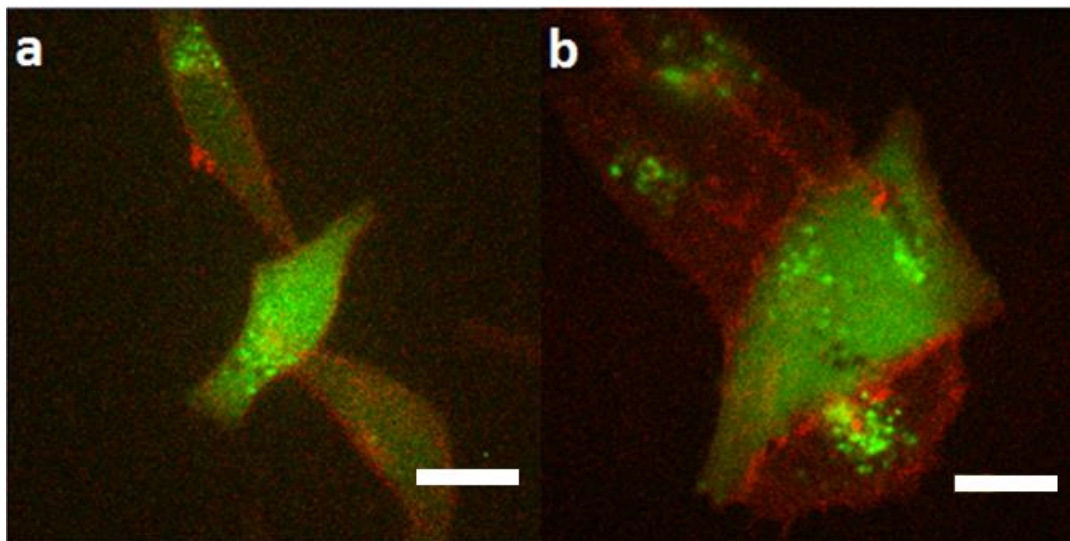


Figure 4.24: a, b) HeLa cells with exosome coated MIL-88A particles after four days of incubation. The scalebar (white) represents 20 μm.

Release Experiments

The release experiments were performed on a PTI fluorescence spectrometer. Hollow caps were filled with 50 μL of a 1 mg/mL particle stock solution for exosome coated and calcein loaded particles. Depending on the experiment either 150 μL water, 150 μL ALF or 90 μL water and 10 μL Triton 100-X were added. The caps were then sealed with a dialysis membrane and placed into cuvettes filled with either water or ALF and a stirring rod. The cuvettes were heated to 37 $^{\circ}\text{C}$ to simulate the cell environment. Each experiment lasted 14 h with one measurement per second. The excitation wavelength was 495 nm and the measured emission wavelength was 512 nm.

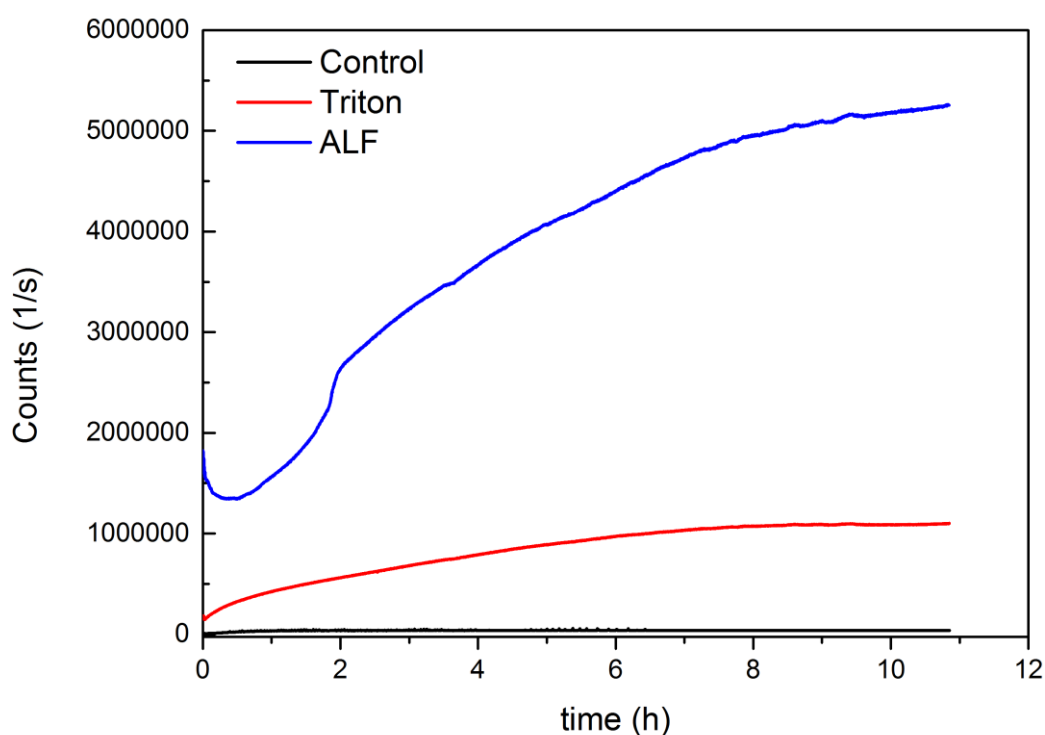


Figure 4.25: Fluorescence experiment of the exosome coated MIL-88A NPs showing that they are stable and do not release in water (black). When dissolved in ALF (blue) or Triton X-100 (red) containing media release from the particles can be observed that reaches saturation after about 10 hours.

To account for quenching 10 mL of a 1 mM solution of calcein were diluted with 990 mL PBS. Next 10 mL of this new solution were added to 4 mL water or ALF in cuvettes. In addition 10 mL triton X-100 was added to one sample. Then the fluorescence spectra of these solutions were measured to find a normalization factor between them (Figure 4.26). This factor was then used to calculate the offset for the individual fluorescence measurements. The normalization factor determined by comparing the measurements for water and triton X-100 to those for ALF is

2.17 and was implemented in the fluorescence experiments.

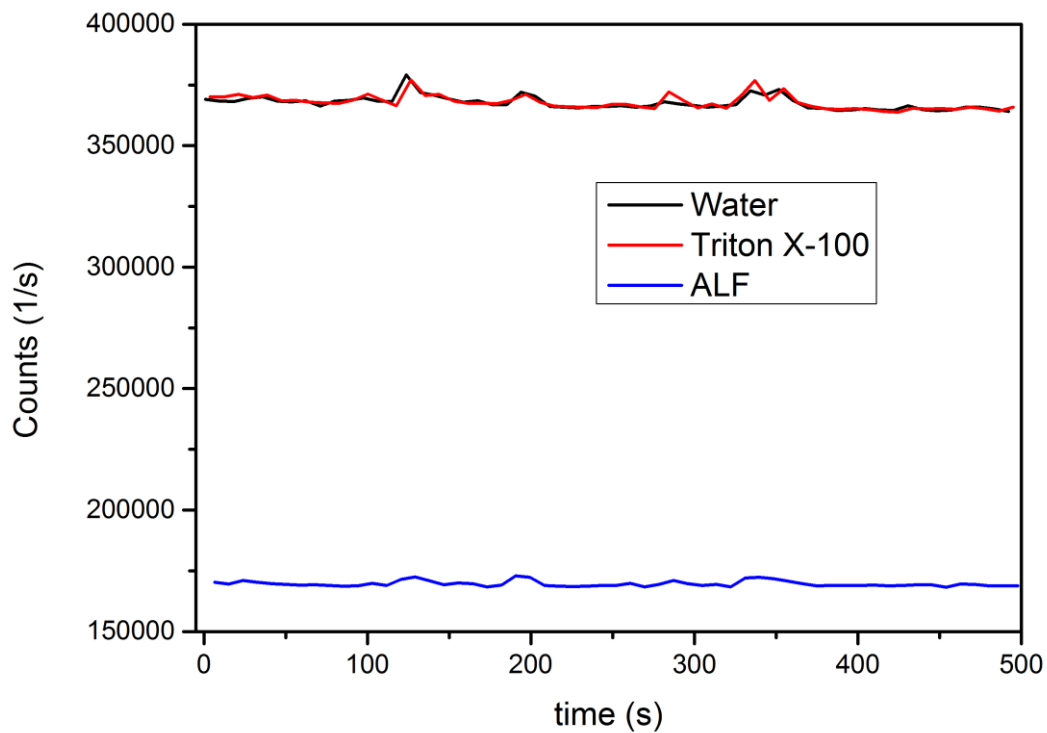


Figure 4.26: Fluorescence measurement to determine the quenching of the different media used in the fluorescence measurements.

UV/Vis measurements

To evaluate the loading capacity of the coated MIL-88A NPs, UV/Vis spectra of a 1 mM calcein solution, the remaining supernatant of the calcein solution after the particles were loaded, a 1 mg/mL solution of loaded particles dissolved by ALF, and a 1 mg/mL solution of coated, loaded particles were measured (Figure 4.27). In addition a solution containing the calculated amount of calcein loaded in the MOF was also measured. For each measurement 100 mL of the sample were diluted with 3 mL water.

The calcein loading capacity was calculated from the difference in absorbance of the measured solutions. The calcein stock solution used for loading the particles had a concentration of 1mM, i.e. 0.622 mg/mL. As 1 mL of the stock solution was used for loading, 1 mg of the particles have taken up 0.158 mg calcein or 15.8 wt%, using the ALF measurement as a basis. A quarter of the calcein was taken up by the MIL-88A particles and released. As the particles dissolve in ALF all of the loaded particles should be released. The difference in absorbance between the loaded particles and the particles dissolved in ALF can be attributed to quenching of the fluorescence as long as the calcein still resides in the MOF.

The spectrum of calcein in ALF and the sample containing the calculated amount of calcein match very well. This shows that the remains of the disintegrated MOF do not affect the UV/Vis measurements and this measurement can thus be used for determining the amount of encapsulated and released calcein.

In previous works, in which drugs like Doxorubicin and Paclitaxel were loaded into exosomes, loading efficiencies of 7.2 to 11.7% were reached.²⁸⁻³⁰ These values are comparable but lower than those of the exosome coated MIL-88A NPs presented in this work which could reach loading capacities of up to 15.8 wt%.

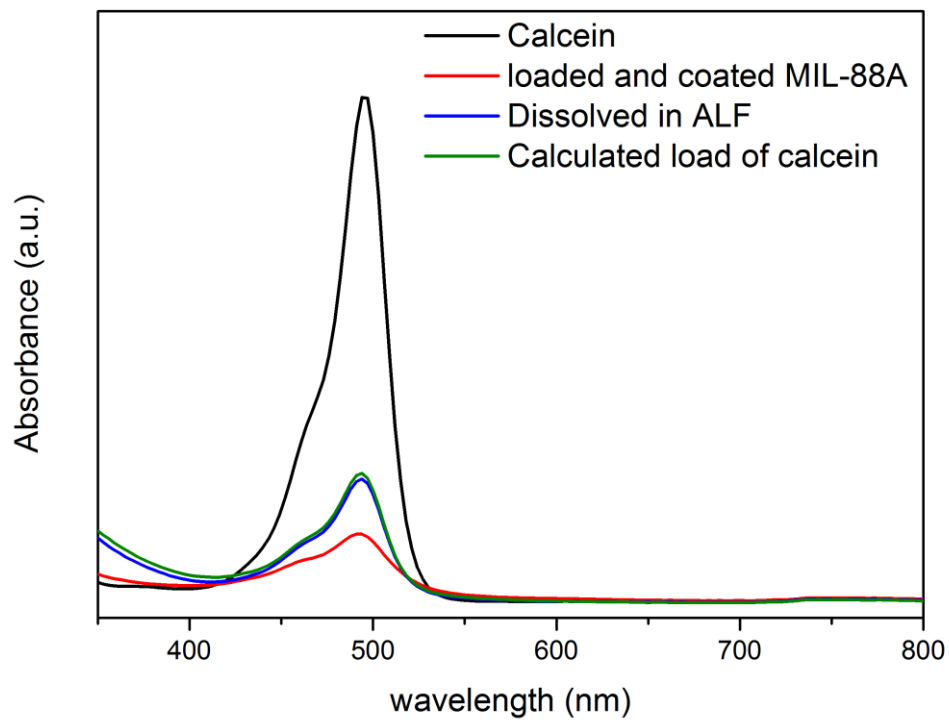


Figure 4.27: UV/Vis measurements of several different calcein and particle solutions

HDAC1 Assay to determine the SBHA loading

Due to SBHA being hardly detectable with standard analytical techniques, an HDAC1 activity assay was performed. SBHA is an inhibitor of HDAC1. The assay kit used was the HDAC1 Inhibitor Screening Assay Kit from Cayman Chemical. For the quantification different dilutions of SBHA were prepared and tested on their inhibition of HDAC1 and then compared to the inhibition of dissolved SBHA loaded particles to determine how much SBHA was loaded into the particles (Figure 4.28).

From that we calculated the theoretical dilution at 50% inhibition for SBHA (1:42.2) and the SBHA loaded MIL-88A NPs (1:5.40). From these dilutions and the concentrations of the stock solutions we could calculate the how much SBHA (4.835 μg) and SBHA loaded particles (185 μg) were needed to inhibit 50% of the available HDAC1. By comparing these numbers we can then calculate the loading capacity: 13.1 % of the initially available 1 mM SBHA or 2.61 wt% in relation to the weight of the MOF NPs were loaded into the particles.

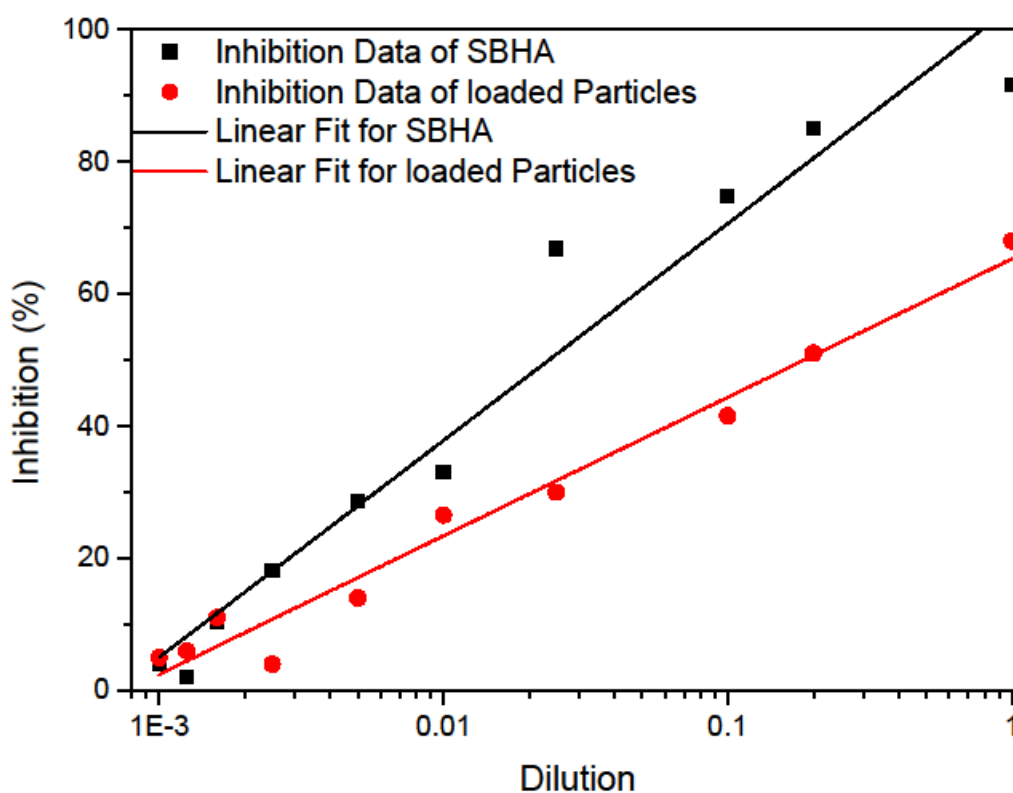


Figure 4.28: Graphical representation of the results of the HDAC1 Inhibition Assay.

High-Content Quantification Experiments

96-well plates from Costar were seeded with 5000 HeLa cells per well and a volume of 100 μL DMEM medium. After incubating for 1 day at 37 $^{\circ}\text{C}/5\%$ CO_2 the particles were added. Each concentration (0, 10, 20, ..., 140, 150 $\mu\text{g}/\text{mL}$) was tested in three different wells. Before the measurement the plate was washed twice with 100 μL per well PBS to remove dead cells and excess calcein. Both transmission and GFP channel images were recorded. Four images were recorded per well. The images were evaluated with the MetaXpress software, by counting the number of cells showing release and the total number of cells and calculating the release percentage from these numbers.

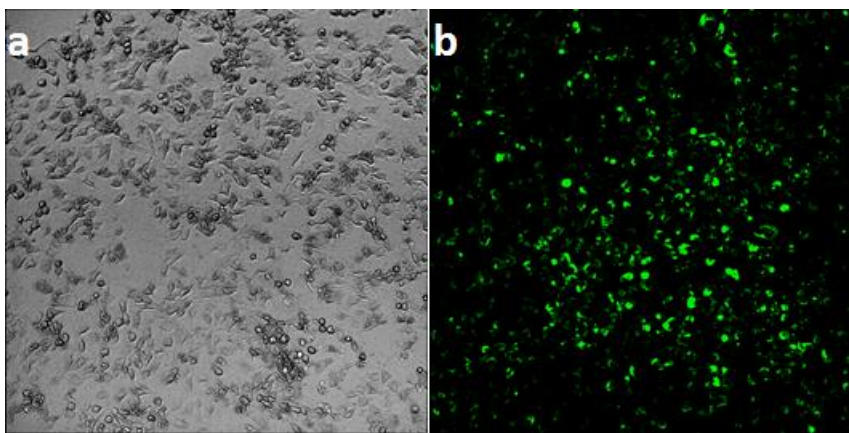


Figure 4.29: Sample images as used for the quantification measurements: a) Transmission image used to count the total number of cells; b) Fluorescence image used to count the number of cells showing release.

4.4.6 MTT-assays

5000 cells were seeded in each well of a 96-well plate and covered with 100 μL DMEM. After 1 day of incubation at 37 $^{\circ}\text{C}/5\%$ CO_2 , the particles were added (0, 2, 4, 8, 20, 60, 100, 140 $\mu\text{g}/\text{mL}$). Each concentration was tested in triplicate. The supernatant was recovered via centrifugation (14000 rpm, 5 min) from a 1mg/mL loaded exosome coated MIL-88A NP stock solution after one day of incubation in PBS. The MTT-assays were performed after 3 and 4 days of incubation.

The MTT reagent concentration used was 0.5 mg reagent per 1 mL medium. The sample was washed three times with 100 μL HBSS buffer per well before 100 μL of the reagent solution was added in each well. After two hours of incubation at 37 $^{\circ}\text{C}/5\%$ CO_2 the wells were emptied and the whole plate was frozen at -80 $^{\circ}\text{C}$ for an hour. After defrosting 100 μL DMSO was added to each well and after dissolving any remaining crystals the MTT-assays were performed. MTT-assays were performed in triplicate and repeated on at least three different days.

In addition to the coated variants uncoated Mil-88A NPs were also investigated (Figure 4.30). They showed low toxicity with cell viabilities of over 70 %.

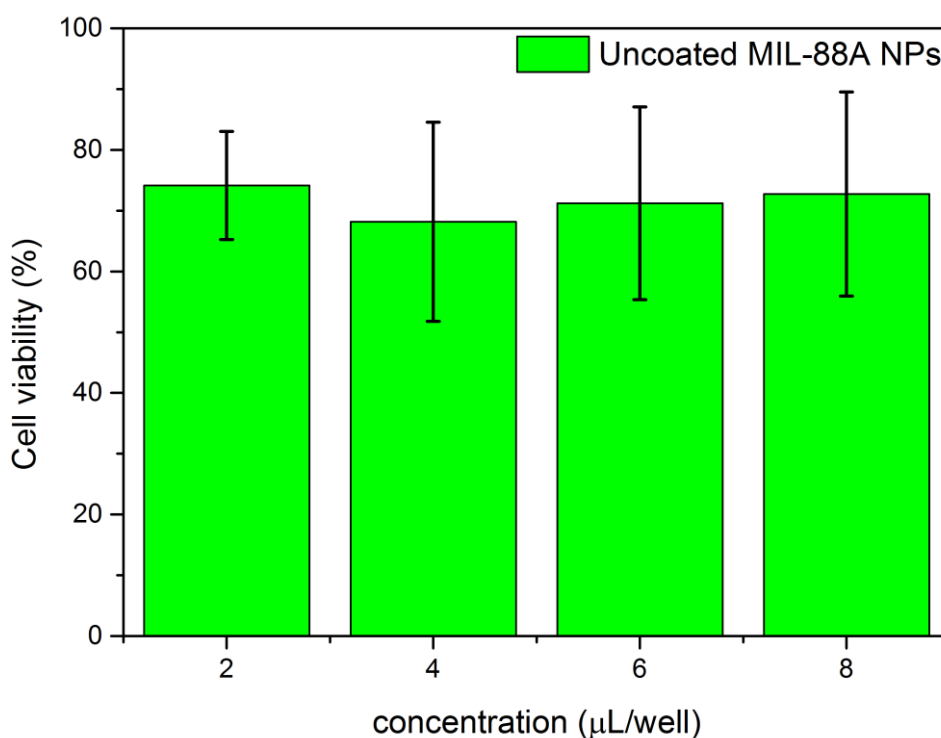


Figure 4.30: MTT Assay of HeLa cells after 3 days of incubation with uncoated MIL-88A NPs. The error bars signify the SD.

To investigate the efficacy of pure SBHA, a 1 mM solution of SBHA in PBS was added to HeLa cells in increasing amounts (Figure 4.31). Lower concentrations, below 20 $\mu\text{L}/\text{mL}$, proved to be nontoxic, while higher concentrations lead to very low cell viability of about 5%. Comparing the effect of free SBHA with that of transported SBHA shows that the transported SBHA possesses a higher efficacy and leads to more cell deaths. 1 μL of SBHA in PBS corresponds to 0.204 mg of pure SBHA.

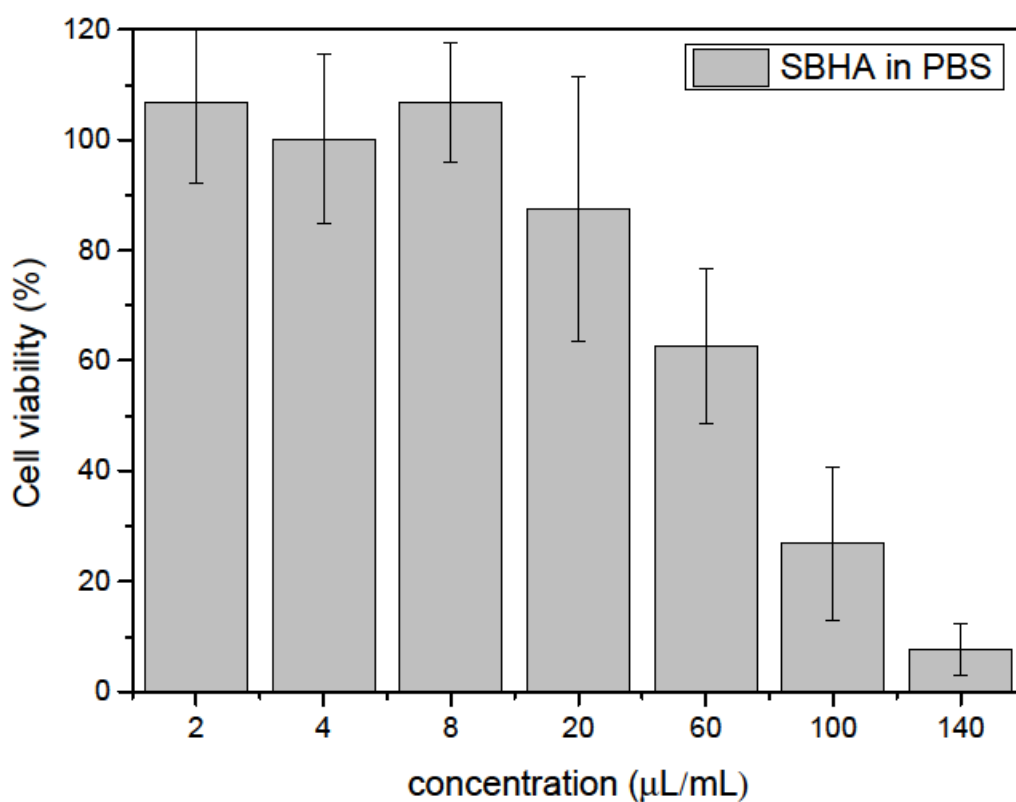


Figure 4.31: MTT Assay of HeLa cells after three days of incubation with a 1 mM solution of SBHA in PBS. The error bars signify the SD.

4.4.7 Cell targeting

Beyond potential inherent targeting through proteins naturally inserted into the exosomes, our exosome coated MOF NPs offer the option to additionally functionalize the exosome shell as has been shown earlier with liposomal coatings around NPs.^{29, 31} This can be done via spontaneous insertion of lipids functionalized with a targeting moiety such as folate. Folate receptors are known to be overexpressed on cancer cells and thus are a common receptor used for targeting. To show this optional targeting via inserted ligands, we added such folate functionalized lipids into the exosomal coating of the MOF NPs and performed targeting experiments

The MIL-88A NPs were loaded and coated as described previously, and then incubated overnight with 1,2-dipalmitoyl-sn-glycero-3-phosphoethanolamine-N-(6-((folate)amino)hexanoyl) to replace some of the lipids in the exosome coating.³¹ The modified particles are not taken up in media saturated with folate, but are efficiently taken up in HeLa cells incubated with folate-free DMEM (Figure 4.32 Figure 4).

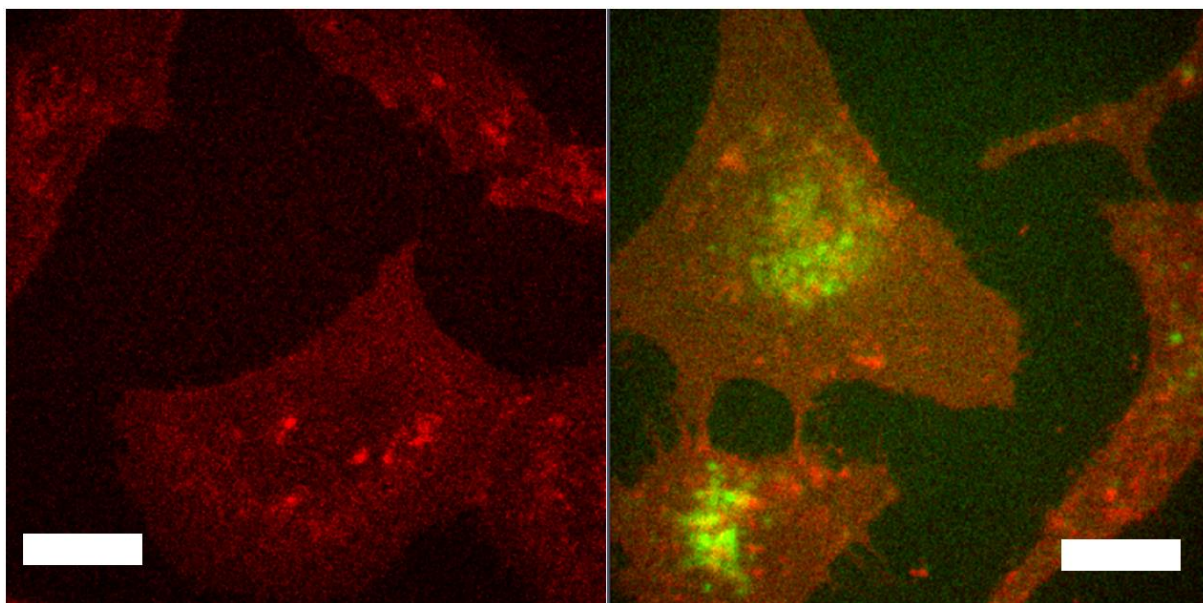


Figure 4.32: No uptake of folate modified LipMIL particles in HeLa cells incubated in a folate rich media (left). Uptake of folate modified LipMIL particles in HeLa cells in normal folate free DMEM. The scale bars in both images represent 15 μm .

4.5 References

1. Wuttke, S., Lismont, M., Escudero, A., Rungtaweeworanit, B. & Parak, W.J. Positioning metal-organic framework nanoparticles within the context of drug delivery – A comparison with mesoporous silica nanoparticles and dendrimers. *Biomaterials* **123**, 172-183 (2017).
2. He, C., Liu, D. & Lin, W. Nanomedicine Applications of Hybrid Nanomaterials Built from Metal–Ligand Coordination Bonds: Nanoscale Metal–Organic Frameworks and Nanoscale Coordination Polymers. *Chem. Rev.* **115**, 11079-11108 (2015).
3. Falcaro, P. et al. Application of metal and metal oxide nanoparticles@MOFs. *Coord. Chem. Rev.* **307**, 237-254 (2016).
4. Zhou, H.-C., Long, J.R. & Yaghi, O.M. Introduction to Metal–Organic Frameworks. *Chemical Reviews* **112**, 673-674 (2012).
5. H. C. Zhou, S.K. *Chem. Soc. Rev.* **43**, 5415 (2014).
6. Anna G. Slater, A.I.C. *Science* **348** (2015).
7. Zimpel, A. et al. Imparting Functionality to MOF Nanoparticles by External Surface Selective Covalent Attachment of Polymers. *Chemistry of Materials* **28**, 3318-3326 (2016).
8. Chalati, T., Horcajada, P., Gref, R., Couvreur, P. & Serre, C. Optimisation of the synthesis of MOF nanoparticles made of flexible porous iron fumarate MIL-88A. *J. Mater. Chem.* **21**, 2220-2227 (2011).
9. Horcajada, P. et al. Porous metal-organic-framework nanoscale carriers as a potential platform for drug delivery and imaging. *Nat Mater* **9**, 172-178 (2010).
10. van Meer, G., Voelker, D.R. & Feigenson, G.W. Membrane lipids: where they are and how they behave. *Nat Rev Mol Cell Biol* **9**, 112-124 (2008).
11. Allen, T.M. & Cullis, P.R. Liposomal drug delivery systems: From concept to clinical applications. *Advanced Drug Delivery Reviews* **65**, 36-48 (2013).
12. Cauda, V. et al. Colchicine-Loaded Lipid Bilayer-Coated 50 nm Mesoporous Nanoparticles Efficiently Induce Microtubule Depolymerization upon Cell Uptake. *Nano Lett.* **10**, 2484-2492 (2010).
13. Wuttke, S. et al. MOF nanoparticles coated by lipid bilayers and their uptake by cancer cells. *Chemical Communications* **51**, 15752-15755 (2015).
14. Schloßbauer, A. et al. Cascaded Photoinduced Drug Delivery to Cells from Multifunctional Core–Shell Mesoporous Silica. *Advanced Healthcare Materials* **1**, 316-320 (2012).
15. de Bruin, K.G. et al. Dynamics of photoinduced endosomal release of polyplexes. *Journal of Controlled Release* **130**, 175-182 (2008).
16. Yang, Y. et al. Lipid coated mesoporous silica nanoparticles as photosensitive drug carriers. *Physical Chemistry Chemical Physics* **12**, 4418-4422 (2010).
17. Febvay, S., Marini, D.M., Belcher, A.M. & Clapham, D.E. Targeted Cytosolic Delivery of Cell-Impermeable Compounds by Nanoparticle-Mediated, Light-Triggered Endosome Disruption. *Nano Letters* **10**, 2211-2219 (2010).
18. Ludwig, A.-K. & Giebel, B. Exosomes: Small vesicles participating in intercellular communication. *The International Journal of Biochemistry & Cell Biology* **44**, 11-15 (2012).
19. Bang, C. & Thum, T. Exosomes: New players in cell–cell communication. *The International Journal of Biochemistry & Cell Biology* **44**, 2060-2064 (2012).
20. Ha, D., Yang, N. & Nadihe, V. Exosomes as therapeutic drug carriers and delivery vehicles across biological membranes: current perspectives and future challenges. *Acta Pharmaceutica Sinica B* **6**, 287-296 (2016).
21. Tibbitt, M.W., Dahlman, J.E. & Langer, R. Emerging Frontiers in Drug Delivery. *Journal of the American Chemical Society* **138**, 704-717 (2016).
22. Liu, J., Jiang, X., Ashley, C. & Brinker, C.J. Electrostatically Mediated Liposome Fusion and Lipid Exchange with a Nanoparticle-Supported Bilayer for Control of Surface Charge, Drug Containment, and Delivery. *J. Am. Chem. Soc.* **131**, 7567-7569 (2009).
23. Chalati, T., Horcajada, P., Gref, R., Couvreur, P. & Serre, C. Optimisation of the synthesis of MOF nanoparticles made of flexible porous iron fumarate MIL-88A. *J. Mater. Chem.* **21**, 2220-2227 (2011).
24. Hirschle, P. et al. Exploration of MOF nanoparticle sizes using various physical characterization methods - is what you measure what you get? *CrystEngComm* **18**, 4359-4368 (2016).
25. Andrew Lin, K.-Y., Chang, H.-A. & Hsu, C.-J. Iron-based metal organic framework, MIL-88A, as a heterogeneous persulfate catalyst for decolorization of Rhodamine B in water. *RSC Advances* **5**, 32520-32530 (2015).

26. McKinlay, A.C. et al. Nitric Oxide Adsorption and Delivery in Flexible MIL-88(Fe) Metal–Organic Frameworks. *Chem. Mater.* **25**, 1592-1599 (2013).
27. Yang, T. et al. Exosome Delivered Anticancer Drugs Across the Blood-Brain Barrier for Brain Cancer Therapy in Danio Rerio. *Pharmaceutical Research* **32**, 2003-2014 (2015).
28. Rani, S., Ryan, A.E., Griffin, M.D. & Ritter, T. Mesenchymal Stem Cell-derived Extracellular Vesicles: Toward Cell-free Therapeutic Applications. *Molecular Therapy* **23**, 812-823 (2015).
29. Mackowiak, S.A. et al. Targeted Drug Delivery in Cancer Cells with Red-Light Photoactivated Mesoporous Silica Nanoparticles. *Nano Letters* **13**, 2576-2583 (2013).
30. Ashley, C.E. et al. The targeted delivery of multicomponent cargos to cancer cells by nanoporous particle-supported lipid bilayers. *Nat Mater* **10**, 389-397 (2011).
31. Introduction to Metal–Organic Frameworks. *Chem. Rev.* **112**, 673-674 (2012).

Chapter 5

Liposome coated iron

fumarate metal-organic

framework nanoparticles for

combination therapy

Bernhard Illes, Stefan Wuttke and Hanna Engelke

This chapter was published in Nanomaterials 2017, 7 (11), 351.

5.1 Introduction

Metal-organic frameworks (MOFs) are a uniquely valuable class of materials in that their structure and composition can be controlled at the atomic level. As the name suggests, MOFs are made of metal ions or clusters (inorganic), and organic molecular building units, assembling together into crystalline solids.¹⁻⁴ This construction from building units and a nearly endless pool of different organic and inorganic units to choose from give MOFs their incredible chemical flexibility and give us control on the atomic level. Each possible building unit contributes its own properties and features, which allows us to make MOFs that have very specific degrees of porosity (pore and window size), surface area, functionality and biocompatibility.^{5, 6} All these attributes make them highly interesting to develop nanostructured smart drug delivery systems capable of bypassing extra- and intracellular barriers.⁷⁻¹⁸ In the last 5 years, a number of pioneering studies have been reported that highlight the suitability of MOF nanocarriers as a new type of platform for drug delivery.^{9, 19-27} So far, these reports mainly focused on the delivery of single active agents (e.g. one drug), whereas their application to deliver “cocktails” of drugs is still largely unexplored.^{7, 28} Current chemotherapy faces the challenge that tumours quickly become resistant to a drug during treatment. One possible solution to this problem is the administration of multiple drugs at once to fight resistant cancer strains and prevent formation of new resistances.²⁹⁻³² This combination therapy has proven to be more effective than single-drug therapies, but faces the challenge that each drug has different physicochemical properties, which leads to heterogeneous pharmacokinetics and tissue distribution. In this respect, the use of nanocarriers opens up the possibility to co-encapsulate multiple drugs and thus synchronise their delivery to the cancer cells.²⁹⁻³¹ MOF nanoparticle platforms are especially interesting due to their hybrid nature relying on the synergistic combination of inorganic and organic chemistry.⁷ This allows the creation of chemically diverse internal pore systems able to incorporate drugs with different physicochemical properties. First pioneering studies reporting on such MOF platforms for the delivery of several drugs are very encouraging.³²⁻³⁵ One of them even reports on an enhanced efficiency in tumor reduction due to dual drug delivery with MOF nanoparticles.³⁵ While this study shows great promise, the employed nanoparticles were not fully encapsulated. Such an encapsulation would be desirable though, to prevent the observed drug leakage and to enhance the stability.^{36, 37}

In this paper, we demonstrate that MOF nanoparticles can be simultaneously loaded with multiple drugs. Furthermore, the drug carriers can then be coated with a lipid shell acting as a temporary seal for the encapsulated drugs, and allowing control of interactions with intracellular fluids. The successful synthesis of liposome coated MOF nanoparticles is based on a simple fusion method. The resulting particles, once loaded, show no premature leakage. As opposed to a previous study²⁴ the MOF nanoparticles presented here also show an efficient intracellular release. In our study we focus on iron-based MOF nanoparticles, namely MIL-88A, which are composed of iron(III) and fumaric acid, both naturally occurring in the body.³⁸ These particles were loaded with SBHA alone, or the two drugs irinotecan and floxuridine together. The two latter drugs were chosen, because past studies have shown an improved efficacy in preclinical tumour models³⁹ making them interesting candidates for the use in combination therapy. Liposomes loaded with both drugs in a 1:1 ratio are currently in an ongoing clinical trial under the name CPX-1.⁴⁰

5.2 Results and Discussion

5.2.1 MOF nanoparticle synthesis and their lipid coating

MIL-88A nanoparticles were synthesized using a microwave approach before being loaded and then coated with DOPC (1,2-dioleoyl-sn-glycero-3-phosphocholine) derived liposomes using the fusion method after loading⁴¹ (see Appendix for characterisation). The liposome coated MIL-88A nanoparticles, further referred to as Lip-MIL-88A, was used to carry several drugs and investigated towards its loading capacity, release behaviour and effectiveness at loading multiple drugs at once and thus a possible application in combination therapy.

5.2.2 Loading capacity

The first step was to investigate the drug loading capacity of MIL-88A. For this purpose MIL-88A nanoparticles were loaded with irinotecan and floxuridine in different ratios through soaking in 1 mM aqueous solutions of the biotherapeutics, before coating them with liposomes. These particles were then investigated via UV/Vis spectroscopy (Figure 5.1) to determine the loading capacity. The absorption maximum of irinotecan at 360 nm was used as the basis for the calculations. Particles loaded with different ratios of Irinotecan were examined and compared to the UV/Vis spectrum of a pure irinotecan solution to calculate the amount of drug loading. For this 1 mg of MIL-88A nanoparticles were suspended in 1 mL of a 1 mM solution of irinotecan. The amount of irinotecan in the MIL-88A nanoparticles was

quantified by UV/Vis measurements yielding a loading capacity of 21 wt% relative to the nanoparticle weight (205 μg) for loading only irinotecan and 10.3 wt% (102 μg) of irinotecan when a 0.5 mM irinotecan and 0.5 mM floxuridine solution (further referred to as 1:1) is used for the loading. Similarly, the loading capacity of floxuridine was determined to be 3.61 wt% for a 1mM solution of floxuridine only and in the mixtures with irinotecan it was reduced by the respective factor of dilution (measurements see Appendix). Thus, the nanoparticles can successfully be loaded with both drugs at the same time yielding a ratio of the mixture as provided in the loading solution weighted by the loading capacity of the pure drugs.

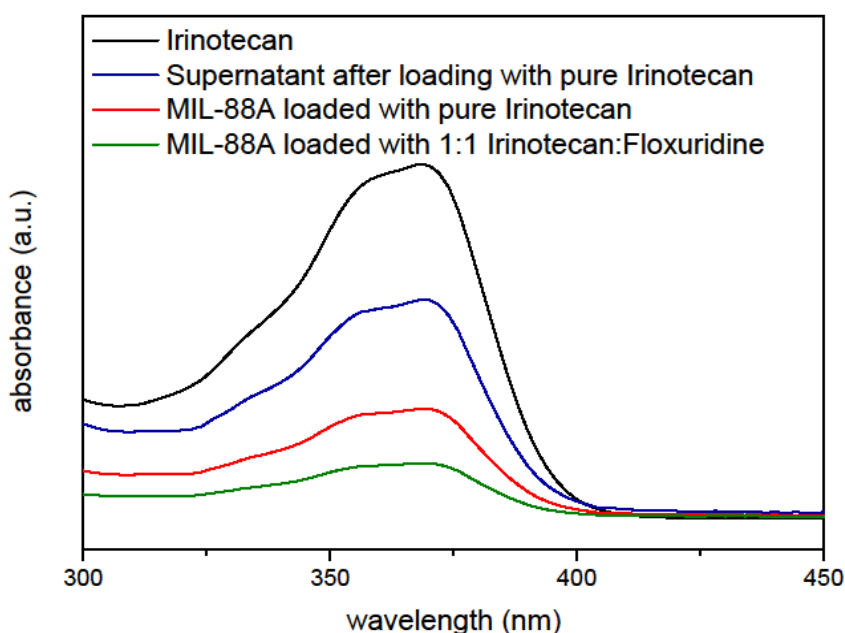


Figure 5.1: UV/Vis measurements to determine the loading capacity of Lip-MIL-88A nanoparticles for Irinotecan.

5.2.3 Fluorescence Release Experiments

To further investigate the loading and especially the release behaviour of the Lip-MIL-88A particles, as well as to test for possible leakage of the cargo from the particles, fluorescence release experiments were performed (Figure 5.2Figure 5.). The particles were loaded with the membrane impermeable dye calcein as a fluorescence marker. An aqueous solution of the calcein loaded Lip-MIL-88A was used as a control and a test for possible leakage. To guarantee a release, a second sample was treated with triton X-100 dissolving the liposome coating. In addition artificial lysosomal fluid (ALF)⁴² was used to simulate the environment the particles encounter in the lysosome after entering the cell. And finally the uncoated particles were also

measured in water. The coated particles in pure water show no release even after several hours, while the uncoated particles exhibit a fluorescence increase and thus leakage, proving the effectiveness of the liposome coating in preventing side effects caused by leakage. Both the triton X-100 and ALF treated samples show a clear release of the calcein from the particles. The large difference in the strength of the release is caused by the complete dissolution of the particle through the ALF in comparison to only opening the membrane in the case of triton X-100. This dissolution of the particles in ALF leads to a full release of the cargo inside the cell.⁷ The difference between the uncoated particles and those treated with Triton 100-X can be explained by the lipid coating. For the uncoated particles a steady release of calcein is observable as the calcein is released without hindrance. That the Triton 100-X treated particles show a strong release in the beginning is most likely due to the calcein detaching from the MOF, but being contained by the lipid membrane, as soon as the membrane is punctured this already freed calcein is released at once leading to the strong initial increase in fluorescence. The difference in the amount of released dye in saturation might be either due to more efficient encapsulation facilitated by the lipid bilayer or due to triton possibly interfering with the interaction between particle and calcein leading to an enhanced release. The release behaviour of the investigated drugs might differ from that of calcein due to its carboxylate groups, which allow it to attach to the surface of the MOF and might lead to a slower release. The general behavior of the particles in the different media should however stay unaffected.

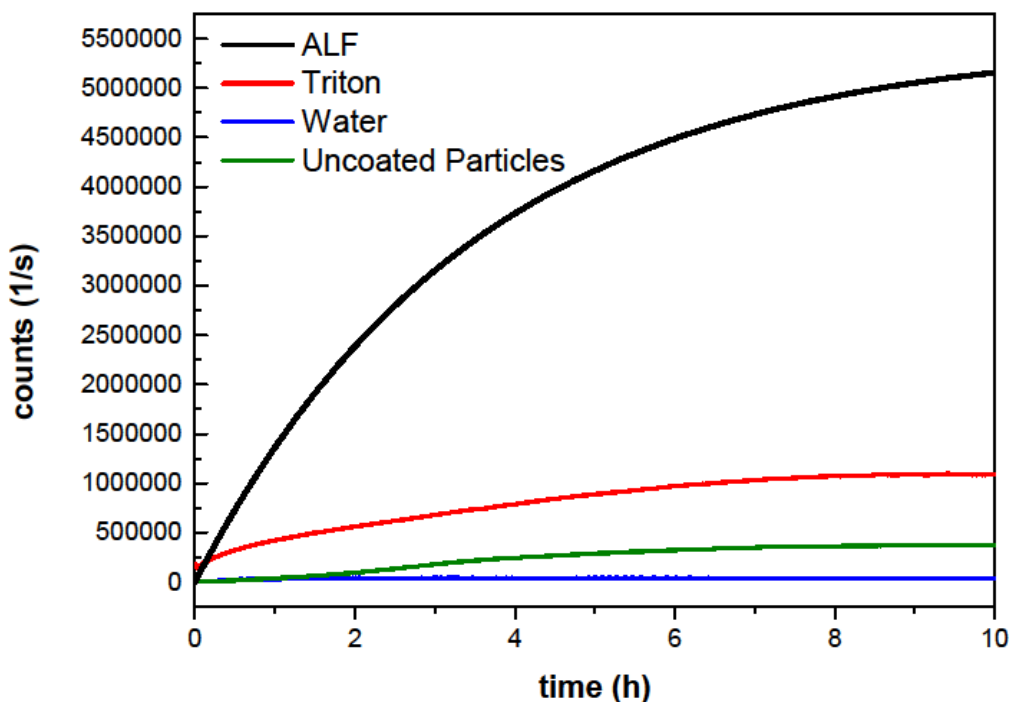


Figure 5.2: Fluorescence release measurement of Lip-MIL-88A in various solvents. Water (blue) and water with addition of Triton X-100 (red), as an additional control, as well as ALF (black), to simulate the environment of the lysosome. As proof that the liposomes prevent the leakage of the cargo uncoated particles (green) were also measured.

5.2.4 Cell Release Experiments

To investigate the cell uptake of the nanoparticles and their drug release behaviour inside cells, especially if the strong release observed after exposure to ALF also takes place in the actual cell environment, Lip-MIL-88A particles, were again loaded with calcein as a model drug and incubated in HeLa cells. As it can be seen in Figure 5.3 after two days the particles were taken up by the cells, but no release of the calcein could be observed yet. After three days of incubation, release of calcein from the particles without any outside stimulus could be observed. Thus Lip-Mil-88A avoids any dangers caused by potentially harmful release triggers, reducing the potential side effects. The observed release can be explained by the results from the fluorescence release experiments: The particles are taken up via endocytosis and while they are not in the lysosomal environment yet, they show no release. Once they are in the lysosomal environment, the particles dissolve leading to a release of their cargo.¹⁰

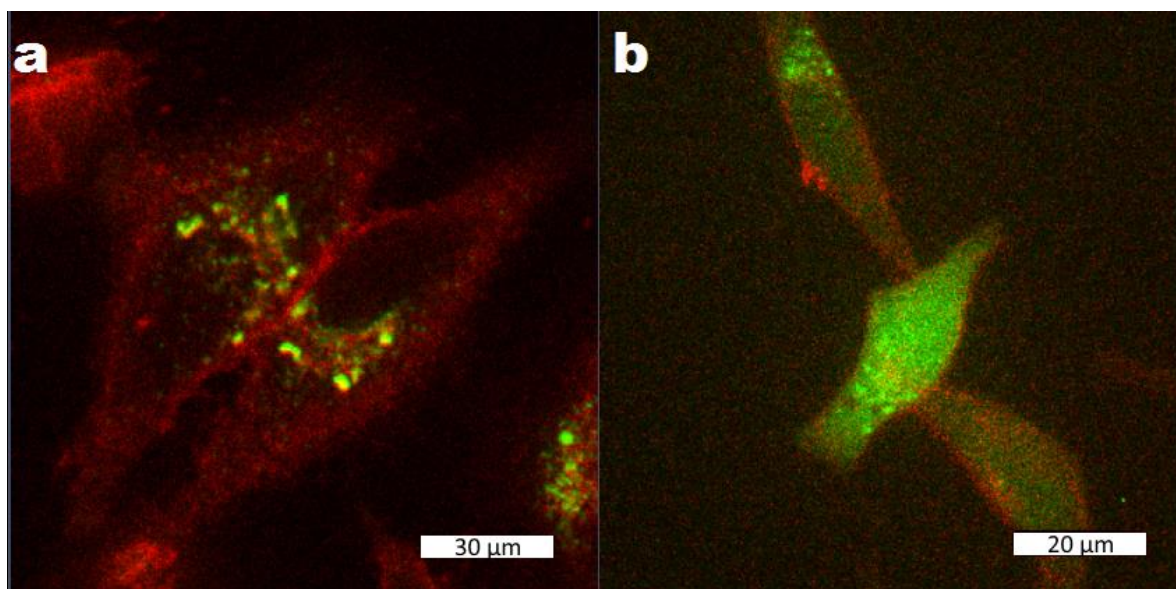


Figure 5.34. Liposome coated MIL-88A nanoparticles loaded with calcein after two (a) and three days (b) of incubation with HeLa cells. The cells have been marked with CellMask Orange. The scale bars correspond to 30 μm (a) and 20 μm (b).

5.2.5 Single Drug MTT Assays

The liposome coated MIL-88A nanoparticles were loaded with subaero hydroxamic acid (SBHA), a histone deacetylase inhibitor, which leads to cell death, as a model drug and to further test its drug carrying capabilities. The particles were then incubated in HeLa cells for 3 to 4 days and MTT-Assays were performed (Figure 5.4 left). The SBHA loaded Lip-MIL-88A proved effective against the HeLa cells, showing cell viabilities of only 15% after 4 days of incubation. The particles proved to be able to safely deliver their cargo to the target cells showing an IC_{50} of about 15 $\mu\text{g}/\text{mL}$ of SBHA loaded Lip-MIL-88A. To investigate if the cell deaths could be caused by leakage of SBHA from the drug carrier, the supernatant was collected and also investigated via MTT-Assay (Figure 5.4 right). These measurements show that no leakage occurred as the cells are still viable even at high concentrations of the supernatant. The loading capacity of this system for SBHA was determined to be 2.90 wt%

with respect to the particles (see Appendix). This further corroborates the general suitability of Lip-MIL-88A as a drug delivery vehicle.

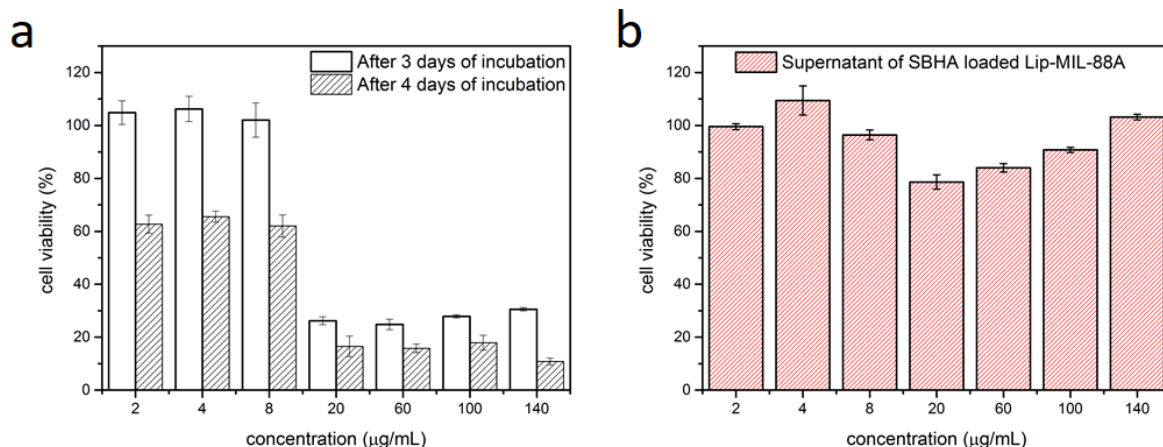


Figure 5.4: a) MTT Assay of HeLa cells incubated with Lip-MIL-88A nanoparticles loaded with SBHA after three and four days of incubation. b) MTT Assay of HeLa cells incubated with the supernatant of the Lip-MIL-88A suspension after four days. The error bars represent the standard deviation.

5.2.6 Multi Drug MTT-Assays

Next, the particles were loaded with both irinotecan and floxuridine in different ratios (Table 5.1) to determine both the effectiveness of each single drug loaded on the particles and the effectiveness of the mixtures. For this purpose particles loaded with pure irinotecan and floxuridine and different ratios of both (1:3, 1:1 and 3:1, with the ratios referring to the molar ratios of the drugs in the loading solution) were incubated with cells. The MTT assays show that both irinotecan and floxuridine could be successfully loaded into the Lip-MIL-88A, leading to a significantly reduced cell viability of 34.6% with an IC_{50} of 4 µg/mL for the irinotecan loaded version. Floxuridine had a significantly lower efficiency that did not even reach a 50% reduction of cell viability within the measured amounts of particle administration. The mixtures of them were also tested (Table 4.1), with the 3:1 ratio showing the best results achieving a comparably low cell viability to irinotecan alone. All tested ratios aside from pure floxuridine reduce the cell viability to 30-40% at the highest tested concentration of 140 µg/mL, while pure floxuridine only manages to reach a reduction to 60% at this particle concentration. This is in accordance to the 1:3 irinotecan:floxuridine ratio being the least effective of the investigated mixtures.

Table 5.2. Comparison of the different MIL88A loadings and their IC₅₀ values

	Irinotecan	3:1 Iri Floxu	1:1 Iri Floxu	1:3 Iri Floxu	Floxuridine
Cell viability at 140 µg/mL (%)	34.6	28.6	30.6	37.9	60.5
I _c 50 (µg/mL)	40	80	80	80	120

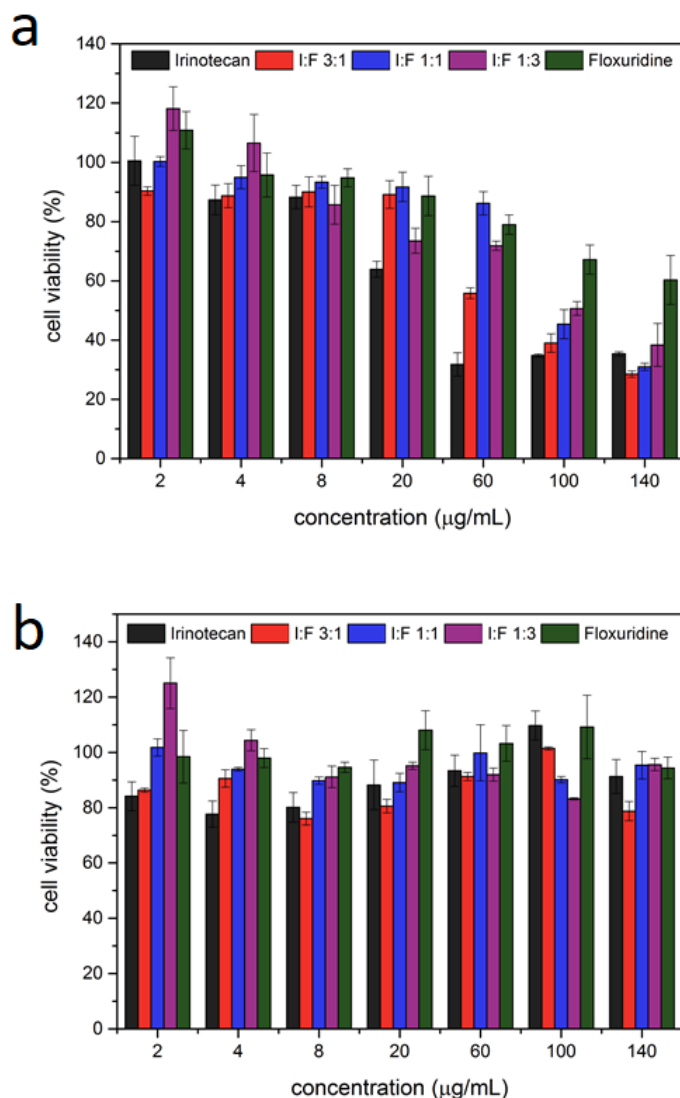


Figure 5.5: a) MTT-Assay of Lip-MIL-88A particles loaded with different ratios of irinotecan/floxuridine incubated in HeLa cells for three days. The error bars represent the standard deviation. b) MTT-Assay of the supernatant of Lip-MIL-88A particles loaded with different ratios of irinotecan/floxuridine after incubation in HeLa cells for three days. The error bars represent SD.

To rule out leakage of the drugs as the responsible factor for the observed reduction in cell viability the particles were stored in PBS for several days before the supernatant was collected and tested for its toxicity (Figure 5.5b) showing no significant decrease in cell viability. With this we can exclude drug leakage from the particles as the reason for the observed cell death. Thus, the liposome-coated MOF nanoparticles can serve as a drug delivery system for dual

therapy preventing leakage and taking advantage of the delivery of two different drugs. Although the combinations of drugs yield lower efficiencies than irinotecan alone due to the lower efficiency of floxuridine, the option of dual drug delivery with these nanoparticles shows great promise in the fight against resistances via combinatorial drug application.

5.3. Conclusion

In conclusion the Lip-MIL-88A platform is a promising tool for use as a platform for combination therapy. It could readily take up a significant amount of biologically active agents (20 wt%) and showed a promising release of its cargo. Due to the liposome coating no leakage of the cargo could be observed. In cell experiments Lip-MIL-88A nanoparticles were readily taken up by cells and showed a significant, intracellular release after three to four days of incubation. Different drugs (SBHA, irinotecan and floxuridine) were successfully loaded into the particles and the drug delivery system enables intracellular release profiles. The successful and uncomplicated loading as well as the effective intracellular release of drugs, compared to normal liposome loading procedures, is a promising start for future applications in combination therapy and could as such contribute to improve cancer chemotherapy.

5.4. Materials and Methods

5.4.1. UV/Vis Measurements

The UV/Vis measurements were performed on a Lambda 1050 UV/Vis/NIR spectrometer from *Perkin Elmer*. The software used to record the measured spectra was *Perkin Elmer UVWinLab*. For the measurements, the loaded coated particles were dissolved in ALF, to facilitate the release of all their cargo. 1 mL of this solution was then diluted with 2 mL H₂O yielding a total of 3 mL and measured in a quartz cuvette. For the pure drugs 1 mL of the aqueous solution was diluted with 1 mL H₂O and 1 mL ALF.

5.4.2. Fluorescence Microscopy

The fluorescence microscope images were recorded with a *Zeiss Observer SD* spinning disk confocal microscope using a Yokogawa CSU-X1 spinning disc unit and an oil objective with 63x magnification and BP 525/50 and LP 690/50 filters. The setup was heated to 37 °C and a CO₂ source was provided to keep the atmosphere at 5% CO₂. For both excitation of the calcein and the cell marker a laser with a wavelength $\lambda = 488$ nm was used. The images were processed with the *Zen* software by *Zeiss* to optimize contrast.

5.4.3. Fluorescence Spectroscopy

The fluorescence spectroscopy experiments were recorded with a MD-5020 setup from *PTI Photon Technology International*. The software *Felix32* was used for recording and evaluating the measured data. For the experiments hollow caps were filled with 50 μ L of a 1 mg/mL particle stock solution. Depending on the experiment 100 μ L of water or ALF or 90 μ L water and 10 μ L 20%triton X-100 solution were added, before the caps were sealed with a dialysis membrane and placed into cuvettes filled with water together with a stirring rod. The measurement temperature was 37°C with an excitation wavelength of 495 nm and an emission wavelength of 512 nm.

5.4.4. Cell culture

All cell experiments were prepared in a *Hera-Safe* cell culture unit from *Heraeus*. The cells were incubated at 37 °C/5 % CO₂ in *Hera Cell incubators* also from *Heraeus*. Cells were grown in DMEM with 10% FBS and 1% PenStrep.

5.4.5. MTT Assays

The MTT-Assays were performed with a *Spectra Fluor Plus* from *Tecan* and were then evaluated with *Excel 2010 and Origin*. 5000 cells were seeded per well and incubated together with 100 µL DMEM (10%FBS, 1% PenStrep) for 1 day before the particles were added. Each concentration was tested on three different days and on each day in triplicate. After the allotted incubation time the plates were washed with HBSS to remove dead cells, before the MTT reagent diluted in DMEM (0.5 mg/mL) was added. After two hours of incubation the MTT reagent solution was removed from the cells and the cells were frozen at -80°C for 0.5 h. Before the measurement 100 µL DMSO were added to each well.

5.4.6. Synthesis of the uncoated and coated MIL-88A nanoparticles

Synthesis of MIL-88A NPs

MIL-88A nanoparticles were synthesized in a microwave assisted approach based on the results of Chalati *et al* [38]. In this synthesis route an aqueous solution of FeCl₃ · 6 H₂O (1.084 g, 4.01 mmol) and fumaric acid (485 mg, 4.18 mmol) are given to water (20 ml, Milli-Q). The reaction mixture was stirred until the metal salt was completely dissolved. The reaction mixture was then given into a Teflon tube (80 ml) and placed into a microwave oven (*Synthos 3000, Anton-Paar*) along with 3 additional vessels. Two of these vessels are filled with water (20 ml, Milli-Q), the third vessel is filled with an aqueous FeCl₃ (20 ml, 1.084 g, 4.01 mmol) and is used to monitor the reaction progress. The vessels were heated under stirring with the sequence shown in Table 4.1:

Table 5.3: MW Heating program for the MIL-88(A) NPs synthesis

Heating	Dwelling	Cooling
30 s	5 min	45 min
To 80 °C	80 °C	To RT

To remove residual reactants the sample was subsequently washed via centrifugation (7840 rpm, 20 min) and redispersion of the pellet in ethanol (20 ml). This washing cycle was repeated 3 additional times. To remove also bulk material formed during the reaction, the dispersion was then centrifuged 3 times (3 min, 3000 rpm) and the pellet fraction of the product discarded.

Preparation of the liposome coating solution

A 1 mg/mL PBS solution of DOPC was prepared and extruded through an extruder with a 100 nm pore sized membrane 11 times for cleaning.

Preparation of the loaded and coated particles

1 mg of MIL-88A NPs were suspended in 1 mL of a 1 mM solution of calcein, suberohydroxamic acid (SBHA), irinotecan or floxuridine and incubated overnight for loading. Next they were centrifuged for 5 min at 14000 rpm, to discard the supernatant and the pellet was dissolved in 0.2 mL of the liposome coating solution and 0.2 mL water and incubated for 2 h. The particles were then centrifuged (5 min at 14000 rpm) and redispersed in 1 mL PBS after washing several times.

For the preparation of the particles loaded with both irinotecan and floxuridine the MIL-88A particles were immersed in mixtures of 1 mM irinotecan and floxuridine solutions in the desired ratios, before following the same coating and washing procedure as outlined above.

5.5 Appendix

5.5.1 Additional Methods

X-Ray Diffraction

X-ray diffraction experiments were performed on the initial MIL-88A NPs. The samples were measured on a *STOE Transmissions-Diffraktometer System STADI P* operating in transmission mode. The setup is using $\text{CuK}_{\alpha 1}$ -radiation with a wavelength $\lambda = 015418$ nm. The resulting diffraction pattern was evaluated using the software package *WinXPOW RawDat v3.0.2.5* and *WinXPOW PowDat_n v3.0.2.7*.

Scanning Electron Microscopy (SEM)

All SEM micrographs were recorded with a *Helios NanoLab G3UC (FEI)* operating at 5 kV. During sample preparation an ethanolic NP dispersion was dried on a carbon film placed on an aluminum sample holder. The sample was stored overnight to evaporate the solvent followed by carbon sputtering prior to the measurement. For evaluation of the SEM micrographs the software *ImageJ v1.49*. was used.

Transmission Electron Microscopy (TEM)

The TEM micrographs of the sample particles were taken on a *Titan Themis (Fei)* that was operated at an acceleration voltage of 300 kV. For sample preparation, an ethanolic NP solution was dried overnight on a carbon-coated copper grid.

Thermogravimetric Analysis (TGA)

A dried sample of MIL-88A NPs (3.125 mg) was heated using a *TASC 414/4 (Netzsch)*. The sample was heated under synthetic air at 10 °C/min up to 900 °C. The resulting data was evaluated using the software *Proteus v4.3*.

Nitrogen sorption

Nitrogen sorption experiments were conducted with an *Autosorb-1 (Quantachrome)*. Prior to the measurement the sample (27.9 mg) was outgassed under high vacuum at 120 °C for 38 h. The resulting data was evaluated with the software *ASiQwin v3.0*. The linearized form of the BET equation was used to calculate BET surface areas. For the calculation of the pore size distribution a QSDFT equilibrium based model was used assuming slit and cylindrical pores.

Dynamic Light Scattering (DLS)

DLS was performed on a *Zetasizer Nano Series (Nano-ZS, Malvern)* equipped with a laser with the wavelength $\lambda = 633$ nm. For sample preparation the freshly prepared nanoparticles (NPs) were dispersed in ethanol or phosphate-buffered saline (PBS) in the case of the capped NPs.

5.5.2 Characterization

XRD

The XRD measurement of the MIL-88A nanoparticles shows a successful synthesis of the particles, showing the characteristic reflexes at 10-11°.

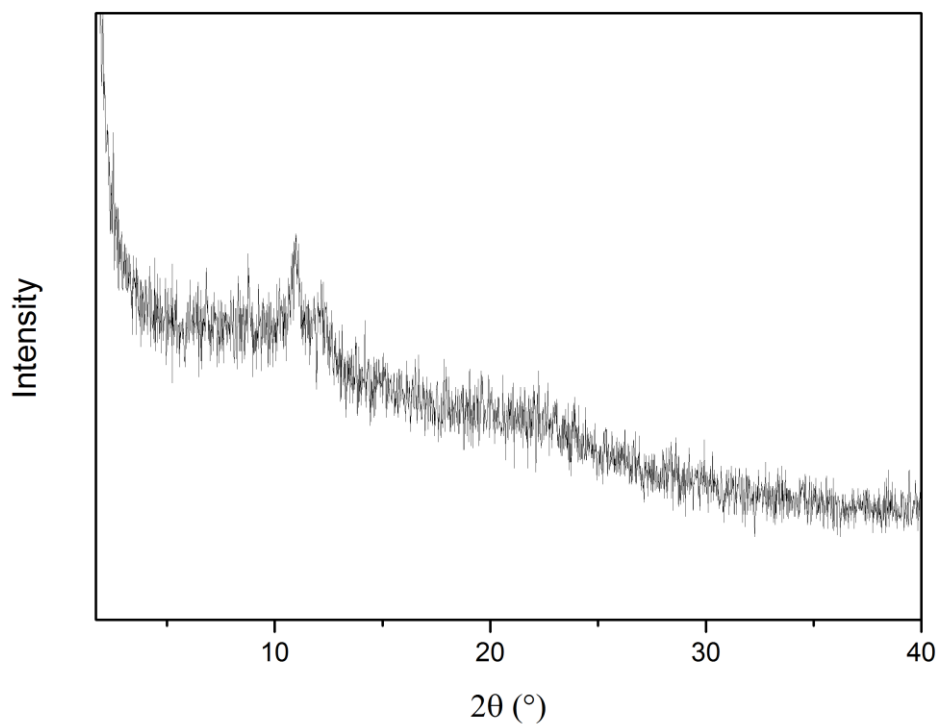


Figure 5.6: XRD measurement of MIL-88A nanoparticles as synthesized

Scanning Electron microscopy (SEM)

SEM measurements show that the MIL-88A nanoparticles possess a round morphology and are fairly homogenous (Figure 5.7) featuring a particle size of about 50 nm.

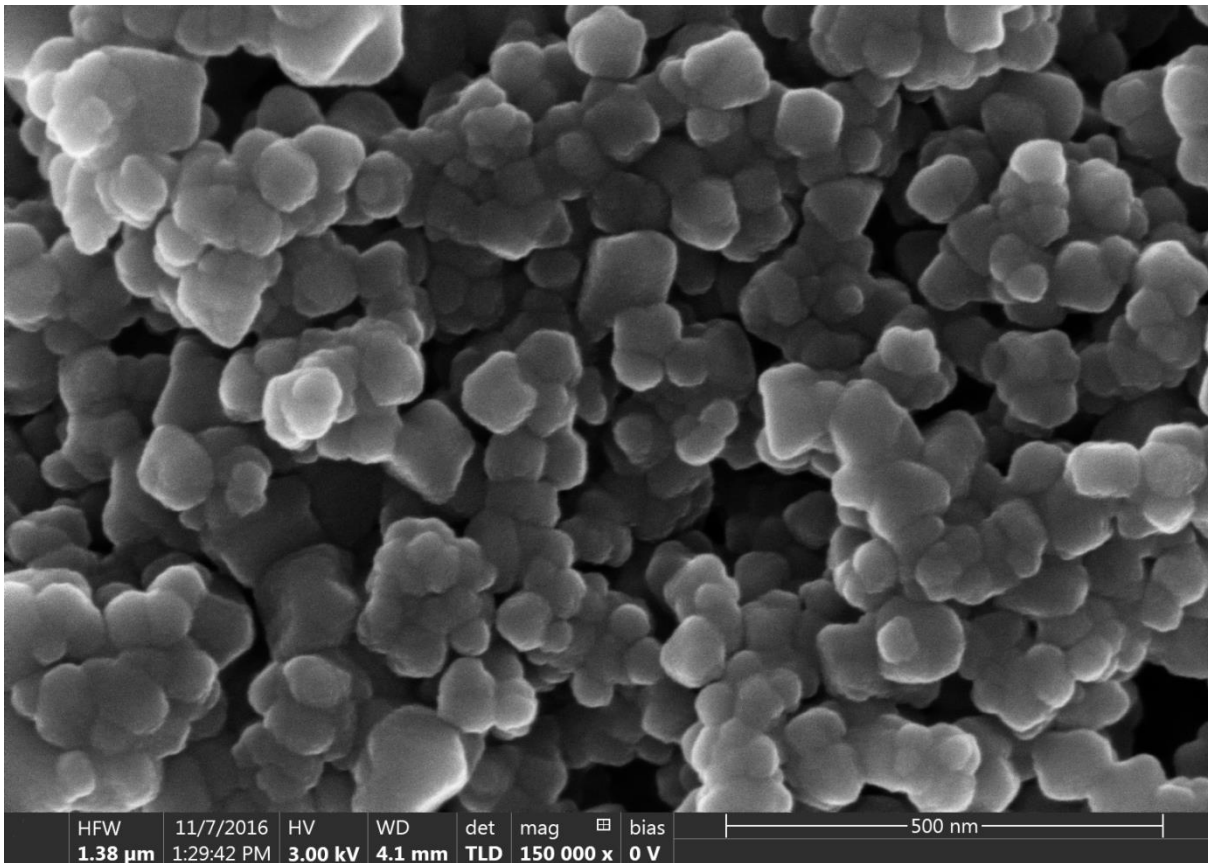


Figure 5.7: SEM image of MIL-88A NPs.

Transmission Electron Microscopy (TEM)

Figure 5.8 depicts a TEM micrograph of the MIL-88A NP sample. The particles feature a round morphology and are connected via thin necks. The MIL-88A sample appears to be fairly homogenous.

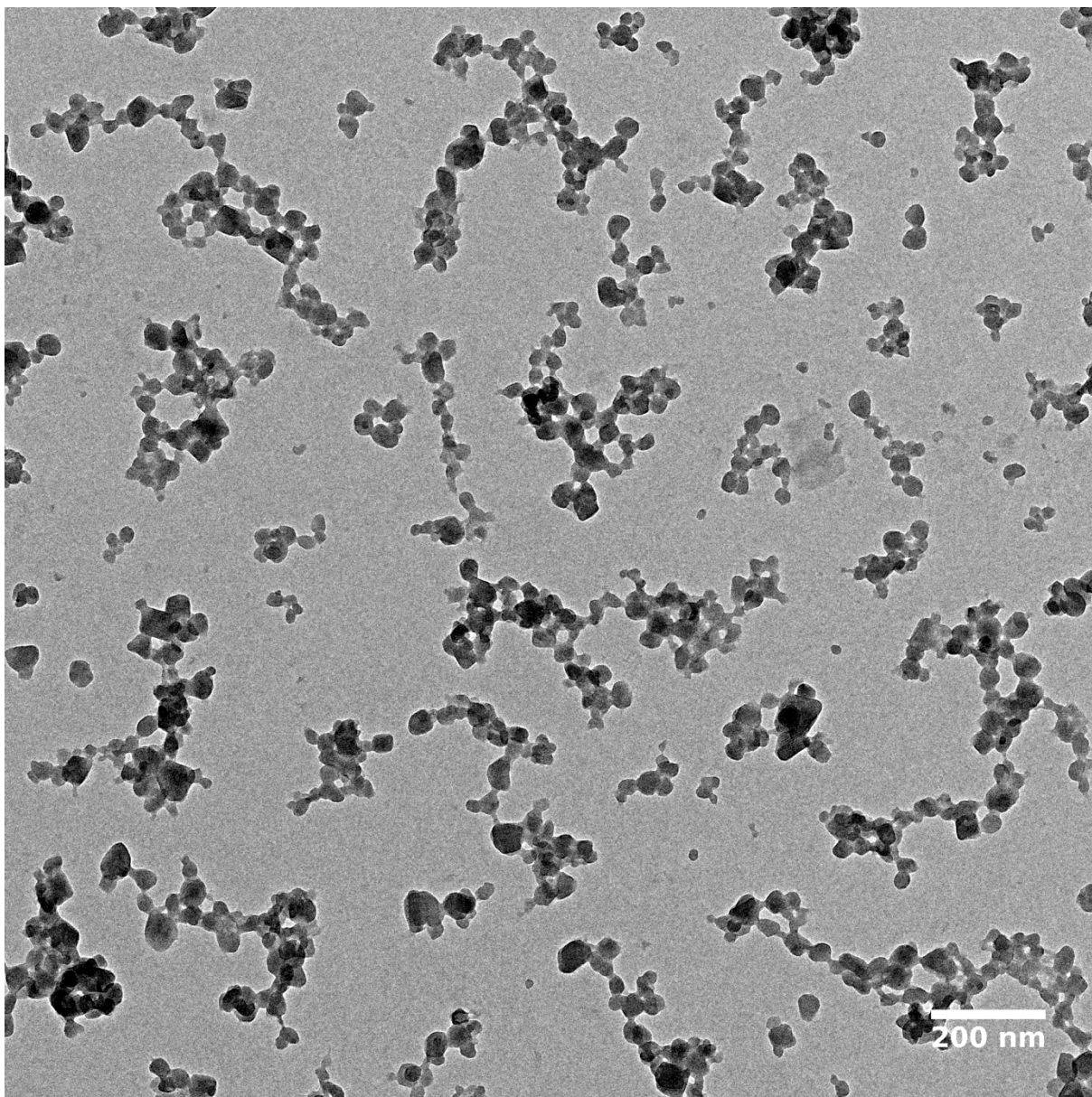


Figure 5.8: Transmission electron micrograph of MIL-88A NPs.

Thermogravimetric Analysis and Nitrogen Sorption

Thermogravimetric analysis of the synthesized MIL-88A was performed. Up to 204 °C the residual solvent in the sample is desorbed resulting in a mass loss of 6 %. Subsequently, in a range between 204 – 433 °C the framework decomposes. The residual mass left of the sample remains at 42%. This data is in agreement with literature data for MIL-88A NPs and shows the successful synthesis of the MOF.⁴³ The Nitrogen Sorption gave a BET surface area of 218 m²/g and a pore size of 11.44 Å, which agrees with literature.⁴⁴ Further information can also be found in Illes et al. “Exosome coated Metal-Organic Framework Nanoparticles – An Efficient Drug Delivery Platform”¹⁰.

Calculating the quenching adjustment factor for the Fluorescence Release Experiments

To account for quenching 10 mL of a 1 mM solution of calcein were diluted with 990 mL PBS. Next, 10 mL of this new solution were added to 4 mL water or ALF in cuvettes. In addition 10 mL triton X-100 was added to one sample. Then the fluorescence of these solutions was measured. The obtained values were used to calculate the offset for the individual fluorescence measurements. The normalization factor determined by comparing the measurements of water and triton X-100 to those of ALF is 2.17 and was implemented in the fluorescence experiments.

UV/Vis of Floxuridine

To determine the loading capacity of floxuridine and the floxuridine content when loading both irinotecan and floxuridine together, UV/Vis measurements were taken. As the irinotecan signal overlays the floxuridine signal at high concentrations the loading for the I:F 3:1 mixture could not be measured.

The floxuridine stock solution contained 1 mM (246 μg) floxuridine. Using this as the base of the calculation leads to the following floxuridine loads for each particle solution: The particles took up 14.7% of the initially provided floxuridine when loading pure floxuridine, 12.4 % when loading with a 1:3 mixture of irinotecan and floxuridine and 6.9 % when loading with a 1:1 mixture of irinotecan and floxuridine. This leads to a maximum floxuridine loading capacity of 3.61 wt% of the particles.

Table 5.3: Floxuridine loading for the different investigated particle solutions.

	Pure floxuridine	I:F 1:3	I:F 1:1
Loading ($\mu\text{g}/\text{mg}$ Lip-MIL-88A) (% of provided floxuridine that was taken up)	36.1 (14.7%)	22.8 (12.4%)	8.50 (6.9%)

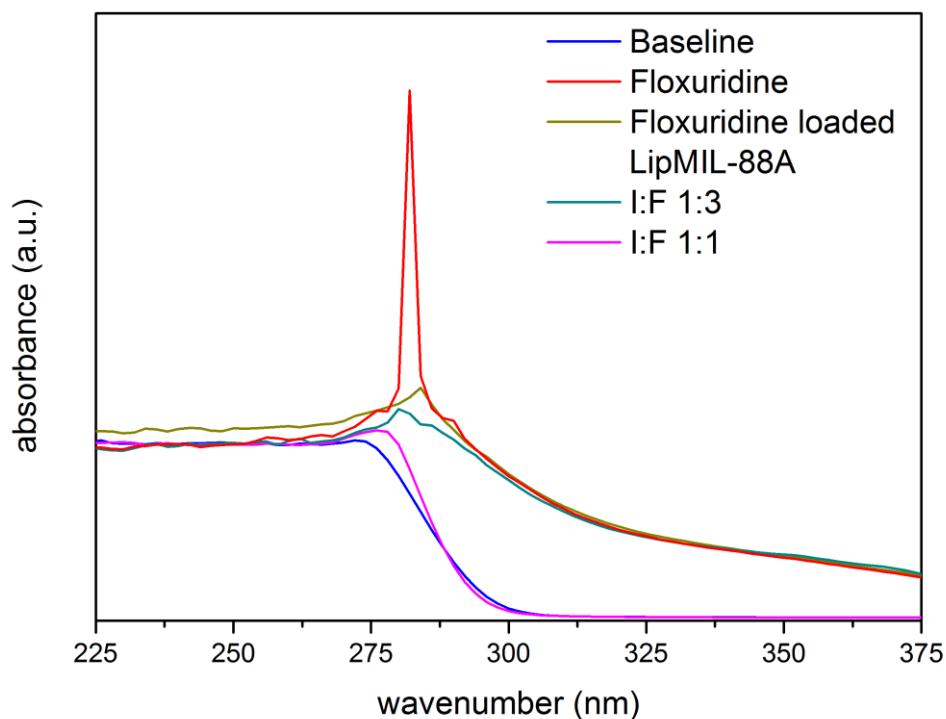


Figure 5.9: UV/Vis measurement of LipMIL-88A loaded with floxuridine and mixtures of floxuridine and irinotecan.

UV/Vis of irinotecan

In addition to the irinotecan measurements provided in the main text, we also measured the supernatant of Lip-MIL-88A loaded with irinotecan one week after preparation to check for potential leakage. There was no observable leakage of irinotecan from Lip-MIL-88A after one week (Figure 5.10).

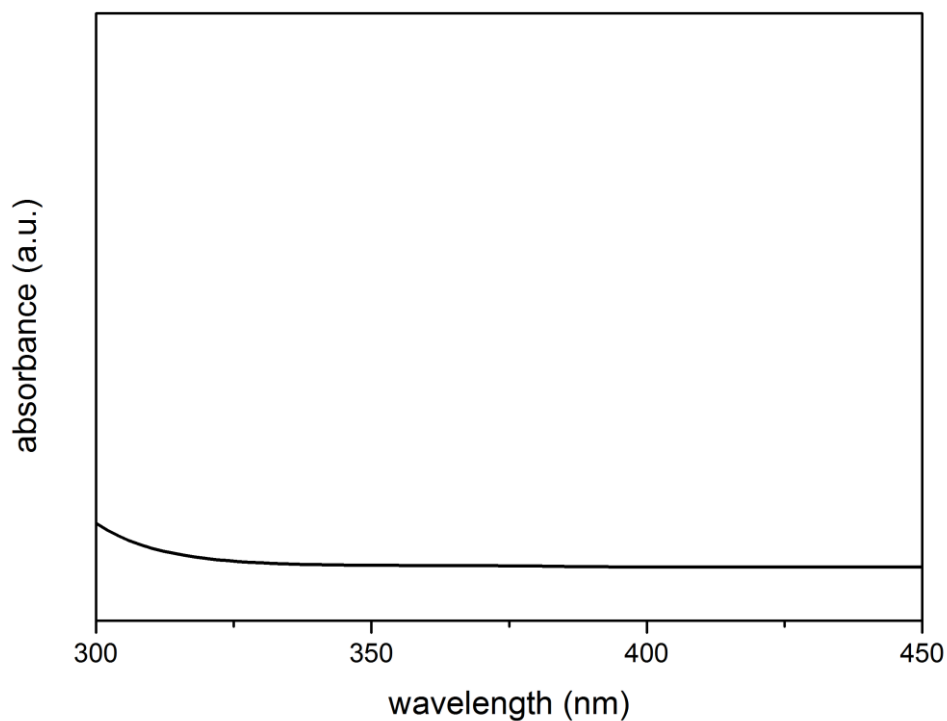


Figure 5.10: UV/Vis of 1 mg/mL Lip-MIL-88A loaded with irinotecan in PBS one week after preparation showing no leakage into the supernatant.

DLS

The DLS measurements show that both the pure and the liposome coated particles have an average size of about 100 nm, with the coated ones being slightly larger. The PDI is 0.153 and 0.143 respectively. The Zeta potential of the particles is -21.0 mV without liposome coating and 26.0 mV with liposome coating at pH 7.4.

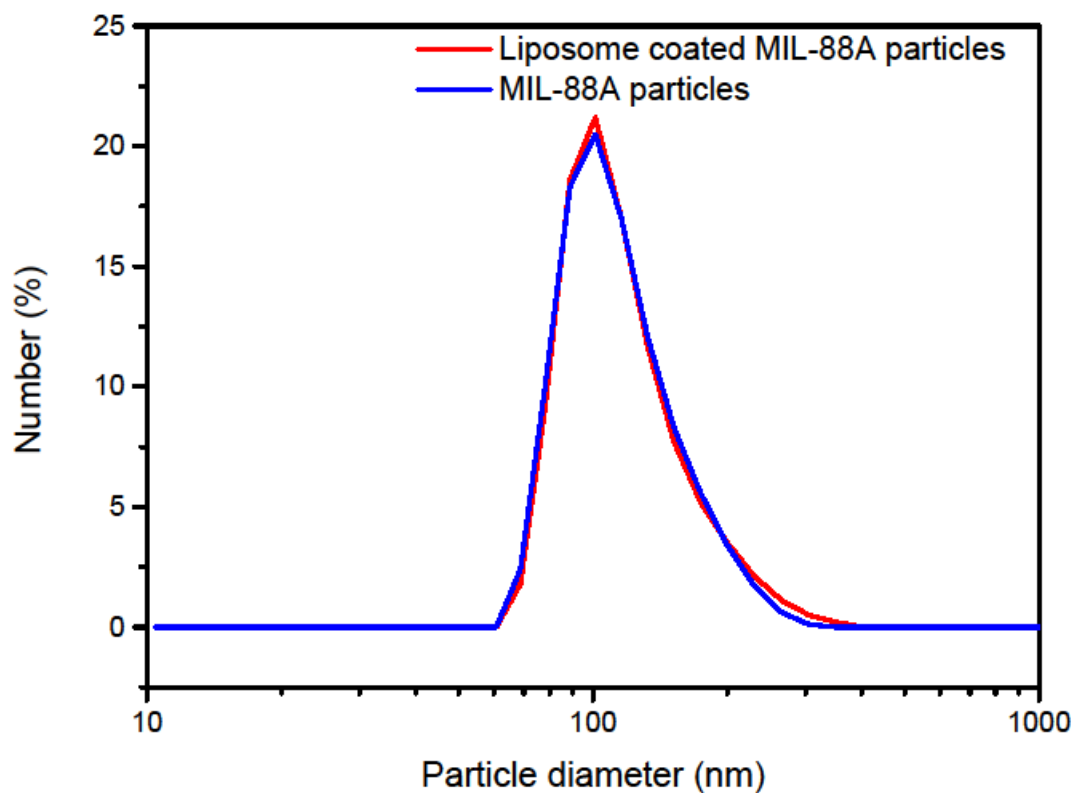


Figure 5.11: DLS measurements of MIL-88A nanoparticles (blue) and liposome coated MIL-88A nanoparticles (red).

Visualizing the Liposome Coating

To investigate if the MIL-88A NPs were successfully coated with liposomes, we performed fluorescence colocalization experiments. The MOF nanoparticles were labeled with Fluo-3 (0.2 μL Fluo-3 solution per 100 μL particle solution, in PBS; Figure 5.12, a), which stains the iron contained in the particles, while the liposomes were labeled with DiD (0.2 μL DiD solution per 100 μL particle solution, in PBS; Figure 5.12, b). A successful coating of the particles should result in a colocalization of both dyes, while a failure in coating the particles should result in an independent distribution. The merged image (Figure 5.12, c) of both channels shows that we could observe the colocalization of both dyes suggesting a successful coating. The slight movement of the particles due to Brownian motion is preventing a complete overlap of both images in the merged channel as it takes time to switch between the different excitation wavelengths needed for the two different dyes. Control experiments with both dyes and only liposomes or MIL-88A particles showed no colocalization of the dyes, corroborating that the colocalization is due to the successful coating of the particles.

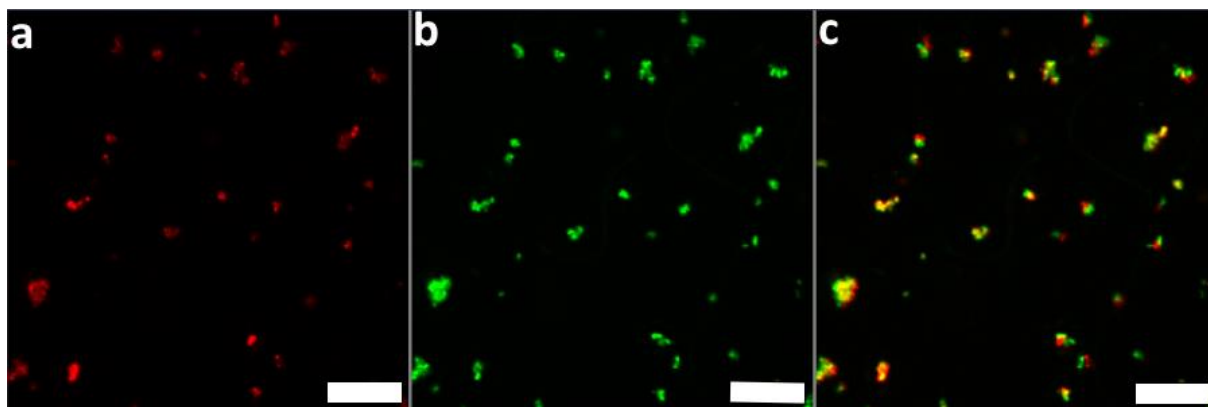


Figure 5.12: a) MIL-88A marked with Fluo-3. b) Liposomes marked with DiD. c) Merged channels of a) and b). The scale bars in all images represents 50 μm .

Quantification through High-Content Experiments

The release behavior of the Lip-MIL-88A was further quantified by incubating different amounts of calcein loaded Lip-MIL-88A (0, 10, ..., 140, 150 mg/L) in HeLa cells and counting the number of cells that show a visible release. For this 5000 HeLa cells were seeded in each well of a 96 well plated together with 100 μ L DMEM (10%FBS, 1% PenStrep). After one day of incubation (37 °C, 5% CO₂) the particles were added. The images were taken after three and four days of incubation. Four images per well were taken and each concentration was measured in triplicate. The images have been evaluated with the MetaXpress software, using the built in functions and a custom module. First the total number of cells in the brightfield images were counted, then the cells showing full fluorescence in the GFP channel were also counted. To investigate the accuracy of the automated counts some of the images were evaluated by hand for a comparison.

By comparing it with the total number of cells the release efficiency of the drug carrier can be estimated. The number of cells that exhibit a successful release of the cargo after 3 to 4 days of incubation steadily grows with increasing concentration until a plateau is reached at a particle concentration of 110 μ g/mL. The maximum of cells that exhibit a successful release of the cargo is between 50 and 60% regardless of the incubation time (Figure 5.13). The difference in incubation time makes no large difference in the cells that show visible release. In the microscope images we could observe that there were cells that also took up Lip-MIL88A, but did not show any signs of release even after four days of incubation (Figure 5.14). One possible reason for this behavior could be that these cells are currently at different stages in the cell cycle than the others.

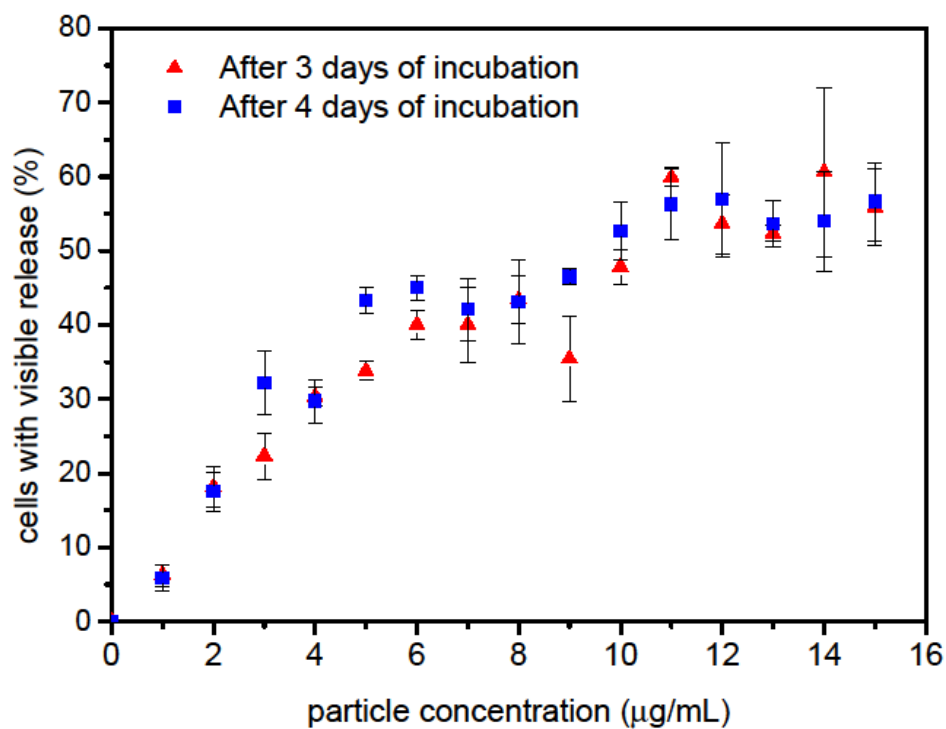


Figure 5.13: Quantification of the release of Lip-MIL-88A. Presented are the cells with visible signs of release for each concentration after 3 (blue) and 4 (red) days of incubation. The error bars represent SD.

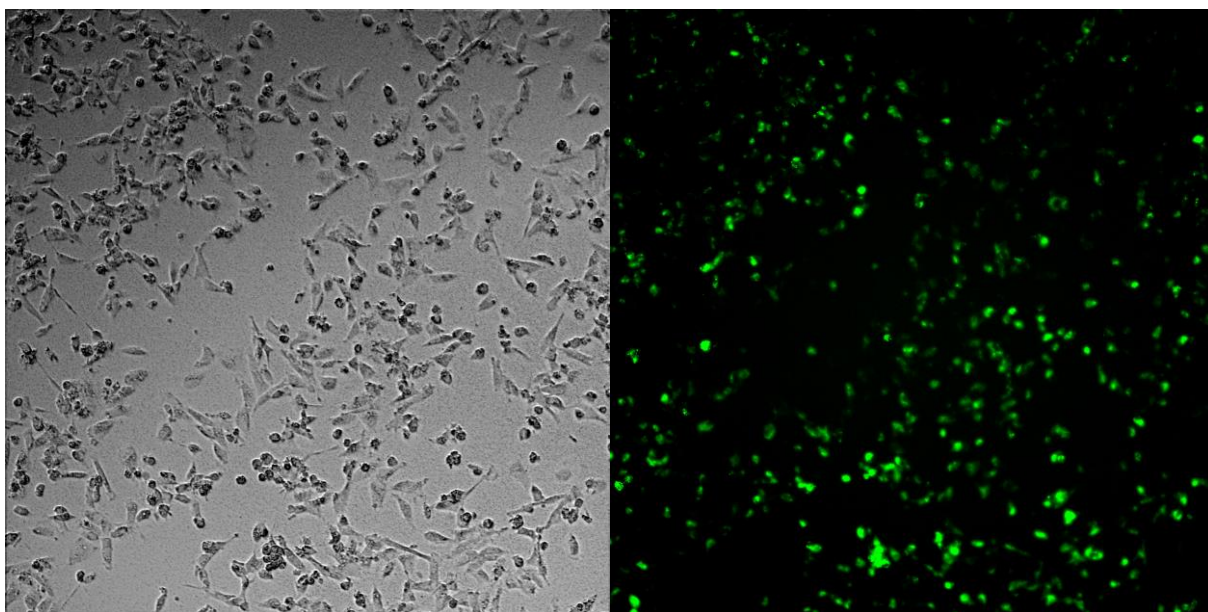


Figure 5.14: Sample images of the High Content Release Quantification of HeLa cells incubated for 3 days with particle concentration of 2 µg/mL. (Brightfield image on the left and the corresponding GFP channel image on the right)

HDAC1 Assay to determine the SBHA loading

SBHA is difficult to detect with standard analytical techniques. For this reason another quantification method had to be used. SBHA is an inhibitor of HDAC1 and we used its inhibition as a quantifier. The assay kit used was the HDAC1 Inhibitor Screening Assay Kit from Cayman Chemical. For the quantification different dilutions of SBHA were prepared and tested on their inhibition of HDAC1 and then compared to the inhibition of dissolved SBHA loaded particles to determine how much SBHA was loaded into the particles (Figure 5.15).

We calculated the theoretical dilution at 50% inhibition for SBHA (1:43) and the SBHA loaded MIL-88A NPs (1:6.1) from the experiment. From these dilutions and the concentrations of the stock solutions we could calculate how much SBHA (4.75 μg) and SBHA loaded particles (163 μg) were needed to inhibit 50% of the available HDAC1. We can then calculate the SBHA loading capacity of Lip-MIL-88A: 14.2 % of the initially available 1 mM SBHA were loaded into the particles or 2.90 wt% in relation to the weight of the MOF NPs.

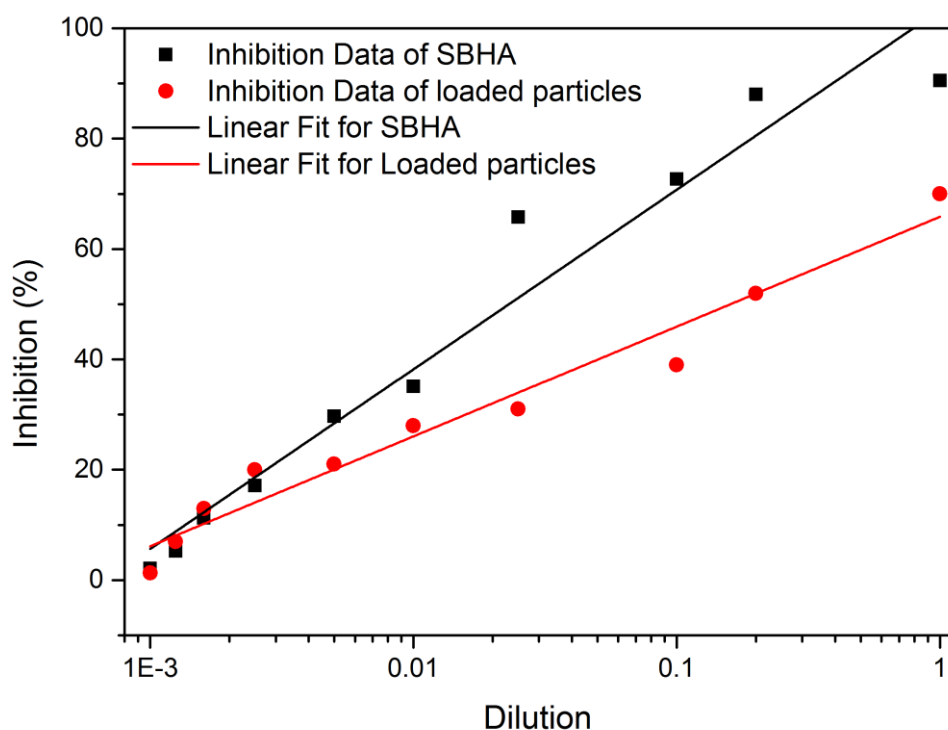


Figure 5.15: Graphical representation of the results of the HDAC1 Inhibition Assay.

5.5.3 MTT-Assays

To confirm that the Lip-MIL-88A shows no leakage and a good release of its cargo MTT tests were performed. For this purpose 5000 HEK 293T or HeLa cells were seeded into each well of a 96-Well Plate with 0.1 mL of DMEM. After one day of incubation the Lip-MIL-88A were added. The MTT test was performed after three days of incubation with the particles. Several different therapeutic drugs and different concentrations of drug loaded Lip-MIL-88A were investigated. For the therapeutic drugs the doses were: 0, 0.2, 0.4, 0.8, 2, 6, 10, 14 $\mu\text{L}/\text{mL}$ of a 1 mM stock solution. For Lip-MIL-88A the concentrations were: 0, 20, 40, 80, 20, 60, 100, 140 $\mu\text{g}/\text{mL}$. Each concentration was tested on three different days and in triplicate on each day. As a comparison to the drug loaded Lip-MIL-88A particles the cells were directly exposed to different concentrations of the pure drugs (Figure 5.16 5.16). As can be seen the drugs show low efficacy for drug concentrations below 2 $\mu\text{L}/\text{mL}$ with cell viabilities of more than 60%, but lead to a strong decrease in cell viability for higher doses, resulting in cell viabilities below 10% for each drug with the highest tested concentration.

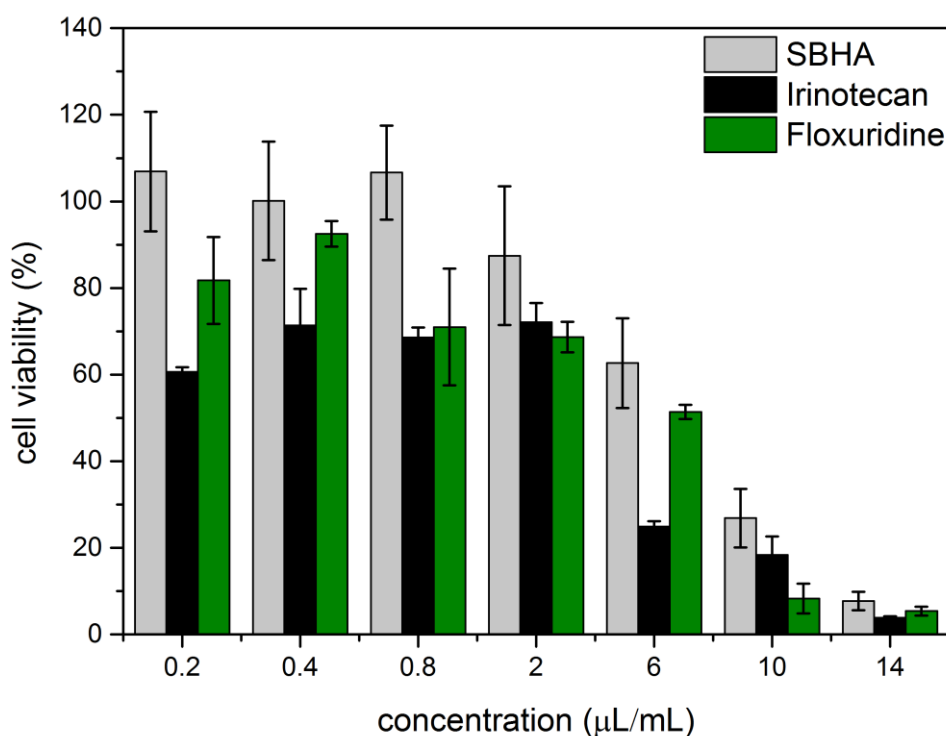


Figure 5.16: MTT-Assays of free drugs incubated for three days with HeLa cells.

MTT-Assays of the uncoated and the liposome coated MIL-88A NPs show that they are non-toxic with cell viabilities above 70% (Figure 5.17).

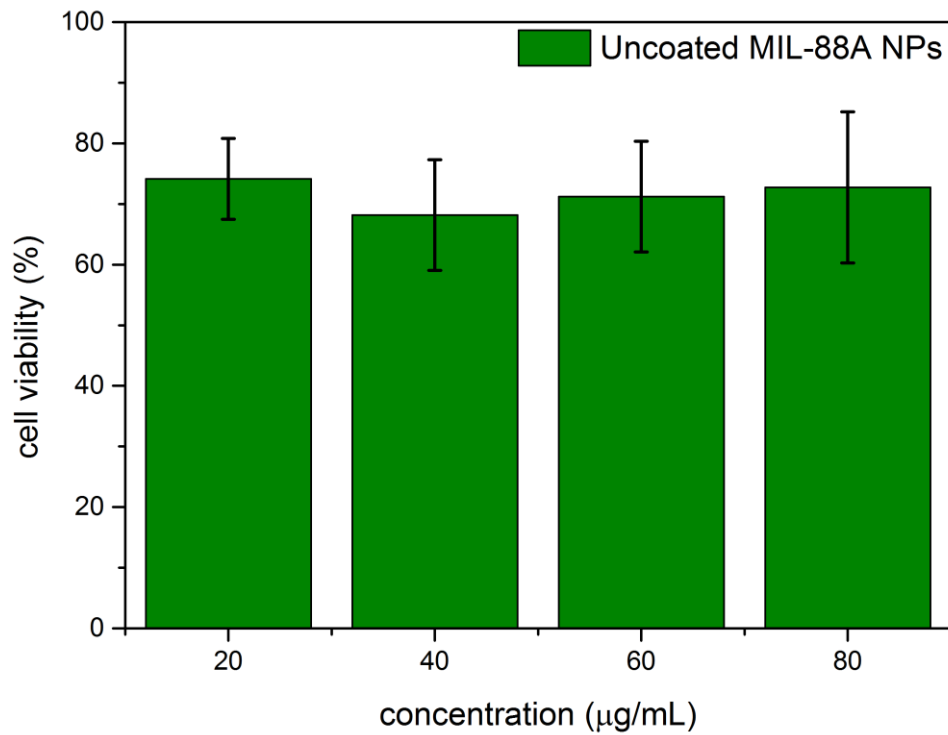


Figure 5.17: MTT-Assay of Uncoated MIL-88A NPs.

Figure 5.18 shows the MTT-Assay of Lip-MIL-88A without any cargo inside. The particles were incubated for three days in HeLa cells and show no toxicity with cell viabilities above 90%.

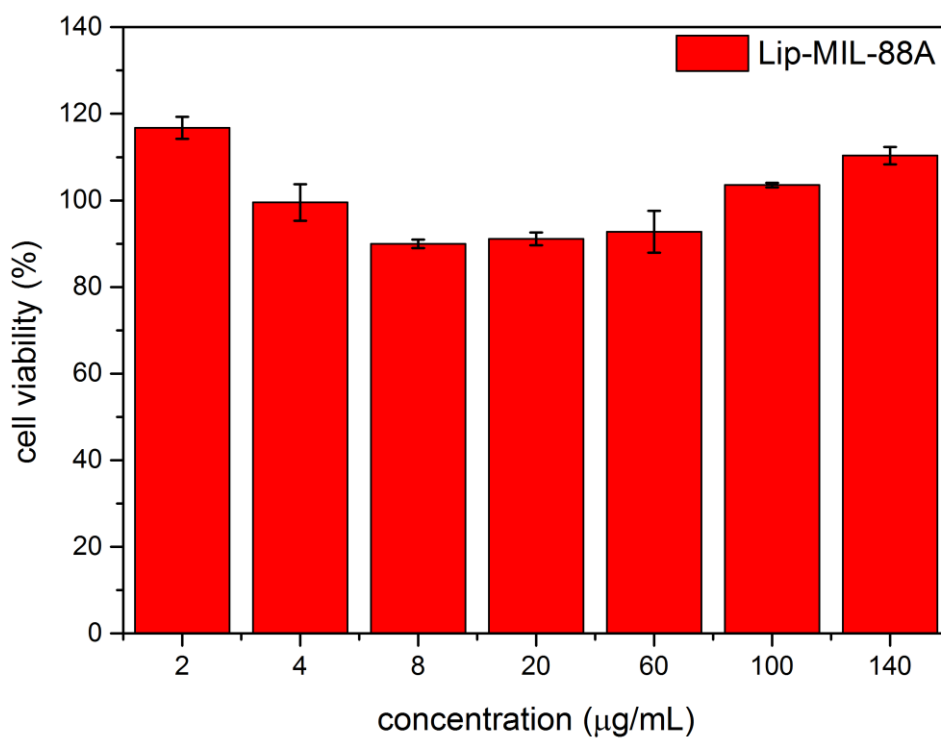


Figure 5.18: MTT Assay of liposome coated MIL-88A NPs without cargo.

5.6 References

1. Introduction to Metal–Organic Frameworks. *Chem. Rev.* **112**, 673-674 (2012).
2. Zhou, H.-C.J. & Kitagawa, S. Metal–Organic Frameworks (MOFs). *Chem. Soc. Rev.* **43**, 5415-5418 (2014).
3. Maurin, G., Serre, C., Cooper, A. & Férey, G. The new age of MOFs and of their porous-related solids. *Chem. Soc. Rev.* **46**, 3104-3107 (2017).
4. Peplow, M. Materials science: The hole story. *Nature* **520**, 148-150 (2015).
5. Furukawa, H., Cordova, K.E., O’Keeffe, M. & Yaghi, O.M. The Chemistry and Applications of Metal-Organic Frameworks. *Science* **341**, 1230444 (2013).
6. Furukawa, H., Müller, U. & Yaghi, O.M. “Heterogeneity within Order” in Metal–Organic Frameworks. *Angew. Chem. Int. Ed.* **54**, 3417-3430 (2015).
7. Wuttke, S., Lismont, M., Escudero, A., Rungtaweivoranit, B. & Parak, W.J. Positioning metal-organic framework nanoparticles within the context of drug delivery – A comparison with mesoporous silica nanoparticles and dendrimers. *Biomaterials* **123**, 172-183 (2017).
8. Wang, J. et al. Combined experimental and theoretical insight into the drug delivery of nanoporous metal–organic frameworks. *RSC Advances* **5**, 85606-85612 (2015).
9. Röder, R. et al. Multifunctional Nanoparticles by Coordinative Self-Assembly of His-Tagged Units with Metal–Organic Frameworks. *J. Am. Chem. Soc.* **139**, 2359-2368 (2017).
10. Illes, B. et al. Exosome-Coated Metal–Organic Framework Nanoparticles: An Efficient Drug Delivery Platform. *Chem. Mater.* **29**, 8042-8046 (2017).
11. Lismont, M., Dreesen, L. & Wuttke, S. Metal-Organic Framework Nanoparticles in Photodynamic Therapy: Current Status and Perspectives. *Adv. Funct. Mater.* **27**, 1606314 (2017).
12. Carné, A., Carbonell, C., Imaz, I. & Maspoch, D. Nanoscale metal–organic materials. *Chem. Soc. Rev.* **40**, 291-305 (2011).
13. Horcajada, P. et al. Metal–Organic Frameworks in Biomedicine. *Chem. Rev.* **112**, 1232-1268 (2012).
14. He, C., Liu, D. & Lin, W. Nanomedicine Applications of Hybrid Nanomaterials Built from Metal–Ligand Coordination Bonds: Nanoscale Metal–Organic Frameworks and Nanoscale Coordination Polymers. *Chem. Rev.* **115**, 11079-11108 (2015).
15. Giménez-Marqués, M., Hidalgo, T., Serre, C. & Horcajada, P. Nanostructured metal–organic frameworks and their bio-related applications. *Coord. Chem. Rev.* **307**, 342-360 (2016).
16. Falcaro, P. et al. MOF positioning technology and device fabrication. *Chem. Soc. Rev.* **43**, 5513-5560 (2014).
17. Furukawa, S., Reboul, J., Diring, S., Sumida, K. & Kitagawa, S. Structuring of metal–organic frameworks at the mesoscopic/macrosopic scale. *Chem. Soc. Rev.* **43**, 5700-5734 (2014).
18. Falcaro, P. et al. Application of metal and metal oxide nanoparticles@MOFs. *Coord. Chem. Rev.* **307**, 237-254 (2016).
19. Wang, S. et al. General and Direct Method for Preparing Oligonucleotide-Functionalized Metal–Organic Framework Nanoparticles. *J. Am. Chem. Soc.* **139**, 9827-9830 (2017).
20. Abánades Lázaro, I. et al. Selective Surface PEGylation of UiO-66 Nanoparticles for Enhanced Stability, Cell Uptake, and pH-Responsive Drug Delivery. *Chem* **2**, 561-578 (2017).
21. Wuttke, S. et al. Validating Metal-Organic Framework Nanoparticles for Their Nanosafety in Diverse Biomedical Applications. *Adv Healthc Mater* **6**, 1600818 (2017).
22. Zimpel, A. et al. Imparting Functionality to MOF Nanoparticles by External Surface Selective Covalent Attachment of Polymers. *Chem. Mater.* **28**, 3318-3326 (2016).
23. Wang, X.-G. et al. A multifunctional metal–organic framework based tumor targeting drug delivery system for cancer therapy. *Nanoscale* **7**, 16061-16070 (2015).
24. Wuttke, S. et al. MOF nanoparticles coated by lipid bilayers and their uptake by cancer cells. *Chem. Commun.* **51**, 15752-15755 (2015).
25. Zhuang, J. et al. Optimized Metal–Organic-Framework Nanospheres for Drug Delivery: Evaluation of Small-Molecule Encapsulation. *ACS Nano* **8**, 2812-2819 (2014).
26. Horcajada, P. et al. Porous metal–organic-framework nanoscale carriers as a potential platform for drug delivery and imaging. *Nature Materials* **9**, 172-178 (2010).
27. Miller, S.R. et al. Biodegradable therapeutic MOFs for the delivery of bioactive molecules. *Chem. Commun.* **46**, 4526-4528 (2010).
28. He, C., Lu, K., Liu, D. & Lin, W. Nanoscale Metal–Organic Frameworks for the Co-Delivery of Cisplatin and Pooled siRNAs to Enhance Therapeutic Efficacy in Drug-Resistant Ovarian Cancer Cells. *J. Am. Chem. Soc.*

- 136**, 5181-5184 (2014).
29. Xu, X., Ho, W., Zhang, X., Bertrand, N. & Farokhzad, O. Cancer nanomedicine: from targeted delivery to combination therapy. *Trends Mol. Med.* **21**, 223-232 (2015).
 30. Greco, F. & Vicent, M.J. Combination therapy: opportunities and challenges for polymer-drug conjugates as anticancer nanomedicines. *Adv Drug Deliv Rev* **61**, 1203-1213 (2009).
 31. Gadde, S. Multi-drug delivery nanocarriers for combination therapy. *MedChemComm* **6**, 1916-1929 (2015).
 32. Hu, C.M. & Zhang, L. Nanoparticle-based combination therapy toward overcoming drug resistance in cancer. *Biochem. Pharmacol.* **83**, 1104-1111 (2012).
 33. Rojas, S. et al. Metal-organic frameworks as potential multi-carriers of drugs. *CrystEngComm* **15**, 9364-9367 (2013).
 34. McKinlay, A.C. et al. Multirate delivery of multiple therapeutic agents from metal-organic frameworks. *APL Materials* **2**, 124108 (2014).
 35. Zhang, H. et al. Rational Design of Metal Organic Framework Nanocarrier-Based Codelivery System of Doxorubicin Hydrochloride/Verapamil Hydrochloride for Overcoming Multidrug Resistance with Efficient Targeted Cancer Therapy. *ACS applied materials & interfaces* **9**, 19687-19697 (2017).
 36. Wang, S. et al. Surface-Specific Functionalization of Nanoscale Metal-Organic Frameworks. *Angew. Chem. Int. Ed.* **54**, 14738-14742 (2015).
 37. Yang, J. et al. Zr-Based MOFs Shielded with Phospholipid Bilayers: Improved Biostability and Cell Uptake for Biological Applications. *Chem. Mater.* **29**, 4580-4589 (2017).
 38. Chalati, T., Horcajada, P., Gref, R., Couvreur, P. & Serre, C. Optimisation of the synthesis of MOF nanoparticles made of flexible porous iron fumarate MIL-88A. *J. Mater. Chem.* **21**, 2220-2227 (2011).
 39. Mayer, L.D. et al. Ratiometric dosing of anticancer drug combinations: Controlling drug ratios after systemic administration regulates therapeutic activity in tumor-bearing mice. *Mol. Cancer Ther.* **5**, 1854 (2006).
 40. Batist, G. et al. Safety, Pharmacokinetics, and Efficacy of CPX-1 Liposome Injection in Patients with Advanced Solid Tumors. *Clin. Cancer Res.* **15**, 692 (2009).
 41. Liu, J., Jiang, X., Ashley, C. & Brinker, C.J. Electrostatically Mediated Liposome Fusion and Lipid Exchange with a Nanoparticle-Supported Bilayer for Control of Surface Charge, Drug Containment, and Delivery. *J. Am. Chem. Soc.* **131**, 7567-7569 (2009).
 42. Margareth R. C. Marques, R.L., May Almukainzi Simulated Biological Fluids with Possible Application in Dissolution Technology. *Dissolution Technologies* **18**, 15-18 (2011).
 43. Andrew Lin, K.-Y., Chang, H.-A. & Hsu, C.-J. Iron-based metal organic framework, MIL-88A, as a heterogeneous persulfate catalyst for decolorization of Rhodamine B in water. *RSC Advances* **5**, 32520-32530 (2015).
 44. McKinlay, A.C. et al. Nitric Oxide Adsorption and Delivery in Flexible MIL-88(Fe) Metal-Organic Frameworks. *Chem. Mater.* **25**, 1592-1599 (2013).

Chapter 6

Biocompatible crosslinked β -cyclodextrin nanoparticles as multifunctional carriers for cellular delivery

Stefan Datz, Bernhard Illes, Dorothee Gößl, Constantin v. Schirnding, Hanna Engelke, Thomas Bein

This chapter was published in Nanoscale, 2018, 10, 16284-16292 - Reproduced by permission of The Royal Society of Chemistry.

6.1 Introduction

Cancer therapy is currently shifting from a standardized systemic approach to a more personalized and specifically customized disease treatment. Such personalized treatments use multifunctional drugs in combination with carrier systems and are ideally based on molecular-level diagnosis.¹ After decades of research, the demand for innovative biocompatible nanomaterials for the transport of therapeutic agents is still growing. In particular, nanoparticle-based targeting of tumor cells has emerged as a potential therapeutic approach to release effective drug doses within the tumorous tissue.²⁻⁶ Because of the prolonged blood circulation time combined with nonspecific accumulation in tumors through the enhanced permeability and retention (EPR) effect, nanoparticles have been regarded as a suitable candidate in the pharmaceutical fields, especially for targeted and personalized cancer therapy. A number of different carrier systems have been investigated in the field of nanobiosciences with differing results in the last decade. Besides inorganic materials, such as mesoporous silica nanoparticles (MSNs),⁷⁻¹⁵ periodic mesoporous organosilica nanoparticles (PMOs),^{8, 14-20} or metal-based materials, e.g. Au-²¹⁻²³ or iron oxide nanoparticles,²⁴⁻²⁹ polymeric micelles,³⁰⁻³² lipids,³³⁻³⁵ and DNA origami are other examples for potential drug delivery systems used in fundamental biomedical research,³⁶⁻³⁸ However, some of these materials have certain drawbacks, e.g. polymeric micelles and lipids often need specific formulations for different cargos, and may face stability issues. Besides small magnetic iron-oxide based materials, none of the other larger solid nanoparticles, such as silica materials, have reached clinical trials, partially due to concerns about the unknown fate of these particles in the human organism.³⁹ In obvious contrast to the ever-growing number of sophisticated nanoparticle-based cell-targeting strategies that effectively target tumor cells *in vitro*, only few studies showed successful tumor-cell specific targeting and controlled cancer cell killing *in vivo*. Even fewer nanoformulations have found their way into clinical studies and practice.⁴⁰ Ligand-assisted targeting of cancer cells with nanoparticles *in vivo* through specific receptor-mediated uptake can be limited due to protein corona formation.⁴¹ Therefore, there is a rapidly growing interest in new nanomaterials which can overcome some of the aforementioned limitations. Sugar-based materials are promising candidates since cancer cells are known to have a faster glycolysis metabolism that selectively leads to an increased glucose uptake compared to healthy cells.⁴²⁻⁴⁵

Here, we present a novel class of biocompatible multifunctional nanomaterials consisting of cross-linked β -cyclodextrin molecules. Cyclodextrins (CDs) are a family of cyclic oligosaccharides composed of six, seven, or eight D(+)-glucose units linked by α -1,4-linkages, which are named α -, β -, and γ -CD, respectively.⁴⁶ These different oligosaccharides are frequently used in the medical field because of their biocompatibility and their low toxicity.⁴⁷⁻⁵⁰ CDs have a hydrophilic exterior and a hydrophobic cavity inside the oligosaccharide rings that can be used to encapsulate different kinds of guest and cargo molecules.⁵¹⁻⁵⁴ This encapsulation is based on supramolecular host-guest interactions such as hydrogen bonding, van-der-Waals forces or hydrophobic interactions, and is used in various application fields including biomedicine, catalysis, environmental protection and separation processes.⁵⁵ Although the use of different CDs in the medical field has been documented for decades, their application is still rather limited due to significant synthetic challenges, hence motivating the development of more specific and controllable CD-containing nanoparticles. Until now, a variety of supramolecular nanoparticles (SNPs) with CD-building blocks have been investigated. However, SNPs are particles in which different building blocks are brought together by non-covalent interactions resulting in larger assemblies.⁵⁶ The assembly is either based on electrostatic interactions or host-guest interactions.^{57, 58} The non-covalent interactions limit their use for drug delivery applications, since they might degrade easily before they reach their target and any new guest molecule that is incorporated or loaded into the particle needs to be optimized regarding its interactions with the particle structure. Thus, a covalently crosslinked CD nanoparticle is viewed as an enabling concept that could facilitate a breakthrough for drug delivery applications. Recently, different approaches were used to prepare covalently crosslinked CD molecule-containing materials. One is defined by crosslinking α -CD-poly-ethyleneglycol (PEG) inclusion complexes by using epichlorohydrin. The nanomaterial was obtained after extracting the PEG chains that penetrated the hydrophobic cavity.⁵⁹ In another approach, Dichtel *et al.* polymerized β -CD in a nucleophilic aromatic substitution reaction with tetrafluoro terephthalonitrile and obtained mesoporous bulk material that was used to rapidly remove organic micropollutants from waste water.⁶⁰ However, no nanoparticles of covalently crosslinked CD molecules were obtained yet. In the following work, we combined these different approaches to crosslink β -CD-PEG inclusion complexes with rigid aromatic groups providing for the first time small, dispersible and thermally stable nanoparticles. These NPs can be covalently labeled with dye molecules

exploiting simple click-chemistry to track them effectively in *in vitro* cell experiments. β -CD NPs were rapidly taken up by cancer cells and could efficiently release different cargo molecules. This novel and biocompatible nanocarrier concept provides a promising platform for the development of controllable and efficient theranostic systems.

6.2 Results and Discussion

Highly dispersible and thermally stable β -CD NPs for possible drug delivery applications were derived from a carefully controlled nucleophilic aromatic substitution reaction with tetrafluoroterephthalonitrile (TFTN, see Figure 6.1A).

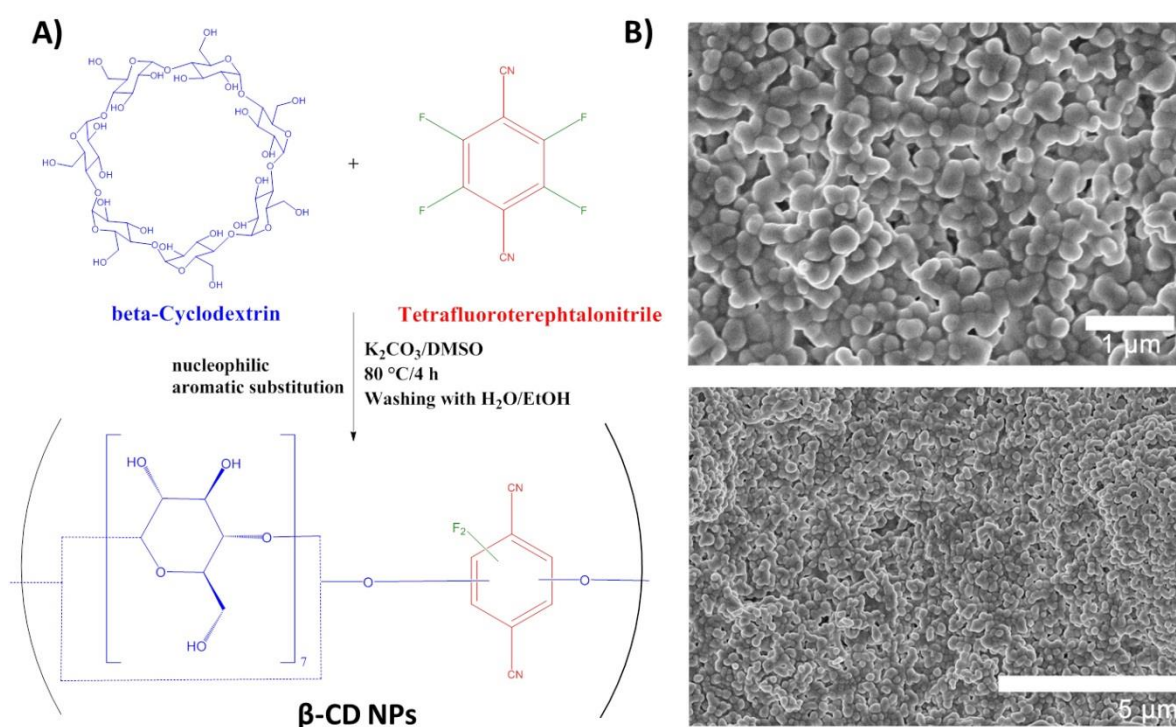


Figure 6.1: Synthesis scheme of β -CD NPs following a nucleophilic aromatic substitution reaction with TFTN (A), SEM images of β -CD NPs showing spherical particles with a narrow particle size distribution (B).

Since cyclodextrins (CDs) are known to form inclusion complexes with certain linear polymer chains such as poly(ethylene glycol) (PEG), this approach was used to create self-assembled aggregates of CD nanostructures.⁶¹ By modifying previously described synthesis procedures, these polyrotaxane structures were reacted with the rigid aromatic linker TFTN to form small and water-dispersible spherical nanoparticles. In this work, the β -CD-PEG inclusion complexes self-assembled with the help of CTAB surfactant into spherical nanostructures and were

subsequently polymerized and cross-linked with TFTN in a suspension of K_2CO_3 in dimethylsulfoxide (DMSO) at 80 °C. Several washing steps were essential to remove the excess of precursors and salt and the included PEG chains, resulting in a pale yellow suspension of β -CD NPs with a yield of 25 %. As can be seen in the scanning electron microscopy (SEM) images in Figure 6.1B the obtained nanoparticles exhibit diameters of 150 to 200 nm with a narrow particle size distribution. Additional transmission electron microscopy (TEM) images can be found in the supporting information. Further characterization of the obtained nanomaterial is shown in Figure 6.2. Dynamic light scattering (DLS, Figure 6.2A) measurements reveal a high colloidal stability with hydrodynamic particle diameters of about 180 nm in water, rendering the obtained β -CD NPs useful for cellular delivery applications. Because of their exceptional colloidal stability without agglomeration in aqueous solutions, no additional hydrophilic coating such as PEGylation is necessary to use them in biotheranostics.⁶² Infrared spectroscopy (Figure 6.2B) was used to follow the formation of β -CD NPs with TFTN as the rigid organic crosslinker. The strong signal (a) at 1035 cm^{-1} corresponds to characteristic R_3C-OH stretching vibrations due to the oligosaccharide rings of the incorporated β -cyclodextrin compounds. Signal (b) at 1260 cm^{-1} is due to saturated aliphatic C-O-C ether vibrations of the sugar rings and newly formed asymmetric alkyl-aryl-ether =C-O-C vibrations of the crosslinked material. The aromatic system of TFTN incorporated into the nanostructure of β -CD NPs is also confirmed by the signals (c) corresponding to aromatic -C=C- stretching vibrations and (d) corresponding to the strong nitrile vibration. The very broad band (e) around 3200 cm^{-1} is attributed to O-H absorption of the incorporated oligosaccharide building blocks. Additional solid-state nuclear magnetic resonance (ssNMR) characterization reveals the presence of both TFTN and β -cyclodextrin in the crosslinked material (see SI). Figure 6.2C displays nitrogen sorption experiments of freeze-dried β -CD NPs and reveals an isotherm with a calculated specific Brunauer-Emmett-Teller (BET) surface area of about 140 m^2/g . The pore size distribution (inset) shows different pore sizes ranging from 1 to 6.5 nm comprising the majority of the accessible pore volume of 0.26 cm^3/g . Thermogravimetric analysis (TGA) of β -CD NPs (Figure 6.2D) indicates the presence of a thermally stable material up to 285 °C and a complete mass loss of almost 100 % up to 900 °C. Zeta potential measurements show that the nanoparticles nanogels have a negative surface charge of about -35 mV at pH 7 due to the free hydroxyl groups of the oligosaccharide compounds. This zeta potential is comparable to other nanocarriers such as unfunctionalized mesoporous silica nanoparticles.⁶³

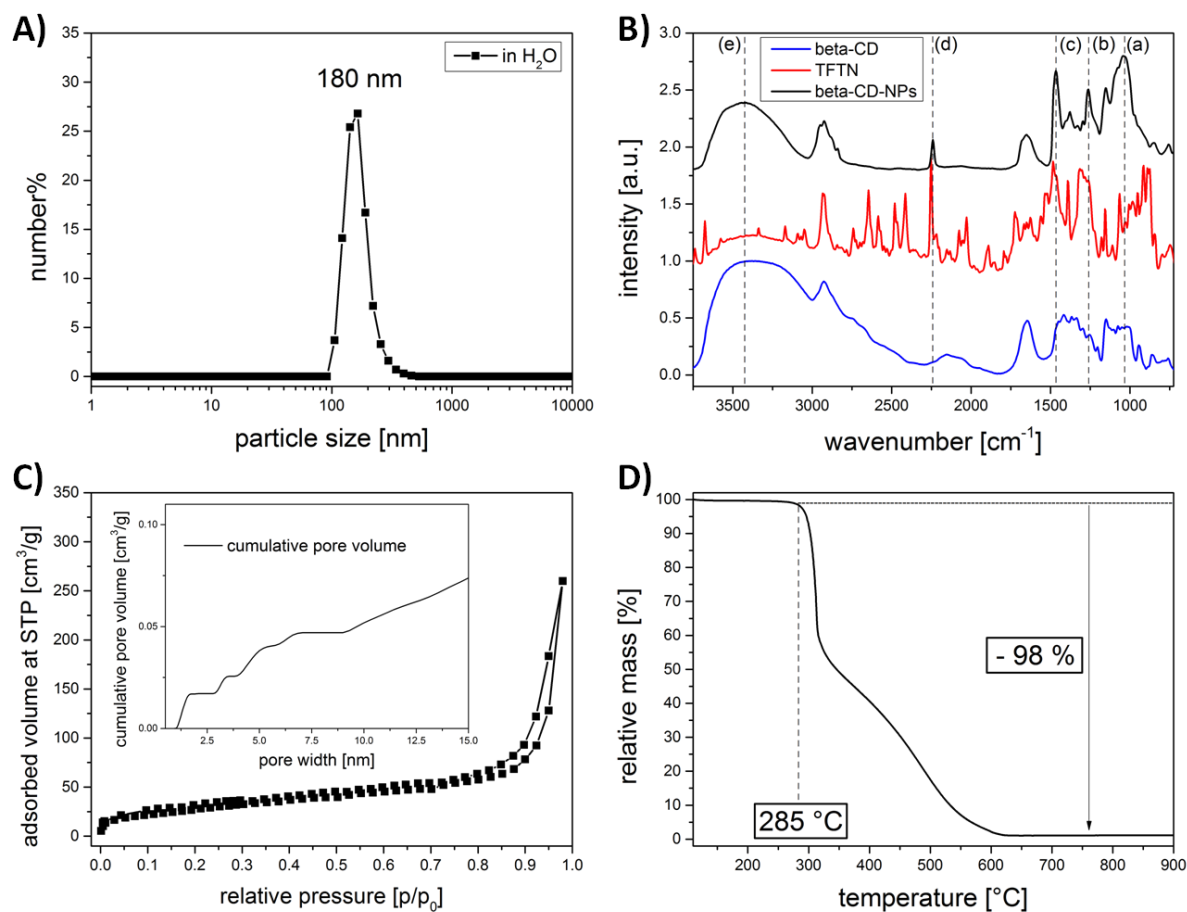


Figure 6.2: Characterization of β -CD NPs. A) Dynamic light scattering (DLS) revealing hydrodynamic particle diameters of about 180 nm in aqueous solution. B) Infrared spectroscopy data of β -CD (blue), TFTN (red) and β -CD NPs (black) with characteristic vibrations. Spectra were normalized and shifted for clarity by 0.75 a.u. along the y-axis. C) Nitrogen sorption isotherm and pore size distribution (inset) of β -CD NPs. D) Thermogravimetric analysis (TGA) up to 900 °C of β -CD NPs.

With this size and zeta potential as well as their porosity maintained even in the dry state, the particles reveal promising properties for drug delivery purposes. Therefore, the synthesized nanoparticles were subsequently used for *in vitro* drug delivery experiments. First, the cell uptake kinetics of rhodamine-labeled β -CD nanoparticles was studied on HeLa cells. To obtain labeled nanoparticles, the free nitrile groups of the incorporated organic crosslinker can be used to covalently attach specific dye molecules. Here, the fluorescent tetramethylrhodamine (TAMRA) azide was used under mild reaction conditions in a zinc-catalyzed formation of a tetrazole-ring with the free nitrile groups of β -CD nanoparticles.⁶⁴ The formation of the compound was followed with IR spectroscopy (see SI). After several washing steps the particles were used for *in vitro* experiments.

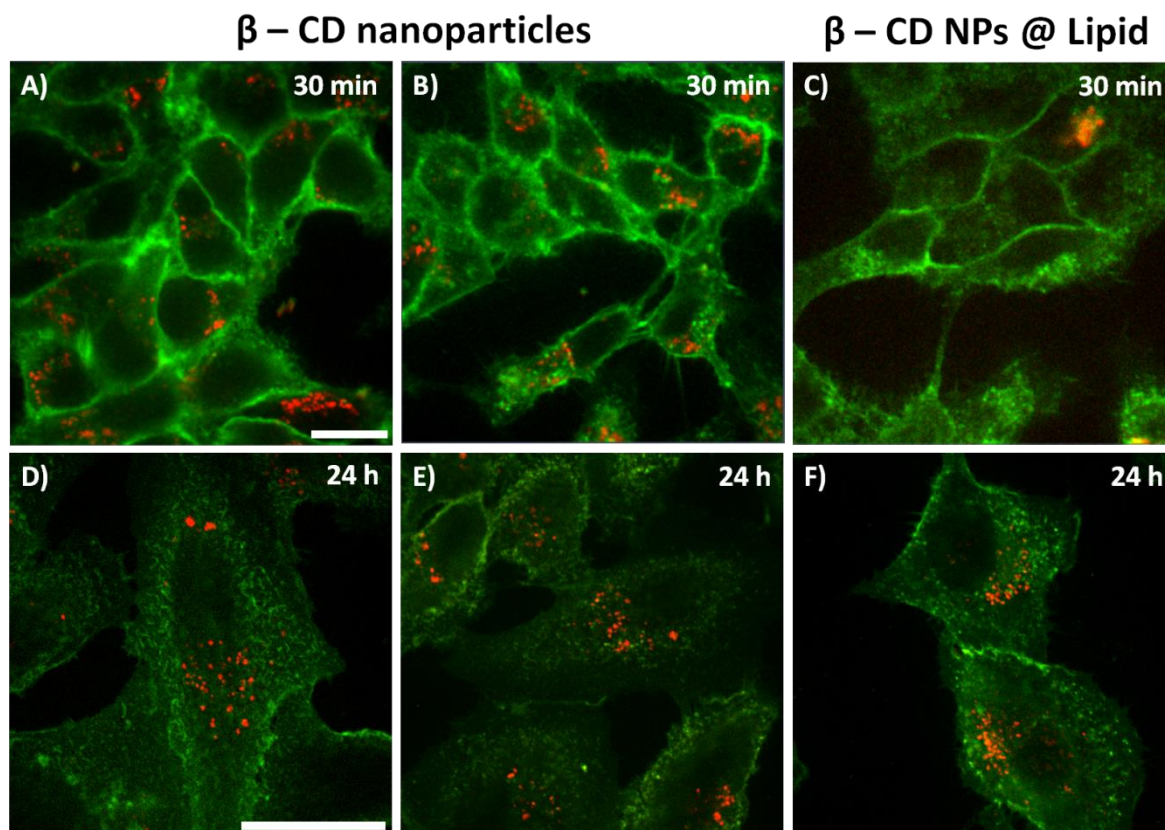


Figure 6.3: Upper panel: *In vitro* cell uptake of rhodamine-labeled β -CD nanoparticles (red) without additional coating (A, B) and with lipid coating (C) after 30 min of incubation on WGA-stained HeLa cells (green). The blurry red spot in C) results from an accumulation of particles on top of the cells. Lower panel: *In vitro* cell uptake of rhodamine-labeled β -CD nanoparticles (red) without additional coating (D, E) and with lipid coating (F) after 24 h of incubation on WGA-stained HeLa cells (green). Scale bar represents 10 μ m, respectively.

The upper panel of Figure 6.3 shows representative confocal microscopy images of particle uptake by HeLa cells after just 30 min of incubation. The red-fluorescent material was efficiently internalized by cancer cells - even after very short incubation times of 30 minutes (Figure 6.3 A, B). Compared to the uptake of other nanomaterials, the internalization was very fast, possibly due to the oligosaccharide nature of the particles and sugar-receptor mediated endocytosis.^{65, 66} As a reference experiment, the particles were coated with a lipid bilayer in order to compare cell uptake kinetics with as-synthesized β -CD nanoparticles (see Figure 6.3 C and F, synthesis and characterization of lipid coating see SI). After 30 min, exclusively uncoated β -CD nanoparticles were taken up by HeLa cells, whereas after 24 h of incubation both particle types are internalized. The experiment leads us to the assumption that the oligosaccharides are effectively taken up via sugar receptors and that the oligosaccharides can be shielded by the lipid coating resulting in slower cell uptake compared to the sugar-receptor mediated

endocytosis of the uncoated particles. This suggests that an additional surface coating for as-synthesized β -CD nanoparticles is counterproductive for cellular uptake.

In order to obtain more insights into the endocytosis pathway of β -CD nanoparticles, an *in vitro* competition experiment was performed. For this purpose, prior to the particle incubation the sugar receptors on the external cell surface of HeLa cells were saturated by adding concentrated aqueous solutions of different mono- and oligosaccharides, namely D-glucose, D-L-arabinose, 2-deoxy-D-glucose and β -cyclodextrin (see SI, Figure 6.9). In all cases the particle uptake was hindered when the receptors were blocked, confirming our hypothesis that the endocytosis of β -CD nanoparticles is mediated via a specific sugar-receptor mediated cell uptake.

Next, the drug delivery and release properties of β -CD nanoparticles were evaluated by the loading and release of different guest molecules, namely Hoechst 33342 as nuclei staining dye and doxorubicin as model chemotherapeutic agent. Rhodamine-labeled β -CD NPs were loaded with Hoechst 33342 or doxorubicin and subsequently used for *in vitro* release experiments. The inclusion capability of the β -CD nanoparticles was evaluated by the loading and release of different guest molecules. Using the porous β -CD cavities that were liberated from the inclusion of PEG, the β -CD nanoparticles could be loaded with either Hoechst 33342 as a nuclei staining dye or with doxorubicin as a chemotherapeutic agent, respectively.

First, we studied loading and release of Hoechst 33342. Strikingly, the benzimidazole-containing compound is effectively loaded and efficiently released after particle endocytosis due to the acidification in the lysosomal compartments that destroys the hydrophobic interaction of Hoechst 33342 and the particle cavities (Figure 6.4).^{67, 68} Since Hoechst 33342 is membrane-permeable, it is able to penetrate the lysosomal membrane and to efficiently stain the nuclei of HeLa cells within very short time periods of less than 10 minutes. As a reference experiment the used particle solution was centrifuged after 2 h and the supernatant was incubated on HeLa cells. No nuclei staining could be observed. Since Hoechst 33342 is a live cell stain, any molecules in the solution would have stained the nuclei. The absence of any staining resulting from the supernatant demonstrates that no cargo molecules were released prematurely and that the *in vitro* nuclei staining is due to the acidification of nanoparticles in the endosomal compartments that triggers the release of the dye. This rapid and efficient delivery and release of Hoechst 33342 as model cargo suggests that the newly synthesized particles can serve as a promising drug delivery platform with controlled release mechanism.

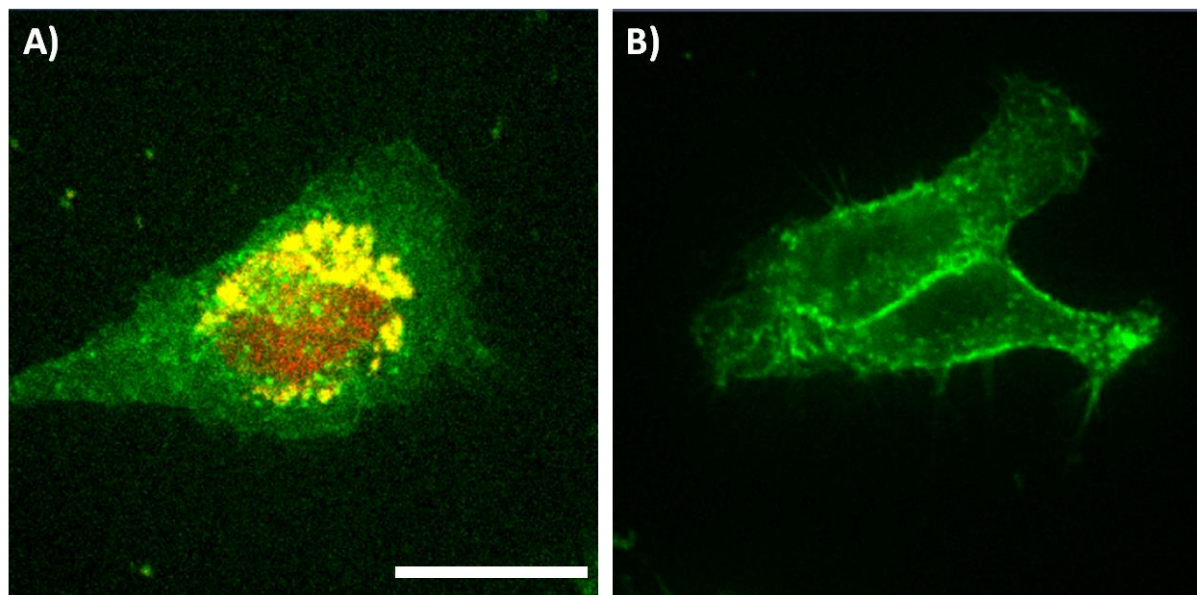


Figure 6.4: *In vitro* Hoechst 33342 release on HeLa cells. A) Rhodamin-labelled β -CD NPs (yellow) released Hoechst 33342 nuclei staining (red) on WGA-stained HeLa cells (green) after just 2 h of incubation time. B) As a control experiment the supernatant of centrifuged particles (after 2 h) was added to HeLa cells showing no nuclei staining, i.e. no premature release of cargo molecules. Scale bar represents 10 μ m.

In order to investigate the ability of our newly developed drug delivery system to transport and release chemotherapeutics and to affect cancer cells with their cargo, we replaced the model cargo Hoechst 33342 with doxorubicin (DOX), a classic cytostatic agent. DOX is known to form inclusion complexes based on hydrophobic interactions with β -cyclodextrin structures similarly to Hoechst 33342 and should therefore exhibit a similar loading and release behavior. Additionally, it should reveal a pH-responsive release behavior due to enhanced solubility when protonated.⁶⁹⁻⁷¹

Hence, the loading and release behavior was tested in a cuvette experiment first. For this, we used our custom-made cuvette setup to measure the time-based pH-dependent release of fluorescent doxorubicin.⁷¹ DOX-loaded nanoparticles were put into a cap, which is sealed with a dialysis membrane (molecular weight cutoff = 14,000 Da) and put on top of a cuvette. Only released doxorubicin is able to diffuse through the pores of the membrane and is measured with a fluorescence spectrometer, while the nanoparticles are prevented from diffusing into the cuvette by the dialysis membrane. To prove successful loading without leakage of the cargo at pH 7.4, a control experiment was performed with HBSS buffer. Furthermore, to prove the efficient release of doxorubicin at lower pH, a second experiment was performed in parallel

with Citric Acid Phosphate Buffer at pH 5. The corresponding release curves are shown in Figure 6.5. They exhibit only a small amount of residual, unbound DOX released at pH 7.4 and efficient release at pH 5.

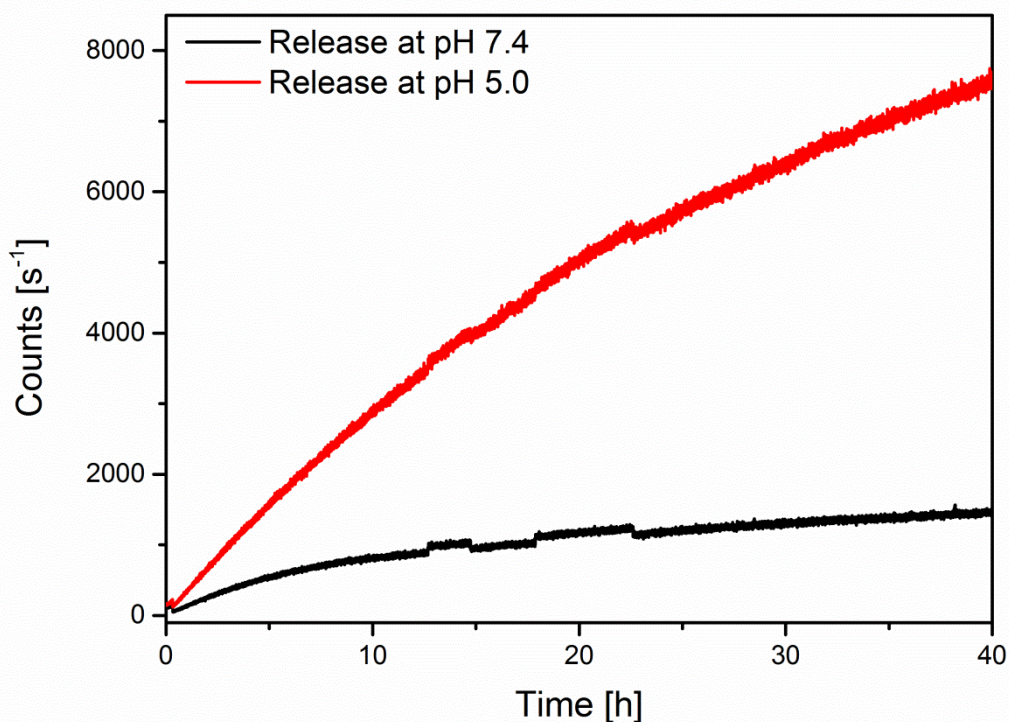


Figure 6.5: Time-based release measurements of doxorubicin at pH 7 (black curve) and pH 5 (red curve) in fluorescence spectrometre.

Next, the effect of particles containing DOX on HeLa cells was investigated. Free DOX is membrane-permeable and is able to induce an uncontrolled cell death within a few hours. Thus, we expected it to escape from the endosomal membrane when released from the particle in the lysosome and to subsequently induce cell death within a few hours after endosomal escape.

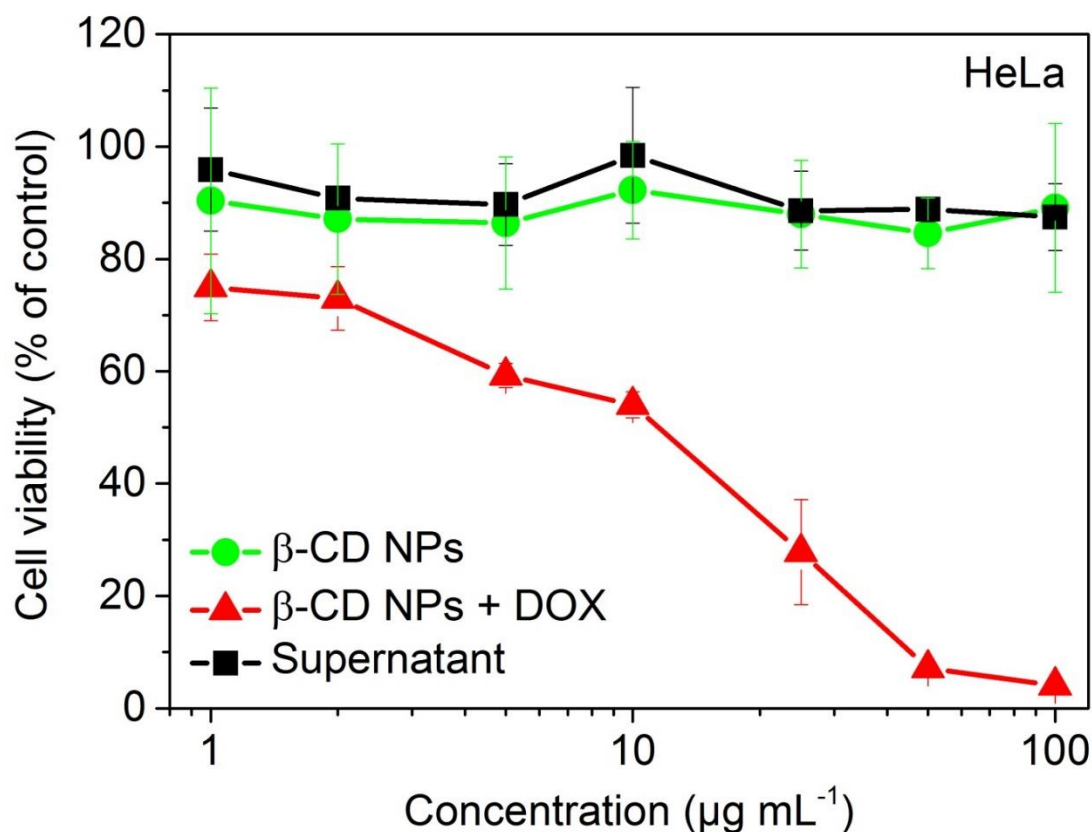


Figure 6.6: Dose-dependent cell-viability study on HeLa cells after 24 h of incubation with β -CD NPs, DOX-loaded β -CD NPs and the supernatant after centrifugation as a reference.

Indeed, our newly developed β -CD NPs provided intracellular DOX release and caused efficient cell death after 24 h of incubation with a calculated IC_{50} value of $7.23 \mu\text{g/mL}$ for the DOX-loaded β -CD particles. In addition, the nanoparticles exhibited a high DOX-loading capacity of about 23 wt% (see SI, Figure 6.10). The dose-dependent cell viability assay demonstrates that DOX was delivered in a controlled manner via the particles and released only after endosomal acidification. In contrast, as-synthesized β -CD NPs without any cargo show good biocompatibility in the dose-dependent cell viability studies (Figure 6.6). As a control experiment the DOX-loaded nanoparticles were centrifuged after 24 h storage and the respective amount of supernatant was incubated on HeLa cells. This control revealed good biocompatibility, i.e. no prematurely released cargo molecules were present. This experiment shows the great potential of β -CD NPs to efficiently deliver chemotherapeutics to cancer cells without premature release. The newly developed biocompatible carrier system provides the ability to act as a general platform for cellular delivery applications with exceptionally fast cell uptake kinetics.

6.3 Conclusion

To conclude, we have developed a novel nanomaterial consisting of covalently crosslinked β -cyclodextrin molecules as the main organic component. The obtained nanoparticles are small (~150 nm) and highly dispersible in aqueous solutions. They exhibit very fast cell uptake kinetics due to sugar-receptor mediated endocytosis and can be covalently labeled with dye molecules to effectively track them in *in vitro* experiments. Furthermore, the porous cavities of the particles can be loaded with different cargo molecules, which are subsequently released in the endosomal cell compartments due to acidification. This triggered release mechanism allows us to show efficient nuclei staining with Hoechst 33342 dye and effective cancer cell killing with doxorubicin as cargos, respectively. Thus, the nanoparticles show great potential for future applications as a biocompatible drug carrier system.

6.4 Experimental Part

Materials. β -cyclodextrin (97 %, Sigma Aldrich), tetrafluoroterephthalonitrile (TFTN, 98 %, Alfa Aesar), polyethylene glycol 2000 (PEG2000, BioUltra, Sigma Aldrich), potassium carbonate (K_2CO_3 , 99.5 %, Grüssing GmbH), tetramethylrhodamine 5-carboxamido-(6-azidohexanyl) (TAMRA azide, Base click), doxorubicin hydrochloride (98 % HPLC, Sigma Aldrich), D-glucose (Sigma Aldrich), D-L-arabinose (Sigma Aldrich), 2-deoxy-D-glucose (Sigma Aldrich), Hoechst 33342 trihydrochloride (ThermoFisher Scientific), cetyl trimethylammonium bromide (Sigma Aldrich), wheat germ agglutinin, Alexa Fluor® 488 conjugate (lifeTechnologies), Dulbecco's modified Eagle's medium (DMEM) (lifeTechnologies), Hank's balanced salt solution (HBSS-buffer, Sigma Aldrich) were used as received. Ethanol (EtOH, absolute, Aldrich), hydrochloric acid (1 M, Bernd Kraft), dimethylsulfoxide (DMSO, anhydrous, >99.9 %, Sigma Aldrich) and dimethylformamide (DMF, >99.9 %, anhydrous, Sigma Aldrich) were used as solvents without further purification. Bidistilled water was obtained from a millipore system (Milli-Q Academic A10).

Characterization. DLS and zeta potential measurements were performed on a Malvern Zetasizer Nano instrument equipped with a 4 mW He-Ne-Laser (633 nm) and an avalanche photodiode detector. DLS measurements were directly recorded in diluted colloidal suspensions of the particles at a concentration of 1 mg/mL. Zeta potential measurements were performed using the add-on Zetasizer titration system (MPT-2) based on diluted NaOH and HCl as titrants. For this purpose, 1 mg of the particles was diluted in 10 mL bi-distilled water. Thermogravimetric analyses (TGA) of the bulk-extracted samples (approximately 10 mg) were recorded on a Netzsch STA 440 C TG/DSC. The measurements proceeded at a heating rate of 10 °C/min up to 900 °C in a stream of synthetic air of about 25 mL/min. Nitrogen sorption measurements were performed on a Quantachrome Instrument NOVA 4000e at -196 °C. Sample outgassing was performed for 12 hours at a vacuum of 10 mTorr at 120 °C. Pore size and pore volume were calculated by a QSDFT equilibrium model of N_2 on carbon, based on the adsorption and desorption branch of the isotherms. A BET model was applied in the range of 0.05 – 0.20 p/p_0 to evaluate the specific surface area. Infrared spectra of dried sample powder were recorded on a ThermoScientific Nicolet iN10 IR-microscope in reflection-absorption mode with a liquid- N_2 cooled MCT-A detector. Cross-polarized ^{13}C -MAS NMR

measurements were performed on a Bruker DSX Avance500 FT spectrometer (11.74 T) in a 4 mm ZrO₂ rotor. The spinning rate was 10 kHz and a total number of 256 scans was recorded. The used contact time was 2 ms and the recycle delay was 1 s. Scanning electron microscopy (SEM) was performed on a FEI Helios instrument at an acceleration voltage of 2.5 kV. For this purpose the samples were put on an adhesive graphite film and sputtered twice with carbon with a BALTEC MED 020 Coating System. Transmission electron microscopy (TEM) data were obtained with a FEI Titan Themis 60–300 microscope at an acceleration voltage of 80 kV. UV/Vis measurements were performed on a Perkin Elmer Lambda 1050 UV-Vis/NIR spectrophotometer with a deuterium arc lamp and a tungsten filament equipped with a 150 mm integrating sphere and an InGaAs detector. Time-based fluorescence release experiments were performed at 37 °C on a PTI spectrofluorometer equipped with a xenon short arc lamp (UXL-75XE USHIO) and a photomultiplier detection system (Model 810/814).

Synthesis of β -CD NPs. In a 40 mL polypropylene reactor, 400 mg β -cyclodextrin (0.35 mmol), 200 mg tetrafluoroterephthalonitrile (TFTN, 1.00 mmol), 600 mg K₂CO₃ (4.34 mmol), 50 mg polyethylene glycol (PEG₂₀₀₀) and 50 mg cetyltrimethylammonium bromide (CTAB, 0.14 mmol) were mixed with 15 mL anhydrous DMSO. The mixture was sonicated (15 min) and subsequently stirred at 900 rpm and 80 °C for 3 h. The orange suspension was cooled to room temperature and 15 mL bidistilled water and 15 mL hydrochloric acid (1 M) were slowly added to the reaction mixture. After centrifugation for 15 minutes at 7830 rpm (7197 rcf) the isolated light yellow solid was washed extensively with water (2 x 40 mL), HCl (1 M, 2 x 40 mL) and ethanol (2 x 40 mL) followed by centrifugation steps (15 min, 7197 rcf), respectively. Finally, the pale yellow powder was dispersed in 10 mL bidistilled water and used for further characterization (150 mg, 25 % yield).

Rhodamine-labelling of β -CD NPs. 1 mg of β -CD NPs in ethanolic solution were mixed with 2 μ L TAMRA-azide (2 mg/mL in anhydrous DMF) and a catalytic amount of zinc(II) acetate dihydrate. The mixture was shaken at 37 °C for 12 h and afterwards washed extensively with ethanol and water (centrifugation steps: 14,000 rpm, 16,837 rcf, 4 min) until no fluorescence could be detected in the supernatant. Finally, the particles were redispersed in 1 mL H₂O and used for *in vitro* uptake experiments.

Cargo loading of β -CD NPs. An aqueous solution of 1 mg/mL β -CD NPs was centrifuged (14,000 rpm, 16,837 rcf, 4 min), washed once with 500 μ L HBSS buffer and redispersed again in a mixture containing 500 μ L HBSS buffer with either 5 μ L doxorubicin hydrochloride (100 mg/mL in DMSO) or 500 μ L Hoechst 33342 (10 mg/mL in water), respectively. The nanoparticles were incubated for 3 h and subsequently washed extensively with HBSS buffer (14,000 rpm, 16,837 rcf, 4 min) until no fluorescence could be detected in the supernatant. Finally, the loaded nanoparticles were redispersed in 1 mL HBSS buffer and used for further *in vitro* release experiments. As a reference sample the particles were centrifuged (14,000 rpm, 16,837 rcf, 4 min) after certain time points and the corresponding amount of supernatant was used on HeLa cells.

Lipid preparation. The following lipids were used: DOPC (1,2-dioleoyl-*sn*-glycero-3-phosphocholine, Avanti Polar Lipids), DOTAP (1,2-dioleoyl-3-trimethylammonium propane, Avanti Polar Lipids). The amount of 2.5 mg of the individual lipids was dissolved in a 1 mL mixture of 40 %vol absolute ethanol and 60 %vol MQ water (conc. 2.5 mg/mL). The amount of 1 mg of nanoparticles in aqueous solution was centrifuged (4 min, 8609 rcf, at 15 °C) and redispersed in 100 μ L of the above DOTAP solution. Upon addition of 900 μ L MQ water (pH adjusted to 9.4 with sodium hydroxide) the formation of the first SLB layer on the external surface of the nanoparticles was induced. After centrifugation (4 min, 8609 rcf, at 15 °C) and redispersion in 100 μ L of a 1:1 mixture of the above DOPC/DOTAP solutions, the formation of a second layer around the nanoparticles was induced by adding 900 μ L HBSS buffer.

Cell Culture. HeLa cells were grown in Dulbecco's modified Eagle's medium (DMEM) (lifeTechnologies) supplemented with 10 % fetal bovine serum (FBS) and incubated at 37 °C under a 5 % CO₂ humidified atmosphere. For live cell imaging the cells were seeded on ibidi 8-well μ -slides 24 h before adding particles, at a cell density of 5000 cells per well.

Uptake studies and *in vitro* Cargo release. The cells were incubated with 2 μ L or 5 μ L of a 1 mg/mL β -CD NPs solution for 0.5 – 24 h prior to the measurements at 37 °C under a 5% CO₂ humidified atmosphere. During the measurements all cells were kept on a heated microscope stage at 37 °C under a 5% CO₂ humidified atmosphere. For imaging, the cells were stained with 1 μ L of a WGA solution and were incubated for 2-5 min at 37°C in a 5% CO₂ humidified atmosphere and then washed twice with DMEM. In addition to the uptake studies, the supernatant of the stock solution was similarly investigated for fluorescence and nucleus

staining. The subsequent imaging was performed as described in the spinning disk confocal microscopy section.

Spinning disc confocal microscopy. Confocal microscopy for live-cell imaging was performed on a setup based on the Zeiss Cell Observer SD utilizing a Yokogawa spinning disk unit CSU-X1. The system was equipped with a 1.40 NA 63x Plan apochromat oil immersion objective from Zeiss. For all experiments the exposure time was 0.2 s and z-stacks were recorded. Hoechst 33342 was imaged with light at 405 nm and a power density of approximately 0.16 W/mm², WGA was imaged at 488 nm with approximately 0.48 W/mm², and Rhodamin was excited at 561 nm with 11 mW/mm². In the excitation path a quad-edge dichroic beamsplitter (FF410/504/582/669-Di01-25x36, Semrock) was used. Separate images for each fluorescence channel were acquired using two separate electron multiplier charge coupled device (EMCCD) cameras (Photometrics EvolveTM).

Cuvette release experiments. To show the successful uptake and release of the cargo, the doxorubicin loaded particles were transferred to a custom made Teflon cap fitting on a fluorescence cuvette. The cap was sealed with a dialysis membrane (ROTH Visking type 8/32, MWCO 14,000 g/mol) and placed on top of a fluorescence cuvette filled with 3 mL of HBSS buffer to show the successful uptake of doxorubicin and with 3 mL of Citric Acid Phosphate Buffer at pH 5 to prove the pH-dependent release. The excitation wavelength was set to $\lambda = 488$ nm and the emission fluorescence intensity was recorded at $\lambda = 590$ nm. All slits were adjusted to 2.0 mm. The measurement was continuously run for more than 40 hours (Figure 6.5).

Cell viability studies. For MTT-Assays we seeded 5000 HeLa cells per well containing 100 μ L of high glucose DMEM medium and treated them with particles 24 h after seeding. After 24 h of incubation the cells were washed twice with HBSS buffer. 100 μ L of 3-(4,5-dimethylthiazol-2-yl)-2,5-diphenyltetrazolium bromide (MTT, 0.5 mg/mL in DMEM) was added to each well of the nanoparticle-treated cells and incubated for further 2 h. Unreacted MTT and medium were removed and the 96-well plates were stored at -80 °C for at least 1 h. Then, 100 μ L DMSO was added to each well. The absorbance was read out by a Tecan plate reader at 590 nm with a reference wavelength of 630 nm. All studies were performed in triplicates. The IC₅₀ and the standard mean deviations were calculated using the Origin 9.0 software.

6.5 Appendix

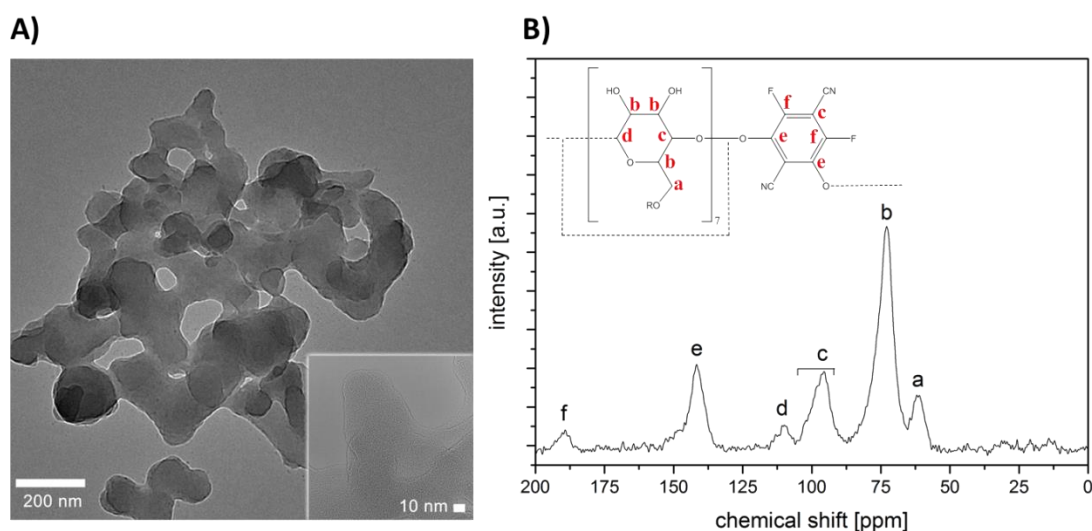


Figure 6.7: A) Transmission electron microscopy (TEM) image of β -CD NPs revealing a particle size distribution of around 100-200 nm. B) ^{13}C -MAS solid-state nuclear magnetic resonance (ssNMR) spectrum of β -CD NPs indicating the successful incorporation of the oligosaccharide compounds and the rigid organic linker into the crosslinked material.

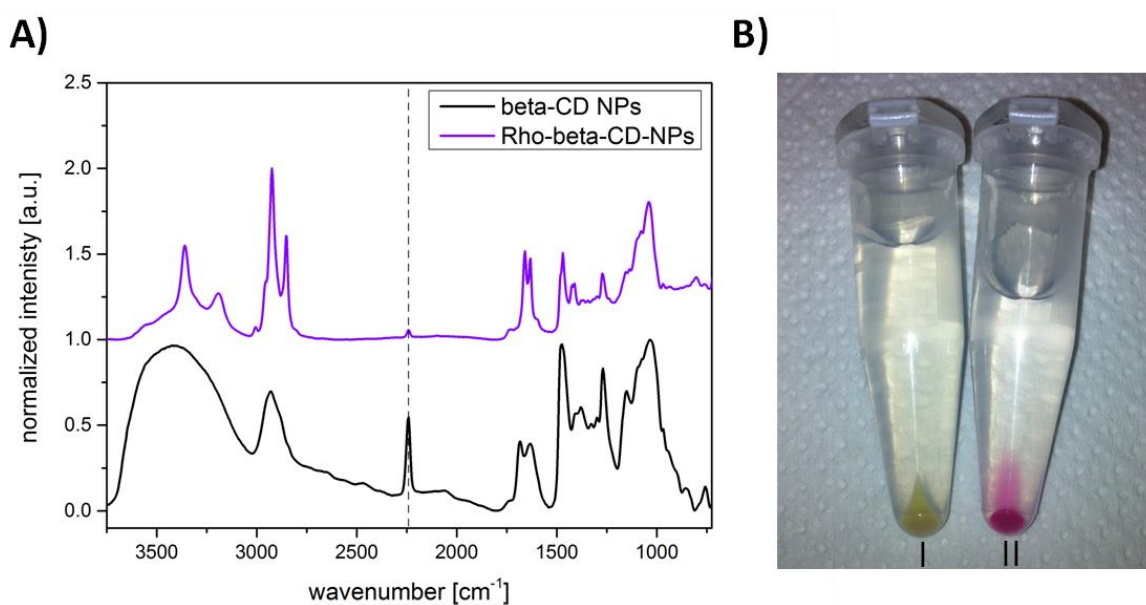


Figure 6.8: A) IR spectroscopy data of as-synthesized β -CD NPs (black) and rhodamine-labeled nanoparticles (violet). The successful attachment can be followed by the vanishing nitrile stretching vibration at 2245 cm^{-1} due to the covalent binding of the dye's azide groups to form tetrazole rings in a 1,3-dipolar cycloaddition. Spectra

were normalized and shifted for clarity by 1.0 along the y-axis. B) Photograph of 1 mg of as-synthesized pale yellow β -CD NPs (I) and pink labeled Rho- β -CD NPs (II) in water after centrifugation, respectively.

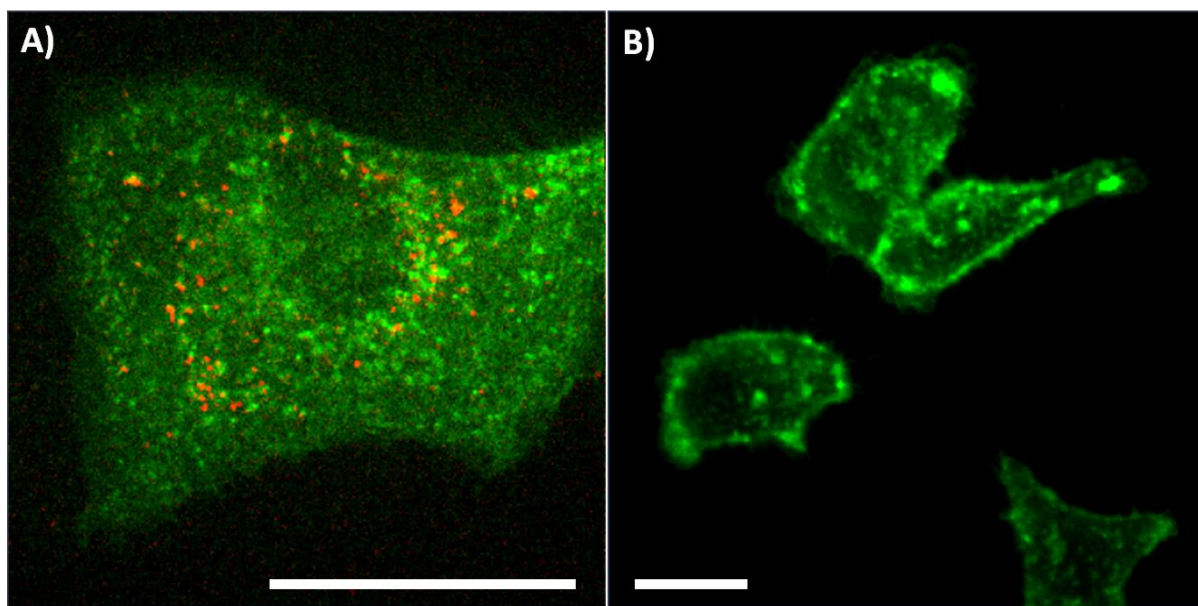


Figure 6.9. Fluorescence microscopy of HeLa cells incubated with rhodamine-labeled β -CD NPs (red) after 30 min (A), or pretreated with free inhibitors (e.g. β -cyclodextrin) for 30 min and incubated with rhodamine-labeled β -CD NPs for 30 min afterwards (B). Cell membranes are stained with WGA (green). Scale bars represent 10 μ m each.

To test the targeting of sugar receptors with β -CD nanoparticles on HeLa cells, the receptors were either blocked or free. The functionality was evaluated in a receptor competition experiment. For this purpose, one part of the HeLa cells was pre-incubated with 5 μ L of an inhibitor solution (10 mM aqueous solutions of D-glucose, D-L-arabinose, 2-deoxy-D-glucose or β -cyclodextrin, respectively), to block the receptors, for 30 min at 37 $^{\circ}$ C under a 5% CO₂ humidified atmosphere. Then the HeLa cells were incubated with 5 μ g of rhodamine-labeled β -CD-NPs for 30 min at 37 $^{\circ}$ C under a 5% CO₂ humidified atmosphere. For staining the cell membrane, the cells were incubated with WGA for 2 min. The cells were washed three times with PBS, fresh medium was added and subsequently the cells were imaged. Clearly an enhanced sugar receptor-mediated cell uptake can be seen when the sugar receptors are available on the cell surface (A) compared to blocked receptors (B).

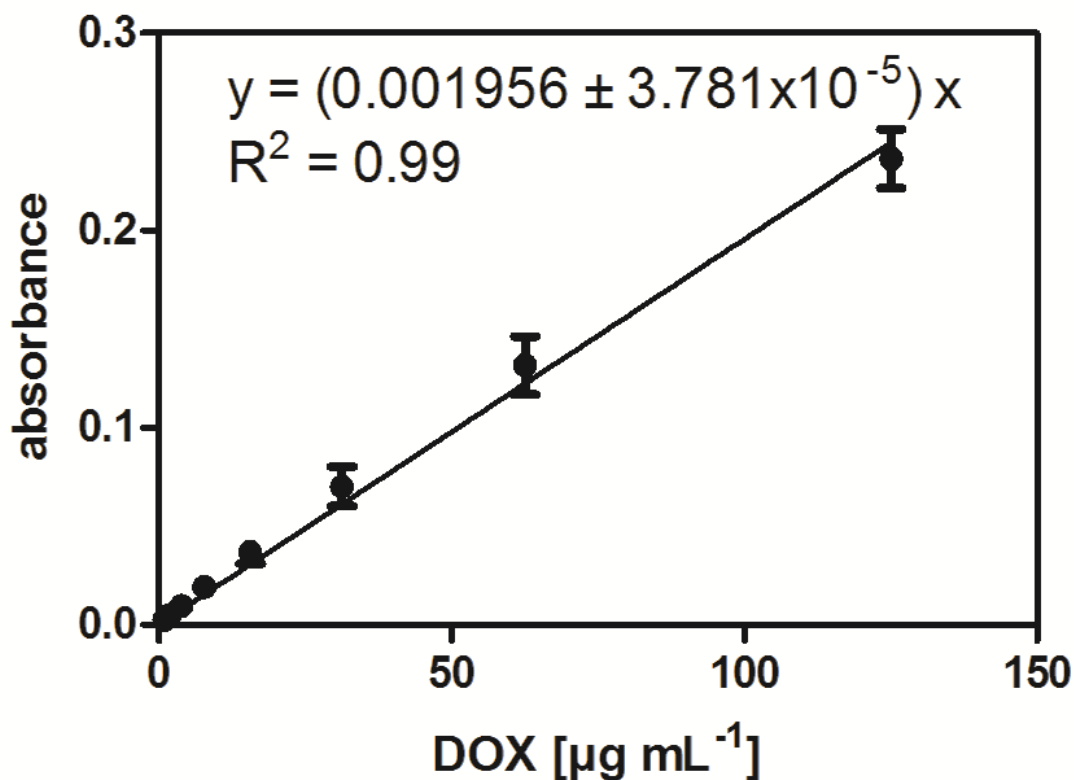


Figure 6.10: Calibration curve for doxorubicin loading capacity measured at 500 nm.

The concentration of the DOX loading solution was 0.5 mg/mL with 0.5 mg nanoparticles. After several washing steps the supernatants were collected and revealed an added-up absorbance of 0.750 ± 0.008 . By using the linear regression fit of the calibration curve this leads to a DOX content of 383 $\mu\text{g/mL}$ in the collected supernatants. Therefore, the total amount of loaded DOX was 117 μg per 0.5 mg nanoparticles leading to a loading capacity of 23 wt%.

To test the pH-responsive release of Hoechst from the nanoparticles, Hoechst-loaded particles were redispersed in 1 ml Potassiumphosphatebuffer at pH 7.4, 6.0, 4.0 respectively. After a 20-minute incubation, particle solutions were centrifuged to separate particles and supernatant and the UV-Vis spectrum of the supernatant containing the released Hoechst was measured. Release increased with decreasing pH as shown in Figure 6.11.

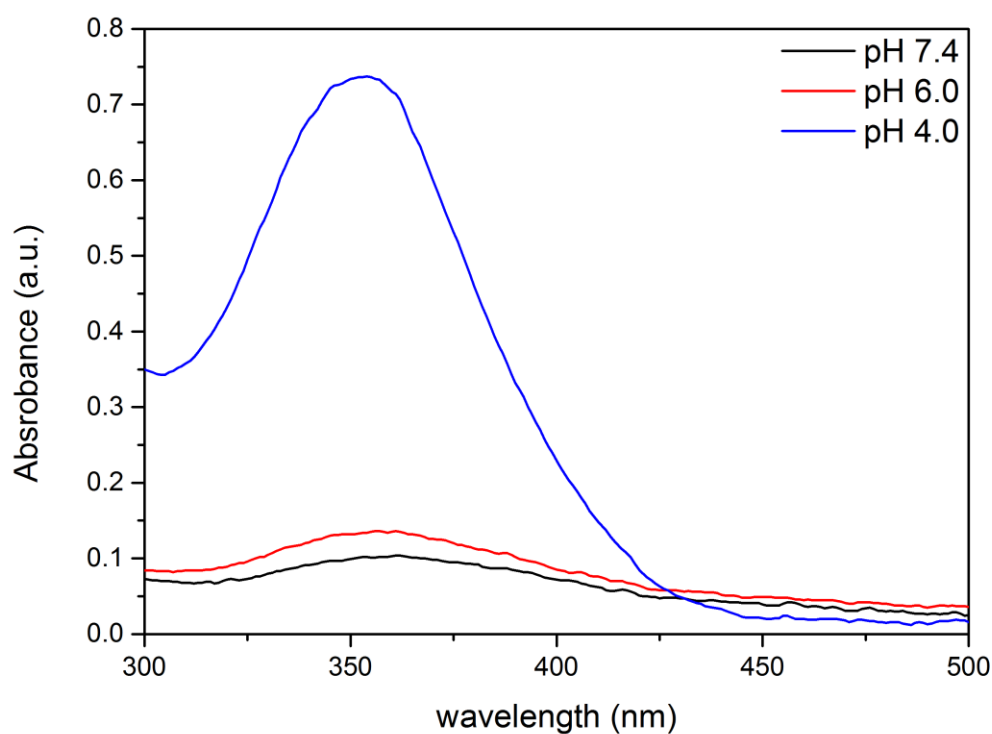


Figure 6.11: UV-Vis measurement of Hoechst released from nanoparticles at various pH values.

To investigate if the coating of the particles with liposomes was successful, fluorescence colocalization experiments were performed (Figure 6.12). For this purpose β -cyclodextrin particles were stained with TAMRA, a rhodamine dye, and the liposomes were marked with WGA 488. In the case of a successful coating the dyes should be colocalized, while an independent distribution indicates a failure to coat the particles. The images (A, B) show that both the liposomes and particles were stained successfully and the merged image (C) shows that both fluorescent stains are colocalized, proving that the particles were successfully coated with liposomes. The slight offset in the positions of the particles and the liposomes between both channels is caused by the Brownian motion of the particles, while switching to a different excitation wavelength to take the second image. Control experiments confirmed that there is no spectral overlap between both dyes, meaning the observed colocalization of the signals is caused by the successful coating.

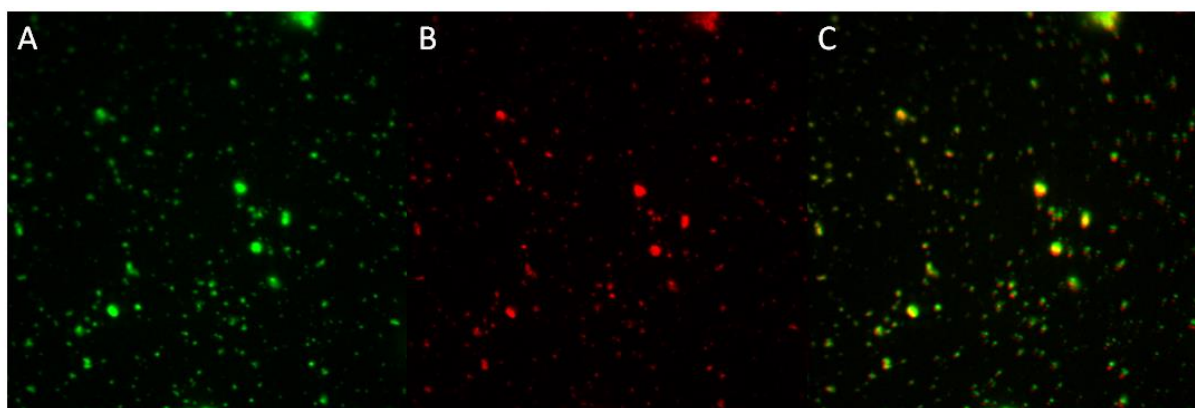


Figure 6.12: Fluorescence Colocalization Images of the liposome coated CD NPs. A) liposomes labeled with WGA 488, B) CD NPs labeled with TAMRA, C) merged image of both channels.

A further proof for successful lipid coating is a comparison of the zeta potentials of lipid-coated and non-coated particles. The β -CD-NPs without any coating show a more or less constant zeta potential over the whole pH-range from 3 to 8 of around 0 mV. After successful lipid coating the measured zeta potential is tremendously increased. This results from the positive charge of the DOTAP lipid and thus confirms successful coating.

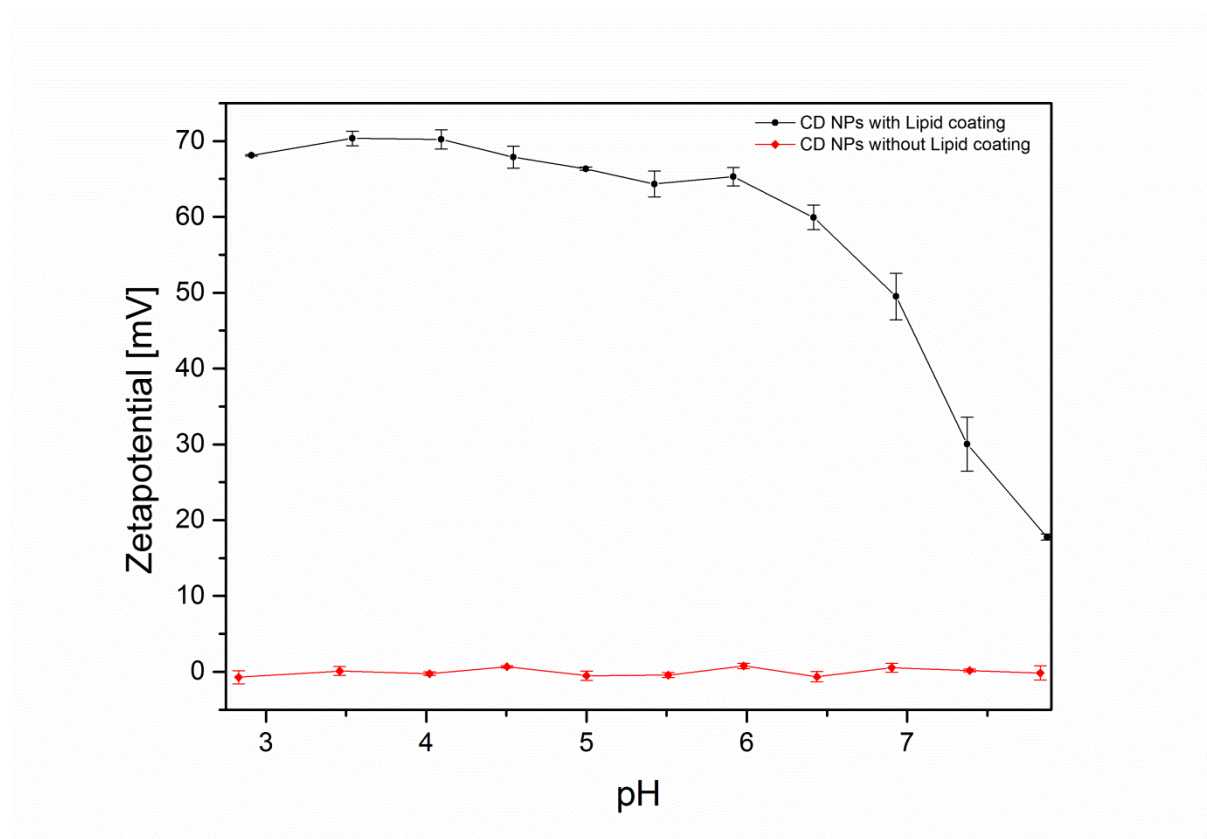


Figure 6.13: Titration curves of coated and non-coated CD NPs.

6.6 References

1. Ambrogio, M.W., Thomas, C.R., Zhao, Y.-L., Zink, J.I. & Stoddart, J.F. Mechanized Silica Nanoparticles: A New Frontier in Theranostic Nanomedicine. *Accounts of Chemical Research* **44**, 903-913 (2011).
2. Wang, Y. et al. Mesoporous silica nanoparticles in drug delivery and biomedical applications. *Nanomedicine: NBM* **11**, 313-327 (2015).
3. Singh, S., Pandey, V.K., Tewari, R.P. & Agarwal, V. Nanoparticle Based Drug Delivery System: Advantages and Applications. (2011).
4. Singh, R. & Lillard, J.W. Nanoparticle-based targeted drug delivery. *Exp. Mol. Pathol.* **86**, 215-223 (2009).
5. Cauda, V. et al. Colchicine-loaded lipid bilayer-coated 50 nm mesoporous nanoparticles efficiently induce microtubule depolymerization upon cell uptake. *Nano Lett.* **10**, 2484-2492 (2010).
6. Mackowiak, S.A. et al. Targeted Drug Delivery in Cancer Cells with Red-Light Photoactivated Mesoporous Silica Nanoparticles. *Nano letters* **13**, 2576-2583 (2013).
7. Niedermayer, S. et al. Multifunctional polymer-capped mesoporous silica nanoparticles for pH-responsive targeted drug delivery. *Nanoscale* **7**, 7953-7964 (2015).
8. Croissant, J. et al. Two-Photon-Triggered Drug Delivery via Fluorescent Nanovalves. *Small* **10**, 1752-1755 (2014).
9. Rühle, B., Saint-Cricq, P. & Zink, J.I. Externally Controlled Nanomachines on Mesoporous Silica Nanoparticles for Biomedical Applications. *ChemPhysChem* **17**, 1769-1779 (2016).
10. van Rijt, S.H. et al. Protease-Mediated Release of Chemotherapeutics from Mesoporous Silica Nanoparticles to ex Vivo Human and Mouse Lung Tumors. *ACS nano* **9**, 2377-2389 (2015).
11. Zhao, Y., Vivero-Escoto, J.L., Slowing, I.I., Trewyn, B.G. & Lin, V.S.Y. Capped mesoporous silica nanoparticles as stimuli-responsive controlled release systems for intracellular drug/gene delivery. *Expert Opin. Drug Delivery* **7**, 1013-1029 (2010).
12. Zheng, Q. et al. A pH-responsive controlled release system using layered double hydroxide (LDH)-capped mesoporous silica nanoparticles. *J. Mater. Chem. B* **1**, 1644-1648 (2013).
13. Datz, S. et al. Genetically designed biomolecular capping system for mesoporous silica nanoparticles enables receptor-mediated cell uptake and controlled drug release. *Nanoscale* **8**, 8101-8110 (2016).
14. Croissant, J. et al. Biodegradable ethylene-bis(propyl)disulfide-based periodic mesoporous organosilica nanorods and nanospheres for efficient in-vitro drug delivery. *Adv. Mater.* **26**, 6174-6180 (2014).
15. Croissant, J.G. et al. Fluorescent periodic mesoporous organosilica nanoparticles dual-functionalized via click chemistry for two-photon photodynamic therapy in cells. *J. Mater. Chem. B* **4**, 5567-5574 (2016).
16. Croissant, J. et al. Two-Photon-Triggered Drug Delivery in Cancer Cells Using Nanoimpellers. *Angew. Chem. Int. Ed.* **52**, 13813-13817 (2013).
17. Mauriello-Jimenez, C. et al. Core-Shell Nanodiamonds-Periodic Mesoporous Organosilica Nanoparticles for Two-Photon Imaging, Photodynamic Therapy and Synergistic pH-Responsive Drug Delivery. *J. Mater. Chem. B* (2016).
18. Datz, S., Engelke, H., Schirnding, C.v., Nguyen, L. & Bein, T. Lipid bilayer-coated curcumin-based mesoporous organosilica nanoparticles for cellular delivery. *Microporous Mesoporous Mater.* **225**, 371-377 (2016).
19. Ajnai, G. et al. Trends of Gold Nanoparticle-based Drug Delivery System in Cancer Therapy. *J. Exp. Clin. Med.* **6**, 172-178 (2014).
20. Arvizo, R., Bhattacharya, R. & Mukherjee, P. Gold nanoparticles: Opportunities and Challenges in Nanomedicine. *Expert Opin. Drug Delivery* **7**, 753-763 (2010).
21. Dreaden, E.C., Austin, L.A., Mackey, M.A. & El-Sayed, M.A. Size matters: gold nanoparticles in targeted cancer drug delivery. *Ther. Delivery* **3**, 457-478 (2012).
22. Baeza, A., Guisasola, E., Ruiz-Hernández, E. & Vallet-Regí, M. Magnetically Triggered Multidrug Release by Hybrid Mesoporous Silica Nanoparticles. *Chem. Mater.* **24**, 517-524 (2012).
23. Dobson, Q.A.P.a.J.C.a.S.K.J.a.J. Applications of magnetic nanoparticles in biomedicine. *J. Phys. D: Appl. Phys.* **36**, R167 (2003).
24. Guo, W., Yang, C., Lin, H. & Qu, F. P(EO-co-LLA) functionalized Fe₃O₄@mSiO₂ nanocomposites for thermo/pH responsive drug controlled release and hyperthermia. *Dalton Transactions* **43**, 18056-18065 (2014).
25. Laurent, S. et al. Magnetic Iron Oxide Nanoparticles: Synthesis, Stabilization, Vectorization, Physicochemical Characterizations, and Biological Applications. *Chem. Rev.* **108**, 2064-2110 (2008).
26. N'Guyen, T.T.T. et al. Functional Iron Oxide Magnetic Nanoparticles with Hyperthermia-Induced Drug

- Release Ability by Using a Combination of Orthogonal Click Reactions. *Angew. Chem. Int. Ed.* **52**, 14152-14156 (2013).
27. Rühle, B., Datz, S., Argyo, C., Bein, T. & Zink, J.I. A molecular nanocap activated by superparamagnetic heating for externally stimulated cargo release. *Chem. Commun.* **52**, 1843-1846 (2016).
 28. Kumari, A., Yadav, S.K. & Yadav, S.C. Biodegradable polymeric nanoparticles based drug delivery systems. *Colloids Surf., B.* **75**, 1-18 (2010).
 29. Liechty, W.B., Kryscio, D.R., Slaughter, B.V. & Peppas, N.A. Polymers for Drug Delivery Systems. *Annu. Rev. Chem. Biomol. Eng.* **1**, 149-173 (2010).
 30. Soppimath, K.S., Aminabhavi, T.M., Kulkarni, A.R. & Rudzinski, W.E. Biodegradable polymeric nanoparticles as drug delivery devices. *J. Controlled Release* **70**, 1-20 (2001).
 31. Kalepu, S., Manthina, M. & Padavala, V. Oral lipid-based drug delivery systems – an overview. *Acta Pharm. Sin. B* **3**, 361-372 (2013).
 32. Puri, A. et al. Lipid-Based Nanoparticles as Pharmaceutical Drug Carriers: From Concepts to Clinic. *Crit. Rev. Ther. Drug Carrier Syst.* **26**, 523-580 (2009).
 33. Shrestha, H., Bala, R. & Arora, S. Lipid-Based Drug Delivery Systems. *J. Pharm.* **2014**, 10 (2014).
 34. Ranjbar, R. & Hafezi-Moghadam, M.S. Design and construction of a DNA origami drug delivery system based on MPT64 antibody aptamer for tuberculosis treatment. *Electronic Physician* **8**, 1857-1864 (2016).
 35. Rothemund, P.W.K. Folding DNA to create nanoscale shapes and patterns. *Nature* **440**, 297-302 (2006).
 36. Zhang, Q. et al. DNA Origami as an In Vivo Drug Delivery Vehicle for Cancer Therapy. *ACS nano* **8**, 6633-6643 (2014).
 37. Hedgire, S., McDermott, S. & Harisinghani, M. in *Nanomedicine-Basic and Clinical Applications in Diagnostics and Therapy*, Vol. 2 96-105 (Karger Publishers, 2011).
 38. Lammers, T., Kiessling, F., Hennink, W.E. & Storm, G. Drug targeting to tumors: principles, pitfalls and (pre-) clinical progress. *J. Controlled Release* **161**, 175-187 (2012).
 39. Salvati, A. et al. Transferrin-functionalized nanoparticles lose their targeting capabilities when a biomolecule corona adsorbs on the surface. *Nat. Nanotechnol.* **8**, 137-143 (2013).
 40. Gatenby, R.A. & Gillies, R.J. Why do cancers have high aerobic glycolysis? *Nat. Rev. Cancer* **4**, 891-899 (2004).
 41. Cairns, R.A., Harris, I.S. & Mak, T.W. Regulation of cancer cell metabolism. *Nat. Rev. Cancer* **11**, 85-95 (2011).
 42. Hsu, P.P. & Sabatini, D.M. Cancer cell metabolism: Warburg and beyond. *Cell* **134**, 703-707 (2008).
 43. DeBerardinis, R.J., Lum, J.J., Hatzivassiliou, G. & Thompson, C.B. The biology of cancer: metabolic reprogramming fuels cell growth and proliferation. *Cell Metab.* **7**, 11-20 (2008).
 44. Szejtli, J. Introduction and general overview of cyclodextrin chemistry. *Chem. Rev.* **98**, 1743-1754 (1998).
 45. Acartürk, F. & Çelebi, N. Cyclodextrins as bioavailability enhancers. *Cyclodextrins in pharmaceuticals, cosmetics, and biomedicine: current and future industrial applications*, 45-64 (2011).
 46. Arima, H., Motoyama, K. & Irie, T. Recent findings on safety profiles of cyclodextrins, cyclodextrin conjugates, and polypseudorotaxanes. *Cyclodextrins in pharmaceuticals, cosmetics, and biomedicine: Current and future industrial applications*, 91-122 (2011).
 47. Bilensoy, E. *Cyclodextrins in pharmaceuticals, cosmetics, and biomedicine: current and future industrial applications*. (John Wiley & Sons, 2011).
 48. Hincal, A.A., Eroğlu, H. & Bilensoy, E. Regulatory status of cyclodextrins in pharmaceutical products. *Cyclodextrins in Pharmaceuticals, Cosmetics, and Biomedicine: Current and Future Industrial Applications*, 123-130 (2011).
 49. Auletta, T. et al. β -Cyclodextrin Host-Guest Complexes Probed under Thermodynamic Equilibrium: Thermodynamics and AFM Force Spectroscopy. *Journal of the American Chemical Society* **126**, 1577-1584 (2004).
 50. Cromwell, W.C., Bystrom, K. & Eftink, M.R. Cyclodextrin-adamantanecarboxylate inclusion complexes: studies of the variation in cavity size. *J. Phys. Chem.* **89**, 326-332 (1985).
 51. Eftink, M.R., Andy, M.L., Bystrom, K., Perlmutter, H.D. & Kristol, D.S. Cyclodextrin inclusion complexes: studies of the variation in the size of alicyclic guests. *Journal of the American Chemical Society* **111**, 6765-6772 (1989).
 52. Schmidt, B.V.K.J., Hetzer, M., Ritter, H. & Barner-Kowollik, C. Complex macromolecular architecture design via cyclodextrin host/guest complexes. *Prog. Polym. Sci.* **39**, 235-249 (2014).
 53. Del Valle, E.M. Cyclodextrins and their uses: a review. *Process Biochem.* **39**, 1033-1046 (2004).
 54. Suárez, L.G., Verboom, W. & Huskens, J. Cyclodextrin-based supramolecular nanoparticles stabilized by balancing attractive host-guest and repulsive electrostatic interactions. *Chem. Commun.* **50**, 7280-7282

- (2014).
55. Yu, S. et al. Synthesis of Paclitaxel-Conjugated β -Cyclodextrin Polyrotaxane and Its Antitumor Activity. *Angew. Chem. Int. Ed.* **52**, 7272-7277 (2013).
 56. Davis, M.E. The first targeted delivery of siRNA in humans via a self-assembling, cyclodextrin polymer-based nanoparticle: from concept to clinic. *Mol. Pharm.* **6**, 659-668 (2009).
 57. Zhu, W., Zhang, K., Chen, Y. & Xi, F. Simple, clean preparation method for cross-linked α -cyclodextrin nanoparticles via inclusion complexation. *Langmuir* **29**, 5939-5943 (2013).
 58. Alsaiee, A. et al. Rapid removal of organic micropollutants from water by a porous β -cyclodextrin polymer. *Nature* (2015).
 59. Wenz, G., Han, B.-H. & Müller, A. Cyclodextrin Rotaxanes and Polyrotaxanes. *Chem. Rev.* **106**, 782-817 (2006).
 60. Jokerst, J.V., Lobovkina, T., Zare, R.N. & Gambhir, S.S. Nanoparticle PEGylation for imaging and therapy. *Nanomedicine (London, England)* **6**, 715-728 (2011).
 61. de Barros, A.L.B. et al. Synthesis, characterization, and biodistribution studies of ^{99m}Tc -labeled SBA-16 mesoporous silica nanoparticles. *Mater. Sci. Eng. C.* **56**, 181-188 (2015).
 62. Vorona, S., Artamonova, T., Zevatskii, Y. & Myznikov, L. An Improved Protocol for the Preparation of 5-Substituted Tetrazoles from Organic Thiocyanates and Nitriles. *Synthesis* **46**, 781-786 (2014).
 63. Moore, A., Weissleder, R. & Bogdanov, A. Uptake of dextran-coated monocrySTALLINE iron oxides in tumor cells and macrophages. *JMRI* **7**, 1140-1145 (1997).
 64. Osaki, F., Kanamori, T., Sando, S., Sera, T. & Aoyama, Y. A Quantum Dot Conjugated Sugar Ball and Its Cellular Uptake. On the Size Effects of Endocytosis in the Subviral Region. *Journal of the American Chemical Society* **126**, 6520-6521 (2004).
 65. Xue, M. et al. pH-Operated Mechanized Porous Silicon Nanoparticles. *Journal of the American Chemical Society* **133**, 8798-8801 (2011).
 66. Meng, H. et al. Autonomous in Vitro Anticancer Drug Release from Mesoporous Silica Nanoparticles by pH-Sensitive Nanovalves. *Journal of the American Chemical Society* **132**, 12690-12697 (2010).
 67. Lu, L., Shao, X., Jiao, Y. & Zhou, C. Synthesis of chitosan-graft- β -cyclodextrin for improving the loading and release of doxorubicin in the nanoparticles. *J. Appl. Polym. Sci.* **131**, n/a-n/a (2014).
 68. Qiu, L.Y., Wang, R.J., Zheng, C., Jin, Y. & Jin, L.Q. β -cyclodextrin-centered star-shaped amphiphilic polymers for doxorubicin delivery. *Nanomedicine* **5**, 193-208 (2010).
 69. Yousef, T. & Hassan, N. Supramolecular encapsulation of doxorubicin with β -cyclodextrin dendrimer: in vitro evaluation of controlled release and cytotoxicity. *J. Inclusion Phenom. Macrocyclic Chem.*, 1-11 (2016).
 70. Cauda, V. et al. Colchicine-loaded lipid bilayer-coated 50 nm mesoporous nanoparticles efficiently induce microtubule depolymerization upon cell uptake. *Nano Lett.* **10**, 2484-2492 (2010).
 71. Torrano, A.A. et al. A fast analysis method to quantify nanoparticle uptake on a single cell level. *Nanomedicine (London, U. K.)* **8**, 1815-1828 (2013).

Chapter 7

Synergistic Combination of Calcium and Citrate in Mesoporous Nanoparticles Targets Pleural Tumors

Constantin von Schirnding, Ioanna Giopanou, Adam Hermawan, Giannoula Ntaliarda, Lisa Wehl, Bernhard Illes, Stefan Datz, Franz Geisslinger, Karin Bartel, Ann-Katrin Sommer, Marina Lianou, Veronika Weiß, Johann Feckl, Angelika M. Vollmar, Christoph Bräuchle, Georgios T. Stathopoulos, Ernst Wagne, Andreas Roidl, Thomas Bein, and Hanna Engelke

This chapter was accepted for publication in Chem.

7.1 Introduction

Calcium phosphate-citrate is a very promising material as a replacement for conventional chemotherapeutics. Unlike conventional chemotherapeutics that are inherently toxic, extracellular calcium phosphate and citrate are well tolerated by organisms. Moreover, calcium phosphate and citrate are even necessary in the body at high concentrations, e.g. calcium phosphate as the main inorganic component of bone and teeth.¹⁻³ Yet, many cellular signalling pathways rely on tightly controlled variations in either Ca^{2+} or citrate concentrations and high intracellular doses of these ions have been shown to induce cell death.^{4, 5} In this context, the induction of high levels of intracellular Ca^{2+} has even been implicated as the main reason for the efficacy of certain drugs against cancer stem cells that are otherwise difficult to treat.⁶ To avoid toxic doses of intracellular Ca^{2+} or citrate, cells control uptake of these ions tightly.^{2, 7} Thus, a formulation consisting of calcium phosphate-citrate that bypasses the cellular uptake regulation mechanisms and leads to an intracellular release of high Ca^{2+} and citrate concentrations could take advantage of the sensitivity of cells to these ion concentrations and facilitate their use as an alternative to conventional chemotherapeutics.

Nanoparticles represent a promising means for the realization of such a formulation. They can be coated to prevent recognition of their cargo and to mediate efficient cellular internalization.^{8, 9} Furthermore, they may be designed to release biologically active agents to the cytosol of target cells creating locally confined high concentrations of these agents.¹⁰ Ideally, they even consist of biologically active building blocks and release those into the cytosol after particle degradation in the endosome of the target cell.¹¹ This avoids solid particles remaining in the organism. Nanosized calcium phosphate materials have been used as nanocarriers for delivery of drugs, DNA, siRNA, and proteins.¹²⁻¹⁴ They are often applied in combination with lipids to enhance their cellular uptake.¹⁵ These nanocarriers show very good biocompatibility and even without drug cargos they are selectively toxic at very high concentrations – too high for therapeutic purposes.^{16, 17} The carrier material consists of apatite or other crystalline forms of calcium phosphate, which do not readily dissolve in the endosome of cells. Only at extremely high particle concentrations the amount of Ca^{2+} dissolved and released is enough to induce apoptosis in cells.¹⁷ Use of calcium phosphate-citrate instead of calcium phosphate changes the degradation properties and allows for co-delivery of high amounts of Ca^{2+} and citrate.

7.2 Results

We designed novel hybrid mesoporous calcium phosphate-citrate nanoparticles (CPC) for efficient nanoparticle degradation in the acidifying endosome followed by co-delivery of toxic amounts of Ca^{2+} and citrate into the cytosol. For this purpose, we synthesized CPC by reacting Ca^{2+} - and PO_4^{3-} - ions with citric acid at a molar ratio of 5:3:5. Citric acid complexes Ca^{2+} and thus has an important role in the reaction kinetics during formation of calcium phosphates.¹⁸ Precipitation of nanoparticles is induced by a rapid pH change upon addition of triethanolamine, and formation of a mesoporous structure is achieved by addition of the surfactant templates cetyltrimethylammonium chloride (CTAC) and Pluronic® F127. Following synthesis, extraction of the surfactant templates yielded the desired mesoporous hybrid CPC nanoparticles as depicted in Figure 7.1a. The successful synthesis of amorphous (Figure 7.1b) CPC nanoparticles was verified by XRD (amorphous nature) and IR-, ssNMR-, and TGA-measurements (incorporation of citric acid into calcium phosphate): the IR-spectrum of CPC, as shown in Figure 7.1c, exhibits some of the characteristics of calciumphosphate materials (such as apatite). Additionally, it shows two strong vibrations at 1414 cm^{-1} and 1590 cm^{-1} that are attributed to the symmetric and the anti-symmetric stretching modes of COO^- groups of citric acid incorporated into the structure.¹⁹ The incorporation of citric acid was further confirmed by solid state nuclear magnetic resonance spectroscopy and was determined to be ~20% using thermogravimetric analysis (see also Figure 7.5 and Figure 7.6). Energy dispersive X-ray and inductively coupled plasma methods yielded a Ca:P atomic ratio of 1.61 (see also Table 7.1). Without further filtration, the particles showed a narrow size distribution with an average hydrodynamic radius of 220 nm in ethanolic solution as measured by dynamic light scattering. Electron microscopy images showed particles of about 50 nm (Figure 7.1d and 7.2a). Their size is suited for cellular uptake. The porosity of the obtained particles was analysed with nitrogen sorption measurements. As shown in Figure 7.1e, we observed a typical type IV isotherm characteristic of mesoporous systems, with CPC featuring an extraordinary Brunauer–Emmett–Teller surface area of $900\text{ m}^2\text{ g}^{-1}$, a very narrow pore size distribution with a maximum at 4.8 nm (inlay), and a cumulative pore volume of $1.0\text{ cm}^3\text{ g}^{-1}$. These remarkable characteristics are very similar to those of the well-established mesoporous silica particles.²⁰ Our observed surface area is almost three times larger than reported before for calcium phosphate-based materials with surface areas of $315\text{ m}^2\text{ g}^{-1}$.²¹

In aqueous solution mesoporous CPC crystallize over time (Figure 7.13). To protect them from water and thus to maintain their amorphous character, we coated them with a lipid layer. We formed a lipid coating consisting of 1,2-dioleoyl-3-trimethylammonium-propane (DOTAP) and 1,2-dioleoyl-sn-glycero-3-phosphocholine (DOPC) around the particles employing a solvent exchange method.²² Successful formation of the lipid coating resulted in a drastic increase in zeta potential from -5 mV to +20 mV at pH 7.4, due to the positively charged DOTAP. To assess the integrity of the lipid coating, we loaded the particles with the non membrane-permeable fluorescent dye calcein and measured its release over a time period of 24 h in a two-compartment cuvette experiment (see also Figure 7.7). We could not detect any significant premature release (< 1 %), confirming a successful lipid coating. Acidification by addition of 0.1 M HCl dissolved the particles and led to a dramatic increase in released fluorescent dye, as measured after neutralization to pH 7.4 (Figure 7.1f and see also Figure 7.7). Most importantly, the lipid coating preserved the amorphous character of the particles (see Figure 7.14).

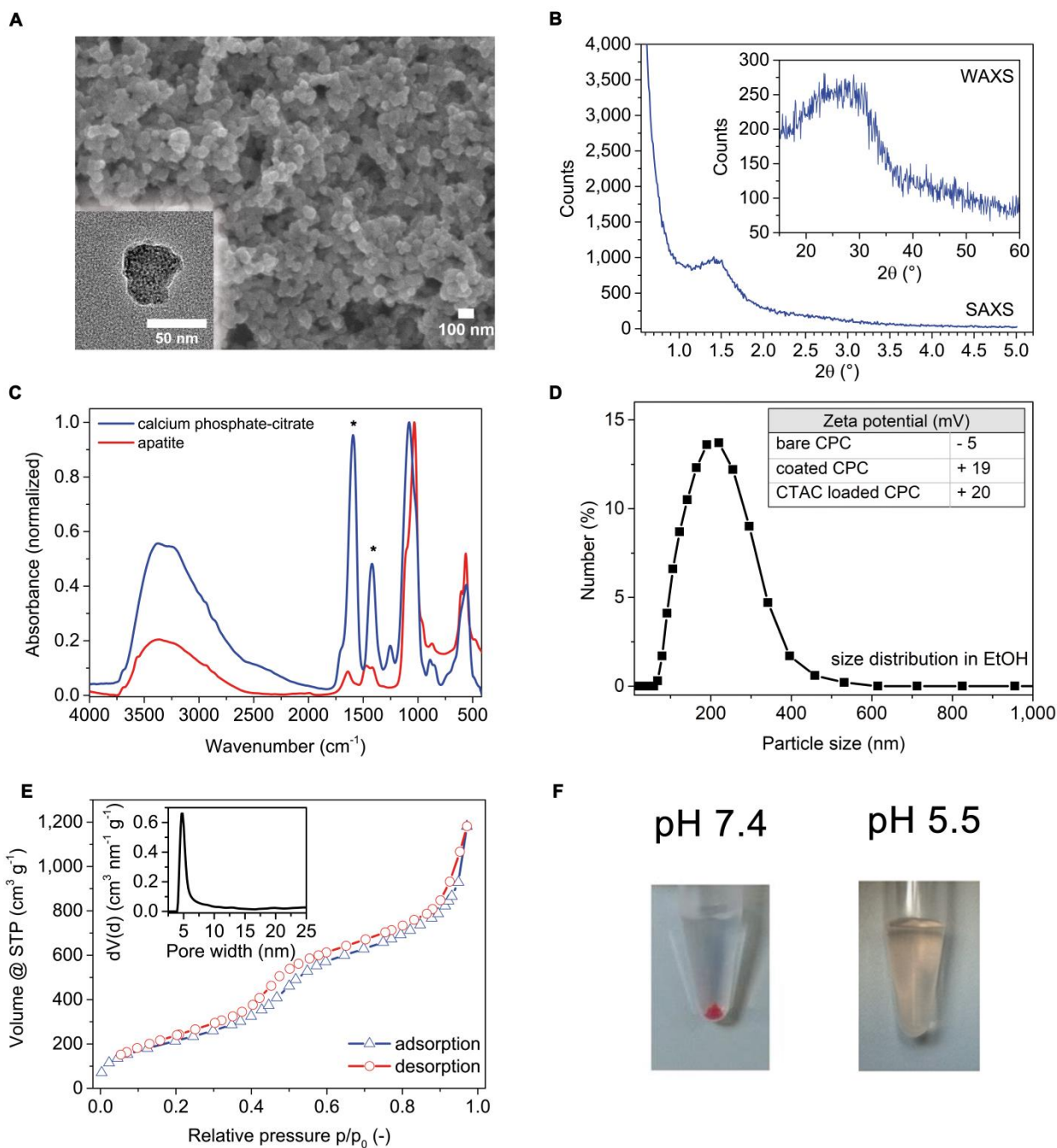


Figure 7.1: Characterization of mesoporous calcium phosphate-citrate nanoparticles (CPC). **(A)** Scanning electron microscopy and transmission electron microscopy (inset) images of spherical particles of 50 nm. Scale bars: 50 and 100 nm. **(B)** WAXS and SAXS measurements exhibit the amorphous nature and the well-defined porous network with a calculated d-spacing of 6.13 nm. **(C)** Infrared spectra of CPC with strong C-O vibrations at 1414 cm^{-1} and 1590 cm^{-1} (marked with asterisk) due to the incorporated citrate in the structure (blue line), in comparison with crystalline apatite (red line). **(D)** Dynamic light scattering data of colloidal CPC show a maximum at a size of 220 nm. Zeta potential measurements of bare and lipid-coated CPC (coated CPC) and CTAC loaded lipid-coated CPC (CTAC loaded CPC) (table insert) in simulated body fluid (pH 7.4) show an increase upon deposition of a positively charged lipid membrane. **(E)** Nitrogen sorption measurement of mesoporous CPC with a BET surface area of $900 \text{ m}^2 \text{ g}^{-1}$, pore size of 4.8 nm (insert), and a pore volume of $1.0 \text{ cm}^3 \text{ g}^{-1}$. **(F)** Lipid coated, CTAC loaded CPC are stable at blood pH 7.4 and can be recovered via centrifugation, but readily dissolve at endosomal pH 5.5

Next, we investigated the uptake of lipid-coated and calcein-loaded CPC by HeLa cells. Lipid-coated CPC were successfully internalized by cells as depicted in Figure 7.2a. Time-resolved experiments showed a particle uptake followed by a weak endosomal release of calcein into the cytosol within the first 2-4 h after incubation of $20 \mu\text{g mL}^{-1}$ of CPCs (see also Movie 7.3). The observed endosomal release was accompanied by a temporary drop in NADPH (and other reduction equivalent) levels without consequences on ATP levels or visible impact on cell viability (see Figure 7.8a and b, black lines). To enhance endosomal release²³, we loaded the particles with a small amount of cetyltrimethylammonium chloride (CTAC), a positively charged surfactant that can destabilize lipid membranes. While adsorbed in the particle, its attraction to the negatively charged particle prevents leakage and destabilization of the lipid coating of the particles. Once the endosomal pH turns acidic²⁴, the particle dissolves and the CTAC molecules are no longer retained in the particle. When incubating HeLa cells with lipid-coated and calcein/CTAC-loaded CPC, we observed an enhanced release of calcein in the cells (see also Movie 7.1) along with a permanent drop in NADPH levels followed by a decrease in ATP levels (Figure 7.2d, and see also Figure 7.8a, b, and d, red lines) and ultimately cell death via apoptosis as observed by the increase in the apoptosis marker caspase 3/7 (Figure 7.2c and see also Figure 7.8c, red lines). We attribute this observation to a rupture of the endosome containing the dissolved particle and its cargo calcein. The subsequent release of the endosomal content including all particle components at high concentrations leads to the observed cell death.^{4, 25} We propose that the efficient degradation of our CPC is based on their amorphous nature and their extremely thin walls with very high surface area. These unique properties create conditions for fast dissolution kinetics and rapid release of high amounts of citrate and Ca^{2+} .

In order to study possible by-stander effects of the remaining substances on the viability of the surrounding cells after successful treatment, we dissolved lipid-coated and calcein/CTAC-loaded CPC and incubated the remaining solution with HeLa cells. We did not detect any significant loss of cell viability (see also Figure 7.9i). Hence, the toxic effect of lipid-coated and calcein/CTAC-loaded CPC seems to be limited to sudden intracellular release of high amounts of their components upon endosomal rupture preventing undesired further damage to neighbouring cells. The above results on HeLa cells suggest very promising properties of CPC when applied as selective anticancer agents avoiding highly toxic chemotherapeutics.

To assess their selectivity towards tumor cells, we studied the effect of CPC on the non-tumorigenic cell line MCF10A. While these cells successfully internalized lipid-coated and calcein/CTAC-loaded CPC, we did not observe any endosomal release (see also Movie 7.2). Accordingly, viability of MCF10A cells was not decreased below 50 % even at high particle concentrations. Based on this result, we tested the toxicity of CPC on a wide variety of cell lines. We performed MTT assays to measure cell viability after 72 h. Neither uncoated nor lipid-coated CPC without CTAC showed any specific reduction of cell viability below 50% up to concentrations of $100 \mu\text{g mL}^{-1}$ in any of the cell lines (Figure 7.2e, f, and see also Figure 7.9, black and green lines). However, viability of all cancer cell lines was strongly decreased after incubation with lipid-coated and calcein/CTAC-loaded CPC even at concentrations of less than $30 \mu\text{g mL}^{-1}$ (Figure 7.2b, f, and see also Figure 7.9, red lines). Interestingly, 50% inhibitory concentration values decreased with increasing malignancy of the cancer cells, reaching the lowest values for highly aggressive cancer cells such as Lewis lung carcinoma (see Figure 7.2b and see also Table 7.2). With this unusual property, CPC belong to a small group of substance that are selectively toxic to cancer cells.²⁶ Strikingly, none of the benign, non-cancerous cell lines tested were significantly affected by CPC up to concentrations of $100 \mu\text{g mL}^{-1}$ (Figure 7.2e and see also Figure 7.9, red lines). These results suggest strong cancer selectivity and a high efficiency in the toxicity of CPC demonstrating their potential as new generation of anticancer agents.

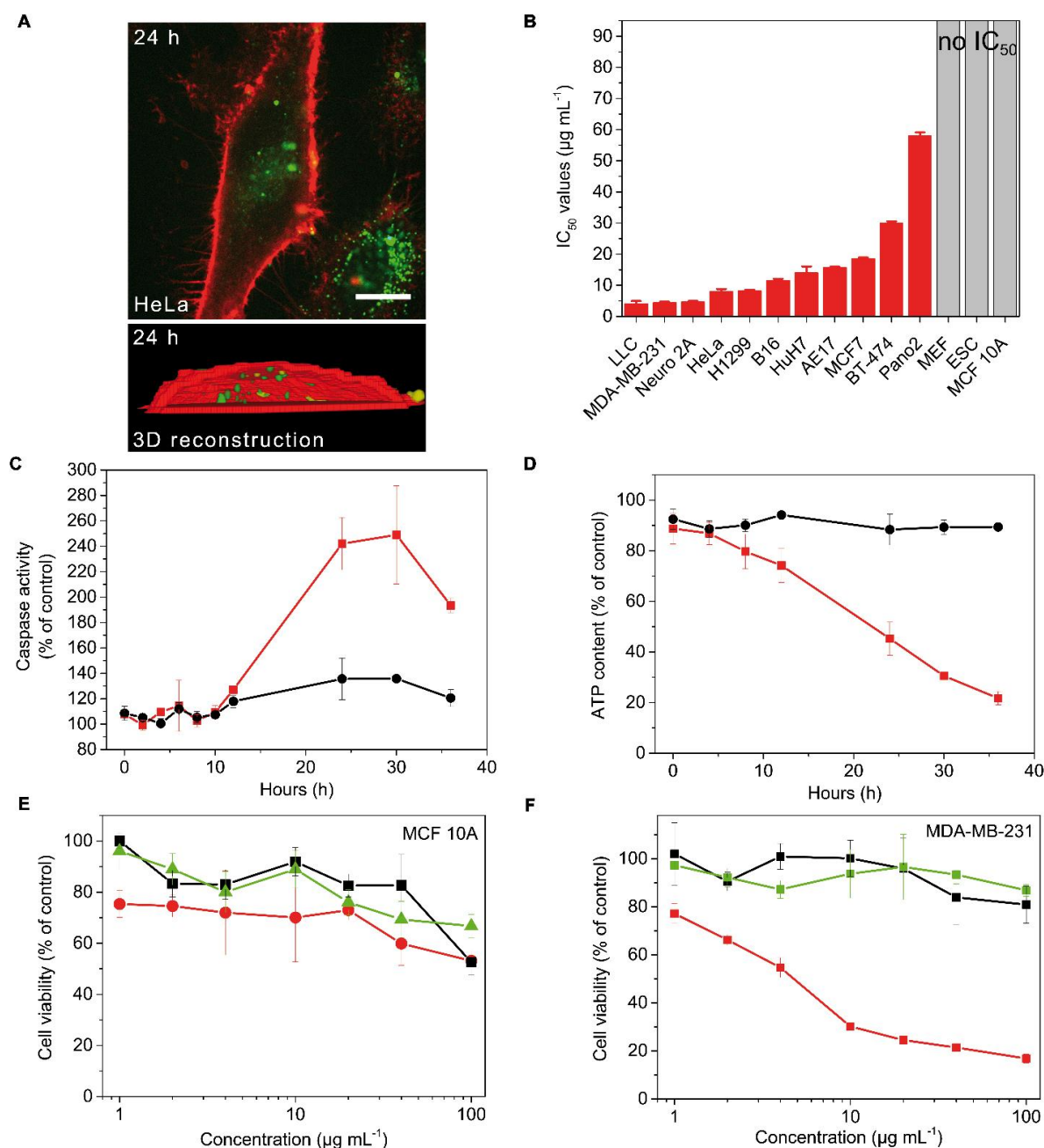


Figure 7.2: Cell studies of calcium phosphate-citrate nanoparticles (CPCs) with respect to their toxicity towards different cell lines. **(A)** Confocal microscopy image of HeLa cells with lipid-coated CPC in green and a WGA-stained cell membrane in red (incubation for 24 h). 3D reconstruction²⁷ of the particle uptake after 24 h of incubation. Scale bar: 20 μm. **(B)** IC₅₀ values of the investigated cancerous (red bars) and the non-tumorigenic (gray bar, no significant cell death observed and no IC₅₀ was calculated) cell lines after treatment with lipid-coated and calcein/CTAC-loaded CPC that escape from the endosome. **(C)** and **(D)** Time-dependent tracking of lipid-coated and calcein/CTAC-loaded CPC (red line) and lipid-coated CPC (black line) on HeLa cells with respect to the caspase activity and ATP content normalized to the data of HeLa cells incubated with SFB buffer only. Lipid-coated and calcein/CTAC-loaded CPC trigger caspase activity and ATP reduction over time, while for lipid-coated CPC no effect was observed. **(E)** Cell viability of the non-tumorigenic epithelial breast cell line MCF 10A with lipid-coated CPC that escape from the endosome (red line), that do not escape from the endosome but are taken up (black line), and CPC without a membrane that are not taken up (green line). **(F)** Same as Figure 7.2 (E) but for mesenchymal breast cancer cell line MDA-MB-231.

To validate the promise of CPC as highly selective and efficient anticancer drugs, we tested their efficacy *in vivo*. We chose a mouse model of pleural adenocarcinoma induced by local injection of LLC or B16F10 cells into syngeneic *C57BL/6* mice²⁸ that recapitulates a highly aggressive disease for which to date no therapy is available.²⁹ This model employs bioluminescent tumor cells (called *pNGL*) enabling non-invasive imaging of tumor mass on a background of full immunocompetence.²⁸ While intrapleural therapies are currently delivered to patients with pleural cancers, selective tumor cell killing without bystander toxicity to the surrounding pleural and pulmonary tissues remains an unmet clinical need.³⁰ We tested whether lipid-coated and calcein/CTAC-loaded CPC can address this need by applying 2 mg CPC suspended in 100 μ L simulated body fluid (SBF) intrapleurally on days 5 and 7 post tumor cell injection (Figure 7.3a), when pleural tumor foci had already been established (intervention group; $n = 8$). Control treatment consisted of intrapleural 100 μ L SBF on days 5 and 7 post tumor cell injection (control group; $n = 9/8$). On day 11/13 post tumor cell injection, mice were sacrificed and analysed for tumor mass (primary end-point, Figure 7.3b and d left panel). Secondary end-points were serial measurements of chest bioluminescence (an indicator of tumor mass, Fig, 7.3c, e, and b and d right panel) and the number of pleural fluid nucleated cells (an indicator of inflammation). Both tumor mass and thoracic luminescence were markedly decreased by $\sim 40\%$ and $\sim 70\%$ respectively in CPC-treated mice (statistical information see Appendix) compared with controls. The number of pleural fluid nucleated cells was not different between groups, indicating that CPC do not induce further inflammation in addition to that caused by the malignant process (see also Figure 7.10).

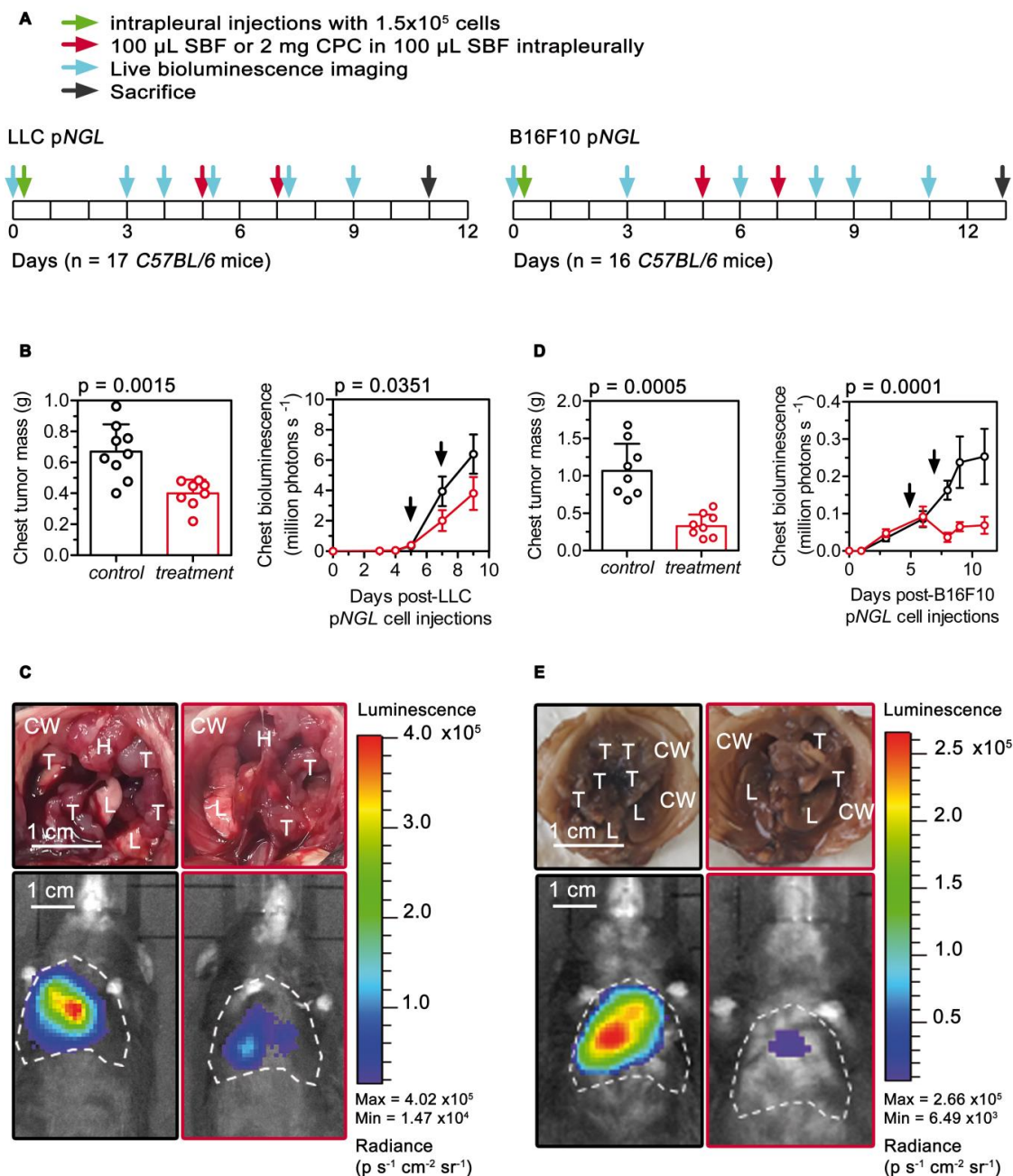


Figure 7.3: *In vivo* studies of lipid-coated and calcein/CTAC-loaded calcium phosphate-citrate nanoparticles (CPC) in two different pleural tumor models induced by intrapleural injection of 1.5×10^5 luminescent (pNGL) LLC or B16F10 cells into C57BL/6 mice. (A) Treatment scheme. (B) Model with LLC pNGL cells. Left panel: The tumor weight of the CPC treatment group ($n = 8$, colour code: red) was reduced by 41% with respect to the control group ($n = 9$, colour code: black). Error bars = SEM. Right panel: Bioluminescence intensity of CPC-treated and control mice over time. (C) Representative images of the mouse pleural cavity showing pleural tumors (t), lungs (l), chest walls (cw), and hearts (h) imaged through the diaphragm (top) and representative bioluminescent images (bottom) obtained at day 11 after pleural injections of LLC tumor cells. (D) Model with B16F10 pNGL cells. Left panel: The tumor weight of the CPC treatment group ($n = 8$, colour code: red) was reduced by 70% with respect to the control group ($n = 8$, colour code: black). Error bars = SEM. Right panel: Bioluminescence intensity of CPC-treated and control mice over time. (E) Representative images of the mouse pleural cavity showing pleural tumors (t), lungs (l), chest walls (cw), and hearts (h) imaged through the diaphragm (top) and representative bioluminescent images (bottom) obtained at day 13 after pleural injections of B16F10 tumor cells.

To assess the safety of CPC further, we performed two long-term experiments. In the first experiment, mice without tumor were injected weekly with 2 mg CPC suspended in 100 μ L SBF or 100 μ L SBF respectively. After two months and 8 injections mice were sacrificed and investigated for effects caused by CPC (Figure 7.4 A-C). Visual inspection of the mice and specifically their pleural cavity did not show any difference. Also the number of macrophages and cells that might result from inflammation were not influenced by the nanoparticles. The only difference we found was an increase in pleural thickening resulting in pleurodesis (obstruction of the pleural space), which is actually therapeutically desirable in patients with pleural malignancies.²⁹ In a second long-term experiment we investigated the safety of CPC in a tumor environment. To this end, we used pleural xenografts of PANO2 cells as model system. They form a very slowly growing tumor and thus allow for a long-term study. The aggressive tumor cell lines used for the treatment efficacy studies would allow only up to 12 days of experiments for the untreated control group. Tumors of PANO2 cells offer the additional advantage that they form tumors, which are not very aggressive, and hence the particles don't show much effect *in vitro* (see Figure 7.9m). Thus, they provide a comparable tumor environment for long-term studies with CPC and control. For the experiment, mice were injected weekly with 2 mg CPC or 100 μ l SBF for 4 weeks starting 4 weeks post tumor cell injection. 8 weeks post tumor injection mice were sacrificed and analyzed similarly to the first experiment. Again, no visible signs of toxicity were observed (Figure 7.4d) and the number of inflammatory macrophages was not significantly different in treatment and control group (Figure 7.4e). The total amount of pleural lavage cells consisting of tumor cells and macrophages was even reduced in the treatment group. This time, after 4 injections in the presence of a tumor, we did not observe an increase in pleural thickening compared to the control. As predicted from the *in vitro* experiments, tumor mass was not affected by CPC treatment confirming the comparable microenvironment conditions during the experiment. Importantly, the survival of PANO2 tumor-bearing mice was not affected by four weekly CPC injections. Thus, CPC show no detectable adverse effects except for some pleural thickening after injection of 16 mg CPC into tumor-free mice. These minor adverse effects combined with the successful treatment of aggressive pleural tumors in mice after only two applications and within a very short treatment window of a few days confirms the promise of CPC to reduce tumors with very high selectivity and efficiency. Importantly, it also presents a new option for a possible treatment of to date mostly lethal pleural tumors.

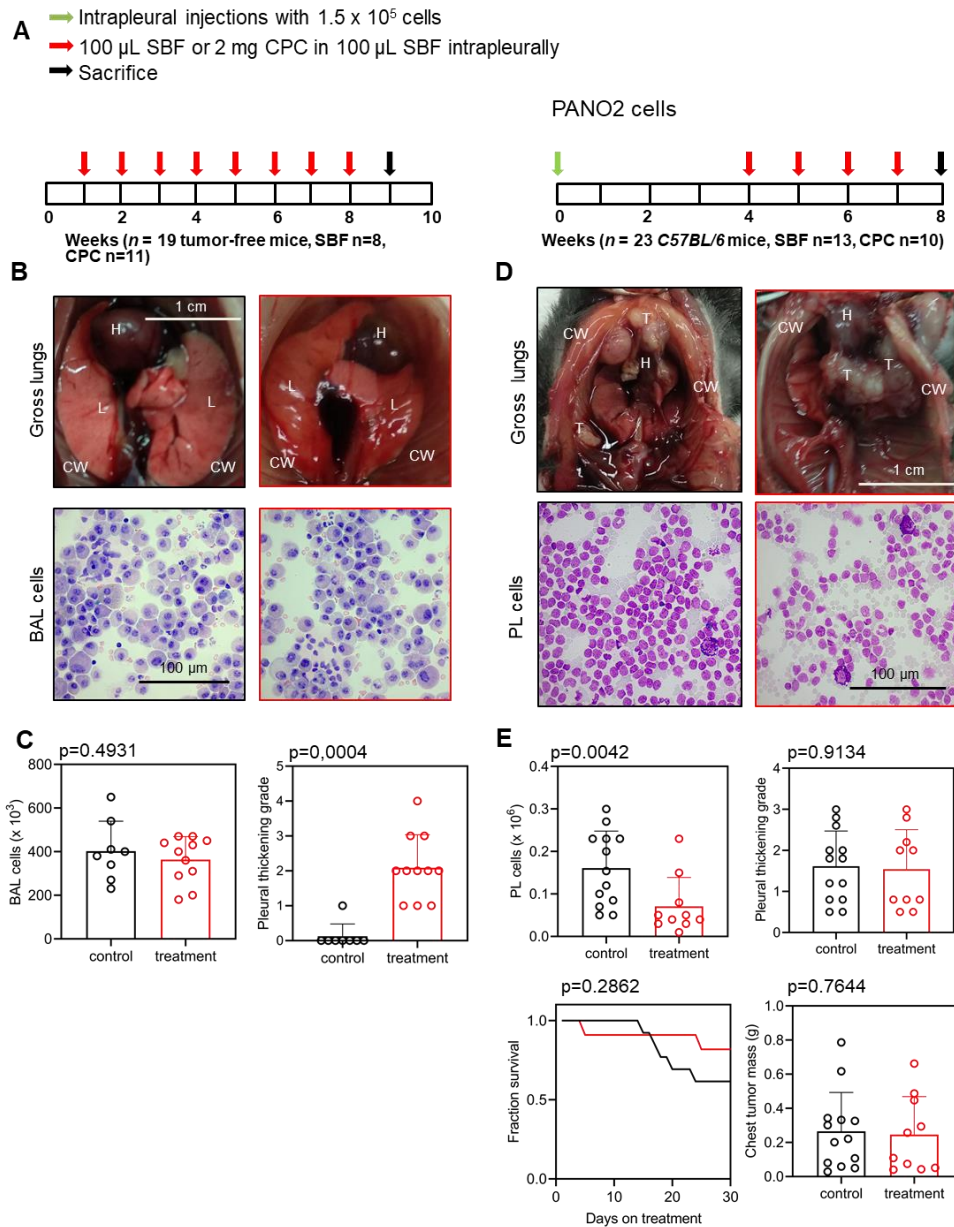


Figure 7.4: Safety studies of lipid-coated and calcein/CTAC-loaded calcium phosphate-citrate nanoparticles (CPC) in two different *in vivo* experiments. **(A)** Treatment scheme. **(B)** Experiment with tumor-free mice. Representative images of the mouse pleural cavity showing lungs (l), chest walls (cw), and hearts (h) imaged through the diaphragm (top) and May-Grünwald-Giemsa staining for bronchoalveolar lavage (BAL) cells (bottom) did not show any difference between treatment ($n = 11$, color code: red) and control ($n = 8$, color code: black) group. **(C)** Quantitative analysis of BAL cell number shows no difference between treatment and control group. Analysis of pleural thickening grade shows a therapeutically desirable enhancement of pleural thickening by 2 grades on average in the treatment group after 8 weeks and 8 injections of 2 mg CPC each. **(D)** Experiments with tumor model induced by intrapleural injection of PANO2 cells. Representative images of mouse pleural cavity of C57BL/6 mice with pleural PANO2 tumors (t), lungs (l), chest walls (cw), and hearts (h) imaged through the diaphragm (top) show no visible difference between treatment ($n = 10$, color code: red) and control ($n = 13$, color code: black) groups. Representative images of pleural lavage (PL) cell staining (bottom) shows a clear reduction of PL cells in the CPC treatment group. **(E)** Quantitative analysis of PL cell number, pleural thickening grade, tumor mass, and survival curve. Pleural lavage (PL) cells were reduced in the treatment group and probability for survival was not significantly altered. Pleural thickening and tumor mass did not show any difference between treatment and control group.

7.3 Conclusion

We thus believe that CPC belong to a new generation of highly selective anticancer drugs that are composed of non-toxic substances that turn toxic only as a composite and in the tumor microenvironment, where they act with high efficiency and selectivity against cancer cells.

7.4 Materials and Methods

Chemicals for Nanoparticle Synthesis:

Calcium nitrate tetrahydrate (AppliChem, 99 %), ammonium dihydrogenphosphate (Alfa Aesar, 99 %), citric acid (Aldrich, 99.5 %), cetyltrimethylammonium chloride (CTAC, Fluka, 25 wt% in H₂O), Pluronic F127 (Aldrich), ethylene glycol (Aldrich, 99.8 %), triethanolamine (TEA, Aldrich, 98%), ethanol (EtOH, Aldrich, >99.5 %), ammonium nitrate (Sigma, 99 %), D-(+)-pantothenic acid calcium salt (Sigma, 99 %), hydrochloric acid (Sigma, 2 M), dipotassium hydrogen phosphate trihydrate (Sigma, 99 %), sodium hydroxide (Sigma, 2 M), simulated body fluid (prepared as written elsewhere, Sigma, >99 %), calcein (Sigma), 1,2-dioleoyl-3-trimethylammonium-propane (DOTAP, Avanti Polar Lipids), 1,2-dioleoyl-sn-glycero-3-phosphocholine (DOPC, Avanti Polar Lipids), sodium hydroxide (Aldrich, 0.1 M).

All chemicals were used as received without further purification. Doubly distilled water from a Millipore system (Milli-Q Academic A10) was used for all synthesis steps.

Cell Lines and Culture:

MCF7, BT-474, and MDA-MB-231 human breast cancer cells, NCI-H1299 human lung cancer cells, MEF mouse embryonic fibroblasts, ESC (ES-J1) mouse embryonic stem cells, and HeLa human cervical cancer cells were purchased from and cultured according to American Type Culture Collection (ATCC). MCF 10A human mammary cell line was purchased from American Type Culture Collection (ATCC) and cultured according to reference.³¹ HuH7 human hepatocellular carcinoma cells were purchased from and cultured according to Japanese Collection of Research Bioresources (JCRB) Cell Bank. Neuro 2A mouse neuroblastoma, LLC mouse lewis lung carcinoma, B16-F0 mouse melanoma, and AE17 mouse mesothelioma were purchased from and cultured according to American Type Culture Collection (ATCC).

MCF7, and MEF cells were grown in DMEM medium high glucose (Sigma Aldrich) supplemented with 20 % fetal calf serum (FCS) (Gibco) and 2 mM L-glutamine (Gibco) at 37 °C

and 5 % CO₂. HeLa cells were grown in DMEM medium low glucose (Sigma Aldrich) supplemented with 10 % FCS (Gibco) and 2 mM L-glutamine (Gibco) at 37 °C and 5 % CO₂. BT-474 and NCI-H1299 cells were grown in RPMI 1640 medium (Sigma Aldrich) supplemented with 10 % FCS and 2 mM L-glutamine (Gibco) at 37 °C and 5 % CO₂. HuH7 cells were grown in a 50:50 mixture of DMEM and Ham's F12 medium (Sigma Aldrich) supplemented with 10 % FCS and 2 mM L-glutamine (Gibco) at 37 °C and 5 % CO₂. MCF 10A cells were grown in DMEM-F12 medium (Gibco) supplemented with 10 % fetal bovine serum (FBS) and 20 ng/mL EGF (Gibco) and hydrocortisone (0.5 µg/mL) at 37 °C and 5 % CO₂. ESC (ES-J1) cells were grown in Mouse ES Cell Basal Medium (ATCC) supplemented with 10 % fetal calf serum (FCS) (Gibco), L-Gln-L-Ala, NEAA, 2i (CHIR 99021 3 µM and PD 0325901 1 µM), and 1,000 U/mL LIF (Gibco) at 37 °C and 5 % CO₂. MDA-MB-231 cells were grown in L-15 Leibovitz's medium (Biochrom) supplemented with 10 % FCS and 2 mM L-glutamine (Gibco) at 37 °C without CO₂. LLC, B16-F0 cells were grown in DMEM medium low glucose (Sigma Aldrich) supplemented with 10 % FCS (Gibco) and 4 mM L-glutamine (Gibco) at 37 °C and 5 % CO₂. Neuro 2A cells were grown in DMEM medium low glucose (Sigma Aldrich) supplemented with 10 % FCS (Gibco) and 2 mM L-glutamine (Gibco) at 37 °C and 5 % CO₂. AE17 cells were grown in 987 CYM medium (ATCC) at 37 °C and 5 % CO₂. Cells were routinely tested and confirmed to be mycoplasma free.

Characterization of Nanoparticles:

Nitrogen sorption measurements were performed on a Quantachrome Instrument NOVA 4000e at 77 K. Samples (25 mg) were outgassed at 120 °C for 12 h *in vacuo* (10 mTorr). Pore size and pore volume were calculated by a QSDFT equilibrium model of N₂ on carbon, based on the desorption branch of the isotherms. The QSDFT method takes into account the effects of surface roughness and heterogeneity. Cumulative pore volumes were evaluated up to a pore size of 10 nm, in order to remove the contribution of inter-particle textural porosity. Surface areas were calculated with the BET model in the range $p/p_0 = 0.05-0.2$. Thermogravimetric analysis of the samples was performed on a Netzsch STA 440 C TG/DSC in a stream of synthetic air with a heating rate of 10 K min⁻¹. Dynamic light scattering measurements were performed on a Malvern Zetasizer-Nano instrument with a 4 mW He-Ne laser (633 nm) in ethanolic suspension with a concentration of 0.5 mg mL⁻¹. Scanning electron microscope images were obtained on a JEOL JSM-6400F. For sample preparation a droplet of the ethanolic colloidal suspension was placed on a 60 °C preheated carbon pad. Samples were sputtered with carbon

before measurement. Transmission electron microscopy was performed on a JEOL JEM 2011 at an acceleration voltage of 200 kV. For sample preparation a droplet of a diluted ethanolic colloidal suspension was deposited on a carbon-coated copper grid, and the solvent was allowed to evaporate. EDX spectra were recorded with an EDAX Apollo XLT SDD Detector (30 mm²). For ICP measurements the samples were solved in concentrated HNO₃ and heated at 110 °C for 30 minutes. After dilution with H₂O the data collection was carried out with a Varian Vista RL ICP-OES with radially viewed plasma. Infrared spectra were measured with a Thermo Scientific Nicolet iN 10 Infrared microscope. XRD patterns were obtained with a Bruker D8 Discover X-ray diffractometer using Cu-K_α radiation (1.5406 Å). ¹³C, ³¹P, and ¹H solid-state NMR (ss-NMR) measurements were performed on a Bruker DSX Avance500 FT spectrometer in a 4 mm ZrO₂ rotor under magic angle spinning conditions. ¹³C ss-NMR data were obtained at 125.8 MHz under cross-polarization conditions with 52000 transients. ³¹P ss-NMR data were acquired at 202.5 MHz under cross-polarization conditions with 8 transients. ¹H ss-NMR data were obtained at 500.2 MHz with 1 run.

MTT-Assay:

All cell viability/cell toxicity tests were performed via MTT test if not stated otherwise. For MTT-assays we treated 5000 cells per well containing 100 μL of the respective medium with therapeutically active CPCs. As reference, control cells were treated with simulated body fluid (i.e. the solvent of the particle solution). After 72 h of treatment, 10 μL 3-(4,5-dimethylthiazol-2-yl)-2,5-diphenyltetrazolium bromide (MTT) was added to the calcium phosphate-citrate treated cells and incubated for further 2 h. Unreacted MTT and medium were removed and the 96-well plates were stored at -80 °C for at least 1 h. Then, 100 μL DMSO was added to each well. The absorbance was read out by a Tecan plate reader. All studies were performed in triplicates. IC₅₀ values were calculated with GraphPad Prism 5 and OriginPro 9. Statistical Analysis: All data are presented as mean ± SD, and were analyzed using GraphPad Prism 5.

RealTime-Glo™ MT Cell Viability Assay (Promega):

To measure NADH content over time, HeLa cells (5.0 x 10³ cells/well) were incubated in 100 μL of the respective medium for 24 hours in a 96-well plate. Then, RealTime-Glo™ MT Cell Viability Substrate and NanoLuc® Enzyme were added (0.2 μL/well) after addition of 20 μg/mL

therapeutically active CPCs and lipid-coated CPCs to each well. As reference, cells were treated with simulated body fluid. Luminescence was measured at the given time points.

This method measures all reduction equivalents (NADPH, NADH,...) and is referred to as measurements of NADPH levels in the main text.

CellTiter-Glo[®] Cell Viability Assay (Promega):

To measure ATP content over time, HeLa cells (5.0×10^3 cells/well) were incubated in 100 μ L of the respective medium for 24 hours in a 96-well plate. Then, cells were treated with 20 μ g/mL therapeutically active CPCs and lipid-coated CPCs for each well. As reference, cells were treated with simulated body fluid. CellTiter-Glo[®] Reagent was added (100 μ L/well) at given time points to the wells of interest and incubated for another 10 minutes. Then, luminescence was measured. This procedure was repeated for all wells to record a time series.

Caspase-Glo[®] 3/7 Assay (Promega):

To measure caspase-3/7 activity over time, HeLa cells (5.0×10^3 cells/well) were incubated in 100 μ L of the respective medium for 24 hours in a 96-well plate. Then, cells were treated with 20 μ g/mL therapeutically active CPCs and lipid-coated CPCs for each well. As reference, cells were treated with simulated body fluid. Caspase-Glo[®] 3/7 Reagent was added (100 μ L/well) at given time points to the wells of interest and gently shaken. After an incubation period of 30 minutes, luminescence was measured. This procedure was repeated for all wells to record a time series.

Live-cell Microscopy:

To visualize nanoparticle internalization by cells, live-cell imaging was performed on a spinning disc microscope based on the Zeiss Cell Observer SD utilizing a Yokogawa spinning disk unit CSU-X1. The system was equipped with a 1.40 NA 63x Plan apochromat oil immersion objective from Zeiss. For all experiments the exposure time was 0.1 s and z-stacks were recorded. Calcein-loaded CPCs were imaged with approximately 0.4 W/mm² of 488 nm excitation light. Atto647 was excited with approximately 11 mW/mm² of 639 nm. In the excitation path a quad-edge dichroic beamsplitter (FF410/504/582/669-Di01-25x36, Semrock)

was used. For two-color detection of calcein and Atto647, a dichroic mirror (560 nm, Semrock) and band-pass filters 525/50 and 690/60 (both Semrock) were used in the detection path. Separate images for each fluorescence channel were acquired using two separate electron multiplier charge coupled device (EMCCD) cameras (Photometrics Evolve™). Immediately before imaging, cell membranes were stained using wheat germ agglutinin Alexa Fluor 647 conjugate at a final concentration of 5 µg/mL. After application of the dye, cells were washed twice.

High Content Live-Cell Fluorescence Microscopy:

Image capture was performed using automated multiparametric analysis on the ImageXpress Micro XLS (Molecular Devices) wide-field high content imaging system, and data were analyzed using MetaMorph software and ImageJ. To the investigated cell lines 5 µL (5 µg) of therapeutically active CPCs were added. After 4 hours the cells were washed with the medium recommended by ATCC. Cells were kept under environmental control at 37 °C with 5 % CO₂ inside the ImageXpress Micro XLS device, and images were recorded for each channel. The objective 20x Super Plan Fluor ELWD DM and Semrock GFP and Cy5 filter cubes were used.

In vivo Experiments:

For all *in vivo* experiments C57BL/6 mice (Jackson Laboratories) were housed in isolated cages with a 12 h day/night cycle and food/water ad libitum. Animals were bred at the Center for Animal Models of Disease of the University of Patras. Animal experiments were performed according to guidelines of the European law of protection of animal life (2010/63/EU) and were approved a priori by the Veterinary Administration (protocol approval #118018/ 578-30.04.2014). Luciferin-expressing (pNGL) Lewis lung carcinoma (LLC), skin melanoma (B16F10), and pancreatic adenocarcinoma (PANO2) cells were from the American Type Culture Collection (ATCC) and cultured in fully supplemented DMEM. The 82 C57BL/6 experimental mice used for these studies were weight- (20-25 g) and age-matched (6-12 weeks), were anesthetized under isoflurane, and some mice received 150.000 LLC pNGL, B16F10 pNGL, or PANO2 cells into the pleural cavity for generation of malignant pleural tumors as described elsewhere.³² Intrapleural injections were done under direct stereoscopic vision via a small incision in the right anterolateral chest skin and fascia. Tumors were allowed to grow for five

(LLC and B16F10 cells) or 30 (PANO2 cells) days and the mice were allocated to two treatments by alternation: repeated injections of 100 μ L (20 mg/mL) therapeutically active CPCs into the right side of the pleural cavity (intervention group) or of 100 μ L SBF (control group). Intrapleural injections of CPC and SBF in tumor-bearing and tumor-free mice were repeated as indicated. On days 11, 13, and 56 after implantation of LLC, B16F10, and PANO2 cells, respectively, or on day 56 after first nanoparticle injection into naïve mice, animals were sacrificed with CO₂. Pleural fluid and tumor mass were isolated and analyzed for the number of nucleated cells and tumor weight, respectively.

Bioluminescence imaging:

Mice with pleural tumors formed by bioluminescent tumor cells were imaged under isoflurane anesthesia after delivery of 1 mg intravenous D-luciferin using a Xenogen Lumina II (Perkin-Elmer, Waltham, MA). Data were analyzed using Living Image v.4.2 (Perkin-Elmer) and ImageJ.

Statistics for in vivo experiments:

Cohen's effect size (d) was calculated online (<https://www.socscistatistics.com/>). Sample size (n ; always biological) was determined *ad hoc* using G*power³³, assuming α -error = 0.05, β -error = 0.20, and Cohen's effect size $d = 1.5$, yielding a required sample size of $n = 9$ /group. Hence $n = 9$ mice/group were enrolled in the acute tumor models (LLC and B16F10 cells) and $n = 12$ -18 mice/group in the chronic tumor model (PANO2). One of the intervention group animals in the LLC experiment died immediately post tumor cell injection due to pneumothorax, leaving $n = 9$ and 8 mice available for analyses in the control and intervention groups, respectively. *Post hoc* analysis of tumor mass results (main text, Figure 3b) yielded an actual effect size $d = 1.95$, $\alpha = 0.038$ assuming $\beta = 0.05$, and 96% power when assuming $\alpha = 0.05$. One mouse from each the control and the intervention group animals in the B16F10 experiment died immediately post tumor cell injection due to pneumothorax, leaving $n = 8$ mice available for analyses in the control and intervention groups, respectively. *Post hoc* analysis of tumor mass results (main text, Figure 3d) yielded an actual effect size $d = 4.84$, $\alpha = 6 \times 10^{-6}$ assuming $\beta = 0.05$, and 100% power when assuming $\alpha = 0.05$. Five and two mice from the control and the intervention group animals in the PANO2 experiment died, leaving $n = 13$ and 10 mice available for analyses in the control and intervention groups, respectively. Data were acquired by three blinded readers (I.G., G.N., and M.L.), were reevaluated if > 20%

deviant (no data were excluded), were examined for normality by Kolmogorov-Smirnov test (all data were distributed normally), and were presented and analyzed as indicated and appropriate. Differences in means were examined by unpaired t-test and in measurements over time by two-way ANOVA with Bonferroni post-tests. Probability values (*P*) are two-tailed and *P* < 0.05 was considered significant. Statistics and plots were done on Prism v5.0 (GraphPad, La Jolla, CA).

Synthesis of Calcium Phosphate-Citrate Nanoparticles (CPC):

The synthesis of CPCs was carried out following a modified Pechini sol-gel process. In a 50 mL polypropylene reactor calcium nitrate tetrahydrate (295 mg, 1.25 mmol), ammonium dihydrogenphosphate (86.3 mg, 0.75 mmol) and citric acid (240 mg, 1.25 mmol) were dissolved in water (20 mL, 1.11 mmol). Then cetyltrimethylammonium chloride (622 mg, 1.94 mmol) and the triblock copolymer Pluronic F127 (100 mg) were added and the synthesis mixture was stirred at 500 rpm at room temperature. After 10 minutes of stirring, ethylenglycol (7.15 g, 115 mmol) was added and the solution was cooled 5 minutes at 0 °C. Then the clear solution was combined with triethanolamine (7.15 g, 48 mmol) under vigorous stirring and was allowed to reach room temperature. The suspension was stirred at 500 rpm at room temperature for 10 minutes. Then the suspension was diluted approximately 1:1 with ethanol. The particles were separated by centrifugation at 19,000 rpm (43,146 RCF) for 15 minutes and redispersed in NH₄NO₃/EtOH (2 wt%, 80 mL). To extract the template the suspension was heated under reflux conditions at 90 °C for 30 minutes. Then the particles were separated by centrifugation at 19,000 rpm (43,146 RCF) for 10 minutes and redispersed in 80 mL ethanol. The mixture was heated under reflux conditions at 90 °C for 30 minutes. The particles were separated by centrifugation at 19,000 rpm (43,146 RCF) for 10 minutes and redispersed in 20 mL ethanol.

Synthesis of Crystalline Apatite:

For the synthesis of crystalline apatite D-(+)-pantothenic acid calcium salt (476 mg, 1 mmol) was dissolved in 12 mL water and the pH was adjusted to a value of 1.5 with hydrochloric acid (2 M). Then dipotassium hydrogen phosphate trihydrate (136.5 mg, 0.6 mmol) was dissolved in 2 mL water and added to the calcium-containing solution. Sodium hydroxide (2 M) was

added dropwise under vigorous stirring until the pH reached a value of 12. The particles were washed 4 times with ethanol by centrifugation at 19,000 rpm (43,146 RCF) for 10 minutes and finally redispersed in 20 mL ethanol.

Preparation of Calcium Phosphate-Citrate Particles for Release and Cell Experiments:

0.5 mg of calcium phosphate-citrate particles were loaded in 1 mL aqueous calcein solution (0.62 mg, 1 mmol, pH 9.4) and if needed cetyltrimethylammonium chloride (6.25 μg , 19.5 nmol) for 30 minutes. The particles were separated by centrifugation at 14,000 rpm (16,873 RCF) for 3 minutes. The loaded particles were redispersed in a lipid solution of 1,2-dioleoyl-3-trimethylammonium-propane (DOTAP, 100 μL of a solution with 12.5 mg mL^{-1} 60/40 $\text{H}_2\text{O}/\text{EtOH}$ Vol%) and bi-distilled water (900 μL , pH adjusted to 9.4 with NaOH) was added. Then the particles were separated by centrifugation at 14,000 rpm (16,873 RCF) for 5 minutes. The particles were redispersed in 100 μL of a 1:1 Vol% lipid solution of DOTAP and 1,2-dioleoyl-sn-glycero-3-phosphocholine (DOPC, 12.5 mg mL^{-1} 60/40 $\text{H}_2\text{O}/\text{EtOH}$ Vol%) and SBF (900 μL , pH 7.4) was added. The lipid-coated calcium phosphate-citrate particles were washed twice by centrifugation at 12,000 rpm (12,396 RCF, 13 $^{\circ}\text{C}$) for 5 minutes with SBF (500 μL , pH 7.4).

7.5 Appendix

IR-Spectra:

The gained IR-spectra (Figure 1c main text) are normalized to the PO_4^{3-} stretching vibration at 1083 cm^{-1} . The peak at 556 cm^{-1} is attributed to the bending vibration of the PO_4^{3-} group.(33) The vibrations at 1414 cm^{-1} and 1590 cm^{-1} are attributed to the symmetric and the anti-symmetric stretching mode of COO^- groups of the incorporated citric acid in the structure.(18) The vibrations at 3100 cm^{-1} to 2800 cm^{-1} also result from the C-H vibrations from citric acid. We synthesized crystalline apatite of which the C-O vibrations compared to calcium phosphate-citrate drastically decreased. The visible C-O bands result from carbonate containing crystalline apatite. (Weng W. et al., 2002) The PO_4^{3-} vibration is shifted to lower wavenumbers at 1033 cm^{-1} that indicates crystalline apatite.³⁴

Elemental Analysis:

The ratio of Ca:P in calcium phosphate-citrate particles is 1.61 as determined with EDX and ICP methods (Table 7.1). Therefore, the particles are similar to the stoichiometric value for apatite of Ca:P of 1.66.

Table 7.1: Atomic ratio of calcium and phosphorus with EDX and ICP methods.

measurement		calcium (atom%)	phosphorus (atom%)	Ca:P
EDX	I	8,69	5,30	1.64
	II	7,04	4,39	1.60
	III	8,69	5,43	1.60
	IV	6,04	3,81	1,58
	V	3,59	2,21	1,62
	VI	6,20	3,91	1,58
	VII	8,69	5,43	1,60
ICP	I	6.21	3.89	1.59
	II	6.19	3.85	1.60
average (EDX)		6.99	4.35	1.61
average (ICP)		6.20	3.87	1.60

ss-NMR:

The resonance of PO_4^{3-} is located at 1.62 ppm in the ^{31}P ss-NMR spectrum (Figure 7.5a). By ^{13}C ss-NMR we prove the successful implementation of citric acid. The resonance of the primary C-atoms is located at 179 ppm, the secondary C-atom is located at 44 ppm, and the tertiary C-atom is located at 74 ppm (Figure 7.5b). The ^1H ss-NMR shows the resonance of structural O-H at 1.14 ppm and a small shoulder from adsorbed H_2O (Figure 7.5c).

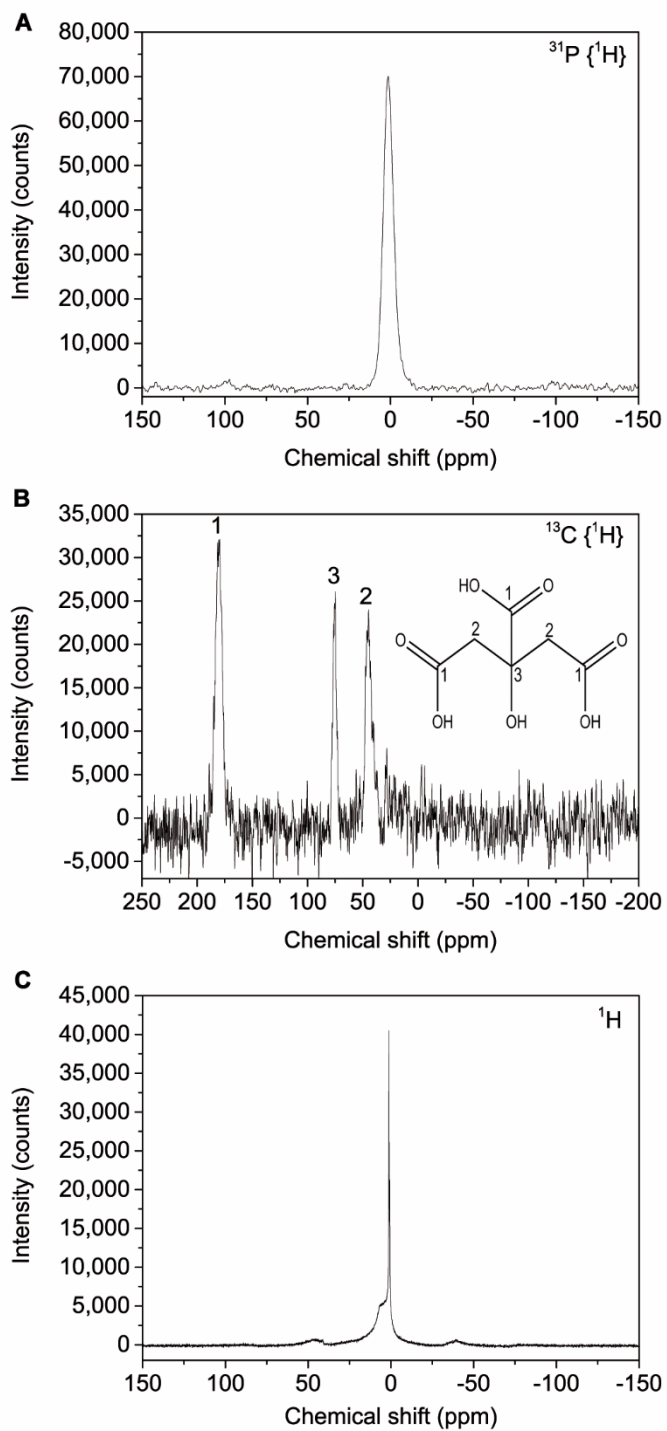


Figure 7.5: ss-NMR of calcium phosphate-citrate nanoparticles (CPCs). Magic angle spinning ss-NMR of CPCs. (A), ^{31}P ss-NMR. (B), ^{13}C ss-NMR. (C), ^1H ss-NMR.

Thermogravimetric Analysis:

The incorporation of citric acid into the framework of the hybrid calcium phosphate-citrate particles was additionally confirmed with TGA measurements (Figure 7.6). The mass loss of calcium phosphate-citrate particles before and after the extraction was investigated with TGA. A moderate mass loss up to 200 °C is attributed to adsorbed water and weakly bound organics (7 wt%). Between 200 °C and 750 °C significant mass loss is observed, which we account to strongly bound organics. Above 750 °C the mass loss stays constant up to 900 °C. Before the extraction of CTAC and Pluronic F127 the mass loss of the organics adds up to 36 wt%. For particles that have been extracted the mass loss of organics is lowered to 20 wt%, which we attribute to the decomposition of citric acid. Due to the incorporation of citric acid in the calcium phosphate-citrate structure the mass loss is shifted to higher temperatures compared to pure citric acid (decomposition temperature: 175 °C). Therefore, we can calculate the amount of CTAC/Pluronic F127 in the pore structure to be 16 wt%.

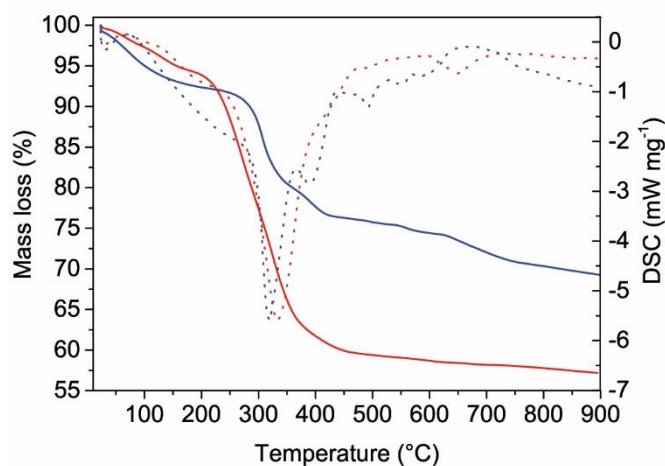


Figure 7.6: Thermogravimetric analysis. Mass loss (left y-axis) of calcium phosphate-citrate particles before (red solid line) and after (blue solid line) extraction. DSC (right y-axis) of calcium phosphate-citrate particles before (red dotted line) and after (blue dotted line) extraction.

X-Ray Scattering:

In small angle X-ray scattering data a broad reflection is observed at $2\theta = 1.44^\circ$, which corresponds to a d -spacing of 6.13 nm. With a pore size of 5 nm obtained from N₂-sorption measurements a wall thickness of 1.13 nm is estimated. In wide angle X-ray scattering data a typical shape for amorphous compounds is observed (main text, Figure 7.2b).

Concentrations

All mentioned concentrations refer to the mass of CPC and not the mass of the overall formulation.

In Vitro Release Fluorescence Measurements:

Lipid-coated calcium phosphate-citrate particles were transferred into the cap of a homebuilt fluorescence setup (0.5 mg particles in 200 μ L SBF) and separated by a cellulose membrane from the measuring cell, which is filled with SBF (Figure 7.7a). Dye that is released from the particles diffuses through the membrane and can be detected in the measuring cell (Figure 7.7b). While detecting the fluorescence of calcein with a spectrometer at 512 nm (excitation at 495 nm) as a function of the time the stimulated release can be observed.

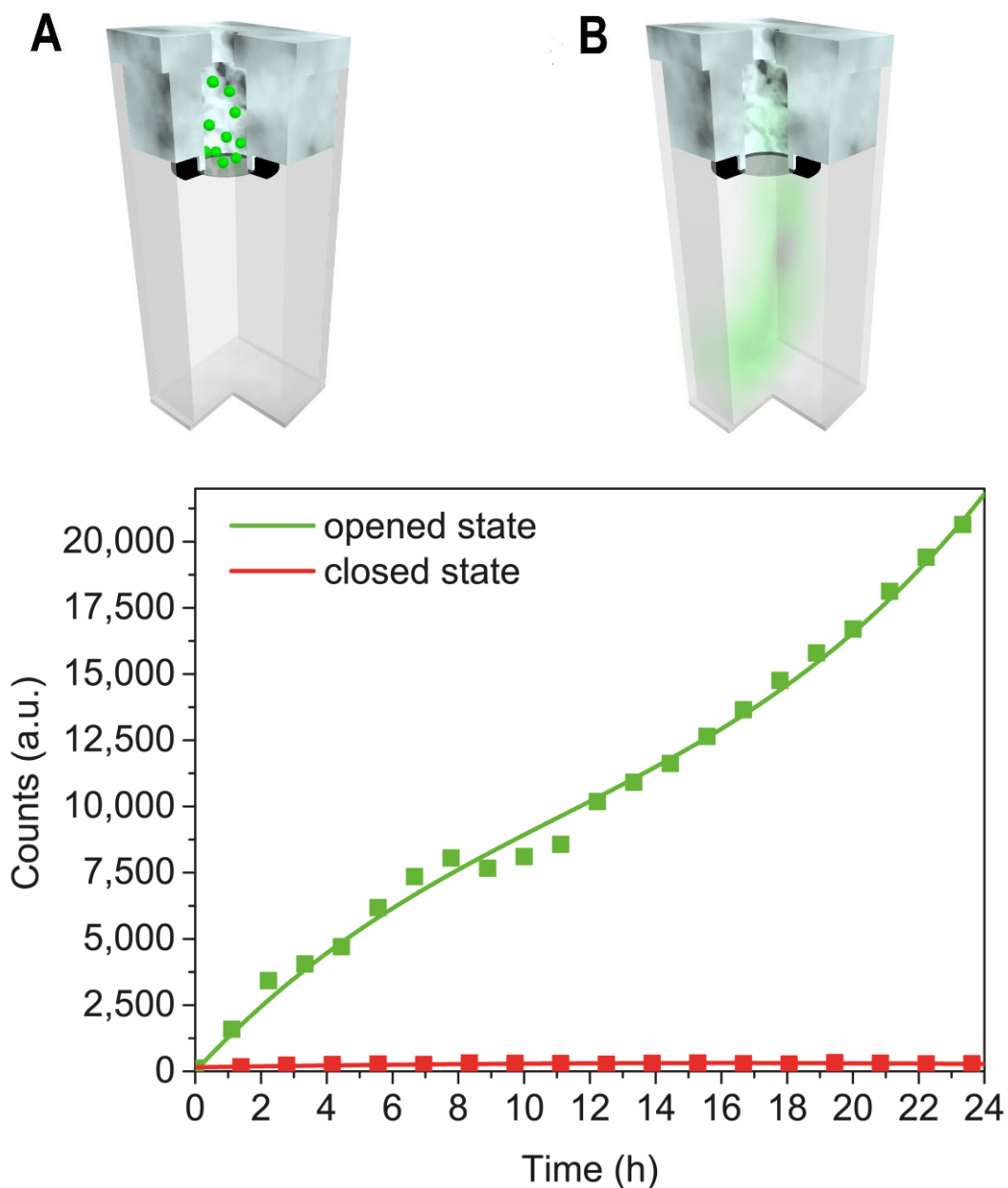


Figure 7.7: Setup for fluorescence measurements. (A), Lipid-coated calcium phosphate-citrate particles in green are separated in the reservoir cap from the measuring compartment by a cellulose membrane (molecular weight cut off 14,000) in simulated body fluid with pH at 7.4. (B), Dissolved lipid-coated calcium phosphate-citrate particles release the loaded model drug calcein, which can penetrate through the cellulose membrane into the measuring compartment and be detected.-Calcein loaded lipid coated CPCs show no premature release at pH 7.4 (red), but show immediate and constant release upon lowering the pH to 5.5 with 0.1 M HCl.

Cell Viability:

Cell viability assays (MTT-assays) were carried out with a total of thirteen cell lines. For MCF 10A and MDA-MB-231 see main text. For MEF, ESC, MCF7, BT-474, HuH7, AE17, B16, Neuro 2A, H1299, LLC, and HeLa see Figure 7.9. RealTime-Glo[®], CellTiter-Glo[®] and Caspase-Glo[®] 3/7 cell viability assays was carried out for HeLa (Figure 7.8). Therapeutically active CPCs that are able to escape from the endosome, show effective cell death with low IC₅₀ values for cancer cells (Table 7.2).

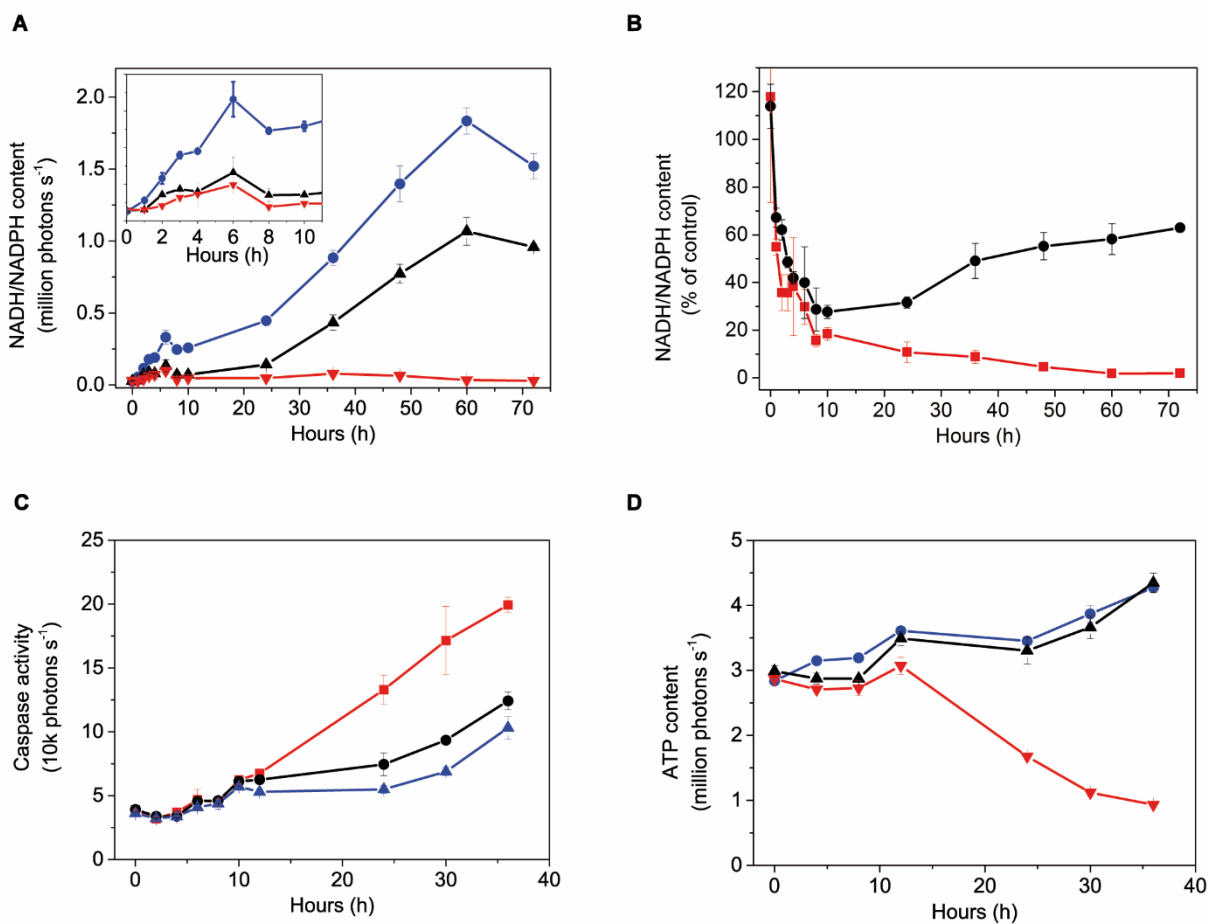
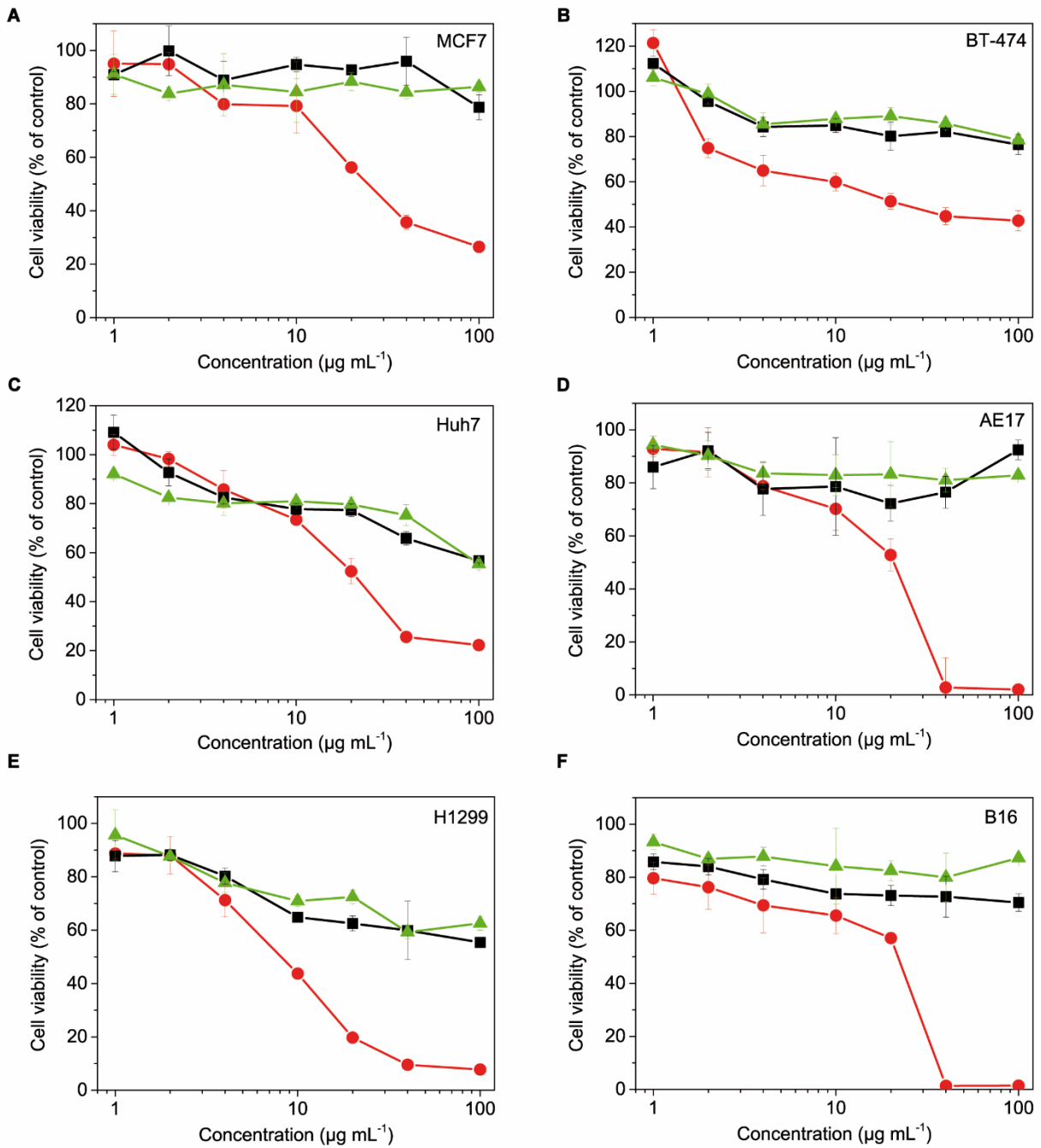


Figure 7.8: NADH/NADPH contents, Caspase-activity, and ATP content over time. Time-dependent tracking of therapeutically active CPCs (red line), lipid-coated CPCs (black line) and SFB (blue line) on HeLa cells with respect to the (A), NADH/NADPH content and (B), NADH/NADPH content normalized to the data of HeLa cells incubated with SFB buffer only, (C), caspase activity and (D), ATP content. Therapeutically active CPCs trigger NADH/NADPH and ATP reduction and an increase of caspase activity over time, while for lipid-coated CPCs no effect was observed.

Table 7.2: IC₅₀ values for investigated cell lines. Therapeutically active CPCs were incubated with the corresponding cell lines at concentrations from 1 to 100 µg/mL. MTT-assays were performed after 72 h of incubation. IC₅₀ values were calculated with GraphPad Prism 5 and OriginPro 9.

Cell line	IC₅₀ (µg/mL)
MCF10A	-
ESC	-
MEF	-
Pano2	58.0
BT-474	30.0
MCF7	18.5
HuH7	14.0
AE17	15.7
B16	11.5
H1299	8.2
HeLa	8.0
Neuro 2A	4.7
MDA-MB-231	4.4
LLC	4.0



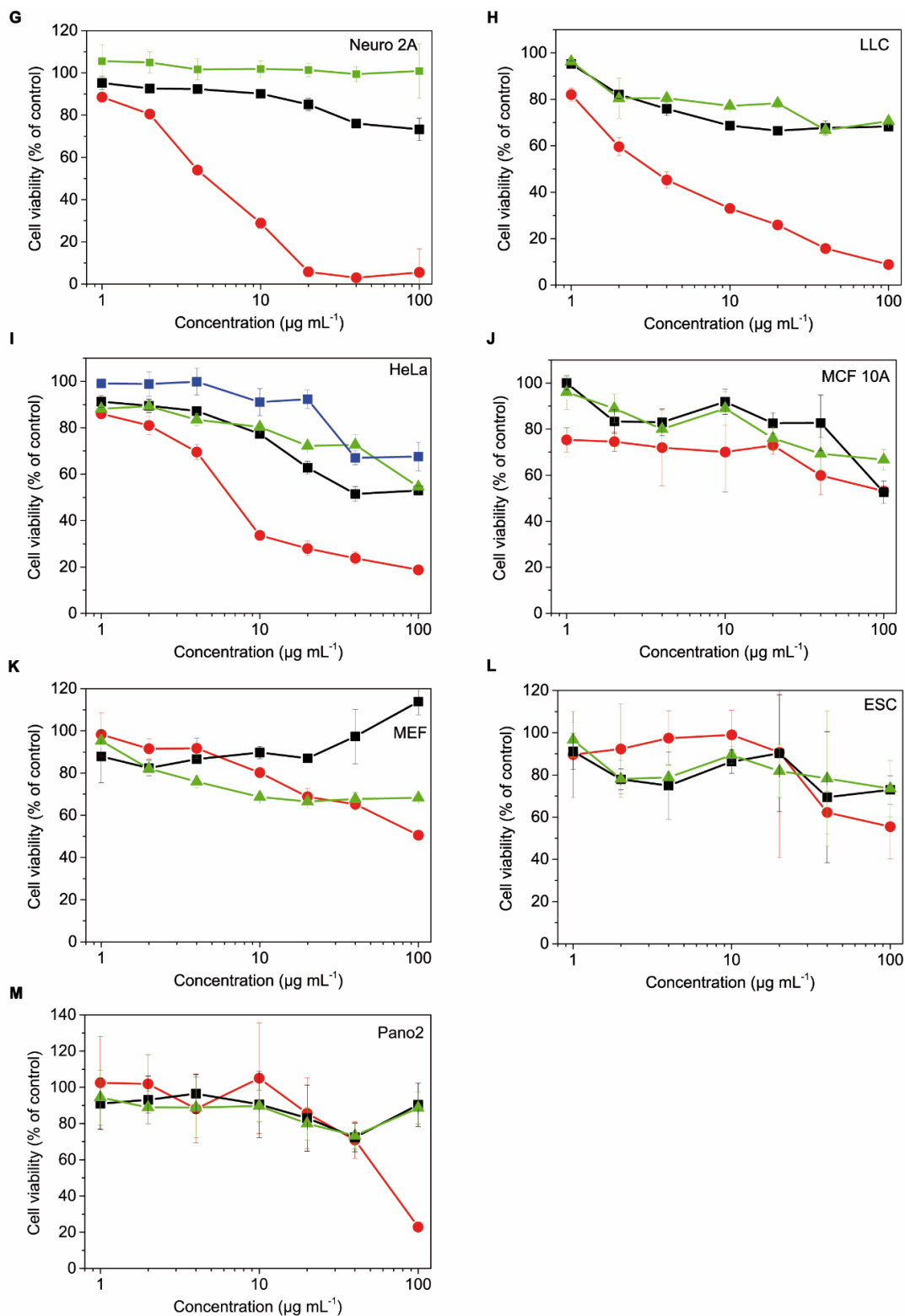
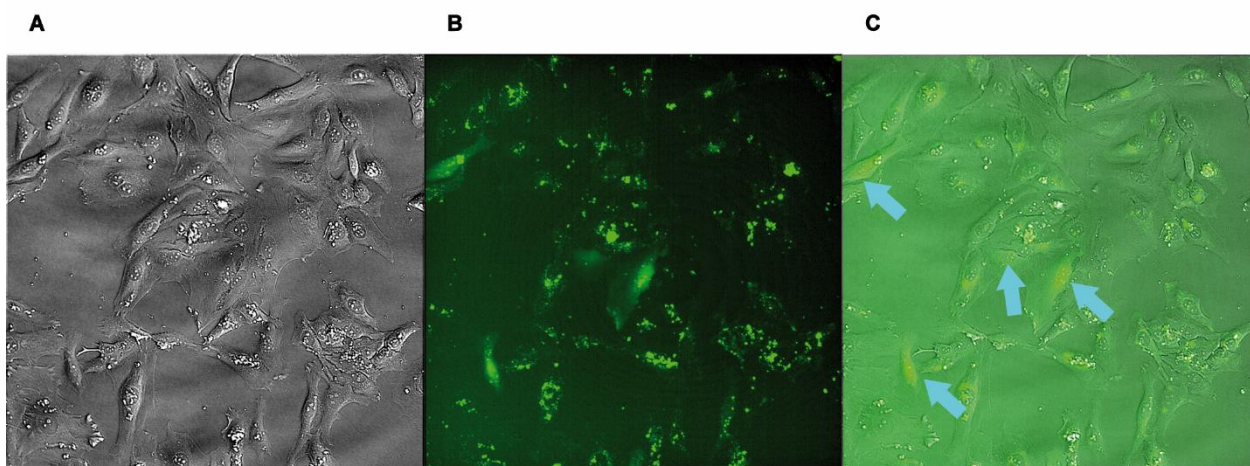
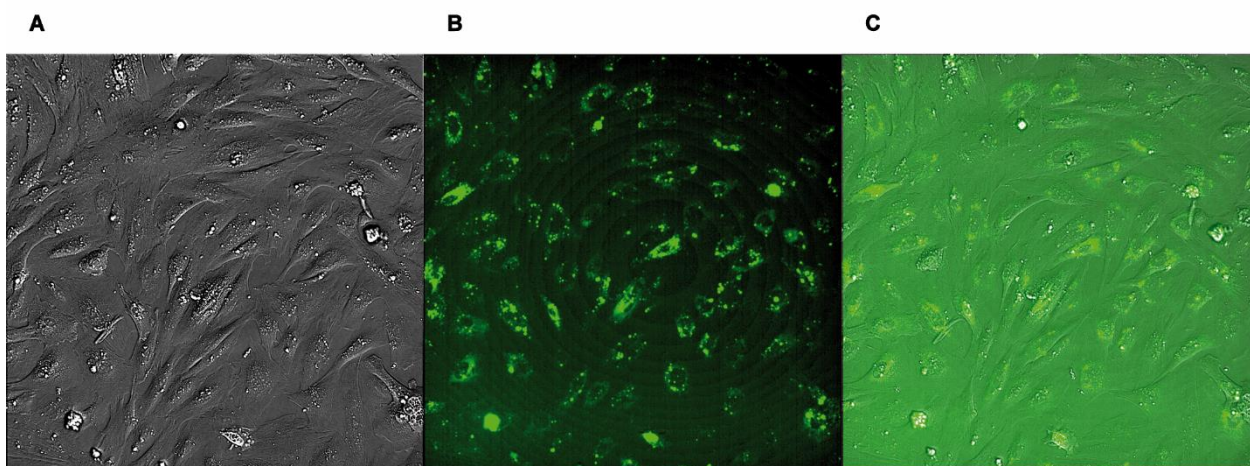


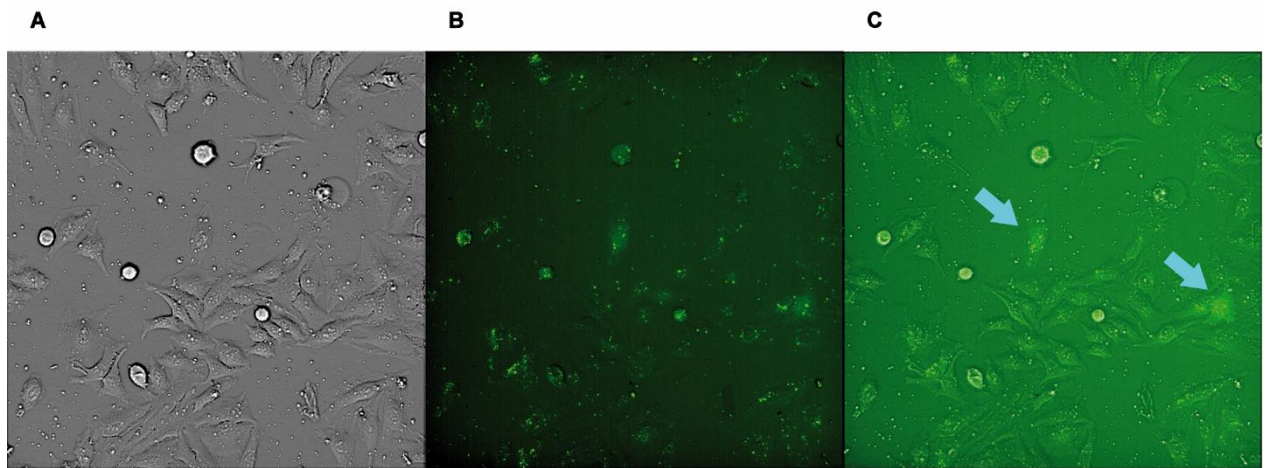
Figure 7.9: Cell viability of investigated cell lines. MTT-assay with readout 72 h after treatment. (A)-(I), Cell lines are named in the upper right corner. Green lines display the effect of calcium phosphate-citrate nanoparticles (CPCs), which crystallize and were not taken up by cells (cf. Figure 7.15). Black lines display lipid-coated CPCs, which were taken up by cells but did not escape from the endosome due to the lack of an additive. Red lines display lipid-coated CPCs that were taken up by cells and showed endosomal escape. As a reference experiment, we tested the toxic effect of remaining substances after dissolution of CPCs on HeLa cells (Figure 7.9i).



Movie 7.1. Movie of HeLa cells after incubation with therapeutically active CPCs and with endosomal release. **(A)**, Transmission image of HeLa cells. **(B)**, The green dots mark the lipid-coated and calcein/CTAC-loaded CPCs. **(C)**, Overlay of transmission and calcein channels. The green dots mark the calcein loaded CPCs. Every 10 minutes images of transmittance- and GFP-channels were recorded and stacked to a movie with 10 fps. During the incubation in various cells a strong increase in fluorescence of calcein released from the endosome is visualized (blue arrows). Afterwards, the morphology of the cell undergoes changes due to the shock from the release of the dissolved CPCs.



Movie 7.2. Movie of MCF 10A cells after incubation with therapeutically active CPCs without endosomal release. **(A)**, Transmission image of HeLa cells. **(B)**, The green dots mark the lipid-coated and calcein/CTAC-loaded CPCs. **(C)**, Overlay of transmission and calcein channels. Every 20 minutes images of transmittance- and GFP-channels were recorded and stacked to a movie with 5 fps. During the incubation no increase in fluorescence of calcein released from the endosome is detected.



Movie 7.3. Movie of HeLa cells after incubation with lipid-coated CPCs that are not toxic to cells. (A), Transmission image of HeLa cells. (B), The green dots mark the lipid-coated and calcein-loaded CPCs. (C), Overlay of transmission and calcein channels. Every 12 minutes images of transmittance- and GFP-channels were recorded and stacked to a movie with 10 fps. During the incubation only in a few cells an increase in fluorescence of calcein released from the endosome is detectable (blue arrows). The amount of calcium released into the cells is far less than that of the therapeutically active CPCs. This leads to the non-toxic effect of lipid-coated CPCs.

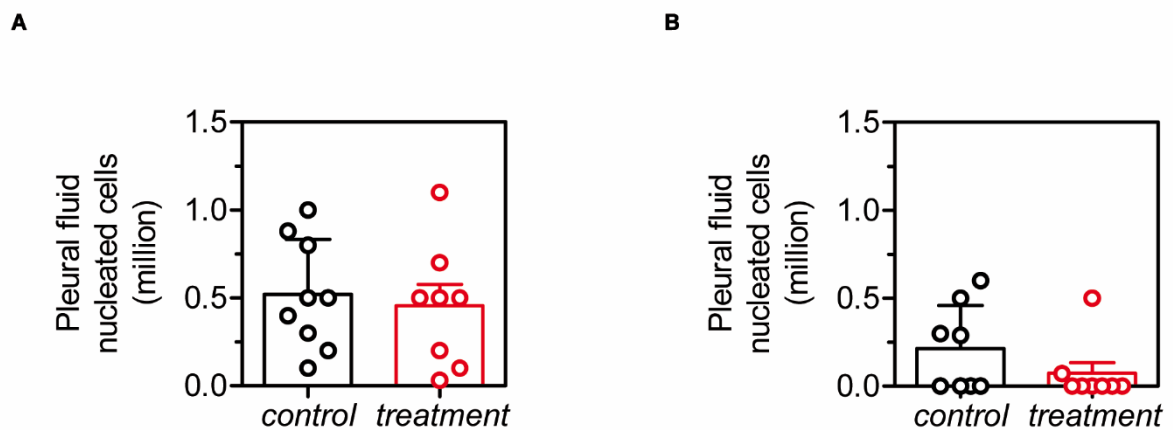


Figure 7.10: Number of pleural fluid nucleated cells.

Pleural fluid nucleated cell counts show no sign of inflammation in response to CPC treatment (A), for the LLC tumor model and (B), for the B16F10 tumor model.

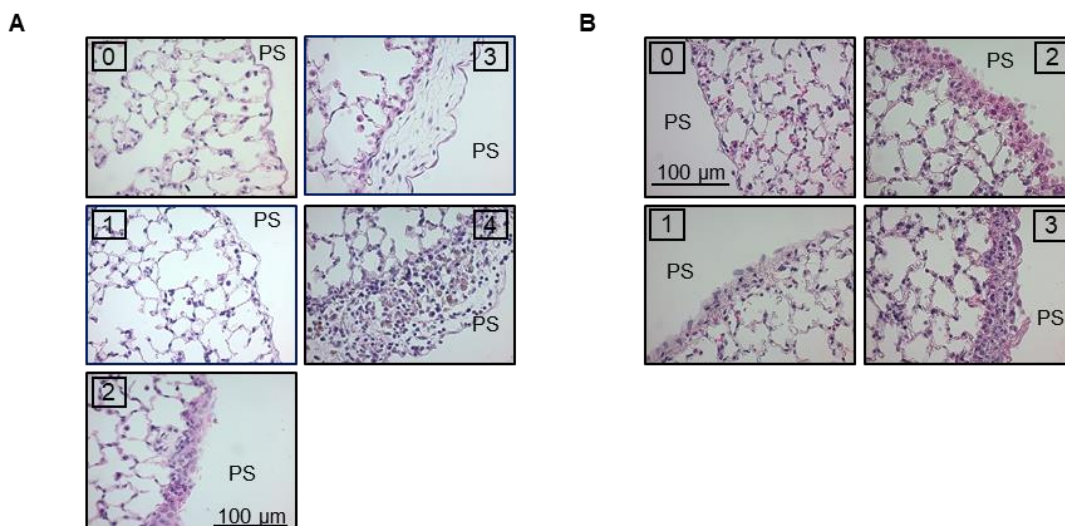


Figure 7.11: Representative images of pleural thickening grade **(A)** for tumor-free mice and **(B)** for the PANO2 tumor model.

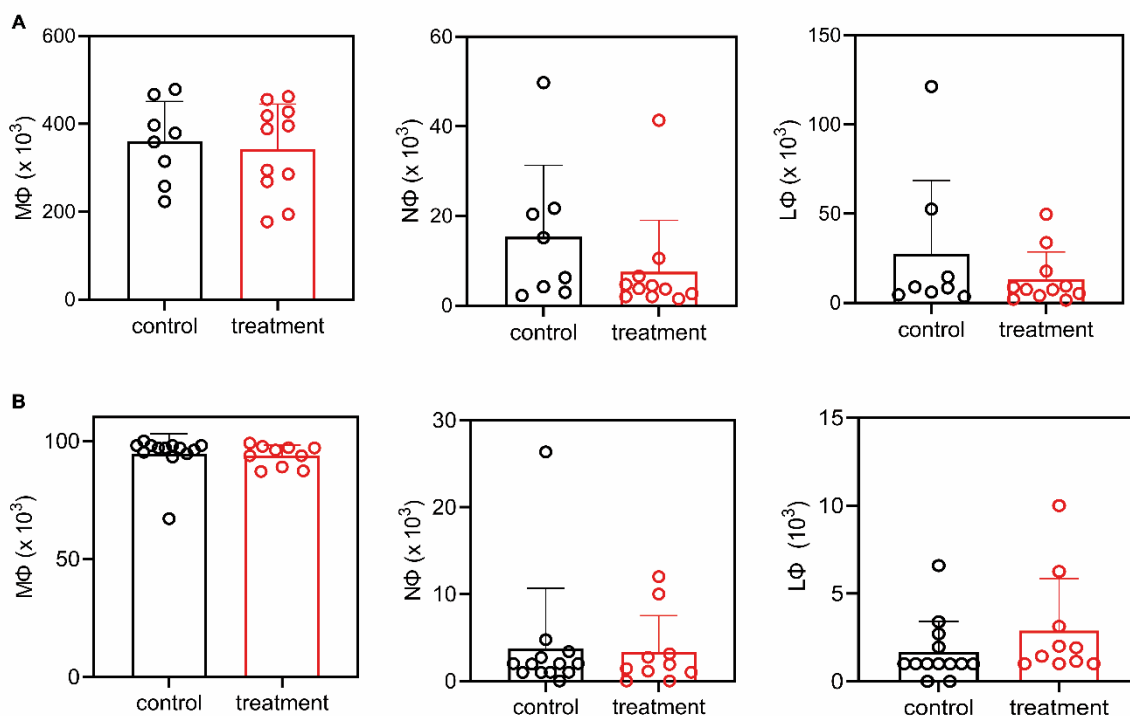


Figure 7.12: Number of macrophages in the pleural cavity after long-term experiments. **(A)** Number of cells identified as mononuclear (MΦ), polymorphonuclear (NΦ) and lymphocytic (LΦ) bronchoalveolar lavage (BAL) cells in the experiments with tumor-free mice. **(B)** Number of cells identified as mononuclear (MΦ), polymorphonuclear (NΦ) and lymphocytic (LΦ) pleural lavage cells in the experiments employing the PANO2 tumor model.

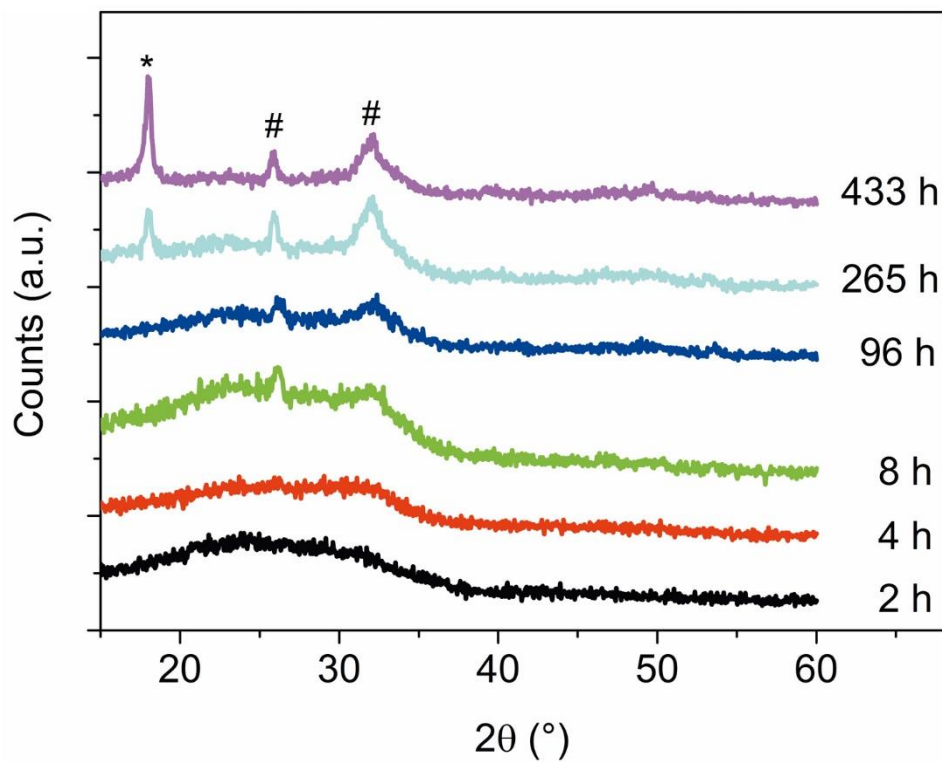


Figure 7.13: Wide angle X-ray scattering of uncoated CPC with a molar ratio of Ca:CA = 1:1 after storage in H₂O (pH = 6.5) for 2, 4, 8, 96, 265, and 433 hours. The crosses mark the typical reflexes of crystalline apatite. The asterisk marks the reflection of crystalline calcium citrate (the graphs were shifted along the y-axis for clarity reasons).

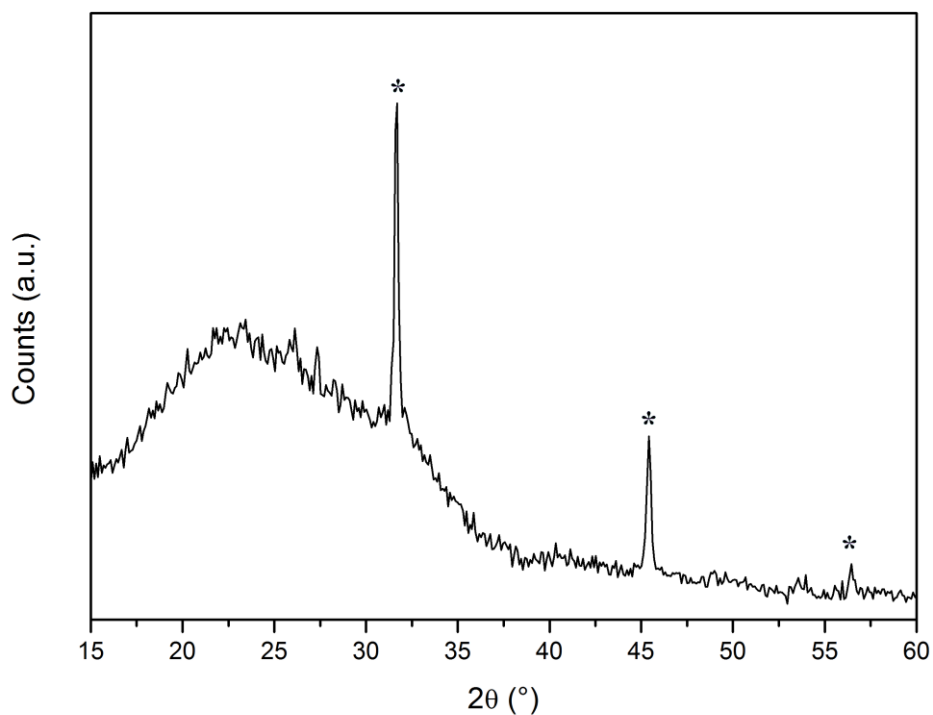


Figure 7.14: Wide angle X-ray scattering of lipid-coated, CTAC-loaded CPCs with a molar ratio of Ca:CA = 1:1 after storage in H₂O (pH = 6.5) for several months. The asterisks marks the reflection of crystalline NaCl from the substrate. The result shows the stabilization of the amorphous structure by the lipids.

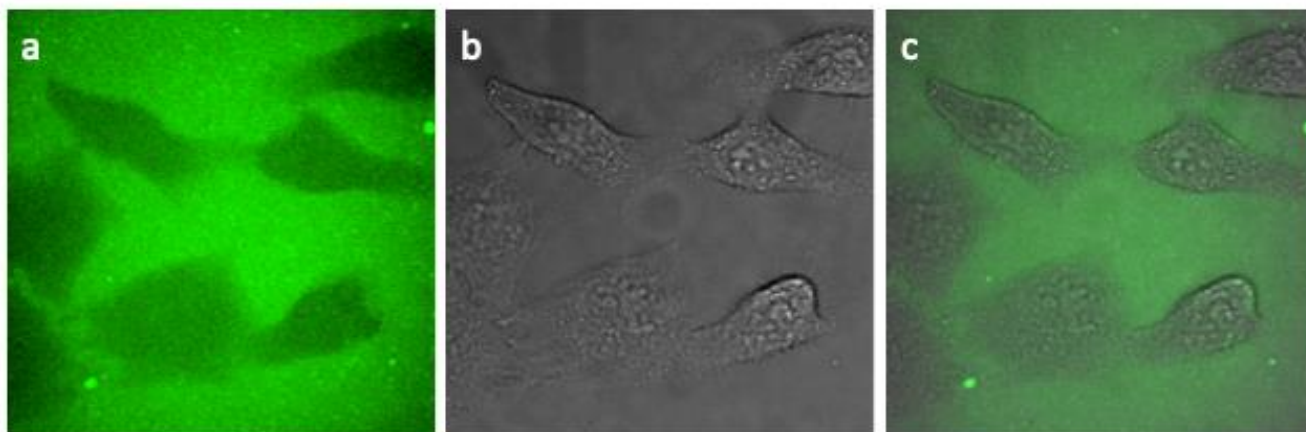


Figure 7.15: Uncoated CPC incubated on HeLa cells for 24h. a) CPC fluorescence b) brightfield image of cells c) composite of a) and b). The images show clearly that uncoated CPC are not taken up.

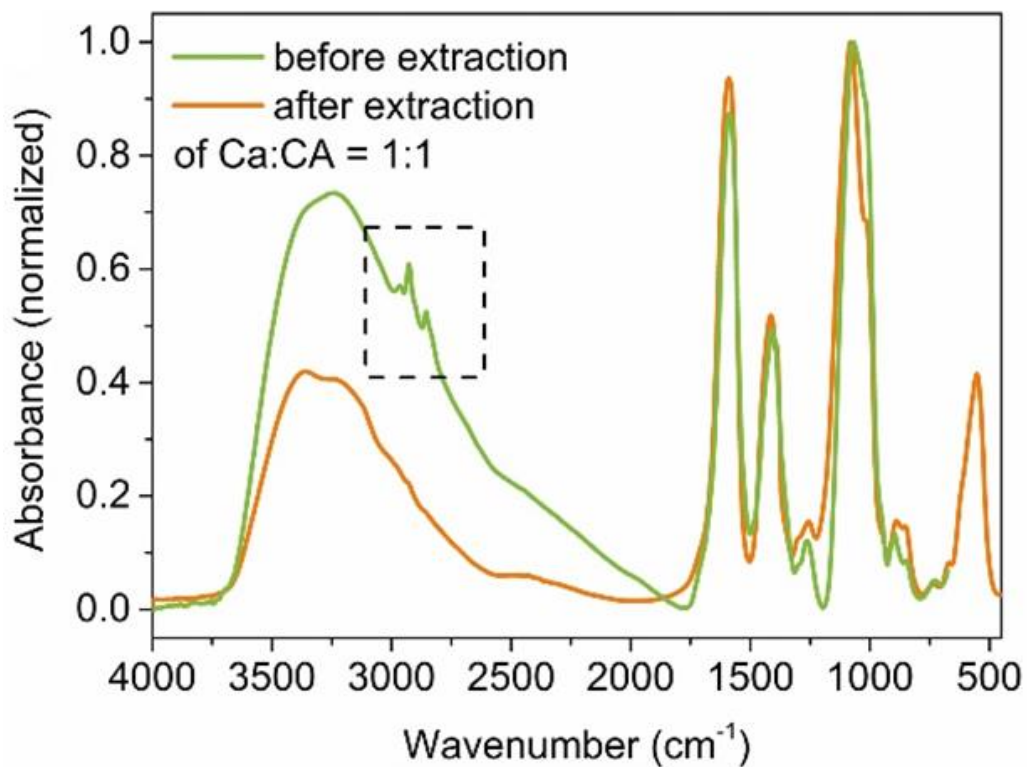


Figure 7.16: IR-spectra of CPC before extraction (green colored line) and after extraction (orange colored line) of the sample with a molar ratio of Ca:CA = 1:1. The dotted box displays the -CH vibrations of the alkane chain of the template, which is removed upon extraction, while the strong COO^- vibrations at 1410 cm^{-1} and 1590 cm^{-1} resulting from citric acid remain constant.

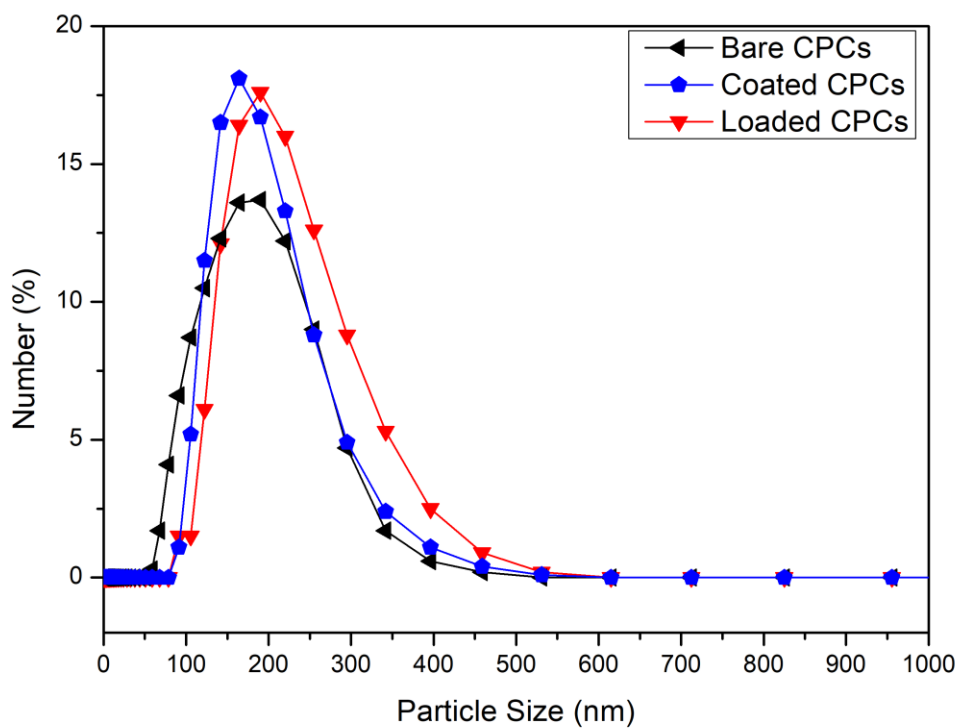


Figure 7.17: DLS measurements of uncoated CPCs (black), lipid coated CPCs (blue) and CTAC loaded, lipid coated CPCs (red).

Table 7.3: Zeta potential of coated and uncoated CPCs

	Bare CPC	Lipid Coated CPC	CTAC loaded, lipid coated CPC
Zeta Potential (mV)	-5	+19	+20

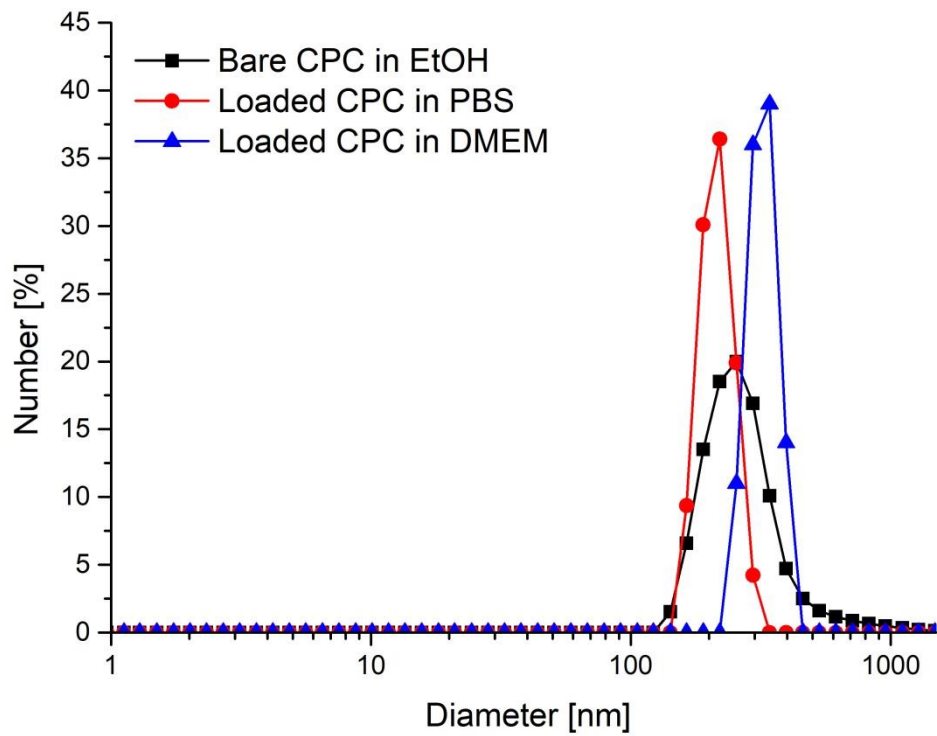


Figure 7.18: DLS measurements of uncoated CPC in EtOH (black), and CTAC loaded, lipid coated CPCs in PBS (blue) and DMEM (red).

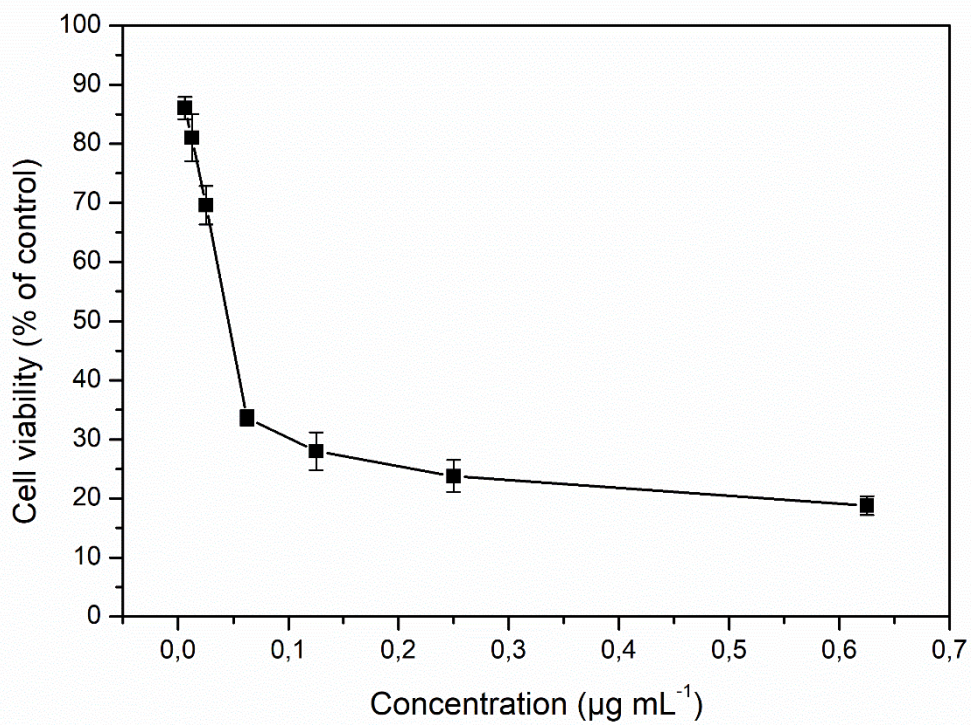


Figure 7.19: MTT measurements of free CTAC on HeLa cells.

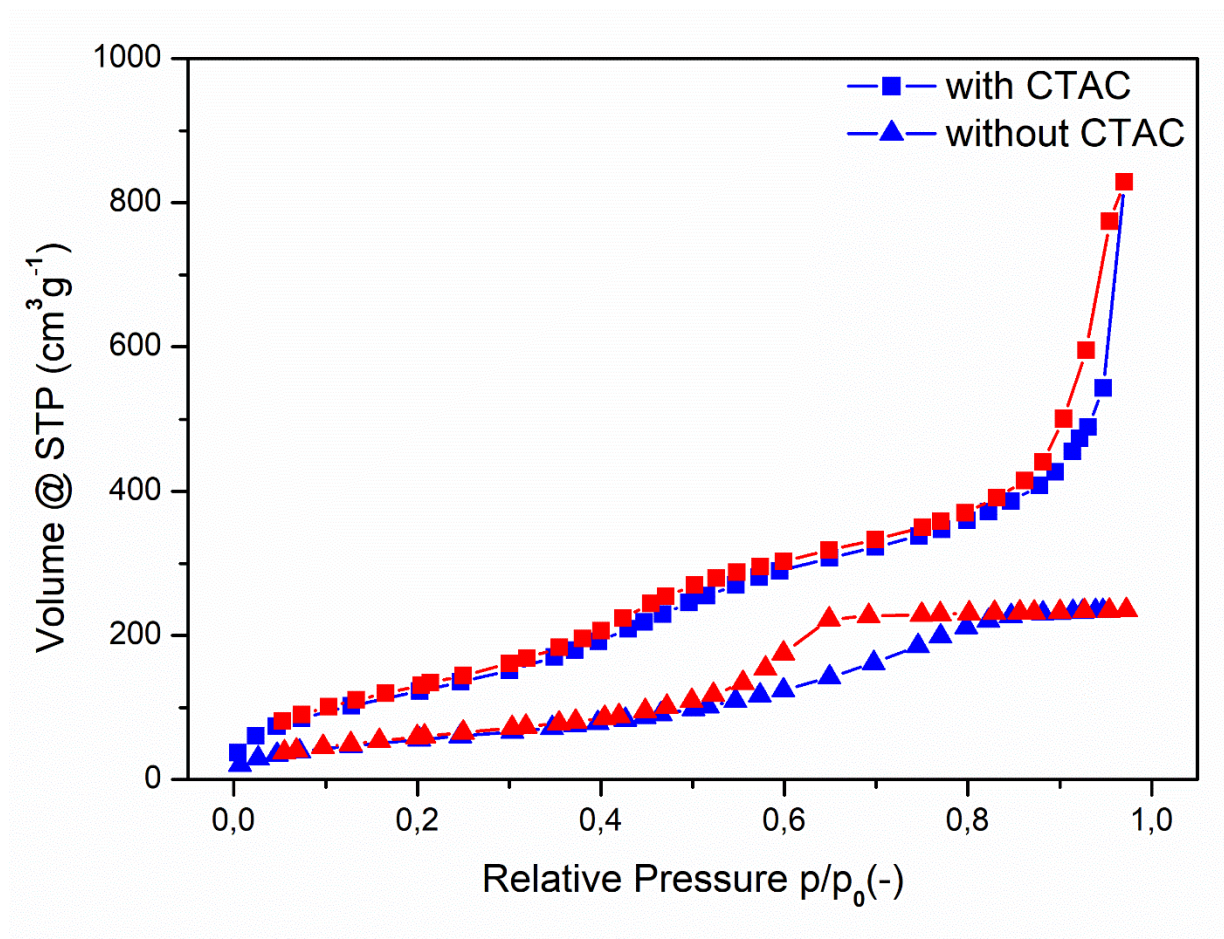


Figure 7.20: Sorption measurements of CPCs synthesized with and without CTAC as a template, showing the importance of a template for high surface areas

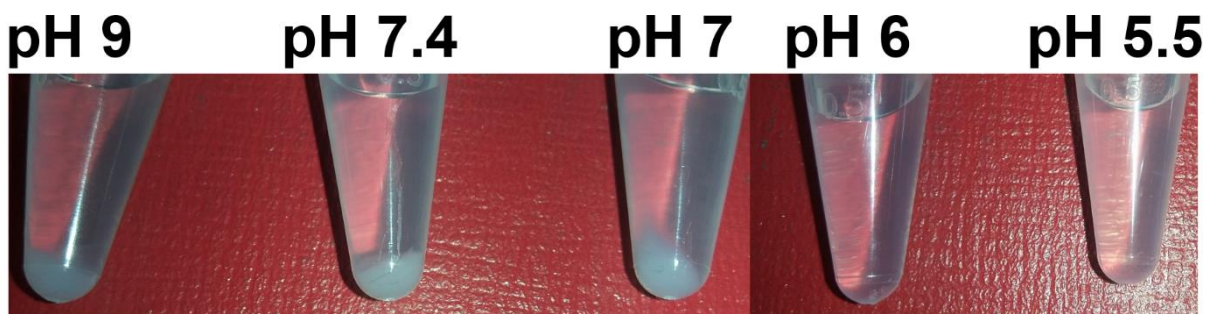


Figure 7.21: Degradation of CPCs at different pH. At pH 7 or above particles can be recovered by centrifugation, while particles are dissolved and irrecoverable at lower pH.

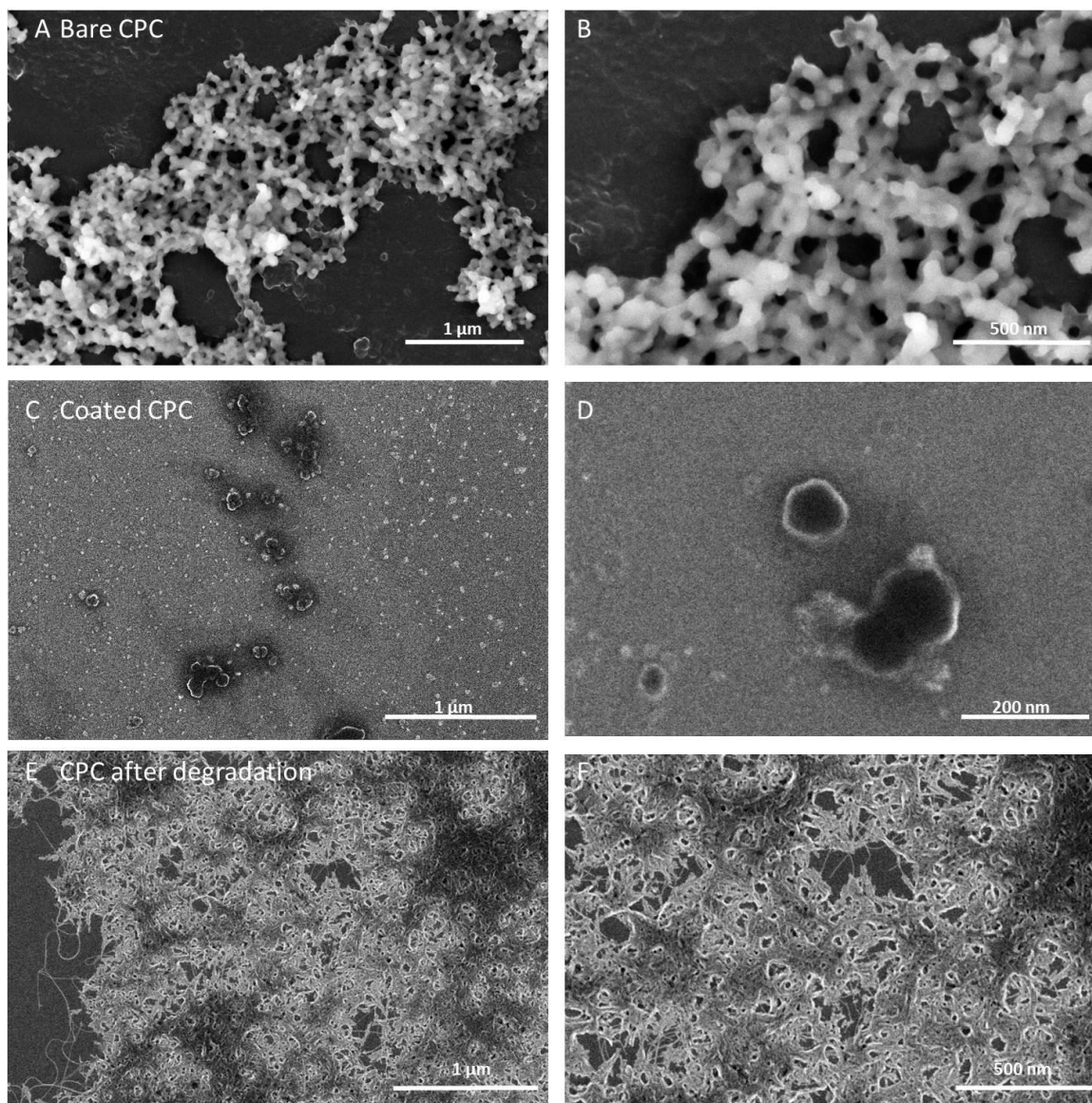


Figure 7.22: STEM images of bare CPC (a-b), lipid coated CPC (c-d) and CPC after degradation (e-f).

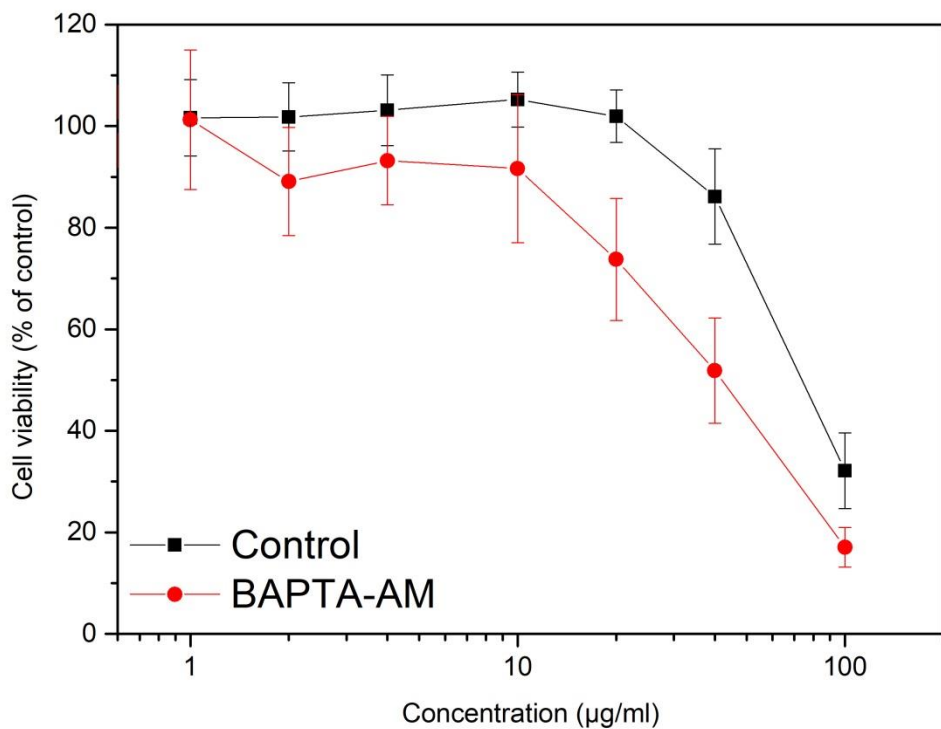


Figure 7.23: Cell viability assay on HeLa cells after 72 h with various concentrations of loaded, lipid-coated CPC without addition of Ca^{2+} chelating agent BAPTA-AM (black line) and with addition of BAPTA-AM (50 μ M) for 1 h after 1 h incubation of CPC (red line).

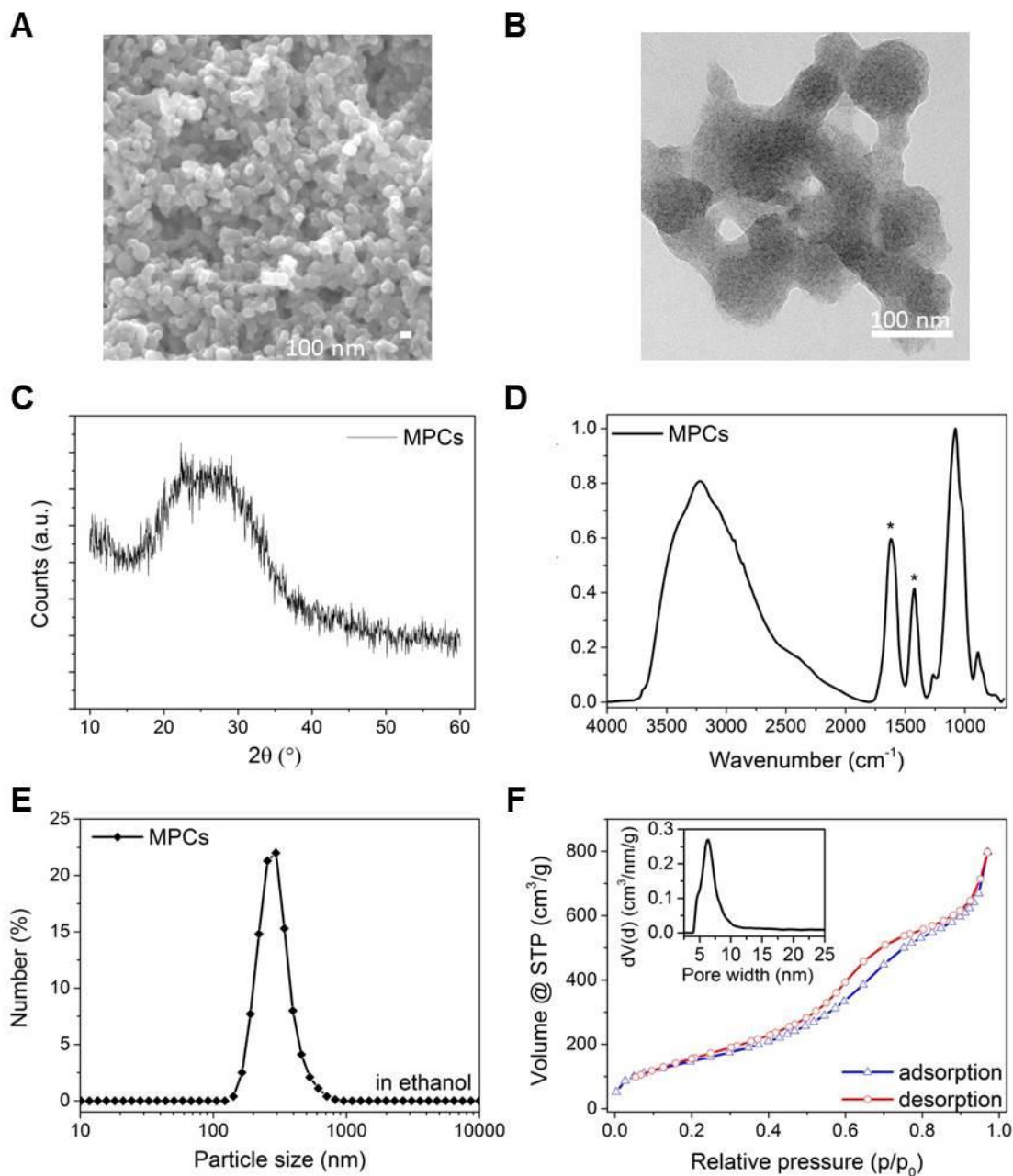


Figure 7.24: Characterization of mesoporous magnesium phosphate-citrate nanoparticles (MPC). **(A)** Scanning electron microscopy and **(B)** transmission electron microscopy images. Scale bars: 100 nm. **(C)** X-ray scattering measurements showing the amorphous nature of MPC **(D)** Infrared spectra of MPC **(E)** Dynamic light scattering data of colloidal MPC. **(F)** Nitrogen sorption isotherm and pore size distribution (inlet).

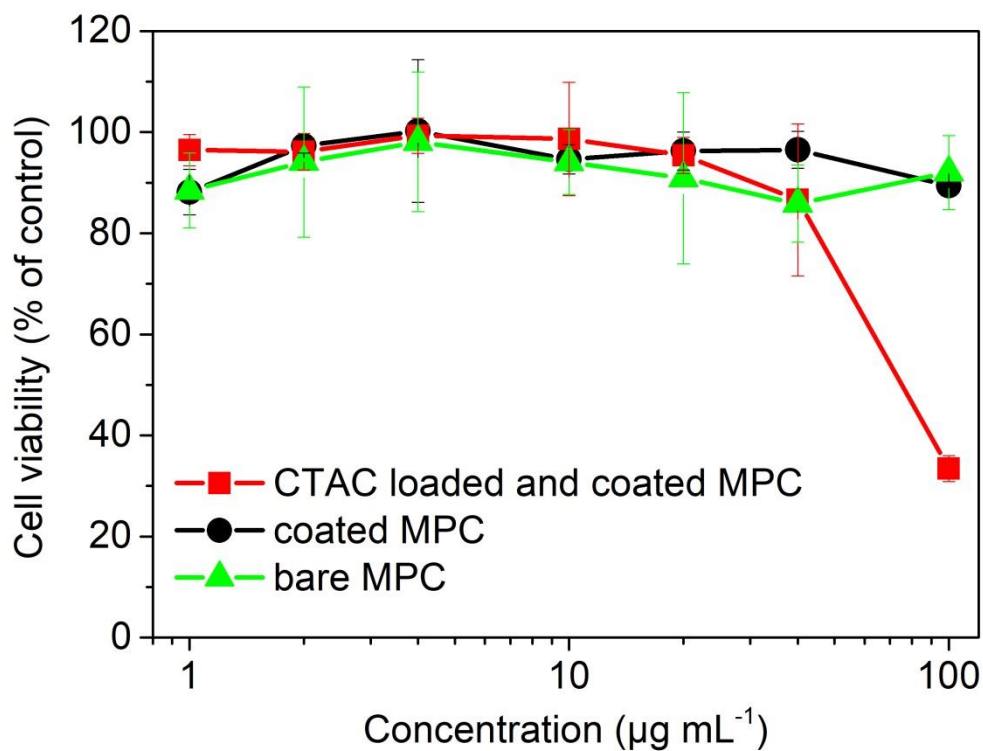


Figure 7.25: MTT-assay of MPC with readout 72 h after treatment.

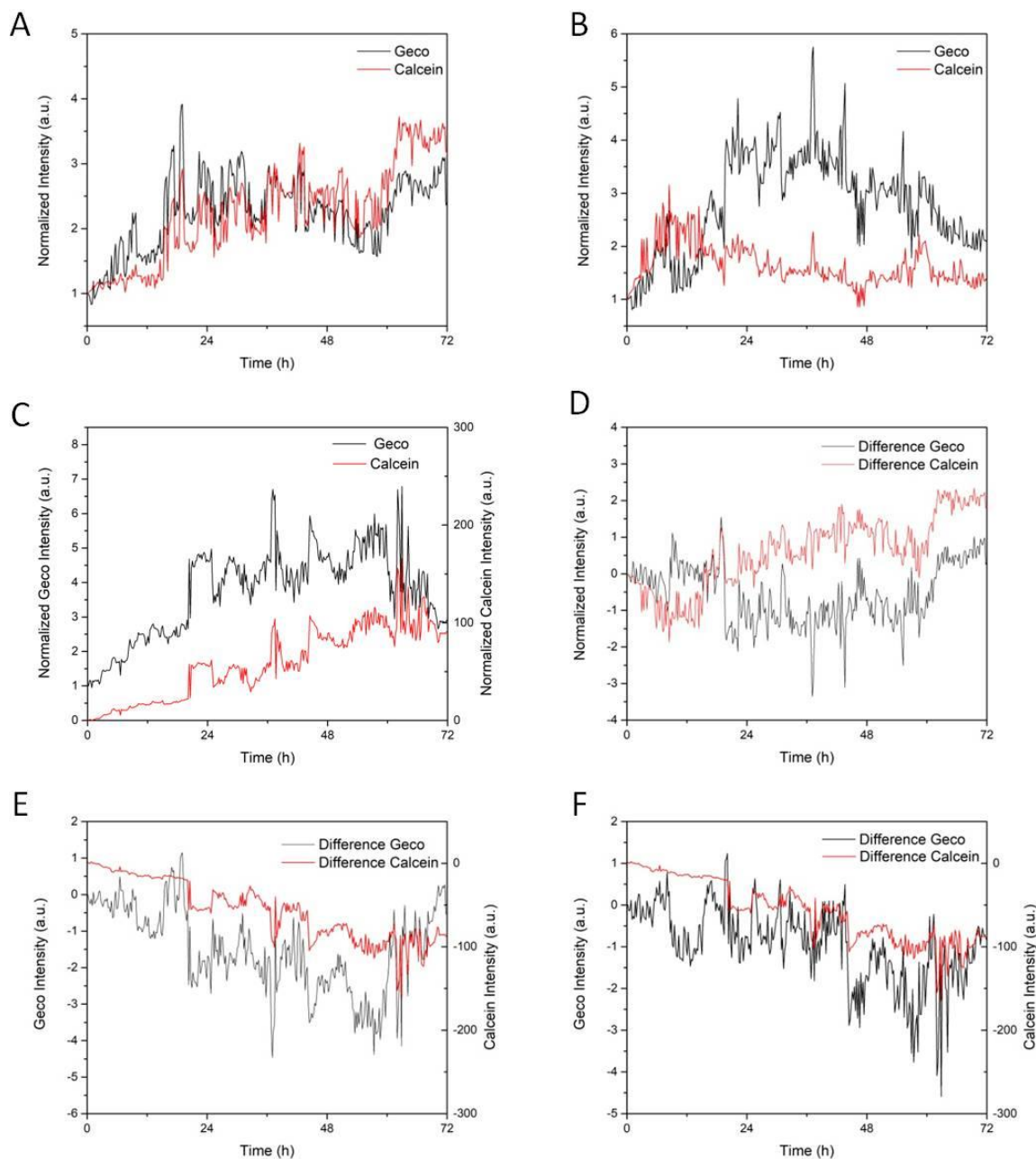


Figure 7.26: Live cell Ca^{2+} GECO assay of GECO transfected HeLa cells with (A) lipid-coated CPC loaded with CTAC (B) without CTAC and (C) without particles. Plots D-F show the difference in the geco and calcein signal of (D) lipid-coated CPC loaded with CTAC minus lipid-coated CPC loaded without CTAC (E) lipid-coated CPC loaded with CTAC minus no particles and (F) lipid-coated CPC loaded without CTAC minus no particles.

7.6 References:

1. Dorozhkin, S.V. & Epple, M. Biological and medical significance of calcium phosphates. *Angew. Chem. Int. Ed. Engl.* **41**, 3130-3146 (2002).
2. Mycielska, M.E. et al. Citrate transport and metabolism in mammalian cells: prostate epithelial cells and prostate cancer. *BioEssays : news and reviews in molecular, cellular and developmental biology* **31**, 10-20 (2009).
3. Vallet-Regí, M. & Ruiz-Hernández, E. Bioceramics: From Bone Regeneration to Cancer Nanomedicine. *Adv. Mater.* **23**, 5177-5218 (2011).
4. Orrenius, S., Zhivotovsky, B. & Nicotera, P. Regulation of cell death: the calcium-apoptosis link. *Nat. Rev. Mol. Cell Biol.* **4**, 552-565 (2003).
5. Ren, J.G. et al. Citrate Suppresses Tumor Growth in Multiple Models through Inhibition of Glycolysis, the Tricarboxylic Acid Cycle and the IGF-1R Pathway. *Sci. Rep.* **7**, 4537 (2017).
6. Boehmerle, W. & Endres, M. Salinomycin induces calpain and cytochrome c-mediated neuronal cell death. *Cell Death Dis.* **2**, e168-e168 (2011).
7. Berridge, M.J., Bootman, M.D. & Roderick, H.L. Calcium signalling: dynamics, homeostasis and remodelling. *Nat. Rev. Mol. Cell Biol.* **4**, 517-529 (2003).
8. Petros, R.A. & DeSimone, J.M. Strategies in the design of nanoparticles for therapeutic applications. *Nature Reviews Drug Discovery* **9**, 615-627 (2010).
9. Torchilin, V.P. Multifunctional, stimuli-sensitive nanoparticulate systems for drug delivery. *Nature Reviews Drug Discovery* **13**, 813-827 (2014).
10. Irvine, D.J. Drug delivery: One nanoparticle, one kill. *Nature materials* **10**, 342-343 (2011).
11. Freund, R., Lächelt, U., Gruber, T., Rühle, B. & Wuttke, S. Multifunctional Efficiency: Extending the Concept of Atom Economy to Functional Nanomaterials. *ACS Nano* **12**, 2094-2105 (2018).
12. Li, J., Yang, Y. & Huang, L. Calcium phosphate nanoparticles with an asymmetric lipid bilayer coating for siRNA delivery to the tumor. *J. Control. Release* **158**, 108-114 (2012).
13. Zhao, X.-Y., Zhu, Y.-J., Chen, F. & Wu, J. Calcium Phosphate Nanocarriers Dual-Loaded with Bovine Serum Albumin and Ibuprofen: Facile Synthesis, Sequential Drug Loading and Sustained Drug Release. *Chemistry – An Asian Journal* **7**, 1610-1615 (2012).
14. Zhang, M. & Kataoka, K. Nano-structured composites based on calcium phosphate for cellular delivery of therapeutic and diagnostic agents. *Nano Today* **4**, 508-517 (2009).
15. Zhang, Y., Schwerbrock, N.M., Rogers, A.B., Kim, W.Y. & Huang, L. Codelivery of VEGF siRNA and gemcitabine monophosphate in a single nanoparticle formulation for effective treatment of NSCLC. *Mol. Ther.* **21**, 1559-1569 (2013).
16. Motskin, M. et al. Hydroxyapatite nano and microparticles: correlation of particle properties with cytotoxicity and biostability. *Biomaterials* **30**, 3307-3317 (2009).
17. Tang, W. et al. Differential cytotoxicity and particle action of hydroxyapatite nanoparticles in human cancer cells. *Nanomedicine (London, U. K.)* **9**, 397-412 (2014).
18. Davies, E. et al. Citrate bridges between mineral platelets in bone. *Proc. Natl. Acad. Sci. U. S. A.* **111**, E1354-1363 (2014).
19. Cifuentes, I., González-Díaz, P.F. & Cifuentes-Delatte, L. Is there a "citrate-apatite" in biological calcified systems? *Calcif. Tissue Int.* **31**, 147-151 (1980).
20. Slowing, I.I., Vivero-Escoto, J.L., Wu, C.-W. & Lin, V.S.Y. Mesoporous silica nanoparticles as controlled release drug delivery and gene transfection carriers. *Adv. Drug Del. Rev.* **60**, 1278-1288 (2008).
21. Chen, F. et al. Multifunctional Biodegradable Mesoporous Microspheres of Eu³⁺-doped Amorphous Calcium Phosphate: Microwave-Assisted Preparation, pH-Sensitive Drug Release and Bioimaging. *J. Mater. Chem. B* **2** (2014).
22. Cauda, V. et al. Colchicine-Loaded Lipid Bilayer-Coated 50 nm Mesoporous Nanoparticles Efficiently Induce Microtubule Depolymerization upon Cell Uptake. *Nano Lett.* **10**, 2484-2492 (2010).
23. Varkouhi, A.K., Scholte, M., Storm, G. & Haisma, H.J. Endosomal escape pathways for delivery of biologicals. *J. Control. Release* **151**, 220-228 (2011).
24. Gruenberg, J. The endocytic pathway: a mosaic of domains. *Nat. Rev. Mol. Cell Biol.* **2**, 721-730 (2001).
25. Hansen, E.L. et al. Dose-Dependent ATP Depletion and Cancer Cell Death following Calcium Electroporation, Relative Effect of Calcium Concentration and Electric Field Strength. *PLoS One* **10**, e0122973 (2015).
26. Gupta, P.B. et al. Identification of selective inhibitors of cancer stem cells by high-throughput screening.

- Cell* **138**, 645-659 (2009).
27. Torrano, A.A. et al. A fast analysis method to quantify nanoparticle uptake on a single cell level. *Nanomedicine (London, U. K.)* **8**, 1815-1828 (2013).
 28. Stathopoulos, G.T. et al. Nuclear factor-kappaB affects tumor progression in a mouse model of malignant pleural effusion. *Am. J. Respir. Cell Mol. Biol.* **34**, 142-150 (2006).
 29. Stathopoulos, G.T. & Kalomenidis, I. Malignant pleural effusion: tumor-host interactions unleashed. *Am. J. Respir. Crit. Care Med.* **186**, 487-492 (2012).
 30. Lee, Y.C., Idell, S. & Stathopoulos, G.T. Translational Research in Pleural Infection and Beyond. *Chest* **150**, 1361-1370 (2016).
 31. Debnath, J., Muthuswamy, S.K. & Brugge, J.S. Morphogenesis and oncogenesis of MCF-10A mammary epithelial acini grown in three-dimensional basement membrane cultures. *Methods* **30**, 256-268 (2003).
 32. Marazioti, A. et al. Myeloid-derived interleukin-1 β drives oncogenic KRAS-NF- κ B addiction in malignant pleural effusion. *Nature communications* **9**, 672 (2018).
 33. Faul, F., Erdfelder, E., Lang, A.-G. & Buchner, A. G*Power 3: A flexible statistical power analysis program for the social, behavioral, and biomedical sciences. *Behav. Res. Methods* **39**, 175-191 (2007).
 34. Weng, W., Han, G., Du, P. & Shen, G. The Effect of Citric Acid Addition on the Formation of Sol-Gel Derived Hydroxyapatite. *Mater. Chem. Phys.* **74**, 92-97 (2002).

Chapter 8

Conclusion

This thesis was focused on two major topics: Developing a tool to control YAP activity in order to learn more about its role in cancer and more specifically its role in cancer spread and invasion. The second topic was the development of novel nanoparticle drug delivery systems with a focus on MOF-based drug carriers.

Chapter 3 details the main work of this thesis: the creation of a photoactivatable YAP. YAP was modified in order to block its main natural nuclear import pathway by exchanging the serine127 with an alanine. To prevent diffusion into the nucleus, its size was increased by the addition of two GFP. To allow for its photoactivation the NLS of SATB1 was appended to YAP and a photoactive caged lysine was used as the activation trigger. The newly created construct was dubbed optoYAP. OptoYAP is concentrated in the cytosol until it is activated via illumination, upon which it relocates to the nucleus and becomes active. The successful activation was proven both by tracking the attached GFP and through antibody staining of YAP. Luciferase assays showed a time dependency of the YAP activity with a maximum approximately 4 hours after activation, which could be corroborated in antibody staining experiments of YAP's different localisations at different times after activation. The activation of optoYAP was shown to increase cell proliferation in 2D environments compared to not-activated samples. qPCR revealed the activation of downstream targets CYR61 and CTGF. HeLa spheroids, embedded in a 3D collagen gel, exposed to optoYAP exhibited a strong increase in size, once activated and the growth could be directed by only illuminating the desired parts of the spheroid. These results demonstrate the successful creation of a powerful tool that allows for further investigations of YAP's role in cancer and the results already suggest that even the singular activation of YAP might be enough to trigger invasive behaviors in cell agglomerates. These first successful experiments show great promise for further applications of optoYAP in cancer and other research.

The subsequent chapters deal with novel drug delivery systems as potential future cancer treatment options. Chapter 4 and 5 discuss a novel approach for MOF drug carriers. The presented drug carrier is based on MIL-88A, a MOF composed of iron(III)-fumarate, which are both biologically common building blocks. Chapter 4 presents the initial synthesis and characterization of this new system. Amorphous MIL-88A nanoparticles were coated with exosomes to create a hybrid material. The coated particles showed high surface areas and high

loading capacities for calcein, as a model cargo, and SBHA as a model drug. The exosomes acted as an effective capping tool that prevented premature leakage. Additionally, it facilitated high cell uptake that was not noticeably impeded by endosomal entrapment and showed an efficient release of the cargo after three to four days of incubation. This carrier system was further developed as seen in chapter 5. The liposome coated MIL-88A nanoparticles were successfully loaded with SBHA as a singular drug and with irinotecan and floxuridine, simultaneously in a different experiment. The successful combined delivery of both cargos showed the potential of liposome coated MOF nanoparticles for combination therapy and further solidified their position as a promising class of hybrid materials for drug delivery.

In chapter 6, we report the development of crosslinked β -cyclodextrin nanoparticles. The obtained nanoparticles exhibit very fast cell uptake kinetics due to sugar-receptor mediated endocytosis and allow for covalent labeling with dye molecules to effectively track them in *in vitro* experiments. The porous cavities of the particles could be loaded with different cargo molecules, Hoechst 33342 as a model drug and doxorubicin as an effective anti-cancer drug. The cargos were successfully released once the particles reached the endosomal cell compartments due to the acidic environment, which lead to either nucleus staining or cell death depending on the cargo. These biocompatible nanoparticles show great potential for future applications as a drug delivery system.

Chapter 7, details the synthesis of lipid-coated calcium phosphate citrate nanoparticles (CPCs) and their application as a novel drug delivery system. They are amorphous particles that feature an extraordinary BET surface and a narrow pore size distribution. Furthermore, experiments on a wide variety of different cell lines, both tumorigenic and non-tumorigenic, were performed. Most cell lines showed uptake of the coated particles. The particles dissolve in the acidic pH of the endosomes, which leads to an ion-shock and apoptosis in cancer cells, but not the non-tumorigenic cell line MCF10A, hinting at a strong selectivity towards cancer cells. More aggressive and malignant cancer cells lines generally showed lower IC₅₀ values and were affected more strongly by the particles. This was further confirmed by mouse experiments with an intrapleural tumor model. A single injection of CPCs could reduce tumor mass by 40%. Long term studies with the less aggressive cancer cell line PANO2 showed no detectable adverse effects of CPC aside from pleural thickening. The high selectivity and

efficacy towards aggressive pleural tumors and low toxicity towards non-cancerous cells make CPCs a highly promising candidate for a new generation of anti-cancer drugs.

In conclusion, we have developed a novel tool for further investigations of YAP's role in cancer and cancer invasion that was successfully applied to induce growth in cancer cell spheroids, which is a promising starting point for further studies. Additionally, we developed novel drug carrier systems. A combination of MOF nanoparticles and lipid membranes was developed. It is a biocompatible nanocarrier that could load and efficiently release a variety of drugs and showed great cell uptake facilitated by the lipid coating. In addition, two novel non-MOF based nanoparticle systems were also developed and successfully applied as drug carriers *in vitro* and one even *in vivo*.

Chapter 9

Publications, Posters and Presentations

9.1 Publications

1) Spatio-selective activation of nuclear translocation of YAP with light directs invasion of cancer cell spheroids

Bernhard Illes, Adrian Fuchs, Florian Gegenfurtner, Evelyn Ploetz, Stefan Zahler, Angelika M. Vollmar, Hanna Engelke

Submitted

2) Exosome-coated Metal-Organic Framework Nanoparticles: An Efficient Drug Delivery Platform

Bernhard Illes, Patrick Hirschle, Sabine Barnert, Valentina Cauda, Stefan Wuttke, Hanna Engelke

Chemistry of Materials, **2017**, 29, (19), 8042–8046.

3) Liposome-Coated Iron Fumarate Metal-Organic Framework Nanoparticles for Combination Therapy

Bernhard Illes, Stefan Wuttke and Hanna Engelke

Nanomaterials, **2017**, 7 (11), 351

4) Biocompatible crosslinked β -cyclodextrin nanoparticles as multifunctional carriers for cellular delivery

Stefan Datz, Bernhard Illes, Dorothee Gößl, Constantin v. Schirnding, Hanna Engelke, Thomas Bein

Nanoscale, **2018**, 10, 16284-16292

5) Synergistic Combination of Calcium and Citrate in Mesoporous Nanoparticles Targets Pleural Tumors

Constantin von Schirnding, Ioanna Giopanou, Adam Hermawan, Giannoula Ntaliarda, Lisa Wehl, Bernhard Illes, Stefan Datz, Franz Geisslinger, Karin Bartel, Ann-Katrin Sommer, Marina Lianou, Veronika Weiß, Johann Feckl, Angelika M. Vollmar, Christoph Bräuchle, Georgios T. Stathopoulos, Ernst Wagne, Andreas Roidl, Thomas Bein, and Hanna Engelke

Accepted for publication in Chem.

9.2 Posters and Presentations

- | | | |
|----|-----------------------------------|--------------|
| 1) | CeNS/SFB1032 Workshop VENICE 2017 | Poster |
| 2) | SFB Summer School 2017 | Presentation |
| 3) | CELLMECH 2019, Milan Italy | Presentation |
| 4) | SFB1032 Jahresworkshop 2020 | Presentation |